APPLIED COMPUTATIONAL ELECTROMAGNETICS SOCIETY JOURNAL

May 2025
Vol. 40 No. 5
ISSN 1054-4887

The ACES Journal is abstracted in INSPEC, in Engineering Index, DTIC, Science Citation Index Expanded, the Research Alert, and to Current Contents/Engineering, Computing & Technology.

The illustrations on the front cover have been obtained from the ARC research group at the Department of Electrical Engineering, Colorado School of Mines

Published, sold and distributed by: River Publishers, Alsbjergvej 10, 9260 Gistrup, Denmark

MAY 2025 REVIEWERS

Mateusz Baran
Grzegorz Bogdan
Mouloud Challal
Yiming Chen
Arkaprovo Das
Stéphane Dufour
Alireza Ghaneizadeh
Srilakshmi Inuganti
Fidan Gamze Kizilçay
Tarun Kumar
Joan E. Lager
Lihua Li
Yangyang Liu
Leszek Nowosielski
Mahdi Oliaei
Andrew Peterson
Masoud Sarabi
Giovanni Maria Sardi
Fusun Oyman Serteller
Waleed Tariq Sethi
Partha Shome
Atul Varshney
Chao-Fu Wang
Dariusz Wojcik
Donghai Xiao
Yongliang Zhang
Zhonghao Zuo

THE APPLIED COMPUTATIONAL ELECTROMAGNETICS SOCIETY JOURNAL

Vol. 40 No. 5 May 2025

TABLE OF CONTENTS

Novel Strategies for Efficient Computational Electromagnetic (CEM) Simulation of Microstrip Circuits, Antennas, Arrays and Metamaterials Part-I: Introduction, Layered Medium Green's Function, Equivalent Medium Approach

Raj Mittra[1], Ozlem Ozgun[2], Vikrant Kaim[3], Abdelkhalek Nasri[4], Prashant Chaudhary[5], and Ravi K. Arya[6]

[1]Department of Electrical & Computer Science, University of Central Florida
Orlando, FL, USA
rajmittra@ieee.org

[2]Electrical & Electronics Engineering Department, Hacettepe University
Ankara, Turkey
ozgunozlem@gmail.com

[3]Centre for Applied Research in Electronics
IIT Delhi, India
vikrant.kaim@gmail.com

[4]XLIM Research Institute
UMR CNRS 7252, Limoges, France
abdelkhaleknasri2012@gmail.com

[5]Department of Electrical & Computer Science, University of Central Florida
Orlando, FL, USA
prashantelec129@gmail.com

[6]Zhongshan Institute of Changchun University of Science and Technology
Zhongshan, Guangdong, China
raviarya@cust.edu.cn

Abstract – Rapid-prototyping plays a critical role in the design of antennas and related planar circuits for wireless communications, especially as we embrace the 5G/6G protocols going forward into the future. While there are a number of software modules commercially available for such rapid prototyping, often they are found to be not as reliable as desired, especially when they are based on approximate equivalent circuit models for various circuit components comprising the antenna system. Consequently, it becomes necessary to resort to the use of more sophisticated simulation techniques, based on full-wave solvers that are numerically rigorous, albeit computer-intensive. Furthermore, optimizing the dimensions of antennas and circuits to enhance the performance of the system is frequently desired, and this often exacerbates the problem since the simulation must be run a large number of times to achieve the performance goal—an optimized design. Consequently, it is highly desirable to develop accurate yet efficient techniques, both in terms of memory requirements and runtimes, to expedite the design process as much as possible. This is especially true when the antenna utilizes metamaterials and metasurfaces for their performance enhancement, as is often the case in modern designs. The purpose of this paper is to present strategies that address the bottlenecks encountered in the generation of Green's Functions for layered media, especially in the millimeter wave frequency range where the dimensions of the antennas and the platforms upon which they are mounted can be several wavelengths in size.

The paper is divided into two parts. Part-I covers the topics of construction of layered medium Green's Function for millimeter wavelengths; the Equivalent Medium Approach (EMA) which obviates the need to construct Green's Function for certain geometries; and the T-matrix approach for hybridizing

Submitted On: November 1, 2024
Accepted On: April 24, 2025

https://doi.org/10.13052/2025.ACES.J.400501

the finite methods with the Method of Moments (MoM).

In Part-II of this paper, we go on to discuss three other strategies for performance enhancement of CEM techniques: the Characteristic Basis Function Method (CBFM); mesh truncation for finite methods by using a new form of the Perfectly Matched Layer (PML); and GPU acceleration of MoM as well as FDTD (Finite Difference Time Domain) algorithms.

The common theme between the two parts is the "performance enhancement" of CEM (Computational Electromagnetics) techniques, which provides the synergistic link between the two parts.

Index Terms – 5G/6G Communication, Antenna Design, Computational Electromagnetics (CEM), Equivalent Medium Approach (EMA), Layered medium Green's Functions, Metamaterials, Method of Moments (MoM), Microwave Circuits, Millimeter-Waves.

I. INTRODUCTION

It is well known that Computational Electromagnetics (CEM) is a mature field with a long history. Some of the pioneering contributors to the field are Harrington [1] who introduced the Method of Moments (MoM); Silvester [2] who did pioneering work on the application of the Finite Element Method (FEM) to electromagnetic problems; Yee [3] who is credited for bringing us the Finite-Difference Time-Domain (FDTD) method; and, Keller [4] and his colleagues who are recognized for introducing to us asymptotic methods for solving electromagnetic scattering problems at high frequencies that are too large to handle by using the three numerical techniques we have mentioned above.

It's worthwhile to mention at this point that much of the CEM activity in the past focused on Radar Cross-Section (RCS) computation, as may be readily verified by referring to the existing CEM literature. Although this field is still regarded as quite important, the focus has appeared to have shifted to other CEM applications that have come to the fore in recent years because of increasing interest in the design of microwave circuits and antennas for communication applications. Even more recently, the advent of 5G/6G in the communication scene has created interest in the millimeter wave frequency range, as for instance in the 24 to 27 GHz band, or even higher, such as the 60 GHz band. It is worthwhile to point out that it is not always just a matter of scaling the design of an antenna, or a microwave circuit, or the way they are numerically modeled, then we go up to millimeter waves from microwave frequencies. Given this background, one of the goals of this work is to present innovative techniques for handling the CEM modeling problems at millimeter waves in a numerically efficient manner without compromising the accuracy of the results.

Figure 1 shows a variety of microwave circuit and antenna problems, some of which will be discussed in this work to illustrate the application of the techniques that we will describe below. A common thread that binds these problems is that they are all printed-circuit types and the first step in the conventional approach for modeling such circuits and antennas is to derive the Green's Function for a layered medium upon which they are printed.

In the next section, we examine this problem and point out the difficulties encountered in generating these Green's Functions for layered media when the operating frequency is in the millimeter frequency range. Next, we present a technique for successfully resolving the difficulties that we have identified earlier. The presentation in this section is based on a recent work by the authors and the interested reader is referred to Ozgun et al. [5] for additional details.

II. LAYERED MEDIUM GREEN'S FUNCTION FOR MILLIMETER WAVES

In this section, we introduce an efficient method for evaluating Sommerfeld integrals, which are essential in calculating spatial-domain Green's Functions in planar multilayered media. The proposed technique effectively overcomes the challenges posed by the highly oscillatory and slowly decaying nature of these integrals, particularly at high frequencies such as millimeter waves—frequencies that are increasingly critical for advanced technologies like 5G and beyond. By employing a strategic interpolation and extrapolation scheme, the method reduces the number of sample points required to accurately represent the integrand, enabling the use of analytical integration. This simplification significantly accelerates the evaluation process. Extensive testing across various Green's functions validates the accuracy and efficiency of the method.

Planar multilayered structures are prevalent in modern technology, with applications ranging from platform-mounted antennas to microstrip printed circuits. Accurate analysis of these structures often relies on the MoM, which is based on the Mixed-Potential Integral Equation (MPIE). A critical component of this method is the Green's Functions, which are initially derived in the spectral domain via the Fourier transform and subsequently converted into the spatial domain through an inverse Fourier transform [6, 7]. This process results in a one-dimensional integral known as the Sommerfeld Integral (SI), defined over a semi-infinite interval of the complex spectral variable.

Evaluating these SIs is challenging due to two primary factors: (i) the presence of singularities on or

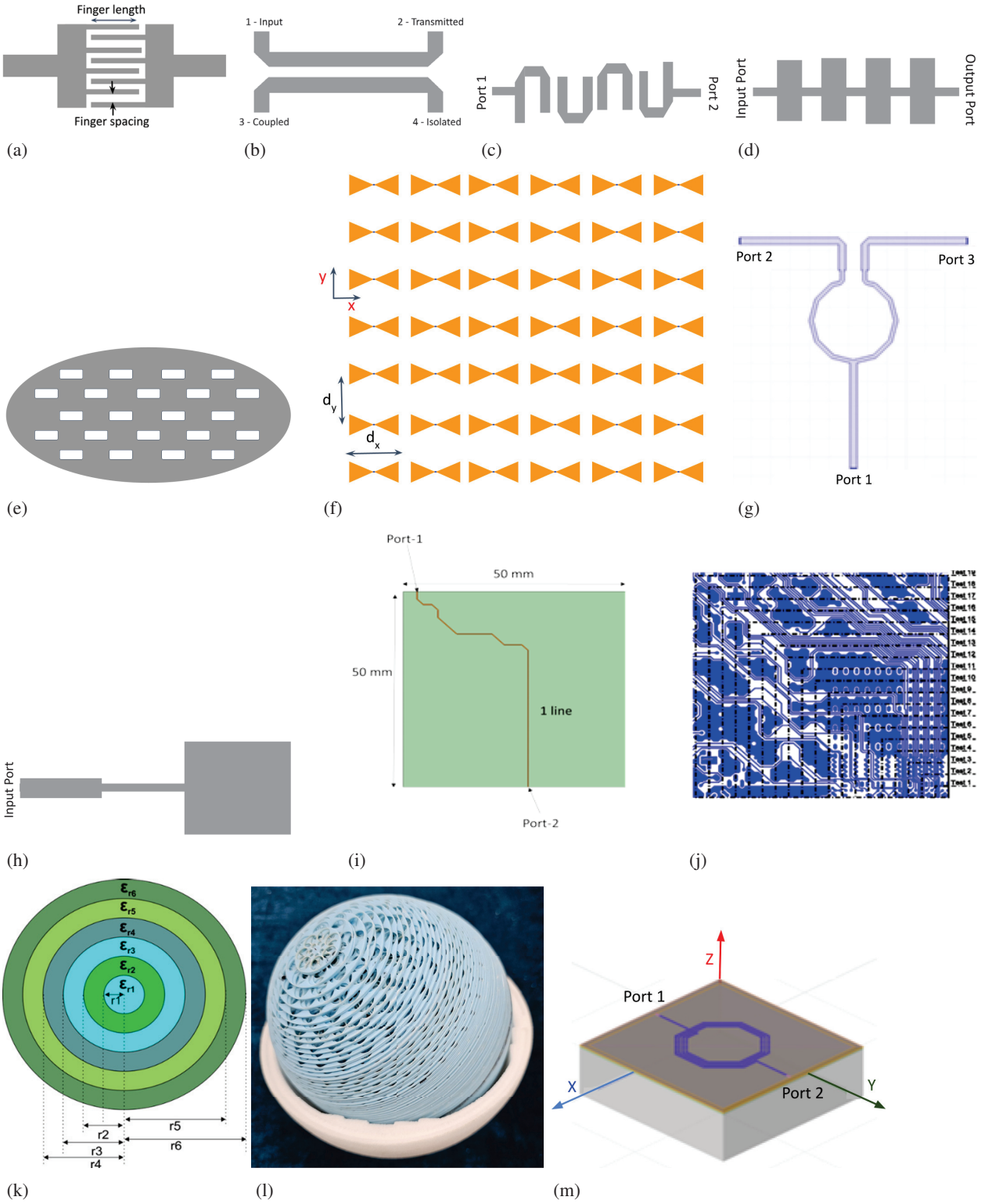

Fig. 1. Various microwave circuits and antenna structures: (a) microstrip line filter, (b) microstrip directional coupler, (c) Hairpin microstrip filter, (d) four-stage bandstop filter, (e) small patch array, (f) large bow-tie patch array, (g) Wilkinson power divider, (h) patch antenna with a wideband matching circuit, (i) packaging board with a single trace, (j) typical package layer, (k) Luneburg lens cross-section, (l) 3D cutout of the interior, and (m) spiral inductor on a multilayer dielectric.

near the integration path and (ii) the highly oscillatory and slowly decaying nature of the integrand. Traditional approaches often handle singularities by deforming the integration path in the complex plane, but the oscillatory behavior remains a significant obstacle. The Discrete Complex Image Method (DCIM) has been widely employed to address this issue [8]. The authors previously developed a Green's Function module for commercial electromagnetic software using DCIM to compute SIs. While this module performed effectively at microwave frequencies, it faced substantial computational challenges at higher frequencies, such as those used in millimeter-wave applications for 5G technology. The core issue stems from the increased oscillatory nature of the SIs as the radial distance between the source and observation points becomes electrically large, a common scenario at millimeter-wave frequencies. Under these conditions, accurately representing the integrand with a few complex exponentials becomes increasingly difficult, leading to inefficiencies and numerical instability in the DCIM.

Recently, the authors introduced an innovative approach that addresses the inherent challenges of conventional DCIM [5, 9, 10]. Our method not only improves the efficiency and accuracy of SI evaluations across a broad frequency range but also simplifies the computational process without sacrificing precision. The key advancement lies in isolating the oscillatory component of the integrand as a cosine function while representing the remaining smooth envelope function using function approximation techniques such as Prony [11] or the Generalized Pencil of Function (GPOF) method [12].

A. Mathematical formulation

When simulating antennas and printed circuits on layered media using the MPIE within the MoM framework, the evaluation of SIs is critical. Solving the MPIE for a general multilayered media problem involves evaluating 16 spectral domain GFs and a total of 22 SIs [6, 7]. These SIs are expressed as:

$$S_n\left\{\tilde{G}\left(k_\rho, z|z'\right)\right\} = \frac{1}{2\pi}\int_0^\infty \tilde{G}\left(k_\rho, z|z'\right) J_n\left(k_\rho\rho\right) k_\rho{}^{n+1} dk_\rho, \quad (1)$$

where the kernel $\tilde{G}$ represents the spectral-domain Green's Function, J_n is the Bessel function of order $n = 0, 1$, k_ρ is the complex spectral variable, z' and z are the vertical coordinates of the source and observation points respectively, and ρ is the lateral distance between these points. These parameters collectively form the foundation of this computational process.

To address the computational challenges, our approach partitions the integration interval into multiple distinct regions (as illustrated in Fig. 2), each handled separately with a novel integration strategy that facilitates closed-form analytical solutions. In Region 2, where the singularity occurs, we deform the integration path and apply a standard numerical method to accurately manage this small but crucial region. Conversely, Regions 1 and 3, which are characterized by an oscillatory integrand due to the Bessel function, are treated differently. In these regions, the integrand behaves as a damped sinusoidal function with a smooth envelope. This behavior is effectively captured using the large-argument form of the Bessel function. Eventually, the integrand (denoted by I) is expressed as follows [5]:

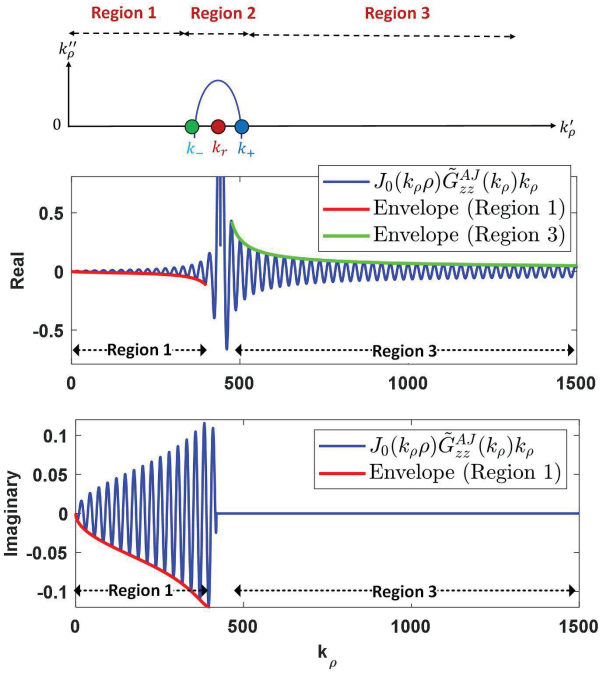

Fig. 2. Illustration of the proposed integration method.

$$I = f\left(k_\rho\right)\cos\left(k_\rho\rho - \frac{n\pi}{2} - \frac{\pi}{4}\right), \quad (2)$$

where $f(k_\rho)$ is the smooth envelope function, which is given by

$$f\left(k_\rho\right) = \sum_{i=1}^{M} a_i e^{-b_i k_\rho}, \quad (3)$$

where a_i and b_i are the poles and residues, respectively, and M is the number of poles/residues.

These parameters are determined through interpolation methods such as Prony or the GPOF method. In our tests, combining the Prony method with the Total Least Squares (TLS) technique, we found that using just a few terms (e.g., $M = 3$ or 4) along with a limited number of envelope samples yielded highly accurate results. The proposed method's ability to reduce the integrand to a few terms enables the use of straightforward closed-form analytical integration techniques. While traditional

DCIM shares this feature, our method is significantly more efficient, particularly when handling the highly oscillatory integrands encountered at millimeter-wave frequencies. This increased efficiency arises because our approach focuses on the smooth envelope function rather than directly dealing with the oscillatory integrand in its original form, as done in traditional DCIM.

B. Numerical results

In this section, we present numerical examples to validate and demonstrate the effectiveness of our proposed approach. We consider a dielectric medium with a permittivity of 3.5, a loss tangent of 0.001, and a thickness of 1 mm, backed by a conducting plane, with an operating frequency of 20 GHz. The integrand corresponding to Green's Function $\tilde{G}_{zz}^{AJ}$ is analyzed, as shown in Fig. 2. Figures 3 and 4 illustrate the envelope functions, assuming a lateral distance of $\rho = 16\lambda_0$ (where λ_0 is the free-space wavelength) with the source and observation points located within the same layer ($z' = 1$ mm, $z = 1$ mm). It is important to note that our method is

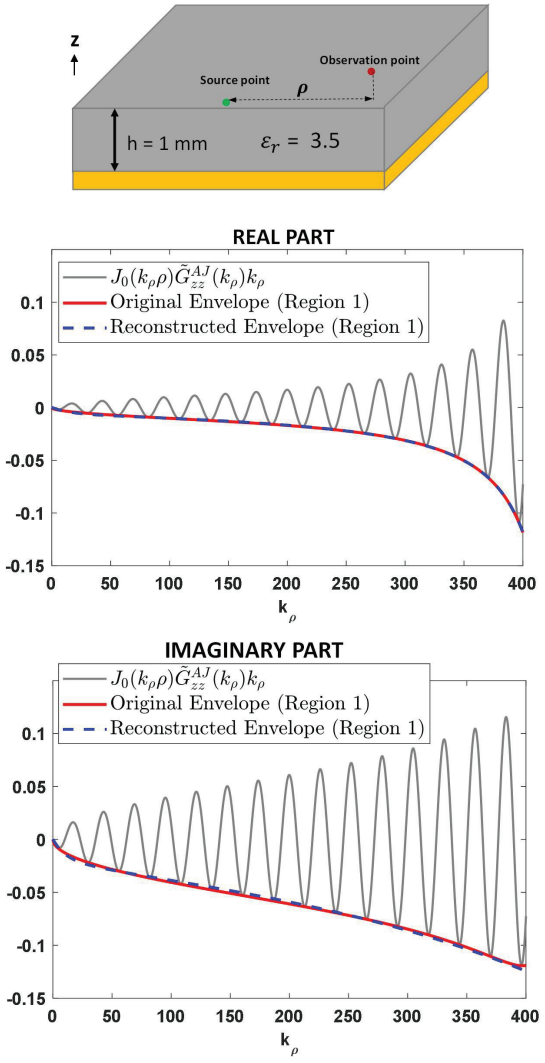

Fig. 3. Original and reconstructed envelope functions in Region 1.

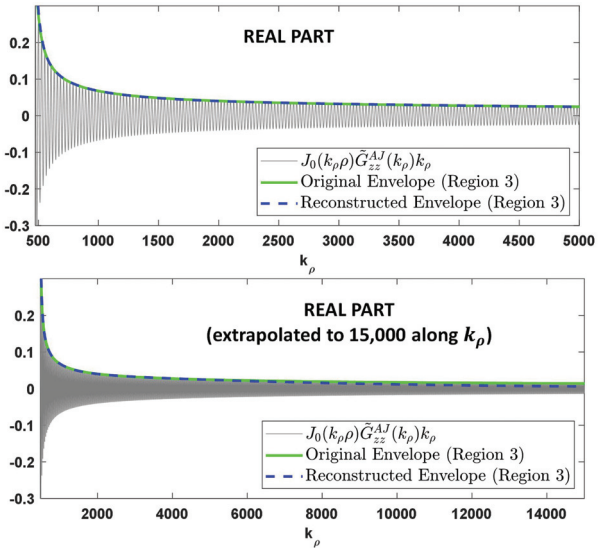

Fig. 4. Original and reconstructed envelope functions in Region 3.

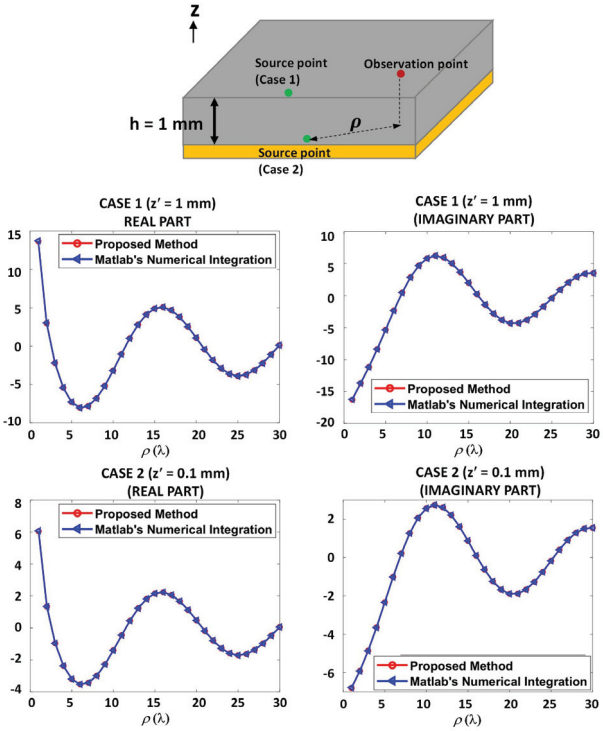

Fig. 5. SI values as a function of radial distance for two different source point positions ($z' = 1$ mm and $z' = 0.1$ mm) when the observation point is $z = 1$ mm.

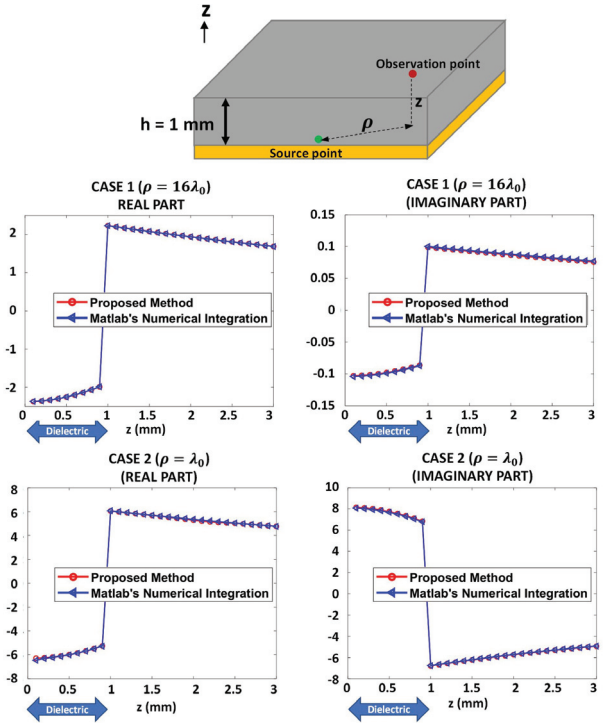

Fig. 6. SI values as a function of vertical distance for two different lateral distances ($\rho = 16\lambda_0$ and $\rho = \lambda_0$) when the source point is $z' = 0.1$ mm.

versatile and can also handle scenarios where the source and observation points are in different layers. For this example, we use $M = 4$ terms in the summation. The envelope function is sampled and interpolated using 20 samples in Region 1 and 45 samples in Region 3. Figures 5 and 6 show the SI values as functions of the radial and vertical distances, respectively. These results are compared with those obtained using MATLAB's numerical integration function, which is significantly more time-consuming than our method. For a single simulation in Fig. 5, the computation times on an Intel i9-10885 CPU are 1.6 seconds and 4.6 seconds using the proposed method and MATLAB's integration routine, respectively. Similarly, for a single simulation in Fig. 6, the computation times are 0.26 seconds and 1.6 seconds using the proposed method and MATLAB's integration routine, respectively. These results demonstrate that the proposed approach significantly accelerates the solution process, which could potentially reduce the matrix fill-time in MoM.

It is also worth noting that, to further enhance computational efficiency, an interpolation scheme can be employed to approximate the SI values along the vertical (z) direction as well. Details of this scheme can be found in [5].

III. EQUIVALENT MEDIUM APPROACH

A. EMA for printed circuits and antennas

In this section, we present a novel technique for numerical modeling of planar circuits and antennas printed on layered media, typical examples of which have been presented earlier in Fig. 1. The novelty of this approach stems from the fact that it totally obviates the need for the construction of the layered medium Green's Function; hence, it is not only less tedious but also far more numerically efficient to use than constructing the more rigorous Green's Function for the layered media. Although empirical, the numerical results generated by using this approach are remarkably accurate as we will see from the results for the S-parameters presented later in this section. In fact, often the difference between the S-parameter results generated by the two different commercial codes, such as CST and HFSS, is of the same order (or larger) than the difference between the numerical results derived by using the complex image method described in the previous section, and the EMA. We note that in HFSS [13], a 3D full-wave frequency-domain electromagnetic (EM) field solver utilizing the FEM is employed, while in CST [14], a time-domain EM field solver based on the FDTD method is used.

The basic strategy of the EMA is relatively simple. We begin with a planar transmission line, such as a microstrip line, printed on a substrate (typically a single-layer dielectric) backed by a ground plane, as shown in Fig. 7 (a). Next, we replace the layered medium with a homogeneous medium in the entire half-space above the ground plane, as shown in Fig. 7 (b). The effective epsilon (ε_{eff}) of the homogeneous medium is obtained by using the equations (4)-(8) that were originally derived in [15], for a microstrip line whose trace width is w, substrate thickness is h, and whose relative permittivity of the substrate is ε_r. Our strategy is to use these effective epsilons to replace the original geometries of the microstrip circuits and antennas with their equivalent geometries (see Figs. 7 (a) and 7 (b)). Another reliable way of doing this is to determine ε_{eff} of the homogeneous medium such that the propagation constant along the original microstrip line in Fig. 7 (a) is the same as that of the transmission line shown in Fig. 7 (b), which is embedded in a homogeneous half-space.

We present two options for determining the ε_{eff}. The first of these is to use the quasi-analytical formulas given in [15], which express the effective epsilon directly in terms of the parameters of the transmission line shown in Fig. 7. The formulas are given in equations (4)-(8):

$$\varepsilon_{eff}(f) = \left[\frac{\sqrt{\varepsilon_r} - \sqrt{\varepsilon_{eff}}}{1 + 4F_1^{-1.5}} + \sqrt{\varepsilon_{eff}}\right]^2, \qquad (4)$$

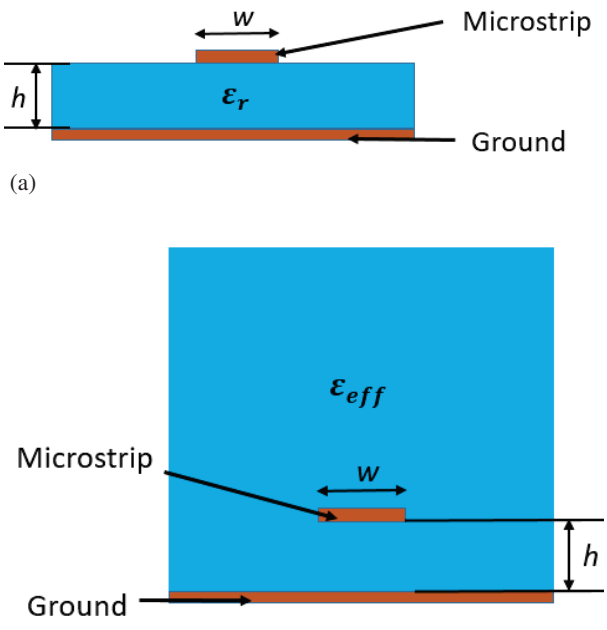

Fig. 7. Comparison of the original geometry in a layered medium and the equivalent geometry in a homogeneous medium: (a) side view of the original geometry with free space above the patch and a dielectric substrate below and (b) side view of the equivalent geometry with an equivalent dielectric above and below the patch.

$$\sqrt{\varepsilon_{eff}} = \frac{\varepsilon_r + 1}{2} + \frac{\varepsilon_r - 1}{2}\left[(1 + 12\frac{h}{w})^{-0.5} + Factor\right] \; if \;\; \frac{w}{h} \leq 1, \tag{5}$$

$$\sqrt{\varepsilon_{eff}} = \frac{\varepsilon_r + 1}{2} + \frac{\varepsilon_r - 1}{2}\left(1 + 12\frac{h}{w}\right)^{-0.5} \; if \;\; \frac{w}{h} > 1, \tag{6}$$

$$Factor = 0.4\left(1 - \frac{w}{h}\right)^2, \tag{7}$$

$$F_1 = \left(\frac{4hf}{c}\sqrt{\varepsilon_r - 1}\right) \times \left[\frac{1}{2} + \left\{1 + 2log_{10}\left(1 + \frac{w}{h}\right)\right\}^2\right], \tag{8}$$

where w is width of the microstrip, h is thickness of the substrate, c is the speed of light in vacuum, f is the frequency of operation, ε_r is dielectric constant of the substrate in Fig. 7 (a), ε_{eff} is equivalent dielectric constant of the homogeneous medium of the half-space in Fig. 7 (b). The second option, referred to herein as the short-circuit method, first terminates the line with a short circuit and then extracts the wave number β from the resulting standing waves on the line by measuring the distance between the minima of the standing waves. The latter approach is more accurate but is also more time-consuming because it requires a numerical simulation of the microstrip transmission line. In any case, the two results for the ε_{eff} are very close to each other.

Let us consider an example to illustrate the extraction procedure of the effective epsilon (ε_{eff}). We begin with an original geometry of a microstrip line whose width w is 4.84 mm, the relative permittivity (ε_r) of its substrate is 2.2, while its thickness h is 1.57 mm. The first method, based on the formula given in equations (4)-(8), provides ε_{eff} = 1.89, at the frequency of interest 2.4 GHz. The second method, based on short circuit termination, yields ε_{eff} = 1.9, for which the propagation constant ($\gamma = j\beta = j157.08$ rad/m) of the line embedded in a homogeneous medium is identical to the propagation constant ($\gamma = j157.08$ rad/m) of the original line in a layered medium at the frequency of 2.4 GHz. We observe that both the methods are reliable and accurate, and we subsequently use the simpler 'equivalent' geometry to model the microstrip circuit, which obviates the need for the construction of the layered medium Green's Function altogether; hence the EMA is numerically efficient.

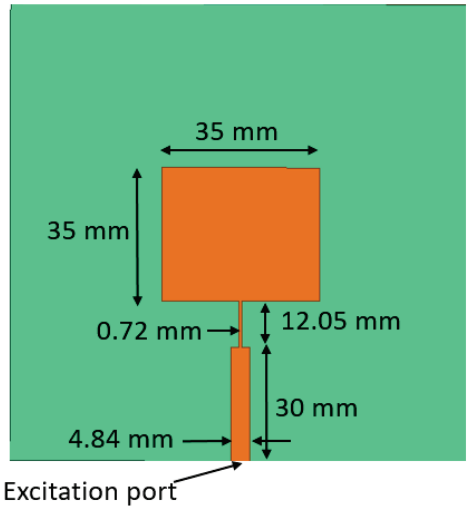

Fig. 8. Top view of the geometry of MPA (backed by full ground plane). The green area shows substrate and the orange area shows copper.

Next, we proceed to illustrate the use of the EMA by considering the example of a microstrip patch antenna (MPA) fed by a stepped transmission line geometry designed to provide the antenna with a wideband match. The antenna configuration is shown in Fig. 8. The relative permittivity (ε_r) of the substrate is 2.2, and its thickness (h) is 1.57 mm. The reason we choose this example is that the width (w) of the trace in this geometry changes

three different times; hence, it brings up an important question that we must resolve before proceeding to simulate this geometry, regardless of which method we use–the formula or the short-circuit termination–to extract the effective epsilon (ε_{eff}). Since this geometry has three different widths, we would generate three different values for the ε_{eff}, two for the two transmission lines with different trace widths, and the third for the patch, which we are still treating as a microstrip line for the purpose of extracting the ε_{eff}. The quasi-analytical formulas, given in equations (4)-(8) generated three different values for the ε_{eff} viz., 1.73, 1.89, and 2.14 for the three trace widths, w = 0.72 mm, 4.84 mm, and 35 mm, respectively, at the frequency of interest 5.5 GHz. (Note: We can apply the same procedure for other frequencies of interest equally well.) The problem is that an MoM code can only deal with a single ε_{eff}, and not with different epsilons in different sub-regions. To address this issue, we propose two different approaches.

In the first approach, we define a composite representation of the ε_{eff} as a weighted average which reads:

$$Composite\ \varepsilon_{eff} = \frac{A_1\varepsilon_{eff1} + A_2\varepsilon_{eff2} + A_3\varepsilon_{eff3}}{A_1 + A_2 + A_3}, \tag{9}$$

$$Modified\ Composite\ \varepsilon_{eff} = \left(\frac{A_1\varepsilon_{eff1} + A_2\varepsilon_{eff2} + A_3\varepsilon_{eff3}}{A_1 + A_2 + A_3}\right) F, \tag{10}$$

where A_1 represents the area of the patch (w = 35 mm), A_2 corresponds to the area of the thin line (w = 0.72 mm), and A_3 denotes the area of the feed line (w = 4.84 mm). The effective permittivities associated with these regions are denoted as ε_{eff1} for the patch, ε_{eff2} for the thin line, and ε_{eff3} for the feed line. Using equation (9), the composite effective permittivity ε_{eff} is computed as 2.11.

This composite ε_{eff} is then used to simulate the antenna, including both the patch and its stepped feedline, and the results are compared with those obtained from a commercial solver for the original layered-medium geometry. Figure 9 presents this comparison, showing the S-parameter ($S11$) of the antenna as a function of frequency, derived using the HFSS simulator. The results indicate a slight shift in the resonant frequency of the antenna when employing the numerical simulation based on the EMA, using the HFSS simulation as the reference.

To further improve the agreement between the two methods, an empirical factor F is introduced (see equation (10)), which scales down the composite ε_{eff} to 2.02. Through numerical experiments, F is determined to be 0.96. Figure 9 illustrates that the $S11$ plot of the original MPA in a layered medium (substrate permittivity ε_r=2.2) closely matches the $S11$ plot of the equivalent MPA geometry when the modified composite ε_{eff} is set to 2.02. The S-parameter results obtained using this adjusted composite permittivity demonstrate the effectiveness of the empirical factor in enhancing the accuracy of the EMA. The agreement achieved through this correction is often comparable to or even better than that obtained by using two different commercial solvers to simulate the same problem geometry.

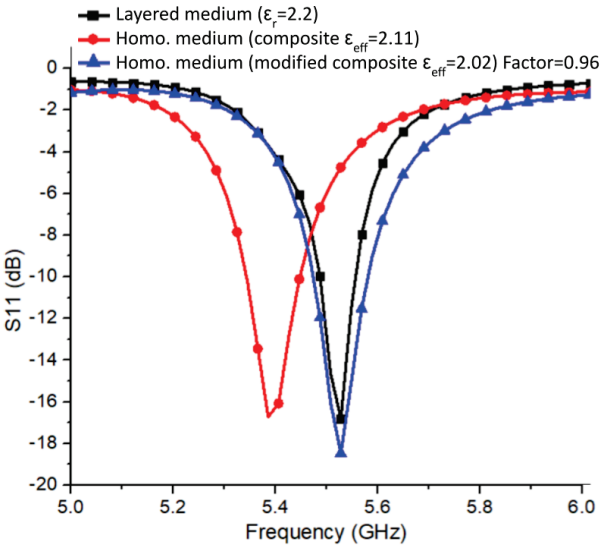

Fig. 9. Comparison plot of $S11$ versus frequency for the MPA geometry between layered medium and homogeneous medium. Terminating impedance, Z_{in} = 50 Ω for both mediums. The simulator used: HFSS.

It is evident that indeed using a modified composite ε_{eff} yields a result that compares very favorably with the one obtained from a rigorous numerical simulation that employs a commercial code such as the HFSS or CST, for instance, and its use provides an obvious time-saving advantage. We now present two other examples to demonstrate the versatility of the EMA utilizing the formula method to derive the effective epsilon of the equivalent geometry of the problem at hand. As an example, we show the results of the geometry of four elements MPA utilizing, as shown in Fig. 10, for the frequency range 2 – 3 GHz. The relative permittivity (ε_f) of the substrate is 2.2 in a layered medium, and its thickness (h) is 1.57 mm. The composite ε_{eff} of the homogeneous medium is calculated to be 2.11 and the empirical factor, F as 0.97, scales down the composite ε_{eff} to 2.05. The comparison is shown in Fig. 11, which plots the S-parameter ($S11$) of the antenna array as a function of frequency, using HFSS, at the frequency of interest 2.4 GHz. We observe that the $S11$ plot of the original MPA array in a layered medium (substrate ε_r = 2.2) matches well with the $S11$ plot of

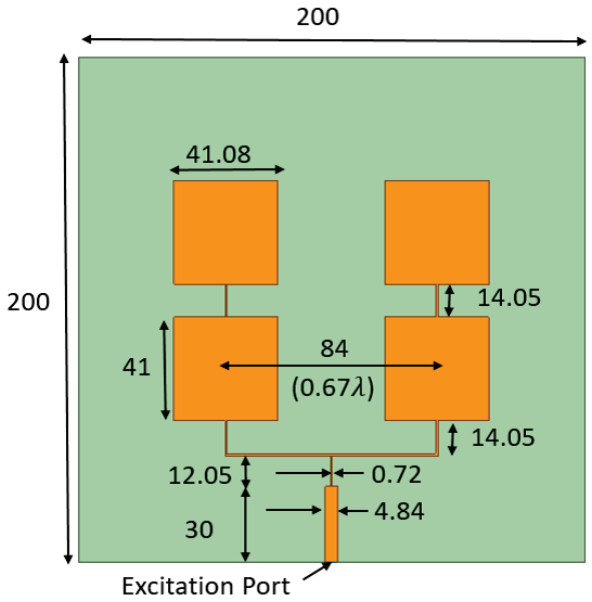

Fig. 10. Top view of the geometry of four elements MPA array (backed by full ground plane). All dimensions are in millimeters (mm). The green area shows substrate and the orange area shows copper.

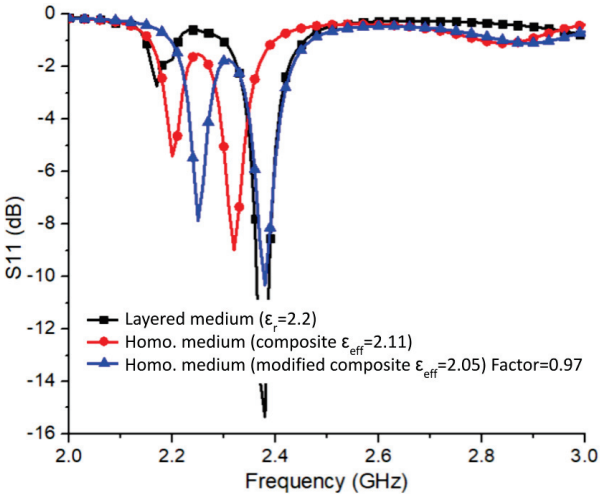

Fig. 11. Comparison of $S11$ as a function of frequency for the MPA array geometry in both layered and homogeneous media. The terminating impedance Z_{in} is 50 Ω in both cases. Simulations were performed using HFSS.

the equivalent geometry of the MPA array in a homogeneous medium, when the modified composite ε_{eff} of the homogeneous medium is 2.05.

Next, we present the results for the two-port stepped filter geometry, shown in Fig. 12, for the frequency range 5–6 GHz. The relative permittivity (ε_r) of the substrate is 4.0, and its thickness (h) is 1 mm. Figures 13 and 14 plot

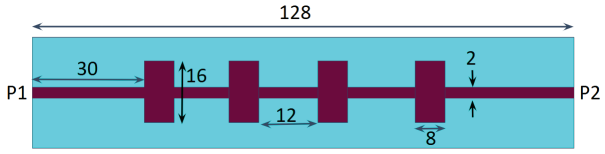

Fig. 12. Top view of the geometry of stepped filter (backed by full ground plane). All dimensions are in millimeters (mm). The green area shows substrate and the brown area shows copper.

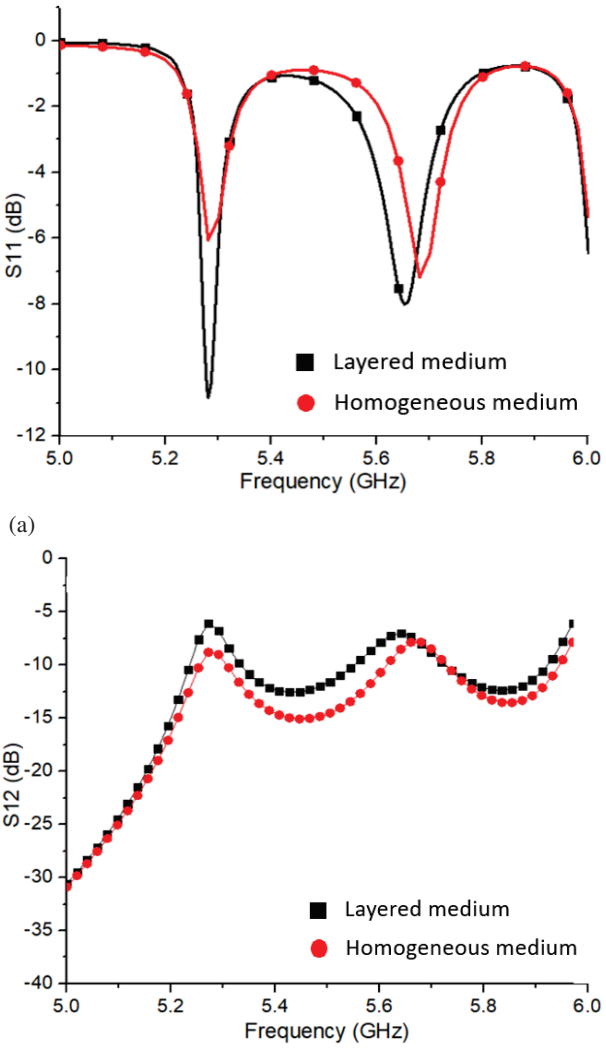

Fig. 13. Comparison of S-parameters as a function of frequency for the stepped filter geometry in both layered and homogeneous media: (a) $S11$, (b) $S12$. The terminating impedance Z_{in} is 50 Ω in both cases. Simulations were performed using HFSS.

the S-parameters ($S11$, $S12$) as functions of frequency obtained by using the HFSS and CST. The S-parameters

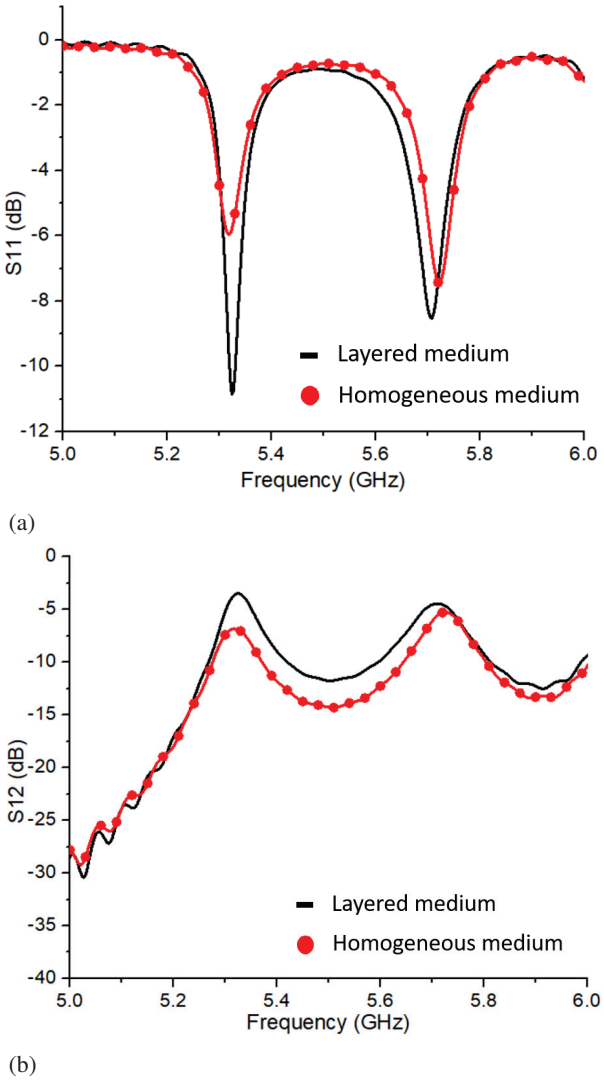

Fig. 14. Comparison of S-parameters as a function of frequency for the stepped filter geometry in both layered and homogeneous media: (a) $S11$, (b) $S12$. The terminating impedance Z_{in} is 50 Ω in both cases. Simulations were performed using CST.

plots of the original geometry of the stepped filter in a layered medium (substrates $\varepsilon_r = 4.0$) match with the S-parameters plot of the equivalent geometry of the stepped filter embedded in a homogeneous medium, at the frequency of interest 5.5 GHz; when the modified composite ε_{eff} of the homogeneous medium is 3.25.

It is worthwhile to mention here that although we have only presented results based on the use of the 'formulas' to obtain the effective epsilons of the microstrip lines, we could have also employed the short-circuit termination method with a slightly different empirical factor F to achieve essentially the same S-parameter results for the problem at hand that agree with the reference results for the same parameters when the simulation is carried out by using the commercial CEM codes. As mentioned before, the 'formula' option is more efficient and, hence, is our preferred choice.

Before closing this section, we would like to mention a novel strategy, which enables us to use multiple effective $\varepsilon's$, as opposed to a single composite one, by combining the EMA with the T-matrix approach. This approach begins with a domain decomposition of the original geometry into several blocks, each of which has its own effective ε that depends on the width of the trace as we have explained earlier. The next step is to extract the S-parameters of each of these blocks by using the EMA. Finally, we generate the S-parameters of the original geometry by cascading the S-parameters of the different blocks by using the T-matrix algorithm [16]. This algorithm will be discussed more fully in section IV, where hybrid CEM methods with finite methods will be presented.

To illustrate the proposed procedure for handling geometries with multiple trace widths, let us consider the case of double-step discontinuity in a 50Ω – 100Ω – 50Ω microstrip line, shown in Fig. 15. The three blocks for this microstrip line geometry are shown in Fig. 15 printed on a substrate ε_r = 4 of thickness 1.5mm. The Line-1, length = 25mm, width = 2.4mm, Line-2, length = 25mm, width = 0.4mm, and Line-3, length = 25mm, width = 2.4mm. Note that the S-parameters of the individual blocks, each of which in this example is a simple uniform transmission line, can be readily derived on paper without having to run any numerical simulation at all. We have verified that the accuracy of this approach is very high, as the numerical results to be presented in section I [17] readily demonstrate.

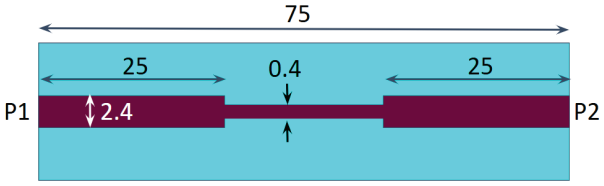

Fig. 15. A 50Ω – 100Ω – 50Ω discontinuous microstrip line. All dimensions are in millimeters (mm).

A similar strategy can be used to simulate the packaging problem shown in Figs. 1 (i) and 1 (j).

B. Equivalent medium approach for metasurfaces and metamaterials

In recent years, there has been an increase in the use of metamaterials (MTMs) and metasurfaces (MTSs) as performance enhancers of communication antennas. Typically, MTMs and MTSs are truncated periodic or

quasi-periodic structures, designed to control the reflection, transmission, or propagation characteristics of a material slab (or a surface) in a desirable manner. However, an extensive search of the literature reveals that very rarely we are provided a clue that explains how to choose the particular shape, size, or material parameters of an element of the quasi-periodic MTS to realize the desired performance of the antenna utilizing the MTS. Designing the MTS typically requires extensive numerical simulations, which can be tedious as well as time-consuming, especially when the antenna, which is typically an array for millimeter wave applications, is several wavelengths in size.

A common strategy for dealing with MTSs is to extract their material parameters, as a first step to numerically modeling them. A number of authors [15, 18–20] have presented techniques for extracting the material parameters (ε, μ) of the unit cell of an MTM slab. The present technique differs from the existing methods for characterizing MTMs and MTSs in two ways. First, it works with ε-only parameters, by assuming that μ is either μ_0 or constant. Second, it extracts the parameters of the ε tensor in a very different way than has been published in the existing literature. The method of extraction proposed herein is not only simple but is also tailored for typical antenna applications, which depend upon the reflection, transmission, and propagation characteristics of MTSs, for instance.

In the previous section, we have presented the details of the EMA for efficient numerical simulation of microstrip circuits and antennas bypassing the generation of Green's Function for layered media. Computational bottleneck also arises when dealing with MTSs and MTMs, in combination with antennas, used to enhance the performance of the antenna or to realize the antenna itself by employing MTMs because the requisite material is unavailable off-the-shelf.

The basic strategy is still to replace the metamaterial – which often has fine or multi-scale features – with an equivalent dielectric, which is much simpler to deal with numerically. The use of this tactic renders the simulation numerical simulation much more efficient than it would be if we were to deal with the original MTM directly, as we would when using a commercial EM simulator. In this section, we provide the details of this procedure, based on the EMA by considering the example of a MPA (or array) covered with an MTS superstrate to enhance its performance.

The EMA to deriving the equivalent dielectric slab is based on matching the phase of the transmission coefficient of the original metasurface and the equivalent dielectric slab based in a unit cell, as shown in Fig. 16.

The first step in this EMA-based procedure is to replace the unit cell of the metasurface with a permittivity tensor by using the procedure described below. The procedure is general and is applicable to both isotropic and anisotropic metasurfaces.

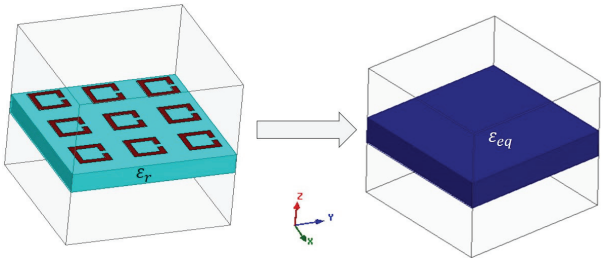

Fig. 16. Original MTS (left) and its equivalent dielectric slab (right).

By using this approach, we can calculate the ε of the metasurfaces in each direction of propagation. Generally, the metasurface is an anisotropic slab and is characterized by using an ε tensor as follows:

$$\varepsilon = \begin{pmatrix} \varepsilon_{xx} & \varepsilon_{xy} & \varepsilon_{xz} \\ \varepsilon_{yx} & \varepsilon_{yy} & \varepsilon_{yz} \\ \varepsilon_{zx} & \varepsilon_{zy} & \varepsilon_{zz} \end{pmatrix}, \tag{11}$$

where x, y, and z are the three propagation directions.

After deriving the equivalent epsilon (ε_{eq}) representation of the original metasurface, we replace it just by the dielectric slab for the numerical simulation of the antenna plus metasurface combination.

For an example of MTS material (shown in Fig. 17 (a)), the diagonal elements in the above matrix are identical for x and y directions and the ε of the dielectric slab can be represented by:

$$\varepsilon = \begin{pmatrix} \varepsilon & 0 & 0 \\ 0 & \varepsilon & 0 \\ 0 & 0 & \varepsilon_{zz} \end{pmatrix}, \tag{12}$$

However, the equivalent epsilon of the dielectric slab for the MTS in Fig. 17 (b), is represented by a uniaxial representation (13):

$$\varepsilon = \begin{pmatrix} \varepsilon_{xx} & 0 & 0 \\ 0 & \varepsilon_{yy} & 0 \\ 0 & 0 & \varepsilon_{zz} \end{pmatrix}, \tag{13}$$

where the ε_{xx} and ε_{yy} are not the same.

For certain anisotropic materials, we only need the diagonal matrix to characterize the permittivity of the material, but for accurately characterizing a chiral material [21], we need to include the off-diagonal terms of the ε tensor as well. Figure 17 (c) shows the layout of the example unit cell of a chiral metasurface, for which the ε for the anisotropic off-diagonal matrix is represented by:

$$\varepsilon = \begin{pmatrix} \varepsilon_{xx} & \varepsilon_{xy} & 0 \\ \varepsilon_{yx} & \varepsilon_{yy} & 0 \\ 0 & 0 & \varepsilon_{zz} \end{pmatrix}, \tag{14}$$

It is worthwhile to mention here that the EMA is very versatile. It is not just limited in its application to

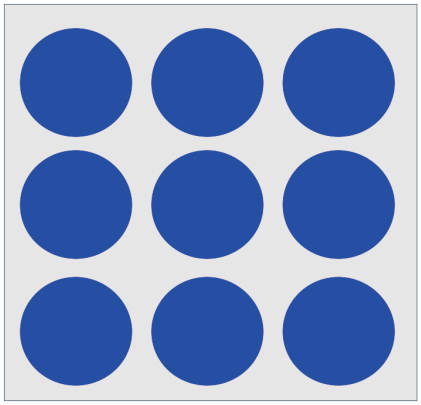

(a)

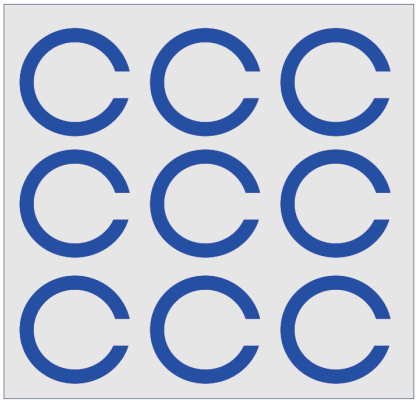

(b)

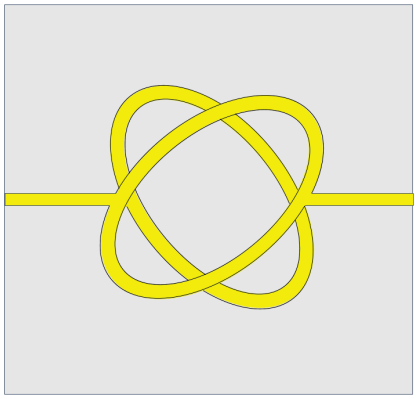

(c)

Fig. 17. Geometries of the example unit cells: (a) MTS material, (b) anisotropic MTS, and (c) chiral MTS.

planar circuits, examples of which have been presented in Fig. 1, but also to other non-planar and inhomogeneous geometries to efficiently simulate other types of geometries such as Luneburg lenses fabricated by using artificial dielectrics (see Figs. 1 (k) and 1 (l)), and spiral inductors printed on multi-layer substrates, shown in Fig. 1 (m). Numerically modeling lens is very time-consuming, especially when the lens diameter is several wavelengths, as it typically is for millimeter wave applications, and the lens is fabricated by using artificial dielectrics as shown in Fig. 1 (l). Similarly, numerically simulating the inductor to extract its circuit parameters is very time-consuming as well as memory-intensive, because the thicknesses of the dielectric layers are very small – in the micron range – which calls for the use of a very fine mesh to represent the geometry under consideration accurately. However, we can obviate this problem by replacing the multi-layered dielectric with one (or two) ε_{eff} layers of moderate thickness, thus rendering the problem very manageable from the numerical simulation point of view.

Additionally, the method is well suited for hybridizing the Integral equation and finite method by using a novel approach which overcomes the roadblock presented by the fact that the MoM deals with induced currents whereas the finite methods work with fields, making the problem of merging the two algorithms to handle a given problem very challenging indeed.

In summary, we have presented the EMA in this section which is very powerful as well as versatile, and, hence, is a very useful tool for numerical simulation of a wide class of problems.

C. Application of EMA to metasurfaces-based antennas

Next, we explain how we use the EMA to first characterize the MTS, and then simulate an antenna (or an array) that utilizes the MTS as a superstrate to enhance its performance, such as its gain. The simulation time for such an antenna plus superstrate combination can be very long when the operating frequency is in the millimeter wave range. Our goal is to replace the original MTS, shown in Fig. 18 (a).

To demonstrate the efficacy of the proposed method, we compare the CPU times and memory burdens when we simulate an array of three microstrip patches covered by a metasurface superstrate, shown in Fig. 18 (a), versus when the superstrate is replaced by an isotropic dielectric as shown in Fig. 18 (b). The dielectric constant of the material and the FSS thickness are, respectively, 17 and 0.6mm, while the remaining dimensions of the unit cell of the MTS Superstrate are shown in Fig. 19.

Table 1 presents the comparison time and memory requirement for the patch array covered with metasurfaces and with equivalent dielectric. We observe a relevant reduction in the utilized RAM and in the CPU time by using the EMA. The CPU time simulation and the RAM requirement are reduced by a factor of 5 and 5.5, respectively. The advantage of using the EMA over a direct simulation of the original geometry comprising of the antenna array and the MTS superstrate is clearly evident from Table 1.

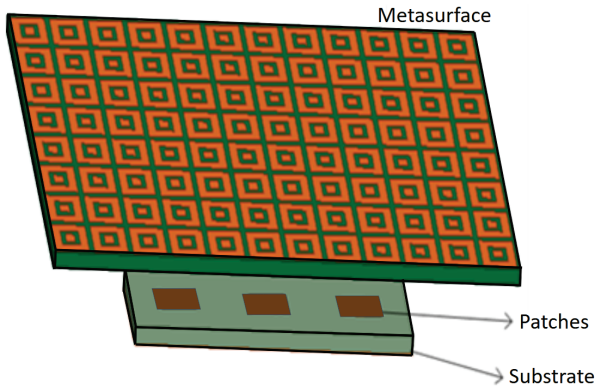

(a)

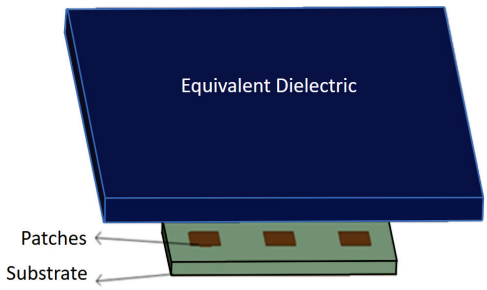

(b)

Fig. 18. Three-element MPA with different superstrates: (a) metasurface superstrate and (b) equivalent dielectric.

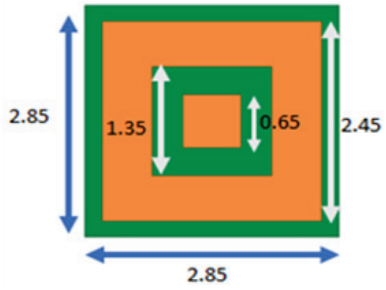

(a)

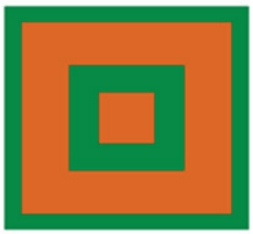

(b)

Fig. 19. Dimensions of the unit cell of the MTS superstrate presented in Fig. 18: (a) top view and (b) bottom view.

Table 1: Comparison of CPU runtimes and required RAM values for the Equivalent Medium approach and the original array covered with the metasurface superstrates (Fig. 18)

Design	Max RAM (GB)	Real Time (hh:mm:ss)	CPU Time (hh:mm:ss)
Three-element patch	1.04	0:14:04	0:13:59
Three element patch+ Metasurface	91.3	72:55:04	95:51:09
Three element patch+ Equivalent Dielectric	24.4	14:56:47	16:57:22

IV. THE T-MATRIX APPROACH FOR CASCADED TWO-PORT NETWORKS

In this section, we present the T-matrix approach to show how to use it in conjunction with the domain decomposition technique to handle a wide variety of printed circuits and antenna geometries, illustrated in Fig. 10 in section III, in a numerically efficient manner.

We start by choosing the geometry of an open-ended stub in a microstrip line, and dividing the original problem into three blocks, as shown in Fig. 20, to detail the T–matrix procedure. The relevant equations for deriving the S-parameters of the original geometry, by utilizing the S-parameters of the three blocks in which the geometry is subdivided, are given below:

$$\begin{bmatrix} S_{11} & S_{12} \\ S_{21} & S_{22} \end{bmatrix} \longrightarrow \begin{bmatrix} T_{11} & T_{12} \\ T_{21} & T_{22} \end{bmatrix} = T_1$$

$$\begin{bmatrix} S_{11} & S_{12} \\ S_{21} & S_{22} \end{bmatrix} \longrightarrow \begin{bmatrix} T_{11} & T_{12} \\ T_{21} & T_{22} \end{bmatrix} = T_2$$

$$\begin{bmatrix} S_{11} & S_{12} \\ S_{21} & S_{22} \end{bmatrix} \longrightarrow \begin{bmatrix} T_{11} & T_{12} \\ T_{21} & T_{22} \end{bmatrix} = T_3$$

$$T_t = T_1 * T_2 * T_3 = \begin{bmatrix} T_{t11} & T_{t12} \\ T_{t21} & T_{t22} \end{bmatrix} \longrightarrow \begin{bmatrix} S_{t11} S_{t12} \\ S_{t21} S_{t22} \end{bmatrix}, \tag{15}$$

where the starting S parameters are for the three blocks and the S_t parameters are for the total stub line. The details of the principle of the T-matrix approach were discussed in section III, part A.

One of the 3D geometries, shown in Fig. 21, is a via, which connects transmission lines from the top to the bottom layer by using the through-hole via. This problem is not amenable to convenient simulation using integral equation methods, not only because of the 3D nature of its geometry but also because it is difficult to

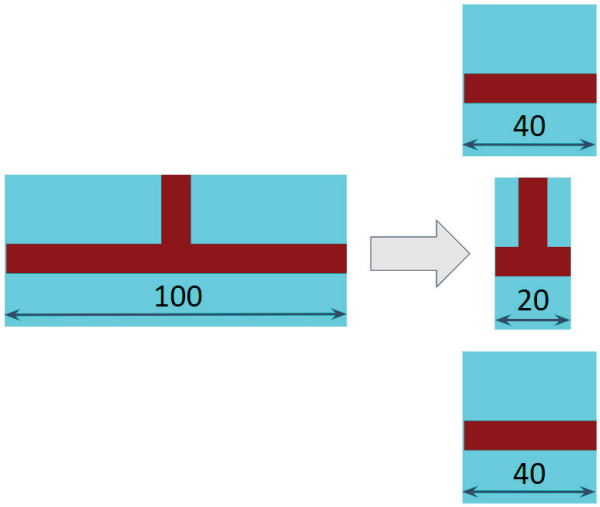

Fig. 20. Example of a stub divided into three blocks.

construct Green's Function for the region in the neighborhood of the through–hole via. However, the T-matrix approach, presented in this section, enables us to handle this problem by using a hybrid algorithm comprised of a combination of finite methods, such as the FEM or FDTD, and integral equation techniques based on the Green's Function that we have discussed previously in section III. The hybrid method is not only powerful and versatile, but it is also numerically more efficient than either the finite method or the integral-equation-based approach when directly applied to the problem at hand, namely the through-hole via with microstrip feed lines printed on top and bottom layers of the configuration.

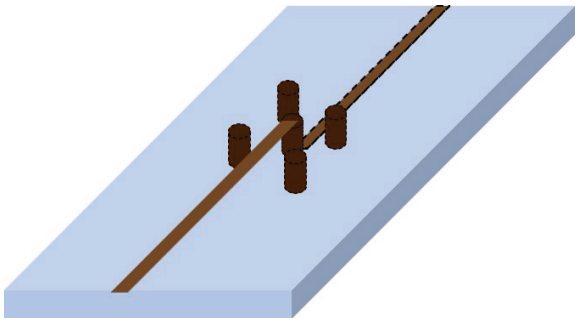

Fig. 21. Example of 3D geometry.

Although not included here, the method has been thoroughly tested and proven to be accurate when applied to a wide variety of problems, including not only planar circuits but also 3D and 2D circuits, as well as antennas, such as those shown in Fig. 22. The MPA arrays with a corporate feed, described in Fig. 22, have the following dimensions and substrate parameters: L = 10.08 mm, W = 11.79 mm, d = 1.3 mm, d = 3:93 mm, L1 = 12:32 mm, L2 = 18.48 mm, D1 = 23.58 mm, D2 = 22.40 mm, ε_r=2.2, d=1.59mm, operating at 9.13 GHz. The T-junction is handled separately using the circuit method.

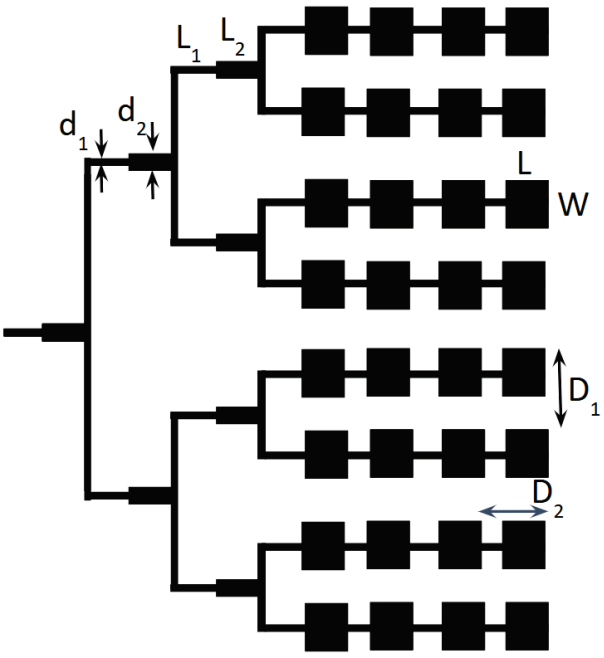

Fig. 22. Microstrip patch antenna array.

In summary, in this section we have presented the EMA which is very powerful as well as versatile, and, hence, is a very useful tool for a wide class of problems. In Part-II [17] of this paper we will go on to discuss three other strategies for performance enhancement of CEM techniques, viz., Characteristic Basis Function Method (CBFM), Mesh Truncation for Finite Methods by using a new form of the Perfectly Matched Layer (PML), and GPU acceleration of MoM as well as FDTD algorithms.

ACKNOWLEDGMENT

The authors acknowledge their team members and research collaborators, including Chao Li, Donia Ouesleti, Koushik Dutta, Yang Su, and others for their contributions and helpful discussions. We thank Dr. Danie Ludick for pointing us to the "cemagg/SUN-EM" GitHub library, which was used to parse FEKO's MoM-based data into MATLAB. We also acknowledge the use of ChatGPT, developed by OpenAI, for assistance in text editing during the preparation of this manuscript. The tool was used solely to improve clarity and language, without contributing to the scientific content of the paper.

REFERENCES

[1] R. F. Harrington, *Field Computation by Moment Methods*. New York, NY: Wiley-IEEE Press, 1993.

[2] P. P. Silvester and R. L. Ferrari, *Finite Elements for Electrical Engineers*. Cambridge: Cambridge University Press, 1996.

[3] K. S. Yee and J. S. Chen, "The finite-difference time-domain (FDTD) and the finite-volume time-domain (FVTD) methods in solving Maxwell's equations," *IEEE Transactions on Antennas and Propagation*, vol. 45, no. 3, pp. 354-363, 1997.

[4] T. Hagstrom and H. Keller, "Asymptotic boundary conditions and numerical methods for nonlinear elliptic problems on unbounded domains," *Mathematics of Computation*, vol. 48, no. 178, pp. 449-470, 1987.

[5] O. Ozgun, R. Mittra, and M. Kuzuoglu, "An efficient numerical approach for evaluating Sommerfeld integrals arising in the construction of Green's functions for layered media," *IEEE J. Multiscale Multiphys. Comput. Tech.*, vol. 7, pp. 328-335, 2022.

[6] K. Michalski and D. Zheng, "Electromagnetic scattering and radiation by surfaces of arbitrary shape in layered media. I. Theory," *IEEE Trans. Antennas Propag.*, vol. 38, no. 3, pp. 335-344, 1990.

[7] P. Yla-Oijala and M. Taskinen, "Efficient formulation of closed-form Green's functions for general electric and magnetic sources in multilayered media," *IEEE Trans. Antennas Propag.*, vol. 51, no. 8, pp. 2106-2115, 2003.

[8] Y. Mengtao, T. Sarkar, and M. Salazar-Palma, "A direct discrete complex image method from the closed-form Green's functions in multilayered media," *IEEE Trans. Microw. Theory Tech.*, vol. 54, no. 3, pp. 1025-1032, 2006.

[9] R. Mittra, O. Ozgun, C. Li, and M. Kuzuoglu, "Efficient computation of Green's functions for multilayer media in the context of 5G applications," in *2021 15th European Conference on Antennas and Propagation (EuCAP)*, pp. 1-5, 2021.

[10] O. Ozgun, C. Li, M. Kuzuoglu, and R. Mittra, "An efficient approach for evaluation of multilayered media Green's functions," in *2021 IEEE International Symposium on Antennas and Propagation and USNC-URSI Radio Science Meeting (APS/URSI)*, pp. 1107-1108, 2021.

[11] A. Fernandez Rodriguez, L. de Santiago Rodrigo, E. Lopez Guillen, J. M. Rodriguez Ascariz, J. M. Jimenez, and L. Boquete, "Coding Prony's method in MATLAB and applying it to biomedical signal filtering," *BMC Bioinformatics*, vol. 19, no. 451, 2018.

[12] Y. Hua and T. Sarkar, "Generalized pencil-of-function method for extracting poles of an EM system from its transient response," *IEEE Trans. Antennas Propag.*, vol. 37, no. 2, pp. 229-234, 1989.

[13] Ansys Corporation. (2024). *ANSYS HFSS, high-frequency electromagnetic field simulation software* [Online]. Available: https://www.ansys.com

[14] Dassault Systèmes. (2024). *CST Studio Suite, electromagnetic field simulation software* [Online]. Available: https://www.3ds.com

[15] D. Smith, D. Vier, T. Koschny, and C. Soukoulis, "Electromagnetic parameter retrieval from inhomogeneous metamaterials," *Physical Review E—Statistical, Nonlinear, and Soft Matter Physics*, vol. 71, no. 3, p. 036617, 2005.

[16] P. C. Waterman, "Matrix formulation of electromagnetic scattering," *Proceedings of the IEEE*, vol. 53, no. 8, pp. 805-812, 1965.

[17] R. Mittra, T. Marinovic, O. Ozgun, S. Liu, and R. K. Arya, "Novel strategies for efficient computational electromagnetic (CEM) simulation of microstrip circuits, antennas, arrays and metamaterials Part-II: Characteristic basis function method, perfectly matched layer, GPU acceleration," *Applied Computational Electromagnetics Society (ACES) Journal*, pp. 000-000, 2025.

[18] A. B. Numan and M. S. Sharawi, "Extraction of material parameters for metamaterials using a full-wave simulator [education column]," *IEEE Antennas and Propagation Magazine*, vol. 55, no. 5, pp. 202-211, 2013.

[19] T. A. Elwi, M. M. Hamed, Z. Abbas, and M. A. Elwi, "On the performance of the 2D planar metamaterial structure," *AEU-International Journal of Electronics and Communications*, vol. 68, no. 9, pp. 846-850, 2014.

[20] M. R. Benson, A. G. Knisely, M. A. Marciniak, M. D. Seal, and A. Urbas, "Permittivity and permeability tensor extraction technique for arbitrary anisotropic materials," *IEEE Photonics Journal*, vol. 7, no. 3, pp. 1-13, 2015.

[21] A. Yahyaoui and H. Rmili, "Chiral all-dielectric metasurface based on elliptic resonators with circular dichroism behavior," *International Journal of Antennas and Propagation*, vol. 2018, no. 1, p. 6352418, 2018.

Raj Mittra is a Professor in the Department of Electrical and Computer Engineering of the University of Central Florida in Orlando, FL., where he is the Director of the Electromagnetic Communication Laboratory. Before joining the University of Central Florida, he worked at Penn State as a Professor in the Electrical and Computer Engineering from 1996 through June 2015. He was a Professor in the Electrical and Computer Engineering at the University of Illinois in Urbana-Champaign from 1957 through 1996, when he moved to Penn State University. Currently, he also holds the position of Hi-Ci Professor at King Abdulaziz University in Saudi Arabia and a Visiting Distinguished Professor in Zhongshan Institute of CUST, China. He is a Life Fellow of the IEEE, a Past-President of AP-S, and has served as the Editor of the Transactions of the Antennas and Propagation Society. He won the Guggenheim Fellowship Award in 1965, the IEEE Centennial Medal in 1984, and the IEEE Millennium Medal in 2000. Other honors include the IEEE/AP-S Distinguished Achievement Award in 2002, the Chen-To Tai Education Award in 2004 and the IEEE Electromagnetics Award in 2006, and the IEEE James H. Mulligan Award in 2011. He has also been recognized by the IEEE with an Alexander Graham Bell award from the IEEE Foundation.

Ozlem Ozgun is currently a full professor in the Department of Electrical and Electronics Engineering at Hacettepe University, Ankara, Turkey. She received her B.Sc. and M.Sc. degrees from Bilkent University and her Ph.D. from Middle East Technical University (METU), all in Electrical and Electronics Engineering. She was a postdoctoral researcher at Penn State University, USA. Her research focuses on computational electromagnetics and radiowave propagation, including numerical methods, domain decomposition, transformation electromagnetics, and stochastic electromagnetic problems. Dr. Ozgun is a Senior Member of IEEE and URSI and a past chair of the URSI Turkey steering committee. She has been selected as a Distinguished Lecturer (DL) by the IEEE Antennas and Propagation Society (AP-S) for the period of 2025-2027. Her awards include the METU Best Ph.D. Thesis Award (2007), the Felsen Fund Excellence in Electromagnetics Award (2009), and the IEEE AP-S Outstanding Reviewer Award (2023-2024). She was recognized among the world's top 2% most influential scientists (Stanford University & Elsevier, 2023–2024) and received the Hacettepe University 2024 Science Award.

Vikrant Kaim (Member, IEEE) received the Ph.D. degree in electronics and communication from the Jawaharlal Nehru University, Delhi, India, in 2022. He was a Postdoctoral Fellow with the Department of Electrical and Computer Engineering, University of Alberta, Edmonton, Canada, from January 2003 to December 2023. In December 2023, he joined the Department of Electronics and Communication Engineering as an Assistant Professor at the Faculty of Technology, University of Delhi, Delhi, India. Since Dec. 2024, he has been working as an Assistant Professor at the Centre for Research in Electronics (CARE), Indian Institute of Technology Delhi (IIT Delhi). His research interests include applied electromagnetics with focus on bioelectromagnetics and biomedical devices for wearable, implantable and ingestible applications such as wireless power transfer, retinal prosthesis, cardiac implants, and capsule endoscopy. Mr. Kaim was a recipient of the prestigious CSIR Senior Research Fellowship in 2019. He has authored/co-authored 26 publications in reputed international journals and conferences. He is also credited with 3 Indian patents. He is serving as a reviewer for the *IEEE Transactions on Antennas and Propagation, IEEE Transactions on Microwave Theory and Techniques*, and *IEEE Transactions on Biomedical Engineering*.

Abdelkhalek Nasri received the B.Sc. degree in electronic systems and the Ph.D. degree in electronics from the Faculty of Sciences of Tunis, Tunisia, in 2011 and 2017, respectively. He is currently a Postdoctoral Fellow at XLIM in Limoges, France. From 2021 to 2022, he was a Research Scholar at the University of Central Florida, Orlando, FL, USA. His research interests include antennas, phased arrays, frequency-selective surfaces, substrate-integrated waveguides, scattering of electromagnetic waves, and bioelectromagnetics.

Prashant Chaudhary received his B.Sc. (Honors) in Electronics, followed by an M.Sc. in Electronics, and a Ph.D. from the University of Delhi, Delhi, India. He is currently a research assistant in the Department of Electrical and Computer Engineering (ECE) at the University of Central Florida, USA. His research interests include planar antennas, MIMO (Multiple Input Multiple Output) systems, circularly polarized antennas, 5G communication technology, metasurfaces, magnetic substrates, and metamaterials. He has published over 15 research papers in journals and conferences.

Ravi K. Arya is a Distinguished Professor and Director of the Xiangshan Laboratory Wireless Group at the Zhongshan Institute of Changchun University of Science and Technology (ZICUST), China. He earned his Ph.D. in Electrical Engineering from Pennsylvania State University, USA, under the supervision of Prof. Raj Mittra, following an M.Tech in RF and Microwave Engineering from the Indian Institute of Technology (IIT) Kharagpur (advised by Prof. Ramesh Garg) and a B.Tech from Delhi Technological University, India. With a career spanning both academia and industry, Dr. Arya has held positions at ECIL (India), C-DOT (India), Ansys Inc. (USA), and ALL.SPACE (USA), as well as academic roles at NIT Delhi (India) and JNU (India). He has authored over 90 peer-reviewed publications, seven book chapters, and four patents. His research focuses on antenna design, computational electromagnetics, machine learning applications in electromagnetics, and RF system modeling.

Design of Integrated Polygonal UWB MIMO Antenna With EBG Structure Based on Characteristic Mode Analysis

Fukuan Zhang[1], Zhonggen Wang[1], Wenyan Nie[2], Ming Yang[3], and Chenlu Li[4]

[1]School of Electrical and Information Engineering
Anhui University of Science and Technology, Huainan 232001, China
2023200725@aust.edu.cn, zgwang@ahu.edu.cn

[2]School of Mechanical and Electrical Engineering
Huainan Normal University, Huainan 232001, China
wynie5240@163.com

[3]School of Electrical and Communications Engineering
West Anhui University, Lu'an 237012, China
myang@ahu.edu.cn

[4]School Electrical and Information Engineering
Hefei Normal University, Hefei 230061, China
chenluli@hfnu.edu.cn

Abstract – This paper presents an analytical design of an integrated polygonal ultra-wideband (UWB) MIMO antenna, featuring a stepped electromagnetic band gap (EBG) integrated with a T-shaped stepped stub and utilizing characteristic mode analysis (CMA). The overall size of the antenna is $27\times22\times0.8$ mm^3. It comprises two symmetric octagonal radiating units, a T-shaped stepped floor, and an EBG structure positioned between the two radiating units. By analyzing the current and electric field distributions of the antenna's characteristic modes, the feed point is identified at the rectangular microstrip line of the radiating unit, ensuring the simultaneous excitation of the antenna's eight characteristic modes to achieve ultra-broadband characteristics. Meanwhile, the characteristic mode theory offers clear physical insights into antenna optimization. The bandwidth is improved by etching three positive T-slots on the floor. In comparison, the antenna isolation is enhanced by employing the EBG structure to suppress coupling currents and etching two inverted T-slots to modify the current path. Simulation and measurement results show that the antenna covers the 3.06-14 GHz band with isolation exceeding 20 dB. The antenna exhibits excellent radiation performance and a low envelope correlation coefficient (ECC).

Index Terms – Characteristic mode theory, EBG, MIMO antenna, T-slot, UWB antenna.

I. INTRODUCTION

With the emergence of 5G communication technology, the demand for antennas capable of supporting high-capacity data transmission has increased significantly [1]. Ultra-wideband (UWB) MIMO antennas have emerged as a key solution in wireless communication systems to meet this demand. Combining UWB and MIMO techniques offers enhanced bandwidth and higher data transmission rates while mitigating multipath fading effects and improving system capacity [2]. Consequently, UWB MIMO antennas find applications in radar detection, wireless data transmission, and medical monitoring systems.

For UWB MIMO antennas designed for portable devices, the primary focus is key characteristics such as compact size, bandwidth, and isolation. Continuous research on UWB MIMO antennas has yielded several approaches to enhance bandwidth and isolation [3–12]. The primary methods for achieving UWB characteristics include tapered geometries [13], resonant structures [14], and slot configurations [15]. To address the coupling issues caused by near-field radiation and current flow, common methods to improve isolation include electromagnetic band gap (EBG) structure [16], T-shaped stubs [17], and defective ground structures [18]. Reference [3] describes an antenna that comprises four monopole units and a sector isolation structure, featuring

Submitted On: December 24, 2024
Accepted On: April 29, 2025

https://doi.org/10.13052/2025.ACES.J.400502

U-shaped patch elements and a defective rectangular ground plane. One of the sector decoupling structures efficiently suppresses coupling currents, thereby enhancing isolation. The antenna achieves a 2-11.08 GHz bandwidth while maintaining isolation exceeding 15 dB across the operational bandwidth. Reference [13] proposes a square slot antenna incorporating stepped transmission line loading, enabling resonance at multiple frequencies to achieve a UWB response spanning 2.1-11.5 GHz. Reference [14] introduces a metal slot array antenna employing a hybrid resonant structure. Through strategic arrangement and modification of the cavity and radiating slots, five resonant frequency points are simultaneously excited and tuned to the operating band, resulting in a bandwidth extension of 31%. Reference [15] proposes a UWB cross-tapered slot antenna on the ground plane, integrating millimeter-wave feed networks into its four 1×4 dipole arrays embedded in the cross-tapered arms. Due to the UWB characteristics of the slot antenna, it effectively covers most communication bands below 6 GHz. The antenna described in reference [16] incorporates a 2×3 EBG array between two electromagnetically coupled radiating patches to suppress surface wave coupling, with coupling further mitigated by a hairpin DGS on the ground plane. Compared to the original MIMO antenna, the EBG results in an average isolation enhancement of 13.9 dB in the 5G band, and the DGS provides a maximum isolation enhancement of 47.7 dB at 27.94 GHz. Reference [17] details a T-shaped grounding stub positioned between two radiating patches on the ground plane to suppress mutual coupling between MIMO elements and achieve an impedance bandwidth of 3.3-6 GHz with isolation exceeding 18 dB. Finally, the antenna in reference [18] leverages parasitic strips and defective ground structures to deliver wide bandwidth and enhanced isolation. It supports the n77/n78/n79 bands for 5G New Radio as well as the 5 GHz band for wireless local area networks, with isolation between any two ports greater than 15 dB.

All of the above techniques apply to the design of UWB MIMO antennas. However, achieving good operating bandwidth and high isolation—particularly in the low-frequency region of UWB—remains challenging, as these designs often rely on trial-and-error methods without detailed physical insights or theoretical guidance. In this context, characteristic mode analysis (CMA) offers purposeful optimization for antenna design and provides clear physical insights to enhance UWB MIMO antenna performance [19–32].

The ground MIMO antenna proposed in reference [20] leverages CMA to identify and excite three orthogonal modes (TM10, TM01, and TM20), incorporating a double-slot structure and an I-shaped patch into the coupling paths to enable simultaneous triple-band operation with high isolation. Reference [21] introduces a UWB antenna featuring dual-band trapping characteristics validated through CMA. The dual-trap band is achieved by embedding an L-shaped short interceptor into a trap rectangular patch, and the two trap bands are confirmed via CMA analysis of modal significance (MS) and characteristic angle (CA). Reference [25] employed CMA to modify the antenna shape to simultaneously excite multiple broadband modes through the feed slot, significantly enhancing bandwidth. The four-port antenna in reference [26] was entirely designed using CMA, covering a bandwidth of 2.8-11.4 GHz and achieving isolation exceeding 26 dB across its operational bandwidth.

In summary, this paper presents a novel dual-port UWB MIMO antenna structure consisting of two symmetric octagonal radiating units, a stepped EBG structure, and a T-shaped stepped stub, which enhances bandwidth and isolation through five T-shaped slots etched on the stepped stub and the integration of the stepped EBG structure. The proposed antenna achieves an operating bandwidth of 3.06-14 GHz, covering the entire UWB spectrum, with isolation exceeding 20 dB across the operating bandwidth while demonstrating excellent radiation and diversity performance. Additionally, the antenna evolution design is conducted using CMA. By analyzing the current and electric field distributions of the characteristic modes of antenna, the antenna feed point is located at the rectangular microstrip line of the radiating unit, ensuring simultaneous excitation of the eight characteristic modes of antenna to achieve ultra-broadband characteristics.

II. ANTENNA DESIGN

A. Antenna structure

In this paper, CST Studio suite is used to simulate the antenna. The antenna structure proposed in this paper is illustrated in Fig. 1. The antenna is printed on an FR4 dielectric substrate, featuring total dimensions of $27\times22\times0.8$ mm^3, a relative dielectric constant of 4.4, and a loss tangent of 0.02. Two integrated octagonal radiating units are fed by a microstrip line. The top and bottom rectangular patches connecting the inner and outer octagons are 1.125×0.5 mm, while the left and right rectangular patches measure 0.875×0.5 mm. Between these units, two cells form a stepped EBG, separated by a distance of 0.15 mm and connected by a rectangular patch with a width of 0.5 mm. A T-shaped stepped stub on the bottom surface of the substrate is connected via a cylinder with a radius of 0.5 mm. Each unit has a border width of 0.5 mm, and the internal rhombus patch is linked to the border through a 0.5 mm square patch. Additionally, five T-slots are etched on the T-stepped stub to extend

the bandwidth and improve the isolation. Table 1 lists the antenna's parametric dimensions.

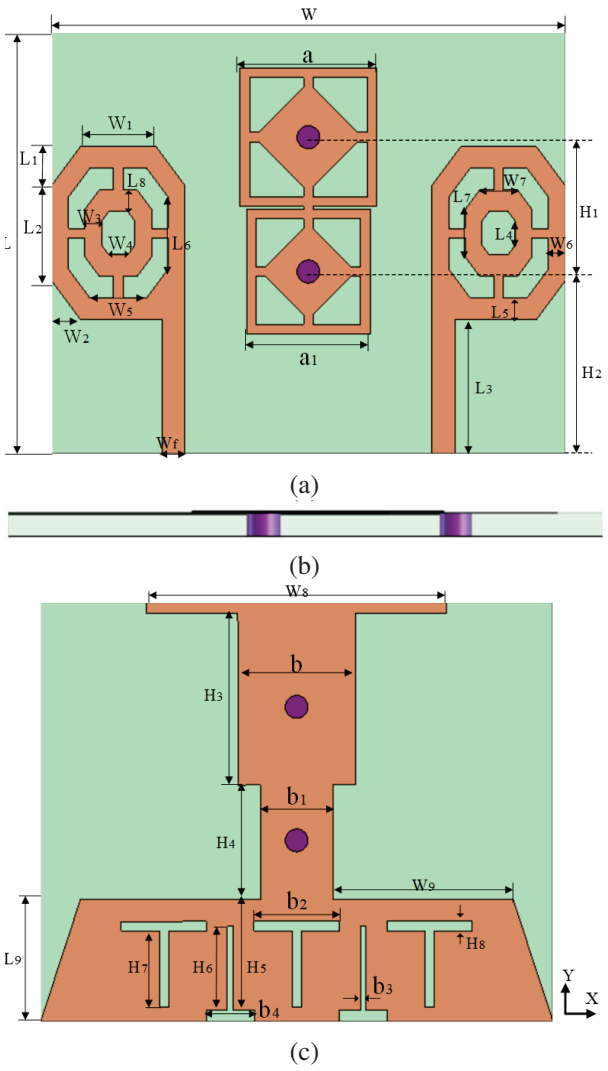

Fig. 1. Proposed UWB MIMO antenna structure: (a) top view, (b) side view, and (c) bottom view.

B. Antenna evolution and analysis

Figure 2 illustrates the evolution of the antenna structure, while Fig. 3 presents the corresponding simulated S-parameter curves. Figure 4 presents the MS and CA of antenna 1, while Fig. 5 illustrates the current distribution at resonance points for its characteristic modes. MS represents the extent to which each mode resonates within a specific frequency range. An MS value closer to 1 indicates that the mode can be more effectively excited under appropriate feeding conditions, whereas an MS value below 0.707 indicates a low likelihood of resonance. Similarly, CA represents the antenna's resonance performance, and a CA value closer to 180 signifies a higher probability of mode resonance.

Table 1: Parameter dimensions of the antenna

Parameters	W	L	W_1	L_1	W_2	L_2
Value(mm)	27	22	4	2	1.5	5
Parameters	W_3	L_3	W_4	L_4	W_5	L_5
Value(mm)	0.875	7	1	1.25	3	1.125
Parameters	W_6	L_6	W_7	L_7	W_9	L_9
Value(mm)	0.875	3.75	2	2.5	9.5	6.4
Parameters	W_8	W_f	H_8	b	b_1	b_2
Value(mm)	15.8	1.2	0.5	6.2	3.8	4.5
Parameters	L_8	b_3	b_4	a	a_1	H_1
Value(mm)	1.125	0.5	2.5	7.2	6.5	7
Parameters	H_2	H_3	H_4	H_5	H_6	H_7
Value(mm)	9.5	9	6	5.8	4.4	4

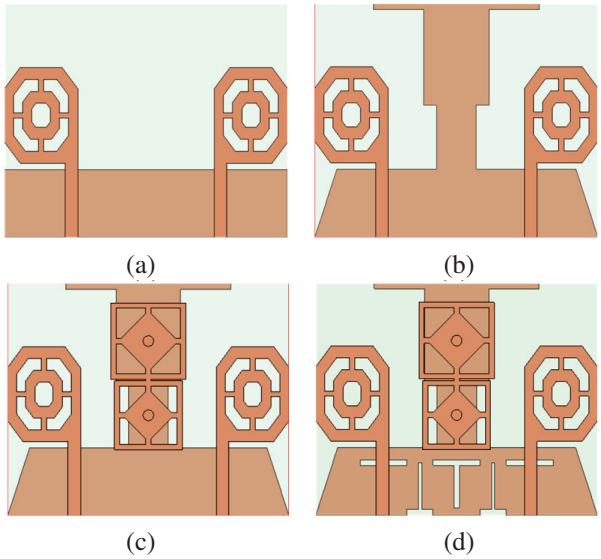

Fig. 2. Design development of antenna structure: (a) antenna 1, (b) antenna 2, (c) antenna 3, and (d) antenna 4.

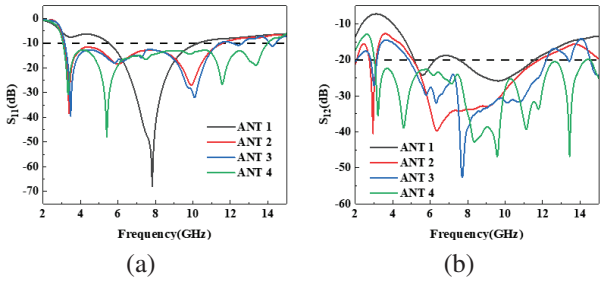

Fig. 3. Simulated S-parameter plot of the antenna: (a) S11 and (b) S12.

An analysis of Fig. 4 indicates that, among the 12 characteristic modes, modes 1, 2, 4, 5, 7, 9, 10, and 12 are theoretically excited under appropriate feeding conditions. However, an analysis of Fig. 5 reveals that the

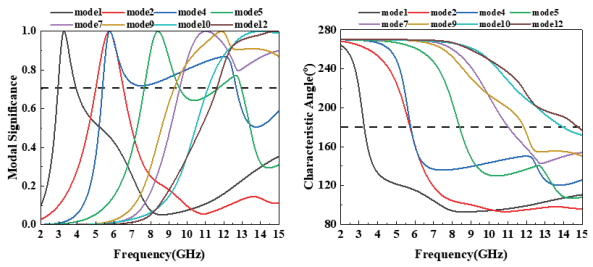

(a) (b)

Fig. 4. Results of mode analysis of antenna 1: (a) MS and (b) CA.

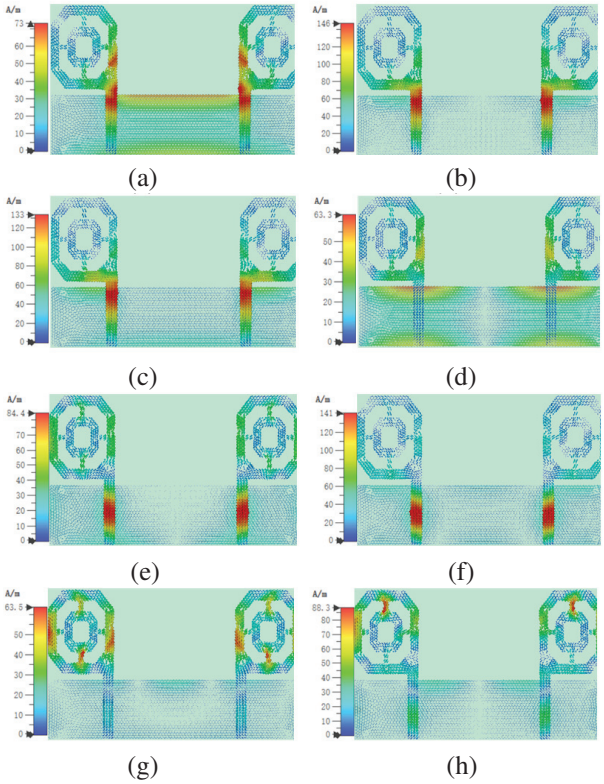

(a) (b) (c) (d) (e) (f) (g) (h)

Fig. 5. Mode current distribution of antenna 1: (a) mode 1 at 3.28 GHz, (b) mode 2 at 5.73 GHz, (c) mode 4 at 5.71 GHz, (d) mode 5 at 8.40 GHz, (e) mode 7 at 11.02 GHz, (f) mode 9 at 11.86 GHz, (g) mode 10 at 13.97 GHz, and (h) mode 12 at 14.77 GHz.

currents of mode 5 are primarily distributed on the floor, while the currents of modes 10 and 12 are mainly concentrated on the outer octagon of the radiating patch. These mode currents are weak, located far from the feed ports, cannot be effectively excited, and therefore do not contribute to the bandwidth. The currents of modes 1, 2, 4, 7, and 9 are primarily concentrated in the rectangular feeder of the radiating patch and are effectively excited. However, the bandwidth of mode 4 overlaps with that of modes 2, 7, and 9 and, thus, the combined bandwidth they provide fails to meet the UWB requirements. The bandwidth of antenna 1, as shown in Fig. 3 (a), is in the range 5.52-10.3 GHz, indicating that the structure is insufficient to satisfy the UWB requirement. Therefore, the structure of antenna 1 was improved and optimized, as depicted in Fig. 2 (b).

To enable more distinct excitable patterns and ensure the combined bandwidth meets the UWB requirement, antenna 2 modifies the rectangular floor of antenna 1 into a stepped T-shaped floor, as shown in Fig. 2 (b). Figures 6 and 7 present the characteristic modes, CAs, and mode current distribution of antenna 2. Compared to antenna 1, antenna 2 exhibits changes in the characteristic mode shapes and effective bandwidth. Specifically, the resonant frequency of mode 10 shifts from a high to a low frequency, and the effective bandwidth is reduced. Meanwhile, the resonant frequencies of modes 1, 2, and 4 shift slightly toward higher frequencies, with minor changes in shape and increased bandwidth. The resonant frequency of mode 5 shifts to a lower frequency by 0.48 GHz, while mode 7 shifts by 3.45 GHz to a lower frequency. Mode 9 has a resonant frequency of 0.86 GHz, and mode 12 shifts by 2.74 GHz toward a lower frequency. The combined bandwidths of these modes fully cover the UWB ranges from 3.1 to 10.6 GHz. As shown in Fig. 7, the current of mode 7 primarily distributes at the top of the floor, far from the feed point, and cannot be excited. However, the other modes have strong currents at the feed point and can be excited, collectively contributing to the UWB requirement. The S-parameters of antenna 2, as shown in Fig. 3, indicate that antenna 2 achieves a UWB band of 3.12-11.6 GHz compared to antenna 1. However, the isolation in this band is greater than 12.6 dB, failing to meet the isolation requirements for MIMO antennas. Therefore, the structure of antenna 2 was further refined.

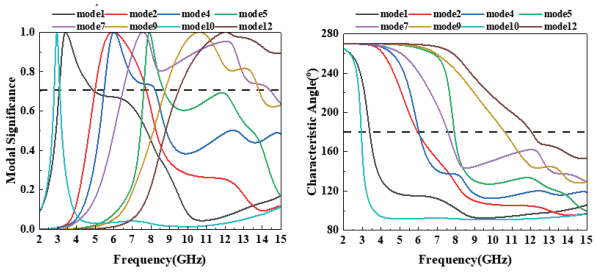

(a) (b)

Fig. 6. The results of mode analysis of antenna 2: (a) MS and (b) CA.

To enhance antenna isolation, antenna 3 incorporates an EBG structure derived from antenna 2, as shown in Fig. 2 (c). The metal cylinder in the EBG structure

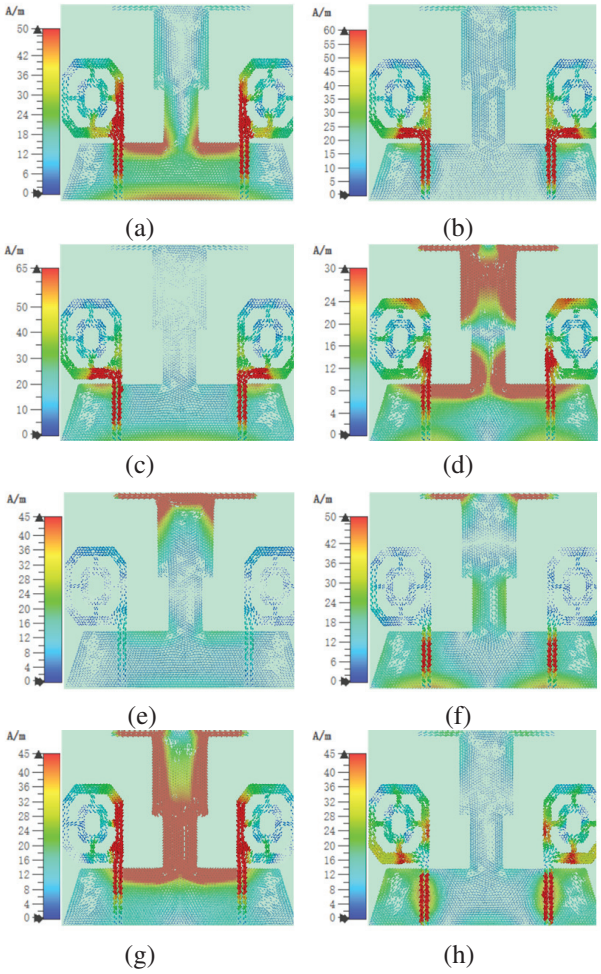

Fig. 7. Mode current distribution of antenna 2: (a) mode 1 at 3.38 GHz, (b) mode 2 at 5.96 GHz, (c) mode 4 at 6.03 GHz, (d) mode 5 at 7.92 GHz, (e) mode 7 at 7.57 GHz, (f) mode 9 at 10.61 GHz, (g) mode 10 at 2.93 GHz, and (h) mode 12 at 12.03 GHz.

links the upper surface of the floor to the antenna structure, focusing floor currents onto the rectangular patch within the EBG structure. This configuration effectively suppresses surface and space wave propagation, reduces mutual coupling between antenna radiating units, and enhances antenna isolation. Introduction of the EBG structure modifies the overall antenna structure, altering its characteristic modes and currents, as illustrated in Figs. 8 and 9.

Figure 8 illustrates the characteristic modes and angles of the antenna, while Fig. 9 depicts the characteristic current distribution at resonance points. A comparison of Figs. 9 and 7 reveals that the EBG structure enables mode 7, previously unexcited in antenna 2, to be excited in antenna 3, thereby broadening the bandwidth. Compared to antenna 2, the resonance frequencies of characteristic modes of antenna 3 shift by

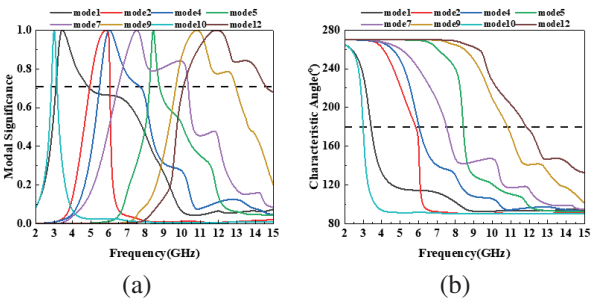

Fig. 8. Results of mode analysis of antenna 3: (a) MS and (b) CA.

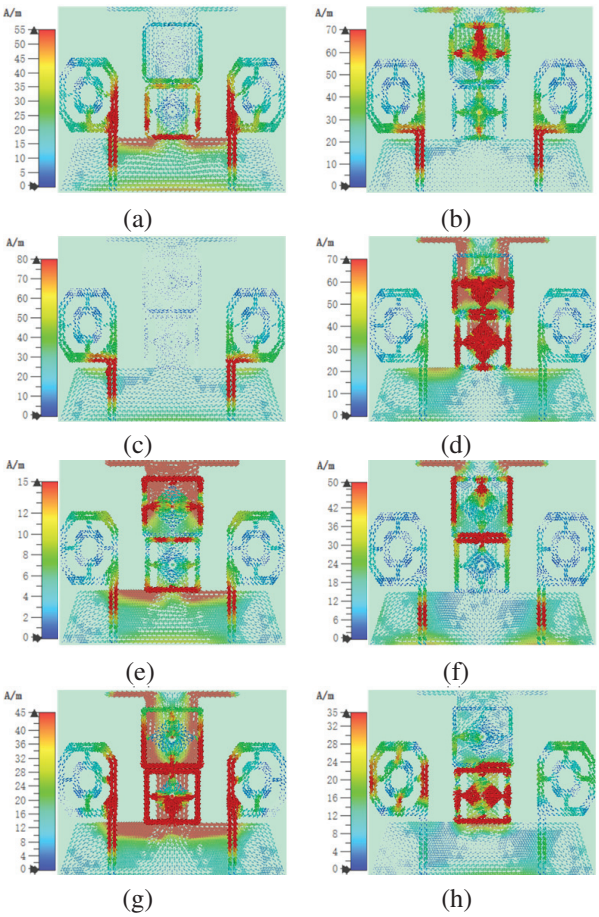

Fig. 9. Mode current distribution of antenna 3: (a) mode 1 at 3.42 GHz, (b) mode 2 at 5.84 GHz, (c) mode 4 at 6.02 GHz, (d) mode 5 at 8.41 GHz, (e) mode 7 at 7.50 GHz, (f) mode 9 at 10.81 GHz, (g) mode 10 at 3.00 GHz, and (h) mode 12 at 12.03 GHz.

approximately 0.2 GHz toward either lower or higher frequencies with minimal variation, resulting in an effective bandwidth meeting the UWB requirement. Figure 3 shows that antenna 3 achieves a bandwidth of 3.16-11.4 GHz, with isolation exceeding 14.51 dB across this range. Compared to antenna 2, the EBG structure

reduces low-frequency isolation by 1.91 dB. Although this remains below the MIMO antenna isolation requirement of 17 dB, the bandwidth is slightly reduced, failing to fully cover 3.1-10.6 GHz. To address these issues, five T-slots are etched on the floor of antenna 3 to broaden the bandwidth and improve isolation, resulting in the final antenna structure shown in Fig. 2 (d).

Figure 3 demonstrates that the etched T-slot enables the antenna to cover the band range of 3.06-14 GHz, fully complying with UWB requirements and achieving isolation greater than 20 dB. Three positive T-slots are responsible for bandwidth enhancement, while two inverted T-slots improve antenna isolation. Figures 10 and 11 illustrate that etching of the T-slots modifies the antenna structure and influences distribution of its characteristic modes and currents. As shown in Fig. 11, the current distribution of characteristic modes of antenna 4 is more concentrated near the feed point, enabling excitation. Figure 10 shows that the combined bandwidth contributed by these modes completely covers 3-14 GHz, which aligns with Fig. 3 (a), confirming that antenna 4 covers the band range 3.06-14 GHz.

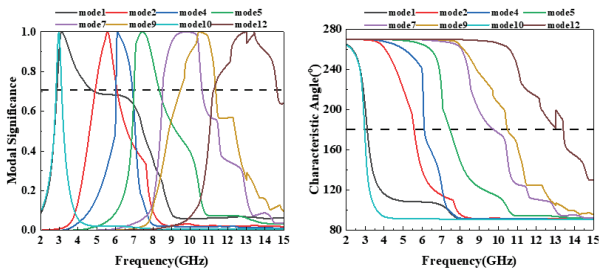

(a) (b)

Fig. 10. Results of mode analysis of antenna 4: (a) MS and (b) CA.

C. Antenna parameter analysis

A systematic study was conducted to analyze the impact of various antenna parameters on its performance. The objective was to assess how antenna parameters influence bandwidth and isolation. Four parameters were studied, namely b_2 and H_7 for positive T-slots and b_4 and H_6 for inverted T-slots. The first three parameters were selected due to their influence on both bandwidth and isolation, while the last parameter was chosen for its significant role in enhancing isolation.

The analysis process involves varying one parameter while keeping the others constant. The parameter analysis results are presented in Fig. 12. Figure 12 shows that b_2 significantly impacts the high-frequency region of the S-parameters, as increasing b_2 worsens the high-frequency matching of S11 and reduces coverage while improving S12 performance. Thus, b_2 is set to 4.5 mm.

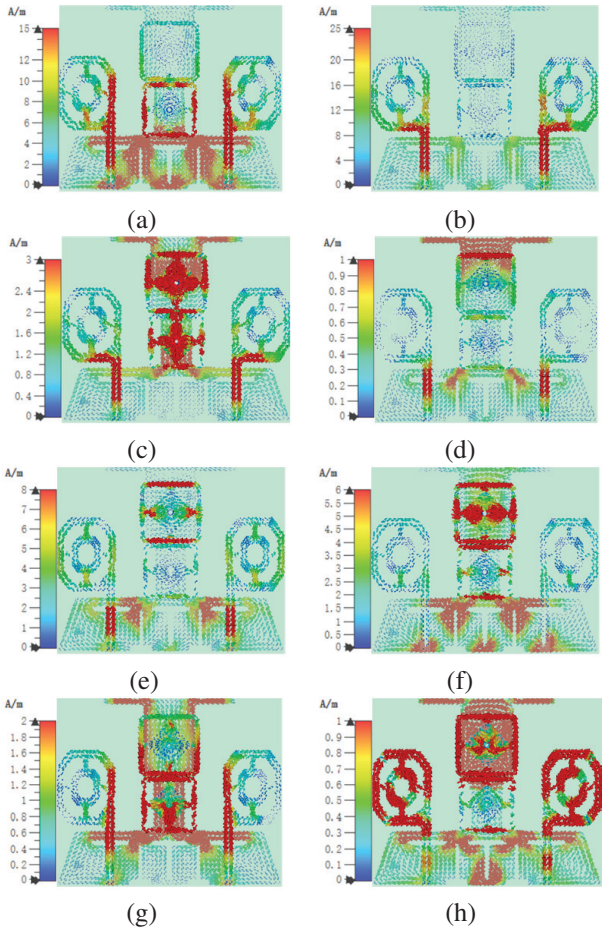

Fig. 11. Mode current distribution of antenna 4: (a) mode 1 at 3.10 GHz, (b) mode 2 at 5.56 GHz, (c) mode 4 at 6.10 GHz, (d) mode 5 at 7.45 GHz, (e) mode 7 at 9.75 GHz, (f) mode 9 at 10.48 GHz, (g) mode 10 at 2.97 GHz, and (h) mode 12 at 13.41 GHz.

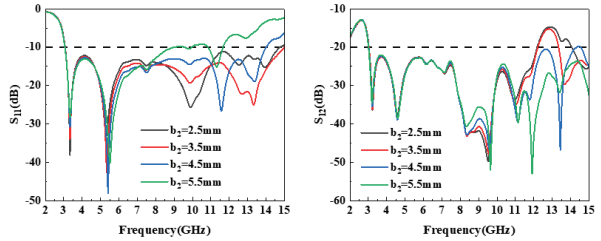

(a) (b)

Fig. 12. Effect of different b_2 lengths on antenna S-parameters: (a) S11 and (b) S12.

Figure 13 indicates that H_7 primarily influences the high-frequency resonance point of S11. As H_7 increases, the high-frequency resonance point of S11 shifts towards the mid-frequency region and its depth decreases, while the

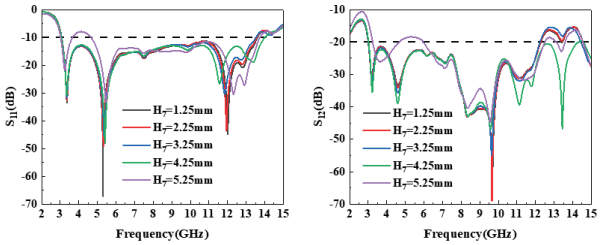

(a) (b)

Fig. 13. Effect of different H_7 lengths on antenna S-parameters: (a) S11 and (b) S12.

opposite trend is observed for S12. When H_7 increases from 4.25 mm to 5.25 mm, the low-frequency matching of the S-parameters degrades. Thus, H_7 is set to 4.25 mm.

Figure 14 shows that, as b_4 increases from 1.5 mm to 2.5 mm, the antenna transitions from impedance mismatch to a matched state. Subsequently, the high-frequency resonance point of S11 shifts upward, and the 5.4 GHz resonance point shifts leftward with increasing length. Thus, b_4 is set to 2.5 mm. Figure 15 demonstrates that H_6 significantly influences S12. As H_6 increases, bandwidth remains constant while isolation improves progressively. Considering the resonance depth of S11, H_6 is set to 4.4 mm.

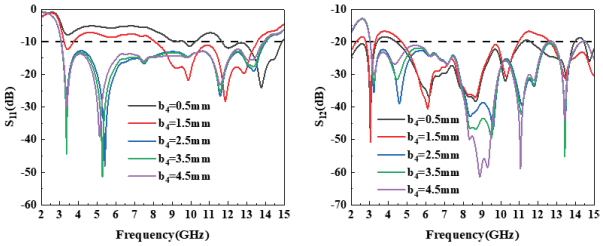

(a) (b)

Fig. 14. Effect of different b_4 lengths on antenna S-parameters: (a) S11 and (b) S12.

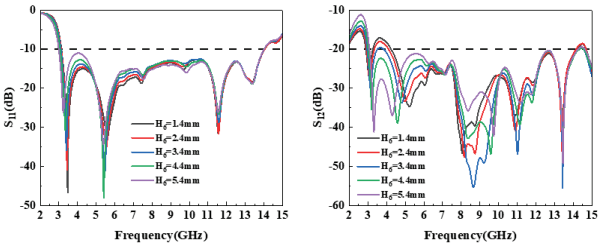

(a) (b)

Fig. 15. The effect of different H_6 lengths on antenna S-parameters: (a) S11 and (b) S12.

III. RESULTS AND DISCUSSION

A. S-parameters

To test the actual performance of the antenna, the antenna model is processed as shown in Fig. 16 (b). The antenna S-parameters were measured using an Agilent N5235A vector network analyzer, and the antenna microwave darkroom measurement environment is shown in Fig. 16 (a). Figure 17 shows the simulated and measured S-parameters of the antenna. From Fig. 17, it can be seen that the antenna covers the band 3.06-14 GHz and contains the UWB band. In addition, the S12 parameter of the antenna stays below -20 dB in the UWB band, showing good isolation. Please note that the difference between the simulated and measured results may be due to manufacturing processes and soldering errors. However, in general, their results match very well, and the overall performance of the antenna remains consistent.

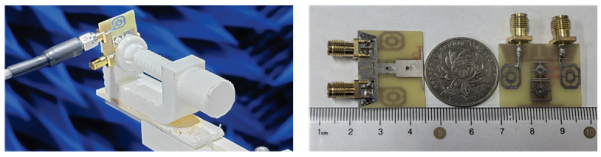

(a) (b)

Fig. 16. Proposed antenna: (a) S-parameters measurement environment and (b) fabricated prototype.

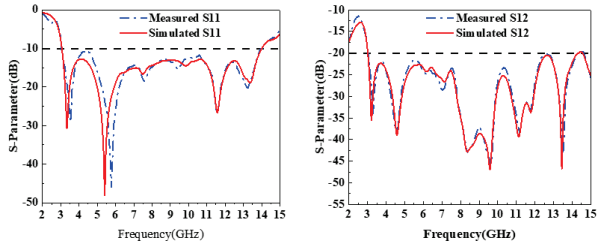

(a) (b)

Fig. 17. MIMO antenna simulated and measured S-parameters: (a) S11 and (b) S12.

B. Radiation properties

Figure 18 depicts the two-dimensional radiation patterns of the antenna in the E-plane and H-plane at 3.34 GHz, 5.4 GHz, 11.57 GHz, and 13.37 GHz. From Fig. 18, it can be seen that the shape of the radiation pattern in the E-plane and H-plane at 3.34 GHz and 11.57 GHz approximates a circle and exhibits good omnidirectional radiation characteristics. At the resonance frequency of 5.4 GHz, the radiation pattern of the E-plane is circular and that of the H-plane is in the shape of a cashew nut. The maximum radiation direction of the H-plane is in the range 150-180° ($\varphi = 0$) and 120-180°

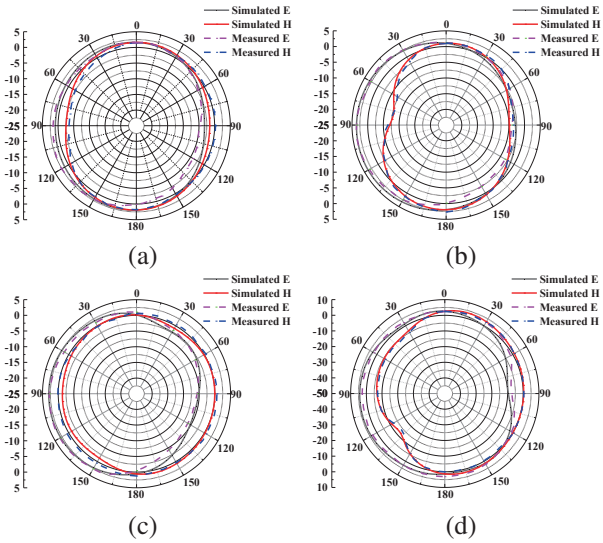

Fig. 18. Simulated and measured radiation patterns at (a) 3.34 GHz, (b) 5.4 GHz, (c) 11.57 GHz, and (d) 13.37 GHz.

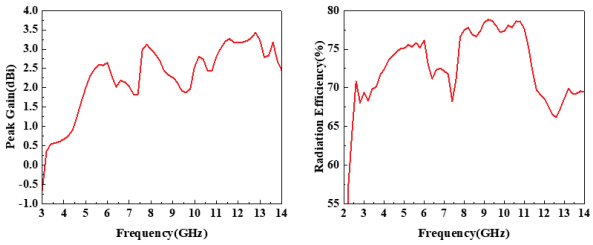

Fig. 19. (a) Peak realized gain and (b) radiation efficiency of the proposed antenna.

($\varphi = 180°$), whereas that of the E-plane is omnidirectional, which indicates better radiation characteristics. At the resonance frequency of 13.37 GHz, the radiation pattern in the E-plane is concave inward in the 90° ($\varphi = 0$) azimuth, and the radiation pattern in the H-plane is concave inward in the 120-150° ($\varphi = 180°$) azimuth. Both show a circular shape in the rest of the directions, which almost achieves an omnidirectional radiation characteristic.

Figure 19 shows the radiation efficiency and peak gain of the antenna over the operating band. The peak gain of the antenna can reach a maximum of 3.42 dBi. In addition, the antenna has a high radiation efficiency of more than 66% over the entire operating band.

C. MIMO antenna performance

1. DG and ECC

The diversity and mutual coupling characteristics of a MIMO antenna can be measured by its envelope correlation coefficient (ECC) [33]. ECC quantifies the correlation between received signal amplitudes of different antenna elements, with lower ECC values indicating better independence between the antenna elements, as calculated in equation (1). Diversity gain (DG) is a key metric indicating signal amplification or attenuation in MIMO systems and is determined by equation (2). Generally, the ECC of a MIMO antenna is expected to be lower than 0.5, indicating compliance with S-parameters (dB), radiation efficiency (%), and peak gain (dBi) requirements. Furthermore, a DG value closer to 10 suggests better MIMO antenna performance. As shown in Fig. 20, the ECC of this antenna is below 0.005, and the DG approaches 10, demonstrating that the antenna meets the communication requirements within the 3.06-14 GHz band.

$$ECC = \frac{\left|S_{11} * S_{12} + S_{21} * S_{22}\right|^2}{\left(1 - \left|S_{11}\right|^2 - \left|S_{21}\right|^2\right)\left(1 - \left|S_{22}\right|^2 - \left|S_{12}\right|^2\right)}. \quad (1)$$

$$DG = 10 \times \sqrt{1 - |ECC|}. \quad (2)$$

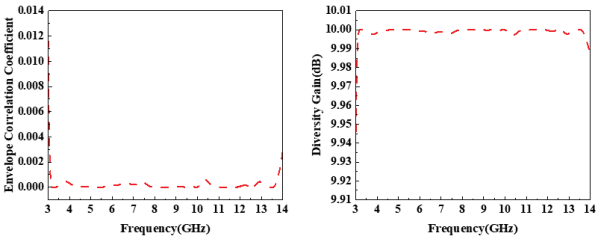

Fig. 20. (a) ECC and (b) DG of the proposed antenna.

2. TARC

The total effective reflection coefficient (TARC) is a critical parameter for assessing the efficiency of a MIMO antenna system. To achieve low reflection loss, stable phase performance, and reliable signal transmission in the MIMO antenna system, the TARC should be less than -10 dB. The calculation formula for TARC is:

$$TARC = \sqrt{\frac{(S_{11} + S_{12})^2 + (S_{21} + S_{22})^2}{2}}. \quad (3)$$

Figure 21 illustrates the TARC performance of the proposed antenna. As shown in Fig. 21, the TARC is less than -32 dB within the frequency band of 3.06-14 GHz, indicating minimal coupling within the MIMO system. This ensures channel independence at both transceiver and receiver ends while effectively leveraging the multipath effect to enhance system capacity.

3. Comparative study

Table 2 presents a performance comparison between the proposed antenna and several existing designs in

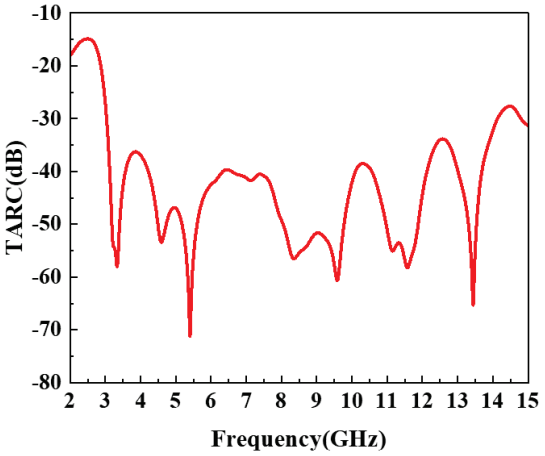

Fig. 21. TARC of the proposed antenna.

Table 2: Performance comparison of the proposed MIMO antenna with other antennas

Ref	Size (mm^2)	Bandwidth (GHz)	Isolation (dB)	ECC
[2]	27×22	3.07-11.1	>20	<0.014
[3]	36×36	2-11.08	>15	<0.13
[5]	52×26	2.3-11.5	>16	<0.012
[6]	79.8×79.8	3.38-10.56	>20	<0.36
[8]	70×70	3.2-11.2	>20	<0.002
[9]	40×40	3-13.5	>15	<0.4
[10]	30×30	2.77-12	>15	<0.1
[11]	62.5×60.5	3.5-11	>20	<0.01
[26]	40×40	2.8-11.4	>26	<0.001
[27]	48×58	2.7-12.6 3.0-11.0	>20 >16	<0.01
[30]	64×64	1.32-12.15	>20	<0.001
This Work	27×22	3.06-14	>20	<0.005

terms of size, bandwidth, isolation, and ECC. From Table 2, it can be observed that the antenna offers larger bandwidth and lower ECC than [2] while providing a smaller size, wider bandwidth, and lower ECC than [6, 11]. These advantages indicate the superior diversity performance and space utilization of the antenna. It also achieves a smaller size and larger bandwidth than [8]. At the same time, it has the same isolation properties as [2, 6, 8, 11]. Compared to reference [26], the proposed antenna exhibits a smaller size and broader bandwidth coverage, while preserving similar isolation and ECC levels. In addition, our design demonstrates stronger isolation characteristics and enhanced diversity performance in the 3.0-11.0 GHz frequency range, compared to reference [27]. Compared to reference [30], the proposed antenna has a smaller size while maintaining comparable isolation characteristics, which substantially enhances space utilization without compromising the radiation characteristics. Additionally, the antenna demonstrates a smaller size, higher isolation, larger bandwidth, and superior diversity performance compared to [3, 5, 9, 10] and it enables the antenna to show enhanced isolation performance and superior space utilization without compromising the radiation characteristics. In conclusion, the proposed antenna offers notable advantages regarding size, bandwidth, isolation, and diversity performance.

IV. CONCLUSION

This paper analyzes and designs an integrated polygonal UWB MIMO antenna with an EBG structure based on characteristic mode theory for high isolation. In the process of antenna evolution, the antenna structure is optimized by analyzing its characteristic modes and characteristic current distribution to adjust the bandwidth and mode coverage, ensuring simultaneous excitation of the eight characteristic modes and achieving UWB characteristics. Characteristic mode theory provides detailed physical insights and guides antenna optimization, resulting in a design with two symmetric octagonal radiating units, a T-shaped stepped floor, and an EBG structure. Additionally, five T-slots on the floor redirect current flow, enhancing antenna isolation to over 20 dB. Simulated and measured results demonstrate a bandwidth of 3.06-14 GHz, covering UWB and supporting 5G, WiFi6E, and X-band applications. The antenna also features a compact structure, small size, high radiation efficiency, and low ECC. In summary, the antenna exhibits excellent performance, making it suitable for various wireless communication bands.

ACKNOWLEDGMENT

This work was supported in part by the Natural Science Research Project of Anhui Educational Committee under grant no. 2022AH051583, no. 2022AH052138, and no. 2023AH052650; in part by the Anhui Province Graduate Academic Innovation Project under grant no. 2023xscx074; in part by the Funding Project of Scientific Research Starting for the High-level Talents of West Anhui University under grant no. WGKQ2022009.

REFERENCES

[1] M. A. Chung, C. C. Hsu, M. C. Lee, and C. W. Lin, "Enhancing multi-band MIMO antenna stability for various electronic applications with human-body interaction consideration," *IEEE Access*, vol. 11, pp. 129376-129398, 2023.

[2] W. Li, L. Wu, S. Li, X. Cao, and B. Yang, "Bandwidth enhancement and isolation improvement in compact UWB-MIMO antenna assisted by characteristic mode analysis," *IEEE Access*, vol. 12, pp. 17152-17163, 2024.

[3] W. Ren, Z. G. Wang, M. Yang, J. Zhou, and W. Y. Nie, "Design of a simple four-port UWB-MIMO antenna based on a fan-shaped isolator," *Progress Electromagnetics Research M*, vol. 126, pp. 117-126, 2024.

[4] S. Jayant, G. Srivastava, and S. Kumar, "Quad-port UWB MIMO footwear antenna for wearable applications," *IEEE Transactions on Antennas and Propagation*, vol. 70, pp. 7905-7913, 2022.

[5] S. H. Kiani, H. S. Savci, M. E. Munir, A. Sedik, and H. Mostafa, "An ultra-wide band MIMO antenna system with enhanced isolation for microwave imaging applications," *Micromachines*, vol. 14, p. 1732, 2023.

[6] S. Jayant and G. Srivastava, "Close-packed quad-element trip-band-notched UWB MIMO antenna with upgrading capability," *IEEE Transactions on Antennas and Propagation*, vol. 71, pp. 353-360, 2023.

[7] B. T. Ahmed, "High isolation compact UWB MIMO antennas," *Wireless Personal Communications*, vol. 128, pp. 3003-3029, 2023.

[8] Y. Yao, Y. Shao, J. Zhang, and J. Zhang, "A transparent antenna using metal mesh for UWB MIMO applications," *IEEE Transactions on Antennas and Propagation*, vol. 71, pp. 3836-3844, 2023.

[9] A. A. Khan, S. A. Naqvi, M. S. Khan, and B. Ijaz, "Quad port miniaturized MIMO antenna for UWB 11 GHz and 13 GHz frequency bands," *AEU-International Journal of Electronics and Communications*, vol. 131, p. 153618, 2021.

[10] A. G. Alharbi, U. Rafique, S. Ullah, S. Khan, S. M. Abbas, E. M. Ali, M. Alibakhshikenari, and M. Dalarsson, "Novel MIMO antenna system for ultra-wideband applications," *Applied Sciences*, vol. 12, p. 3684, 2022.

[11] M. Abdelghany, M. Fathy, A. Desai, and A. Ibrahim, "4-Port octagonal shaped MIMO antenna with low mutual coupling for UWB applications," *Computer Modeling in Engineering & Sciences*, vol. 136, pp. 1999-2015, 2023.

[12] R. N. Tiwari, V. Kaim, P. Singh, T. Khan, and B. K. Kanaujia, "Semi-flexible diversified circularly polarized millimeter-wave MIMO antenna for wearable biotechnologies," *IEEE Transactions on Antennas and Propagation*, vol. 71, pp. 3968-3982, 2023.

[13] P. M. Paul, K. Kandasamy, M. S. Sharawi, and B. Majumder, "Dispersion-engineered transmission line loaded slot antenna for UWB applications," *IEEE Antennas and Wireless Propagation Letters*, vol. 18, pp. 323-327, 2019.

[14] L. Sang, J. Wang, Z. Liu, W. Wang, W. Huang, and H. Tu, "A UWB metal waveguide slot array antenna based on hybrid resonant structural components," *IEEE Antennas and Wireless Propagation Letters*, vol. 22, pp. 923-927, 2023.

[15] Y. Cheng and Y. Dong, "Ultrawideband shared-aperture crossed tapered slot antenna for 5G applications," *IEEE Antennas and Wireless Propagation Letters*, vol. 22, pp. 472-476, 2023.

[16] S. Dey, S. Dey, and S. K. Koul, "Isolation improvement of MIMO antenna using novel EBG and hairpin shaped DGS at 5G millimeter wave band," *IEEE Access*, vol. 9, pp. 162820-162834, 2021.

[17] M. S. Aung and T. T. Hla, "Two-port wideband MIMO antenna for sub-6 GHz 5G applications," in *IEEE Conference on Computer Applications (ICCA),* Yangon, Myanmar, pp. 1-6, 2024.

[18] Y. Hei, J. He, and W. Li, "Wideband decoupled 8-element MIMO antenna for 5G mobile terminal applications," *IEEE Antennas and Wireless Propagation Letters*, vol. 20, pp. 1448-1452, 2021.

[19] Z. G. Wang, R. You, M. Yang, J. Zhou, and M. Wang, "Design of a monopole antenna for WiFi-UWB based on characteristic mode theory," *Progress in Electromagnetics Research M*, vol. 125, pp. 107-116, 2024.

[20] J. Su, S. Di, C. Yao, and X. Chen, "A compact high-isolation tri-band MIMO antenna based on characteristic mode analysis," *Progress in Electromagnetics Research M*, vol. 129, pp. 1-10, 2024.

[21] S. Grandhi Venkata and S. R. K. Kalva, "UWB monopole antenna with dual notched bands verified by characteristic mode analysis (CMA)," *Progress in Electromagnetics Research C*, vol. 121, pp. 39-48, 2022.

[22] L. Qu, "Common-loop MIMO antenna design with decoupling inductors using characteristic mode analysis," *IEEE Antennas and Wireless Propagation Letters*, vol. 22, pp. 3172-3176, 2023.

[23] N. W. Liu, B. B. Huang, and L. Zhu, "Isolation and bandwidth improvements of multimode single MPA with copolarized pattern using characteristic modes analysis," *IEEE Antennas and Wireless Propagation Letters*, vol. 22, pp. 1356-1360, 2023.

[24] J. Chen, M. Berg, K. Rasilainen, Z. Siddiqui, M. E. Leinonen, and A. Parssinen, "Broadband cross-slotted patch antenna for 5G millimeter-wave applications based on characteristic mode analysis," *IEEE Transactions on Antennas and Propagation*, vol. 70, pp. 11277-11292, 2022.

[25] X. Wang, L. Guo, W. Zhou, and Q. Zhang, "A double-layer multimode metasurface antenna using characteristic mode analysis," *IEEE Antennas and Wireless Propagation Letters*, vol. 23, pp. 3237-3241, 2024.

[26] A. C. Suresh and T. S. Reddy, "Experimental investigation of novel frock-shaped miniaturized 4×4 UWB MIMO antenna using characteristic mode analysis," *Progress in Electromagnetics Research B*, vol. 101, pp. 45-61, 2023.

[27] Z. J. Tang, J. Zhan, B. Zhong, L. Cheng, and G. Zuo, "Design of a coplanar UWB-MIMO ground antenna based on the theory of characteristic modes," *Progress in Electromagnetics Research C*, vol. 117, pp. 221-237, 2021.

[28] Y. Jia, J. Luo, X. Ren, G. Shi, and Y. Liu, "Design of low-RCS Vivaldi antenna based on characteristic mode analysis," *IEEE Antennas and Wireless Propagation Letters*, vol. 23, pp. 1246-1250, 2024.

[29] T. L. Yang, X. Zhang, Q. S. Wu, and T. Yuan, "Miniaturized wideband circularly polarized triangular patch antennas based on characteristic mode analysis," *Applied Computational Electromagnetics Society (ACES) Journal,* vol. 38, pp. 783-791, 2023.

[30] W. Y. Ren, Z. G. Wang, W. Y. Nie, W. D. Mu, C. L. Li, and M. Q. Wang, "A transparent ultra-wideband antenna fed by CPW based on characteristic mode theory," *Applied Computational Electromagnetics Society (ACES) Journal,* vol. 39, pp. 987-998, 2024.

[31] S. Liu, L. Yang, and X. Wu, "A low-profile wideband circularly polarized metasurface antenna based on characteristic mode theory," *Applied Computational Electromagnetics Society (ACES) Journal,* vol. 37, pp. 1110-1117, 2022.

[32] Z. Z. Wang, N. W. Liu, and L. Fang, "Low-profile dual-polarized filtering antenna with improved gain and impedance bandwidth using characteristic mode analysis," *Applied Computational Electromagnetics Society (ACES) Journal,* vol. 38, pp. 767-773, 2023.

[33] Z. G. Wang, G. X. Song, W. Y Nie, M. Yang, C. L. Li, and M. Q. Wang, "A racket-like UWB MIMO antenna with high isolation," *Progress in Electromagnetics Research C*, vol. 144, pp. 159-168, 2024.

Fukuan Zhang received the B.E. degree from Anhui University of Science and Technology in 2023. He is currently pursuing the M.S degree at Anhui University of Science and Technology. His current research interests include the theory and design of UWB MIMO antenna based on characteristic mode analysis.

Zhonggen Wang received the Ph.D. degree in electromagnetic field and microwave technique from the Anhui University of China (AHU), Hefei, P.R. China, in 2014. Since 2014, he has been with the School of Electrical and Information Engineering, Anhui University of Science and Technology. His research interests include computational electromagnetics, array antennas, and reflect arrays.

Wenyan Nie is a professor at Huainan Normal University. She received the B.S. and M.S degrees from Anhui University of Science and Technology in 2007 and 2012, respectively. Her research interests include computational electromagnetic methods, and antenna theory and design.

Ming Yang received the B.S. degree from Huaibei Normal University in 2005, and the M.S. and Ph.D. degrees in electromagnetic field and microwave technology from Anhui University, Hefei, China, in 2010 and 2019, respectively. He is currently the Deputy Director of the School of Electronics and Information Engineering, at West Anhui University, Lu'an, China. He is the author and co-author of about 20 scientific papers published in journals and presented at international conferences in the field of antenna design. His current research interests include MIMO antennas for hand-held devices, SIW antennas, base station antennas, multi-band antennas, millimeter wave antennas, and antenna array design.

Chenlu Li received the Ph.D. degree from Anhui University in 2017. She is currently working at Hefei Normal University. Her research interests include electromagnetic scattering analysis of targets and filtering antenna design.

Low-profile, Broadband, and High-gain Circularly Polarized Metasurface Antenna using Characteristic Mode Analysis

Yibiao Fan[1], Zhan Jin[2], Zhihe Fu[1], Xiaowei Cai[1], and Qi Lin[2]

[1]College of Physics and Mechatronic Engineering
Longyan University, Longyan 364012, China
8200617@lyun.edu.cn, fuzhihe@lyun.edu.cn, 82013030@lyun.edu.cn

[2]College of Communication and Electronic Engineering
Qiqihar University, Qiqihar 161006, China
jinzhan@qqhru.edu.cn, 17336248936@163.com

Abstract – In this paper, a low-profile broadband and high-gain circularly polarized (CP) metasurface antenna (MSA) is proposed. The characteristic mode analysis is employed to select the valuable modes for the 4×4 square metasurface elements printed on the top of the single-layer dielectric slab. The coplanar waveguide feeding structure combines a horizontal aperture and two slots rotated in a counter-clockwise direction is utilized to excite the CP radiation of the MSA. The proposed CP MSA is fabricated and measured, which achieves a -10 dB impedance bandwidth ranging from 4.83 GHz to 6.35 GHz, with a fractional bandwidth of 27.2%, the overlapped 3 dB axial ratio (AR) bandwidth is 20.1% (covers from 4.83 GHz to 5.91 GHz). Furthermore, the peak boresight gain measured at 5.2 GHz reaches 9.88 dBic. The average gain consistently maintains 8.94 dBic throughout the overlapped AR bandwidth, while the 3 dB gain bandwidth fully encompasses the entirety of the 3 dB overlapped AR bandwidth showing good performance for 5G Wi-Fi band utilization.

Index Terms – Broadband, characteristic mode analysis, circular polarization (CP), high-gain, low-profile, metasurface antenna (MSA).

I. INTRODUCTION

Circularly polarized (CP) antennas possess brilliant characteristics with immunity to polarization mismatch and multi-path effects, which have been popularly applied to wireless communication, radar, and remote sensing areas. The most traditional method to realize CP radiation for the patch antenna is to use a probe and single-feeding the patch at the diagonal position [1, 2]. However, this way is often accompanied by a narrow impedance bandwidth (IBW) and axial ratio (AR) bandwidth. To broaden the IBW and AR bandwidth, the thick substrate for the CP patch antenna is employed [1]. Though the AR bandwidth is improved from 2% to 8%, the over-thick substrate could excite the unexpected higher-mode, which will decrease the radiation efficiency of the CP antenna. Elsewhere, the multi-layer stacked CP antenna is proposed [2–4], and the AR bandwidth is further improved from 8% to 15%. However, the aforementioned thick substrates or multi-layer stacked CP antennas are inevitably high-profile and costly to manufacture.

A multi-fed [5–7] or multi-mode resonance [8, 9] scheme is a common approach for broadband CP antenna design. The sequentially rotated array antenna in [6] achieves 3 dB AR bandwidth from 5.15 to 7.9 GHz with a peak realized gain of 11.3 dBic for the multi-fed CP antenna. In addition, the proposed three modes resonance CP proposal actualized by U-slot in [9] obtains 3 dB AR bandwidth of 21.1% and boresight peak gain of 7.4 dBic. Despite this, the multi-fed scheme ordinarily needs an extra feeding network to excite the CP antenna, and the height of the multi-mode design is inevitably larger than a fraction of one free-space wavelength at the center of the working frequency.

To achieve a wide AR bandwidth but with a low profile for a CP antenna, parasitic elements are proposed and placed around the main radiator for CP radiation in [10, 11]. However, the peak realized gain of the CP antenna at the boresight direction is not very high (the usual value is in the vicinity of 6∼8 dBic).

In recent years, metamaterial (MTM) or metasurface (MTS) based antennas have been widely researched on broadening the IBW and decreasing the radiation aperture for linearly polarized metasurface antenna (MSA) [12, 13] and CP MSA [14, 16] utilization. Characteristic mode analysis (CMA) can bring a physical insight view to the antenna designer [12, 15, 16] and, with the guidance of CMA, the wanted CP radiation modes of the MSA can be selected at the interested frequency band.

Submitted On: July 23, 2024
Accepted On: April 27, 2025

https://doi.org/10.13052/2025.ACES.J.400503

Although the IBW can be enhanced, these CP MSAs still suffer from some constraints, such as the existence of the multi-layer stacked circuit structure[17–21], the overlapped bandwidth of AR and IBW, and the boresight gain is not satisfactory to some degree[22–25]. Hence, how to realize a low-profile, broadband, and high-gain CP antenna is still a challenge.

In this paper, a low-profile broadband high-gain single-layer CP MSA with 4×4 square MTS elements is proposed. With the assistance of CMA, the useful modes of the MSA are chosen for 5G Wi-Fi band utilization, the coplanar waveguide (CPW) combines a horizontal aperture, and two counter-clockwise rotated slot structures are employed to excite the MSA and achieve CP radiation. The proposed CP MSA obtains -10 dB IBW from 4.83 GHz to 6.35 GHz, and the 3 dB overlapped AR bandwidth is 20.1% (from 4.83 GHz to 5.91 GHz). The measured peak boresight gain of this CP MSA achieves 9.88 dBic and the 3 dB gain bandwidth covers its whole AR bandwidth, in addition, the profile height is only 0.07 λ_0. As verification, a prototype of the proposed CP MSA is manufactured and tested, and the tested results agree well with the simulated ones.

II. PROPOSED CP MSA AND CMA ANALYSIS

A. Geometry of the CP MSA

As depicted in Fig. 1 (a), the configuration of the proposed CP MSA is printed on the top surface of the square substrate (F4BM300) with a relative dielectric constant of 3.0 and a loss tangent of 0.002. The CPW feeding structure combines a horizontal aperture and two counter-clockwise rotated slots, which are coated on the bottom of the slab with a profile height h. MTS is comprised of a 4×4 uniformly spaced square MTS elements array and located on the top side of the substrate as depicted in Fig. 1 (b). All the square MTS elements are kept with the same side length w_E and the spacing of the MTS elements in both x- and y-axis directions is g_E. It can be seen from Fig. 1 (c), the horizontal aperture with a length of l_{S1} and a width of w_{S1}, which will combine

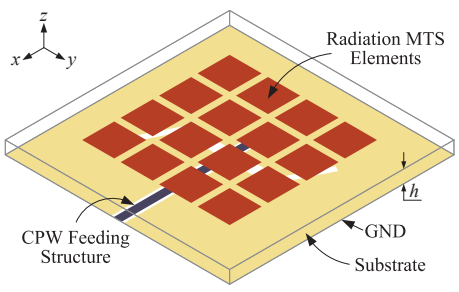

(a)

Fig. 1. *Continued.*

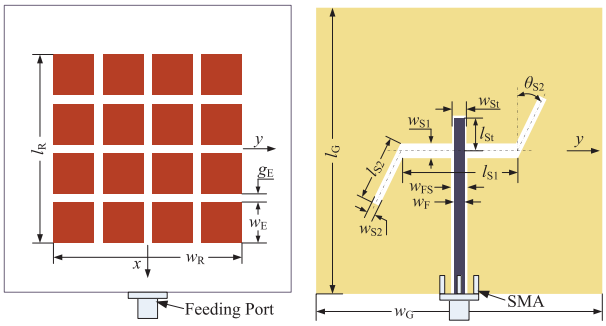

(b) (c)

Fig. 1. Configurations of the proposed CP MSA. (a) 3D view of the CP MSA. (b) Top view of the radiation MTS elements. (c) Bottom view of the CPW feeding structure. (unit: mm) $h = 4.0$, $l_R = 46.0$, $w_R = 46.0$, $w_E = 10.0$, $g_E = 2.0$, $w_G = 70.0$, $l_G = 70.0$, $w_F = 2.5$, $w_{FS} = 4.0$, $l_{S1} = 28.7$, $w_{S1} = 3.6$, $l_{S2} = 16.0$, $w_{S2} = 2.0$, $l_{St} = 8.0$, $w_{St} = 3.5$, $\theta_{S2} = 26.0°$.

two counter-clockwise rotated slots with a length of l_{S2} and a width of w_{S2} as the CP radiation source for the proposed 4×4 MTS elements.

B. Design process of the CP MSA

In the domain of CP radiation antenna design, the focal point resides in crafting an electric field or magnetic field with the same amplitude but a phase difference of 90° within the interested frequency band. Herein, the CMA is employed to select the wanted modes of the MSA for 5G Wi-Fi band utilization in this paper. It's worth mentioning that the CPW feeding structure and the coupling slots are removed from the ground plane of the 4×4 MTS elements during the process of CMA. Furthermore, the size of the ground plane is set to infinity and the PEC boundary conditions are imposed on the MTS elements and ground plane respectively.

The characteristic modes of the proposed MSA are analyzed by CST microwave studio ranging from 4 GHz to 7 GHz. The first five modes and their related modal significance (MS), modal surface current distributions, and the 3D radiation patterns are presented in Fig. 2. Regarding the MS, a value of 1 indicates an effective resonance, while a value of 0 signifies the absence of resonance excitation. It can be observed from the MS for Mode 1 and Mode 2 in Fig. 2, that a complete coincidence occurs in the whole frequency band. Meanwhile, the modal currents of J_{01} for Mode 1 are orthogonal to J_{02} for Mode 2, which are consistent with our common sense due to the excellent symmetry on physical scale of the proposed MTS elements. The even current distribution in the diagonal direction on each MTS surface for J_{01} and J_{02} will cause a high directivity with 11.6 dBi at 6 GHz.

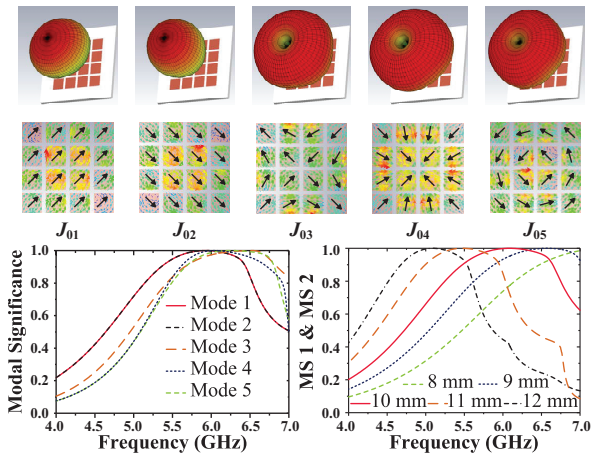

Fig. 2. Modal significance, modal current, and radiation patterns of the first five modes for the 4 × 4 square MTS antennas.

With respect to the last three modal currents J_{03}, J_{04}, and J_{05}, the currents on their corresponding MTS elements are presented as the centrally symmetric but out-of-phase distribution. As a consequence, the radiation nulls will be found in the boresight direction for the associated modal currents J_{03}, J_{04}, and J_{05}. For this reason, modal currents J_{01} and J_{02} are the targeted modes for boresight radiation in the frequency band of 5G Wi-Fi. Figure 2 also illustrates the changing tendency of MS for the first two modes (modes 1 and 2) from 4.0 GHz to 7.0 GHz. It's found that the resonance frequency of the MSA, when MS1 and MS2 are both equal to 1, decreases with the increase in the size of the MTS elements. When w_E equals to 10.0 mm, the MS1 and MS2 are both larger than 0.707, ranging from 5 GHz to 6.6 GHz, therefore an optimal -10 dB IBW of the MSA for 5G Wi-Fi can be obtained [12, 15]. Although these two modes can be excited simultaneously at $+45°$ and $-45°$, respectively, the resulting radiation pattern remains linearly polarized due to the lack of a phase difference between the modes.

To achieve a broadband CP radiation antenna during the interested frequency band, the CP radiation feed structure with a phase difference can be adopted to excite the two mutually orthogonal modes (Mode 1 and Mode 2). As shown in Fig. 1 (c), the horizontal aperture combines two counter-clockwise rotated slots and is considered as a CP radiation source for the proposed MTS elements. For the aims of further reducing the profile height and the number of dielectric layers of the MSA, the CPW feeding structure is employed to excite the CP radiation slots for the proposed 4 × 4 square MTS elements.

As shown in Fig. 3, the folded dipole antenna is used to explain the generating mechanism of phase difference of the CP radiation source. The simulated reflection coefficient S_{11} of it has two resonance modes. The surface current of Mode 1 of J_{M1} at 2.7 GHz characterizes the traditional dipole antenna and propagates along with the dipole antenna from one end to another, therefore a linear polarization wave with a high AR value of 39 occurs at 2.7 GHz. However, when the antenna works at Mode 2 of J_{M2} (higher-order mode) at 6.5 GHz, the direction of the current distribution of two rotated arms is opposite to the direction of Mode 1 of J_{M1}. Due to this, the phase difference can be obtained, therefore the corresponding AR value at 6.5 GHz declines obviously to 10 dB.

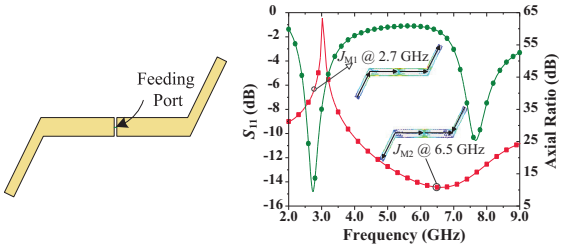

Fig. 3. Simulated reflection coefficient S_{11} and AR for the folded dipole antenna.

According to the mirror equivalent principle in the electromagnetic field, a coupling slot antenna with a phase difference can be simultaneously obtained from the folded dipole antenna as given in Fig. 4 (a) of the coupling slot antenna. Instead of an ideal lumped port for the slot antenna, the CPW transmission line with a matching stub is employed to excite the slot. So the electromagnetic waves from the feeding port will propagate along with the 50-ohm feeding line and then reach the proposed CP radiation slots with a phase difference to simultaneously excite the selected 4 × 4 square MTS elements. As shown in Fig. 4 (b), the simulated CP radiation slot with a -6 dB IBW covers from 5.0 GHz to 5.8 GHz. Furthermore, the radiation pattern for the CP source is radiation towards $+z$ direction and the AR declines simultaneously, which means this CP radiation slot could be utilized to excite the proposed 4 × 4 square MTS elements in the Wi-Fi band.

To further validate it, Fig. 5 also illustrates the phase difference between the $\overrightarrow{E_x}$ and $\overrightarrow{E_y}$ in the boresight direction and ratio of $\left|\overrightarrow{E_x}\right| / \left|\overrightarrow{E_y}\right|$ of the CP radiation source and CP MSA. Obviously, the phase difference of the CP radiation slot is located around from 26° to 43°, which further verifies that a phase difference can be obtained by the proposed CP radiation slot. In addition, when the selected 4 × 4 square MTS elements are loaded upon the radiation slot, the phase difference of the CP MSA is located around from 78° to 93°. Moreover, the ratio of

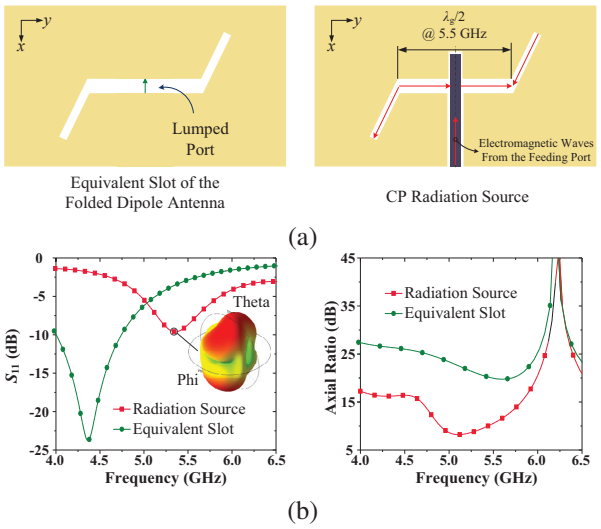

Fig. 4. (a) The equivalent slot of the folded dipole antenna and the proposed CP radiation source and (b) Simulated reflection coefficient S_{11} and AR of themselves.

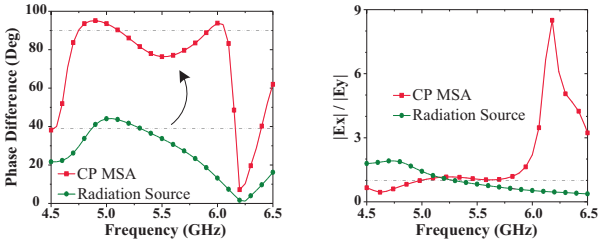

Fig. 5. The phase difference and ratio of $\left|\overrightarrow{E_x}\right| / \left|\overrightarrow{E_y}\right|$ of the CP radiation source and CP MSA.

$\left|\overrightarrow{E_x}\right| / \left|\overrightarrow{E_y}\right|$ also nears 1 ranging from 4.8 GHz to 5.8 GHz, which means a wideband CP antenna is obtained.

C. Parameters analysis

The coupling radiation slots of the proposed CP MSA serve as a crucial structure for achieving CP radiation. Hence, analyzing its dimensions is essential for determining both the reflection coefficient S_{11} and AR. Figure 6 (a) presents the effects of the counter-clockwise rotated slot length l_{S2} on antenna performance. To better analyze the impacts of the key parameters on the performance of the proposed CP MSA, the single factor variable method is adopted. It can be observed that the -10 dB IBW of the CP MSA increases synchronously with the increase of l_{S2} ranging from 14 mm to 18 mm. However, the 3 dB AR bandwidth exhibits a trend of initially increasing and then decreasing, with the optimal 3 dB AR bandwidth achieved at a value of 16 mm for l_{S2}.

After that, the rotated angle θ_{S2} between the counter-clockwise rotated slot and x-axis is studied in Fig. 6 (b). It is found that the influence of rotation angle

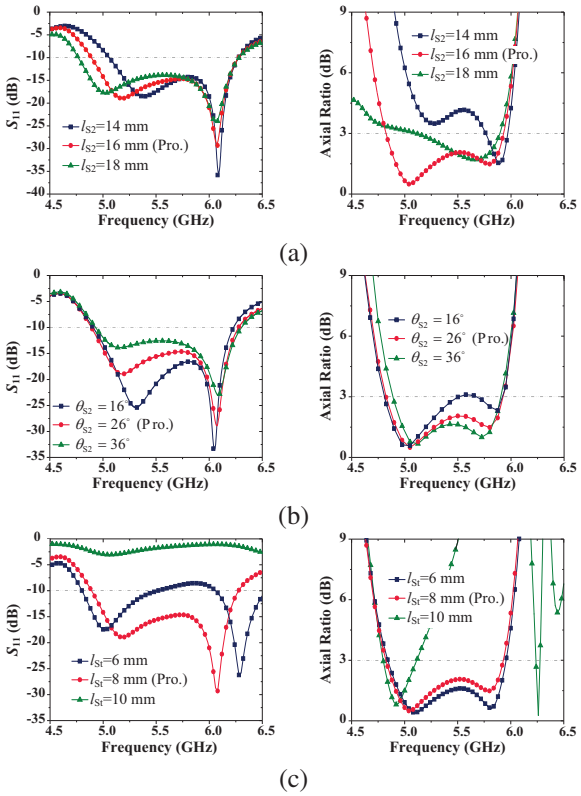

Fig. 6. The effects of the CP radiation structure parameters (a) l_{S2}, (b) θ_{S2}, and (c) l_{St} on the reflection coefficient S_{11} and AR of the CP MSA.

on the IBW is relatively minor compared to its depth, with the value of θ_{S2} increasing the AR bandwidth also increases and tends to be stable from 16° to 26°. Considering the depth of -10 dB IBW, the desired rotated angle with a value of 26° for θ_{S2} is selected in this CP MSA.

The impacts of the open matching stub length l_{St} of the 50-ohm CPW feeding line are also analyzed in Fig. 6 (c). The length of l_{St} significantly affects the reflection coefficient and AR. The tendency for 3 dB AR bandwidth of the CP MSA shows decreases with the increase of l_{St}. Considering the IBW will mismatch when l_{St} equals 6 mm and 10 mm, respectively. The selected value for l_{St} is 8 mm. The dimension parameters for the CP radiation slots are given in the caption of Fig. 1.

III. EXPERIMENTAL VERIFICATION

In order to validate the proposed CP MSA, a prototype of it is fabricated and tested. As shown in Fig. 7 (a) the Rohde & Schwarz ZND vector network analyzer is employed to test the reflection coefficient S_{11}. As depicted in Fig. 8, the measured -10 dB IBW spans from 4.83 GHz to 6.35 GHz, with a fractional bandwidth of 27.2%, demonstrating excellent agreement with the simulated results. The far-field radiation performance

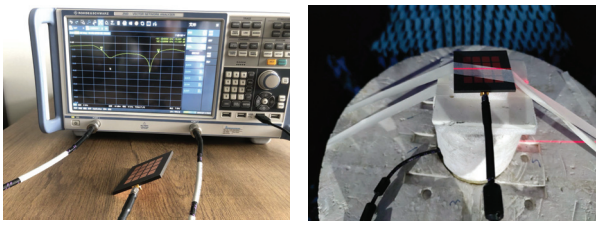

(a) (b)

Fig. 7. Photographs of the proposed CP MSA under testing: (a) reflection coefficient S_{11} and (b) far-field radiation performance.

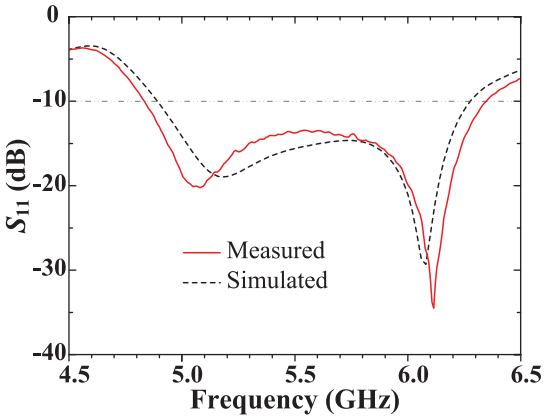

Fig. 8. The simulated and measured reflection coefficient S_{11} of the proposed CP MSA.

including the radiation pattern, AR bandwidth, and the boresight gain of the proposed CP MSA is tested in the microwave anechoic chamber as presented in Fig. 7 (b). It can be observed from Fig. 9, that the measured 3 dB AR bandwidth ranges from 4.53 GHz to 5.91 GHz, and the overlapped fractional bandwidth achieves 20.6% (from 4.83 GHz to 5.91 GHz) which is better than the simulated one. Furthermore, the measured peak boresight gain at 5.2 GHz is 9.88 dBic, and the average boresight gain during the whole overlapped bandwidth obtains 8.94 dBic which shows excellent far-field radiation performance.

With respect to Fig. 10, which shows the normalized far-field radiation pattern in the *xoz* plane and *yoz* plane at 5 GHz and 5.8 GHz respectively. The measured right-handed (RH) CP (co-polarized) radiation patterns of the proposed CP MSA at both frequencies present good consistency with the simulated ones. The measured left-handed (LH) CP (cross-polarized) radiation patterns show a slight difference from the simulated ones, which may be attributed to the effects of the test environment. However, the levels of the LHCP at the boresight direction are all less than -20 dB, showing the perfect working performance of the proposed CP MSA again.

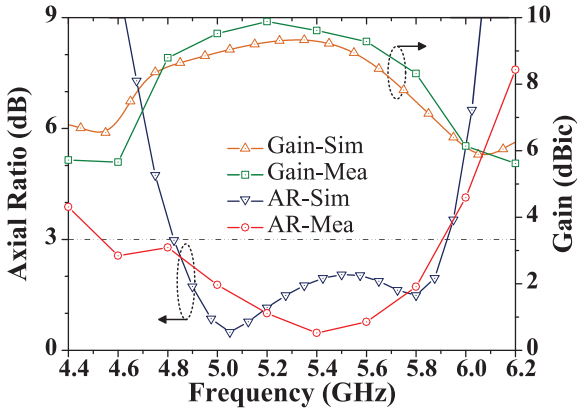

Fig. 9. The simulated and measured AR and gain at boresight direction of the proposed CP MSA.

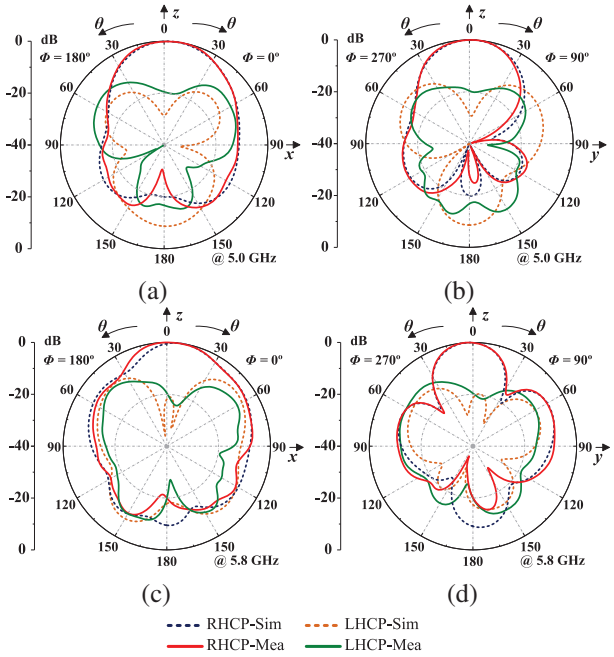

Fig. 10. The simulated and measured normalized radiation patterns for (a) *xoz* plane at 5.0 GHz, (b) *yoz* plane at 5.0 GHz, (c) *xoz* plane at 5.8 GHz, and (d) *yoz* plane at 5.8 GHz.

A performance comparison with the related works published in recent years is listed in Table 1. The primary contribution of the antenna in [17] is a low antenna aperture size, but the profile height reaches 0.19 λ_0 and the peak gain of the antenna is only 5.76 dBic. The merits of the antenna in [18, 20, 22] attribute to the low-profile height, however, the double-layer plate structure makes its manufacturing process more complicated. In [21], a larger AR bandwidth is obtained, but the double-layer structure and the peak gain of 7 dBic of the antenna is still not very good. In [23] and [25], the superiority

Table 1: Performance comparison with related works in recent years

Ref.	Antenna Aperture (λ_0^2)	Thickness (λ_0)	Over-Lapped AR Bandwidth	Peak Gain (dBic)	Layer
[17]	0.37×0.37	0.19	15.9%	5.76	2
[18]	0.75×0.73	0.09	20.0%	~ 8	2
[20]	0.62×0.50	0.07	16.5%	5.8	2
[21]	0.71×0.71	0.04	31.3%	7.01	2
[22]	0.74×0.74	0.04	14.5%	7	2
[23]	0.64×0.64	0.04	12.8%	6.9	1
[25]	0.71×0.72	0.06	16.6%	8	1
This work	0.82×0.82	0.07	20.1%	9.88	1

where λ_0 represents the free-space wavelength at the center frequency in the 3 dB overlapped AR operating bandwidth.

of it is the single-layer and low-profile design, but the overlapped 3 dB AR bandwidth and the peak gain of the antenna are not very satisfactory. With respect to the proposed CP MSA in this paper, the peak boresight gain achieves 9.88 dBic, and the overlapped 3 dB AR bandwidth is 20.1%. The 3 dB gain bandwidth covers the whole overlapped 3 dB AR bandwidth while maintaining the low-profile and single-layer design.

IV. CONCLUSION

In this paper, a low-profile, broadband, single-layer, and high-gain CP MSA is proposed. With the assistance of CMA, the useful modes J_{01} and J_{02} are selected for 5G Wi-Fi band utilization. To achieve the RHCP radiation of the MSA, the horizontal aperture combines two slots rotated in a counter-clockwise direction to excite the MS structure. The prototype of the CP MSA is fabricated and measured. The tested results correlate well with the simulated ones. The peak boresight gain of 9.88 dBic is obtained at 5.2 GHz, and the -10 dB IBW achieves from 4.83 GHz to 6.35 GHz, moreover, the 3 dB gain bandwidth covers its whole 3 dB overlapped AR bandwidth (20.1%, from 4.83 GHz to 5.91 GHz) and the average gain at the boresight direction can reach 8.94 dBic. The profile of the prototype of this CP MSA is only 0.07 λ_0, and the single-layer structure design makes the proposed CP MSA more promising in practical application.

ACKNOWLEDGMENT

The authors would like to express their gratitude for the generous support in part by the Natural Science Foundation of Fujian Province under Grant 2023J01967, in part by the Fundamental Research Funds in Heilongjiang Provincial Universities under Grant 145109145, and in part by the Heilongjiang Higher Education Teaching Reform Research Project under Grant SJGY20220403.

REFERENCES

[1] W. Yang, J. Zhou, Z. Yu, and L. Li, "Single-fed low profile broadband circularly polarized stacked patch antenna," *IEEE Transactions on Antennas and Propagation*, vol. 62, no. 10, pp. 5406–5410, Oct. 2014.

[2] J. Wang, X. Liu, P. Zhang, Z. Xu, A. Li, Z. Chen, and J. Fan, "Wideband center-fed stacked patch circularly polarized antenna used in phased array," *Applied Computational Electromagnetics Society (ACES) Journal*, vol. 38, no. 10, pp. 774–782, Oct. 2023.

[3] T. Mondal, S. Samanta, R. Ghatak, and S. R. B. Chaudhuri, "A novel hexagonal wideband circularly polarized stacked patch microstrip antenna," *Microwave and Optical Technology Letters*, vol. 57, no. 11, pp. 2548–2554, 2015.

[4] K. L. Chung and A. S. Mohan, "A circularly polarized stacked electromagnetically coupled patch antenna," *IEEE Transactions on Antennas and Propagation*, vol. 52, no. 5, pp. 1365–1369, May 2004.

[5] K. L. Chung, W. Li, Y. Li, R. Liu, and P. Zhang, "Chinese character-shaped artistic patch antenna," *Alexandria Engineering Journal*, vol. 18, no. 8, pp. 1542–1546, 2019.

[6] S. Mohammadi-Asl, J. Nourinia, C. Ghobadi, and M. Majidzadeh, "Wideband compact circularly polarized sequentially rotated array antenna with sequential-phase feed network," *IEEE Antennas and Wireless Propagation Letters*, vol. 16, pp. 3176-3179, 2017.

[7] L. Berretti, S. Maddio, G. Pelosi, M. Righini, and S. Selleri, "A six-elements circularly polarized sequential array for dedicated short range communications in C-band," *Applied Computational Electromagnetics Society (ACES) Journal*, vol. 33, no. 10, pp. 1117-1122, Oct. 2018.

[8] K.-F. Tong and T.-P. Wong, "Circularly polarized U-slot antenna," *IEEE Transactions on Antennas and Propagation*, vol. 55, no. 8, pp. 2382–2385, Aug. 2007.

[9] J. Zeng, X. Liang, L. He, F. Guan, F. H. Lin, and J. Zi, "Single-fed triple-mode wideband circularly polarized microstrip antennas using characteristic mode analysis," *IEEE Transactions on Antennas and Propagation*, vol. 70, no. 2, pp. 846–855, Feb. 2022.

[10] M. S. Ibrahim, "Design of low-cost, circularly polarized, and wideband U-slot microstrip patch antenna with parasitic elements for WiGig and

WPAN applications," *IEEE Antennas and Wireless Propagation Letters*, vol. 65, no. 9, pp. 1453–1456, Sep. 2019.

[11] L. Wang, Z. Zhu, and Y. En, "Performance enhancement of broadband circularly polarized slot–microstrip antenna using parasitic elements," *IEEE Antennas and Wireless Propagation Letters*, vol. 20, no. 12, pp. 2255–2259, Dec. 2021.

[12] F. H. Lin and Z. N. Chen, "Resonant metasurface antennas with resonant apertures: Characteristic mode analysis and dual-polarized broadband low-profile design," *IEEE Transactions on Antennas and Propagation*, vol. 69, no. 6, pp. 3512–3516, June 2021.

[13] D. Chen, W. Yang, Q. Xue, and W. Che, "Miniaturized wideband planar antenna using inter-embedded metasurface structure," *IEEE Transactions on Antennas and Propagation*, vol. 69, no. 5, pp. 3021–3026, May 2021.

[14] Z.-J Han, W. Song, and X. Q. Sheng, "Broadband circularly polarized antenna by using polarization conversion metasurface," *Applied Computational Electromagnetics Society (ACES) Journal*, vol. 69, no. 5, pp. 656–661, June 2020.

[15] Y. Chen and C.-F. Wang, *Characteristic Modes: Theory and Applications in Antenna Engineering*. Hoboken, NJ: John Wiley & Sons, 2015.

[16] J. F. Gao and F. H. Lin, "Modeling and analysis of wideband multilayer metasurface antenna array using characteristic-mode analysis," *IEEE Transactions on Antennas and Propagation*, vol. 71, no. 3, pp. 2832–2836, Mar. 2023.

[17] M. Ameen and R. K. Chaudhary, "Metamaterial-based wideband circularly polarised antenna with rotated V-shaped metasurface for small satellite applications," *Electronics Letters*, vol. 55, no. 7, pp. 365–366, 2019.

[18] Y. Huang, L. Yang, J. Li, Y. Wang, and G. Wen, "Polarization conversion of metasurface for the application of wide band low-profile circular polarization slot antenna," *Applied Physics Letters*, vol. 109, p. 051401, 2016.

[19] W. Li, W. Xue, Y. Li, X. Xiong, K. L. Chung, and Z. Huang, "Wideband single-fed circularly polarized stacked patch antenna with L-shaped stub," *Applied Computational Electromagnetics Society (ACES) Journal*, vol. 37, no. 12, pp. 1240–1248, Dec. 2022.

[20] Z. Wu, L. Li, Y. Li, and X. Chen, "Metasurface superstrate antenna with wideband circular polarization for satellite communication application," *IEEE Antennas and Wireless Propagation Letters*, vol. 15, pp. 374–377, 2016.

[21] S. X. Ta and I. Park, "Low-profile broadband circularly polarized patch antenna using metasurface," *IEEE Transactions on Antennas and Propagation*, vol. 63, no. 12, pp. 5929–5934, Dec. 2015.

[22] S. Liu, D. Yang, and J. Pan, "A low-profile circularly polarized metasurface antenna with wide axial-ratio beamwidth," *IEEE Antennas and Wireless Propagation Letters*, vol. 18, no. 7, pp. 1438–1442, July 2019.

[23] Z. Liang, J. Ouyang, and F. Yang, "Low-profile wideband circularly polarised single-layer metasurface antenna," *Electronics Letters*, vol. 54, no. 24, pp. 1362–1364, 2018.

[24] Y. Juan, W. Yang, and W. Che, "Miniaturized low-profile circularly polarized metasurface antenna using capacitive loading," *IEEE Transactions on Antennas and Propagation*, vol. 67, no. 5, pp. 3527–3532, May 2019.

[25] A. El Yousfi, A. Lamkaddem, K. A. Abdalmalak, and D. Segovia-Vargas, "A broadband circularly polarized single-layer metasurface antenna using characteristic-mode analysis," *IEEE Transactions on Antennas and Propagation*, vol. 71, no. 4, pp. 3114–3122, Apr. 2023.

Yibiao Fan received his B.S. degree from Minnan Normal University, Zhangzhou, China, in 2006, and M.S. degree from Huaqiao University, Quanzhou, China, in 2015. Presently, he serves as an associate professor and M.S. Candidate Advisor for College of Physics and Mechatronic Engineering of Longyan University, Longyan, China. His current research interests include metamaterial and microwave antennas.

Zhan Jin received the B.S. degree in Electrical and Information Engineering from Heilongjiang University, Harbin, China, in 2005, and M.S. degree and Ph.D. degree in Information and Communication Engineering from Harbin Engineering University, Harbin, China, in 2009 and 2020, respectively. She joined Qiqihar University, Qiqihar, China, in 2009, where she is currently an associate professor and M.S. Candidate Advisor with the College of Communication and Electronic Engineering. Her current research interests include signal processing, sparse adaptive filtering, and microwave antennas.

Xiaowei Cai was born in Zhangzhou, Fujian, China, in 1986. He received the B.S. degree in electronic information engineering and the M.S. degree in control engineering from Nanchang University, Jiangxi, China, in 2007 and 2013, respectively. Presently, he serves as an associate professor and M.S. Candidate Advisor for College of Physics and Mechatronic Engineering of Longyan University, Longyan, China. His current research interests include intelligent sensing and circularly antennas.

Zhihe Fu was born in Longyan, China, in 1970. He received the B.S. degree in materials physics from Fujian Normal University, Fuzhou, China, in 1992, and the M.S. degree in electronics and communications from Fuzhou University, Fuzhou, in 2011. He joined Longyan University, Longyan, China, in 1992, where he is currently a professor and M.S. Candidate Advisor for College of Physics and Mechatronic Engineering of Longyan University, Longyan, China. His current research interests include electric power systems measurement and control technologies.

Qi Lin is currently pursuing the B.S. degree in communication engineering with Qiqihar University, Qiqihar, China. Her research interests include signal processing, sparse adaptive filtering, and microwave antenna design.

Research on the Composite Electromagnetic Scattering of Rough Surface and Buried Target Based on G-PILE

Juan Zhao

Yichun University
School of Mathematics and Computer Science, Yichun, Jiangxi 336000, China
zj_ycxy@126.com

***Abstract* –** This article proposes a G-PILE (Generalized Propagation Inside Layer Expansion) algorithm for solving the composite electromagnetic scattering of large-scale dielectric rough surfaces and buried dielectric targets. Firstly, the EFIE (Electric Field Integral Equation) is established, and the traditional PILE algorithm is improved to extend its application to studying the composite scattering characteristics of targets under rough surfaces. In the iterative process, the BMIA/CAG (Banded Matrix Iterative Approach Canonical Grid) is introduced to solve the electromagnetic scattering of the rough surface itself, ultimately reducing the complexity of the algorithm to $O(N \log N)$ and achieving acceleration. Meanwhile, a conical incident wave is introduced to reduce the error caused by rough surface truncation. To verify the accuracy of G-PILE, the scattering characteristics of a dielectric cylinder buried under a dielectric rough surface are calculated and compared with existing algorithms. The effectiveness of G-PILE is demonstrated in several aspects. Results show that the algorithm gets excellent performance in accuracy and computation efficiency. Finally, the composite electromagnetic scattering depending on different target parameters is studied. These results are of great significance for understanding and predicting the interaction between rough ground and targets as well as the changes in scattering coefficients.

***Index Terms* –** Dielectric, electromagnetics, generalized propagation inside layer expansion, rough surface, scattering coefficient, target.

I. INTRODUCTION

The study of the composite electromagnetic scattering characteristics [1–7] of targets in a rough sea surface background is of great significance in both civilian and defense applications. Numerical algorithms [8–12] can more accurately simulate and predict the scattering characteristics of rough surfaces and objects. This accuracy is important for practical applications, as it enables us to better understand defensing and tackling real-world problems. For example, in military applications, precise scattering models can help us more accurately locate and track targets; in archaeological applications, precise scattering models facilitate more accurate detection and analysis of underground sites.

In addition to the study of the composite electromagnetic scattering characteristics of targets, the study of the composite scattering characteristics of buried targets is also of great significance [13–19]. For example, in defense, the detection of land mines and hidden targets underground is helpful for strategic decision making. In the archaeology field, the detection of underground sites can reveal the development and remains of historical civilizations. These applications require in-depth research on rough surfaces and targets.

Ishimaru et al. [20] proposed analytical methods for calculating the microrough surface of rough surfaces and the underlying targets. However, the application of analytical methods is limited by the parameters of the rough surface, their application range is relatively narrow, and calculation accuracy is often not high [21–28]. In contrast, numerical algorithms have greater flexibility and higher accuracy. Numerical algorithms can handle various composite rough surface and target models, which can be simulated and verified by computers.

Many scholars have conducted in-depth research on the electromagnetic scattering characteristics of the rough surface and the target. Sami et al. [8] studied the 3D scattering problem of PEC targets buried beneath rough dielectric surfaces. An efficient PILE-ACA (algebraic adaptive cross approximation) algorithm was proposed, and the mixed KA (Kirchhoff approximation)-EFIE formulation was used to extend the solution method of electromagnetic inverse problems, enabling effective simulation and analysis of 3D scattering problems. Mahariq et al. [9] investigated application of the PML (Perfectly Matched Layer) method in the context of SEM (spectral element method) in two-dimensional (2D) frequency domain scattering problems. By using the free space Green's function as the building block of the scattering field, this method was extended to the analysis

Submitted On: November 21, 2023
Accepted On: May 9, 2025

https://doi.org/10.13052/2025.ACES.J.400504

of SEM accuracy in large-scale object scattering. The results indicated that SEM can achieve high accuracy and demonstrated the successful applicability of PML in electromagnetic scattering problems. On the basis of maintaining the same measurement error, [10] compared SEM, FDM (finite difference method), and FEM (finite element method), mainly by studying the accuracy in 1D and 2D boundary value problems and demonstrating the high accuracy of SEM [23]. Kizilay and Yucedag [11] studied the TM wave scattering problem of conducting targets buried in a two-layered lossy medium, while [12] studied the scattering problem of targets in 3D littoral and surf-zone environments with multi-layered elastic sediments. The authors used an interior transmission formulation to more accurately describe the propagation of waves between the sediment and the target. They proposed a new numerical method that combined the finite element and finite difference methods to better handle complex boundary conditions and multi-layered structures. Additionally, the authors considered the elastic properties of the sediment to more accurately simulate wave propagation and scattering in the sediment.

In order to improve the speed of obtaining the electromagnetic scattering characteristics of a buried target under a randomly rough surface with large electrical dimensions, this paper proposes a G-PILE acceleration algorithm. The traditional PILE algorithm is a fast numerical algorithm for calculating the scattering of layered rough surfaces. This paper generalizes the standard PILE algorithm to be applicable to studying the composite scattering characteristics of targets below rough surfaces (G-PILE). To enable the algorithm to be applicable to large rough surfaces, the BMIA/CAG (Banded Matrix Iterative Approach Canonical Grid) algorithm is adopted to accelerate the algorithm. The acceleration algorithm solves the unknown variable $o(N\log N)$. Based on this algorithm, this paper also studies the interaction between the target and the rough surface, then analyzes the characteristics of the rough surface and the target.

II. ELECTROMAGNETIC SCATTERING MODEL

A. Electric Field Integral Equation (EFIE)

A schematic diagram of the target and rough surface is shown in Fig. 1, where the rough surface is denoted S_r. Above the rough surface is free space with permittivity and permeability denoted by ε_0 and μ_0, respectively. It has a medium space with permittivity and permeability denoted by ε_1 and μ_1, respectively. The target is buried below the rough surface, with its surface contour denoted by S_o and a depth of D. The target has permittivity and permeability denoted by ε_2 and μ_2, respectively. Throughout the region, the incident field is denoted by $\psi^{inc}(\boldsymbol{r})$. The total fields in the free space, medium space, and target are denoted by $\psi_0(\boldsymbol{r})$, $\psi_1(\boldsymbol{r})$, and $\psi_2(\boldsymbol{r})$, respectively, which can be collectively represented by $\psi_i(r)$, with subscript i representing different spaces.

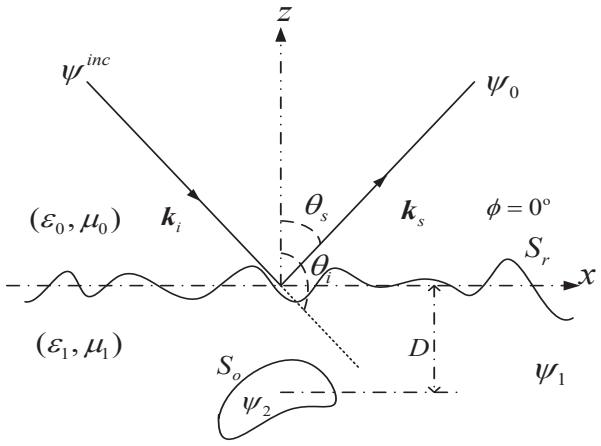

Fig. 1. Schematic of rough surface (S_r) and target (S_o).

When spot $\boldsymbol{r}$ approaches the rough surface and the target surface, the following boundary integral equations and boundary conditions apply.

$$(\boldsymbol{r}\in S_r)$$

for

$$P=-(\text{ outfre }-0.5005)*39.9295753-1.119039$$

$$\frac{1}{2}\psi_0(\boldsymbol{r})=\psi_{\text{inc}}(\boldsymbol{r})+\int_{S_r}\left[\psi_0(\boldsymbol{r}')\frac{\partial G_0(\boldsymbol{r},\boldsymbol{r}')}{\partial \boldsymbol{n}}-G_0(\boldsymbol{r},\boldsymbol{r}')\frac{\partial\psi_0(\boldsymbol{r}')}{\partial \boldsymbol{n}'}\right]ds' \quad (1)$$

$$\frac{1}{2}\psi_1(\boldsymbol{r})=-\int_{S_r}\left[\psi_1(\boldsymbol{r}')\frac{\partial G_1(\boldsymbol{r},\boldsymbol{r}')}{\partial \boldsymbol{n}'}-G_1(\boldsymbol{r},\boldsymbol{r}')\frac{\partial\psi_1(\boldsymbol{r}')}{\partial \boldsymbol{n}'}\right]ds'+\int_{S_o}\left[\psi_1(\boldsymbol{r}')\frac{\partial G_1(\boldsymbol{r},\boldsymbol{r}')}{\partial \boldsymbol{n}'}-G_1(\boldsymbol{r},\boldsymbol{r}')\frac{\partial\psi_1(\boldsymbol{r}')}{\partial \boldsymbol{n}'}\right]ds' \quad (2)$$

$$\psi_0(\boldsymbol{r})|_{\boldsymbol{r}\in S_r}=\psi_1(\boldsymbol{r})|_{\boldsymbol{r}\in S_r}, \quad (3)$$

$$\left.\frac{\partial\psi_0(\boldsymbol{r})}{\partial \boldsymbol{n}}\right|_{\boldsymbol{r}\in S_r}=\frac{1}{\rho_r}\left.\frac{\partial\psi_1(\boldsymbol{r})}{\partial \boldsymbol{n}}\right|_{\boldsymbol{r}\in S_r}. \quad (4)$$

For $(r\in S_o)$:

$$\frac{1}{2}\psi_1(\boldsymbol{r})=-\int_{S_r}[\psi_1(\boldsymbol{r}')\frac{\partial G_1(\boldsymbol{r},\boldsymbol{r}')}{\partial \boldsymbol{n}'}-G_1(\boldsymbol{r},\boldsymbol{r}')\frac{\partial\psi_1(\boldsymbol{r}')}{\partial \boldsymbol{r}'}]ds'+\int_{S_o}[\psi_1(\boldsymbol{r}')\frac{\partial G_1(\boldsymbol{r},\boldsymbol{r}')}{\partial \boldsymbol{r}'}-G_1(\boldsymbol{r},\boldsymbol{r}')\frac{\partial\psi_1(\boldsymbol{r}')}{\partial \boldsymbol{r}'}]ds', \quad (5)$$

$$\frac{1}{2}\psi_2(\boldsymbol{r})=-\int_{S_r}[\psi_2(\boldsymbol{r}')\frac{\partial G_2(\boldsymbol{r},\boldsymbol{r}')}{\partial \boldsymbol{n}'}-G_2(\boldsymbol{r},\boldsymbol{r}')\frac{\partial\psi_2(\boldsymbol{r}')}{\partial \boldsymbol{n}'}]ds', \quad (6)$$

$$\psi_1(\boldsymbol{r})|_{\boldsymbol{r}\in S_o}=\psi_2(\boldsymbol{r})|_{\boldsymbol{r}\in S_o}, \quad (7)$$

$$\left.\frac{\partial\psi_1(\boldsymbol{r})}{\partial \boldsymbol{n}}\right|_{\boldsymbol{r}\in S_0}=\frac{1}{\rho_o}\left.\frac{\partial\psi_2(\boldsymbol{r})}{\partial \boldsymbol{n}}\right|_{\boldsymbol{r}\in S_0}, \quad (8)$$

where $\rho_r = \mu_1/\mu_0$, $\rho_o = \mu_2/\mu_1$ for TE incident wave, and $\rho_r = \varepsilon_1/\varepsilon_0$, $\rho_o = \varepsilon_2/\varepsilon_1$ for TM incident wave. $G_{0,1,2}(r,r')$ represents the Green function of each space, which can be expressed as:

$$G_{0,1,2}(\boldsymbol{r},\boldsymbol{r}') = \frac{i}{4}H_0^{(1)}(k_{0,1,2}\left|\boldsymbol{r}-\boldsymbol{r}'\right|), \tag{9}$$

$$\frac{\partial G_{0,1,2}(\boldsymbol{r},\boldsymbol{r}')}{\partial \boldsymbol{n}} = \frac{ik_{0,1,2}}{4}\hat{\boldsymbol{n}}\cdot\frac{\boldsymbol{r}-\boldsymbol{r}'}{\left|\boldsymbol{r}-\boldsymbol{r}'\right|}H_1^{(1)}(k_{0,1,2}\left|\boldsymbol{r}-\boldsymbol{r}'\right|). \tag{10}$$

B. G-PILE (Generalized Propagation Inside Layer Expansion) algorithm

Using the method of moments based on pulse basis functions, we can discretize the boundary integral equation into the following matrix equation:

$$\mathbf{ZI} = \mathbf{V}. \tag{11}$$

In this equation, $\boldsymbol{Z}$ is the impedance matrix, $\boldsymbol{I}$ is the unknown vector to be solved, and $\boldsymbol{V}$ is the excitation vector. The matrix equation can be further expressed as:

$$\boldsymbol{Z}\cdot\begin{bmatrix}\boldsymbol{I}_r\\ \boldsymbol{I}_o\end{bmatrix} = \begin{bmatrix}\boldsymbol{V}_r\\ \boldsymbol{V}_o\end{bmatrix}, \tag{12}$$

where the excitation vector $\boldsymbol{V} = \begin{bmatrix}\boldsymbol{V}_r\\ \boldsymbol{V}_o\end{bmatrix}$ contains two main components. The first is the rough surface excitation vector $\boldsymbol{V}_r$, which has an expression of $\boldsymbol{V}_r^T = [\psi_{inc}(r_1)\dots\psi_{inc}(r_N),0\dots0]$(It is represented here as a transposed matrix.) The second is the target excitation vector V_o, which has a value of $\boldsymbol{0}$ because the target is not directly illuminated by the incident wave.

Similarly, the unknown vector $\boldsymbol{I} = \begin{bmatrix}\boldsymbol{I}_r\\ \boldsymbol{I}_o\end{bmatrix}$ consists of two parts: the unknown vector $\boldsymbol{I}_r$ of the rough surface and the unknown vector $\boldsymbol{I}_o$ of the target. These two parts can be represented as a transposed matrix

$$\boldsymbol{I}_r^T = \left[\psi_r(r_1)\dots\psi_r(r_N)\frac{\partial\psi_r(r_1)}{\partial n}\dots\frac{\partial\psi_r(r_N)}{\partial n}\right], \tag{13}$$

$$\boldsymbol{I}_o^T = \left[\psi_o(r_1)\dots\psi_o(r_M)\frac{\partial\psi_o(r_1)}{\partial n}\dots\frac{\partial\psi_o(r_M)}{\partial n}\right]. \tag{14}$$

The unknown variables to be solved are ψ_r, $\frac{\partial\psi_r}{\partial n}$, ψ_o, and $\frac{\partial\psi_o}{\partial n}$, and can be obtained by the following matrix equation:

$$\begin{bmatrix}\boldsymbol{I}_r\\ \boldsymbol{I}_o\end{bmatrix} = \boldsymbol{Z}^{-1}\cdot\begin{bmatrix}\boldsymbol{V}_r\\ \boldsymbol{V}_o\end{bmatrix} = \boldsymbol{Z}^{-1}\cdot\begin{bmatrix}\boldsymbol{V}_r\\ \boldsymbol{0}\end{bmatrix}. \tag{15}$$

The key to solving this equation lies in the appropriate treatment of the impedance matrix $\boldsymbol{Z}$. According to [29], $\boldsymbol{Z}$ can be divided into four parts, namely $\boldsymbol{Z}^r$, $\boldsymbol{Z}^o$, $\boldsymbol{Z}^{o\to r}$, and $\boldsymbol{Z}^{r\to o}$. Specifically, $\boldsymbol{Z}^r$ represents the impedance matrix of the rough surface, which reflects the characteristics of the rough surface. $\boldsymbol{Z}^o$ is the impedance matrix of the target, representing the characteristics of the target. $\boldsymbol{Z}^{o\to r}$ and $\boldsymbol{Z}^{r\to o}$ represent the impedance matrix of the interaction between the rough surface and the target, which reflects the interaction between the two. These four parts taken together constitute the impedance matrix $\boldsymbol{Z}$. They satisfy the following relationship:

$$\boldsymbol{Z} = \begin{bmatrix}\boldsymbol{Z}^r & \boldsymbol{Z}^{o\to r}\\ \boldsymbol{Z}^{r\to o} & \boldsymbol{Z}^o\end{bmatrix}, \tag{16}$$

$$\boldsymbol{Z}^{-1} = \begin{bmatrix}\boldsymbol{A} & \boldsymbol{B}\\ \boldsymbol{C} & \boldsymbol{D}\end{bmatrix}, \tag{17}$$

$$\begin{aligned}
\boldsymbol{A} &= (\boldsymbol{Z}^r - \boldsymbol{Z}^{o\to r}(\boldsymbol{Z}^o)^{-1}\boldsymbol{Z}^{r\to o})^{-1}\\
\boldsymbol{B} &= -(\boldsymbol{Z}^r - \boldsymbol{Z}^{o\to r}(\boldsymbol{Z}^o)^{-1}\boldsymbol{Z}^{r\to o})^{-1}\boldsymbol{Z}^{o\to r}(\boldsymbol{Z}^o)^{-1}\\
\boldsymbol{C} &= -(\boldsymbol{Z}^o)^{-1}\boldsymbol{Z}^{r\to o}(\boldsymbol{Z}^r - \boldsymbol{Z}^{o\to r}(\boldsymbol{Z}^o)^{-1}\boldsymbol{Z}^{r\to o})^{-1}\\
\boldsymbol{D} &= (\boldsymbol{Z}^o)^{-1} + (\boldsymbol{Z}^o)^{-1}\boldsymbol{Z}^{r\to o}(\boldsymbol{Z}^r - \boldsymbol{Z}^{o\to r}(\boldsymbol{Z}^o)^{-1}\boldsymbol{Z}^{r\to o})^{-1}\\
&\quad\ \boldsymbol{Z}^{o\to r}(\boldsymbol{Z}^o)^{-1}.
\end{aligned} \tag{18}$$

Combining (15-18),we get:

$$\begin{bmatrix}\boldsymbol{I}_r\\ \boldsymbol{I}_o\end{bmatrix} = \begin{bmatrix}\boldsymbol{Z}^r & \boldsymbol{Z}^{o\to r}\\ \boldsymbol{Z}^{r\to o} & \boldsymbol{Z}^o\end{bmatrix}^{-1}\cdot\begin{bmatrix}\boldsymbol{V}_r\\ 0\end{bmatrix} = \begin{bmatrix}\boldsymbol{A}\cdot\boldsymbol{V}_r\\ \boldsymbol{C}\cdot\boldsymbol{V}_r\end{bmatrix}, \tag{19}$$

where:

$$\begin{aligned}
\boldsymbol{I}_r &= (\boldsymbol{Z}^r - \boldsymbol{Z}^{o\to r}(\boldsymbol{Z}^o)^{-1}\boldsymbol{Z}^{r\to o})^{-1}\boldsymbol{V}_r\\
&= (\boldsymbol{E} - (\boldsymbol{Z}^r)^{-1}\boldsymbol{Z}^{o\to r}(\boldsymbol{Z}^o)^{-1}\boldsymbol{Z}^{r\to o})^{-1}(\boldsymbol{Z}^r)^{-1}\boldsymbol{V}_r,
\end{aligned} \tag{20}$$

$$\begin{aligned}
\boldsymbol{I}_o &= -(\boldsymbol{Z}^o)^{-1}\boldsymbol{Z}^{r\to o}(\boldsymbol{Z}^r - \boldsymbol{Z}^{o\to r}(\boldsymbol{Z}^o)^{-1}\boldsymbol{Z}^{r\to o})^{-1}\boldsymbol{V}_r\\
&= -(\boldsymbol{Z}^o)^{-1}\boldsymbol{Z}^{r\to o}(\boldsymbol{E} - (\boldsymbol{Z}^r)^{-1}\boldsymbol{Z}^{o\to r}(\boldsymbol{Z}^o)^{-1}\boldsymbol{Z}^{r\to o})^{-1}(\boldsymbol{Z}^r)^{-1}\boldsymbol{V}_r\\
&= -(\boldsymbol{Z}^o)^{-1}\boldsymbol{Z}^{r\to o}\cdot\boldsymbol{I}_r.
\end{aligned} \tag{21}$$

$\boldsymbol{I}$ is the identity matrix. If the characteristic matrix $\boldsymbol{M}_c = (\boldsymbol{Z}^r)^{-1}\boldsymbol{Z}^{o\to r}(\boldsymbol{Z}^o)^{-1}\boldsymbol{Z}^{r\to o}$ is defined then, according to the above formulas, the following statement holds:

$$(\boldsymbol{I} - (\boldsymbol{Z}^r)^{-1}\boldsymbol{Z}^{o\to r}(\boldsymbol{Z}^o)^{-1}\boldsymbol{Z}^{r\to o})^{-1} = \sum_{n=0}^{n=\infty}\boldsymbol{M}_c^n. \tag{22}$$

This equation will be difficult to calculate without truncating the order n of the matrix. Therefore, we define a truncation order T_r, and the truncated unknown vector can be expressed as:

$$\boldsymbol{I}_r = \left[\sum_{n=0}^{n=T_r}\boldsymbol{M}_c^n\right](\boldsymbol{Z}^r)^{-1}\boldsymbol{V}_r, \tag{23}$$

$$\boldsymbol{I}_o = -\left[\sum_{n=0}^{n=T_r}\boldsymbol{M}_c^n\right](\boldsymbol{Z}^o)^{-1}\boldsymbol{Z}^{r\to o}(\boldsymbol{Z}^r)^{-1}\boldsymbol{V}_r. \tag{24}$$

The number of sampling points for rough surfaces is usually much larger than that for targets, where the increase in unknown quantities makes the calculation more difficult. Therefore, the key to solving the above process lies in finding the inverse of matrix $(\boldsymbol{Z}^r)^{-1}$(whose computational complexity is $O(N^3)$). To solve this problem, we construct a matrix equation $\boldsymbol{Z}^r\boldsymbol{N} = \boldsymbol{M}$, which transforms the solution of $(\boldsymbol{Z}^r)^{-1}\boldsymbol{M}$ into the solution of $\boldsymbol{N}$. In this matrix equation, $\boldsymbol{Z}^r$ is the impedance matrix of the rough surface itself, so the solution process of this matrix is equivalent to the solution problem of the dielectric rough surface. We use the BMIA/CAG algorithm as an acceleration algorithm to calculate this matrix, which has low computational complexity, simple relative principles, and is easy to

implement. By employing this method, we can effectively accelerate the calculation of dielectric rough surfaces.

The details of BMIA/CAG can be found in [30], which mainly introduces the basic principles and main ideas for accelerated computation. During the iterative solution of $\boldsymbol{Z}^r\boldsymbol{N}=\boldsymbol{M}$, the repeated calculations of $\boldsymbol{Z}^r\boldsymbol{N}$ consume a large amount of computer memory and have low computational efficiency. Therefore, it is essential to take adequate measures to deal with and accelerate it. The advantages of BMIA/CAG are reflected in this processing and acceleration.

Firstly, we define the strong-weak correlation distance R_d and partition $\boldsymbol{Z}^r$ into a strongly correlated impedance matrix $\boldsymbol{Z}_s^r$(banded matrix) and a weakly correlated impedance matrix $\boldsymbol{Z}_w^r$(the remaining part outside the strongly correlated impedance matrix). In this way, the original impedance matrix equation can be transformed into:

$$\boldsymbol{Z}_s^r\boldsymbol{N}+\boldsymbol{Z}_w^r\boldsymbol{N}=\boldsymbol{M}. \tag{25}$$

In practical calculations, due to the small value of R_d, we can directly calculate the strongly correlated impedance matrix using the method of moments. For the weakly correlated impedance matrix, due to its high computational cost, we cannot directly calculate it. Therefore, we adopt the CAG method to deal with it, which is to expand the weak matrix in the x-direction using the Taylor series, then represent the multiplication of the weak matrix and column vector as the multiplication of several terms of Toeplitz matrix and column vector. Next, we use FFT to calculate the matrix vector product. The final computational complexity is $o(N\log N)$. Only $\boldsymbol{Z}_s^r$ needs to be solved, greatly reducing the computer memory requirements.

In order to apply numerical algorithms, the calculated region of the rough surface is limited to a certain range. For 2D scattering problems, in order to limit the rough surface to L, it is artificially stipulated that the surface current is zero when $|x|>L/2$. At this point, the surface current will have a sudden change at $x=\pm L/2$. If a plane wave is used, then artificial reflections will occur at the two ends. To avoid the error caused by truncation [31], we choose the incident wave to be a conical wave. The widely used Thorsos conical wave can well satisfy the Helmholtz wave equation. Its expression is:

$$\psi_{inc}(\boldsymbol{r})=\exp\left[j\boldsymbol{k}_i(1+\omega(\boldsymbol{r}))\right]\cdot\exp\left[-\frac{(x+z\tan\theta_i)^2}{g^2}\right], \tag{26}$$

$$\boldsymbol{k}_i=k(\hat{x}\sin\theta_i-\hat{z}\cos\theta_i), \tag{27}$$

$$\omega(\boldsymbol{r})=\left[2(x+z\tan\theta_i)^2/g^2-1\right]\Big/(kg\cos\theta_i)^2, \tag{28}$$

where g represents the width of the cone, which determines the range of incident wave width and rough surface length. The value of rough surface length is directly related to the efficiency and accuracy of numerical calculation. A larger rough surface value can better reflect the average scattering characteristics of the rough surface, thereby improving the accuracy of numerical calculation. However, this also requires more storage space and calculation time. Therefore, in choosing g, we need to balance the accuracy of the calculation results and the calculation efficiency. Usually, the value range of g can be determined by:

$$g\geq\frac{6}{(\cos\theta_i)^{1.5}}. \tag{29}$$

Following the above calculation steps, we can obtain specific values of the scattering field and scattering coefficient [29]:

$$\psi_s(r)=\frac{ie^{ik_0r}}{4\sqrt{r}}\sqrt{\frac{2}{\pi k_0}}e^{-i\frac{\pi}{4}}\cdot\int_{S_r}\left[-i(\hat{n}\cdot k_s)\psi_r(x)-\frac{\partial\psi_r(x)}{\partial n}\right]e^{-ik_s\cdot r}ds, \tag{30}$$

$$\sigma(\theta_s)=\frac{|\psi_s(r)|^2}{g\sqrt{2/\pi}\cos\theta_i[1-\frac{1+2\tan^2\theta_i}{2k^2g^2\cos^2\theta_i}]}. \tag{31}$$

Through the detailed description of this process, we can better understand and more accurately describe the scattering phenomenon. In order to ensure the accuracy and rigor of this paper, we will analyze these results in detail in subsequent sections and explore their possible applications and implications.

III. ALGORITHM VALIDITY VERIFICATION

A. Verification of rough surface field results

Firstly, the effectiveness of the algorithm for calculating the total field of a rough surface was studied. The scattering field $\psi_s(r)$ of the rough surface at different truncation orders Tr was calculated and presented in Fig. 2, as shown by the black and blue lines. The red line represents the results of strict application of the LU decomposition method under the same conditions, which is stable, and is used to verify the algorithm in this article. The relevant parameters are: rough surface length $L=50\lambda$, number of unknowns N=500, root mean square height $h=0.2\lambda$, correlation length $l=1.0\lambda$, lower medium relative permittivity $\varepsilon_1=2.0+0.2i$. The buried target is a cylinder, which is horizontally placed below the rough surface with depth $D=1.0\lambda$, radius $R=0.5\lambda$, and number of unknowns N=50. The relative dielectric constant is $\varepsilon_2=10.0+0.0i$. The incident angle is $\theta_{inc}=30^\circ$, and the beam width is $g=L/6$.

From Figs. 2 (a) and (c), we can clearly see that, overall, the computational results of the G-PILE algorithm proposed in this paper are largely consistent with those of the LU decomposition method. This consistency

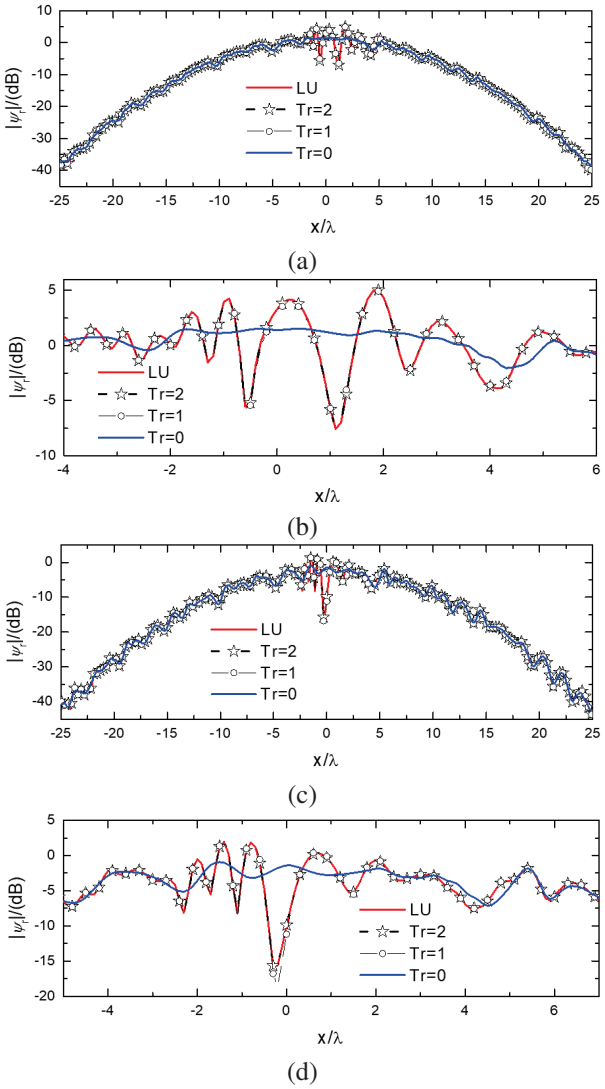

Fig. 2. Verification of rough surface field results. (a) TM incident wave, (b) enlarged view of the area within (-4,6) of (a), (c) TE incident wave, and (d) enlarged view of the area within (-5,7) of (c).

brings credibility to our algorithm and confirms its practicality and effectiveness.

However, we also noticed that the size of the truncation order *Tr* had a certain impact on the accuracy of the results of the two methods. When *Tr* is 0, some fluctuations occur within a distance of ±5 from the center of the rough surface. In order to further explore and study these fluctuations, we zoomed in on this region, as shown in Figs. 2 (b) and (d).

Through observation and comparison, we found that when TM waves are incident, the maximum difference between the blue curve (*Tr*=0) and the red curve (LU reference curve) is 7.8 dB. Except for some fluctuations in the range (-2,4), the calculation results in other regions are in good agreement. This indicates that the G-PILE algorithm has high accuracy and reliability in handling such problems.

When TE waves are incident, the maximum difference is 22.3 dB. The calculated results in all regions except for the (-2.7,2) region also exhibit good agreement. These results indicate that our algorithm can maintain high accuracy and stability in processing different polarized wave incidences.

B. Verification of the results of bistatic-scattering coefficients

In addition, we studied the bistatic-scattering coefficients of buried targets under rough ground conditions using the algorithm presented in this paper by understanding TE and TM polarization incident waves. The results are shown in Fig. 3.

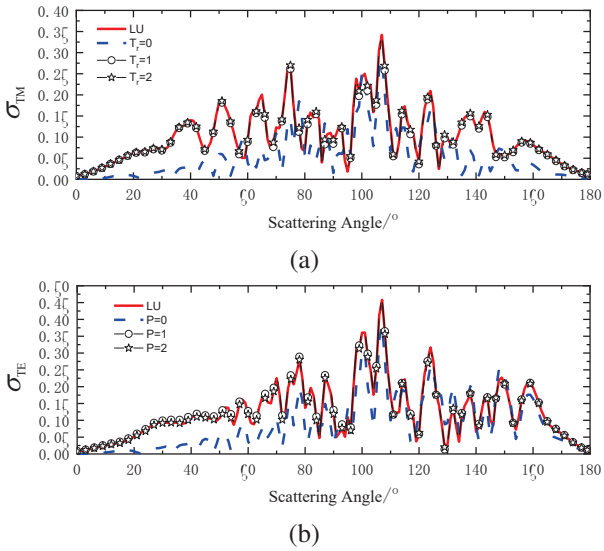

Fig. 3. Verification of bistatic-scattering coefficients. (a) TM incident wave and (b) TE incident wave.

These research results provide valuable information about the performance and applicability of the algorithm in practical problems. By observing Fig. 3, we can see that, regardless of whether the incident wave is TE or TM, the G-PILE algorithm presented in this paper can provide consistent computational results with the reference results. This further validates the accuracy and effectiveness of the algorithm.

At the same time, we also noticed that the accuracy of the computational results gradually increases as the truncation order *Tr* increases. This may be due to the fact that as *Tr* increases, the computational results include more components of the interaction between the target and the rough surface, thus more accurately describing the physical process. These results indicate that our algo-

rithm has good robustness and scalability in dealing with complex problems.

In summary, the G-PILE algorithm presented in this paper exhibits good performance and accuracy in dealing with rough surface scattering problems. By choosing a reasonable truncation order *Tr*, we can further improve the accuracy and stability of the algorithm. These findings have important guiding significance for us to better understand and solve complex scattering problems.

C. Convergence characteristics

In sections III.A and B, it was found that different choices of truncation order significantly impact the final accuracy. Especially when *Tr* vanishes, it can be observed that the final value fluctuates within a small range, indicating poor convergence. This may be due to insufficient consideration of target-rough surface interaction when *Tr* is 0, resulting in a certain degree of accuracy loss. However, from the curves, we can see that when the truncation order is equal to 2, the final value basically converges to the reference value of LU. These curves exhibit the convergence trend and accuracy performance of the algorithm under different truncation orders.

To enhance the rigor of algorithm verification, section C specifically investigated the minimum truncation order required to achieve convergence accuracy with different rough surfaces and target parameters. This research has important practical value because, in real-world applications, we need to choose appropriate truncation orders for different rough surface and target parameter combinations to ensure the convergence accuracy of the algorithm.

Firstly, we explored the minimum truncation order (*Tr*) for achieving convergence accuracy under different target parameters. In this study, we set the buried depth of the target to 1λ, 2λ, and 3λ, and the target radius to 0.1λ, 0.3λ, and 0.5λ, resulting in nine different combinations. By calculating the results under these combinations, we obtained Fig. 4. As shown in Fig. 4, with the increase of *D* and the decrease of *R*, interaction gradually decreases. This is mainly due to the decrease of target-rough surface interaction as the buried depth increases and the target radius decreases. Conversely, as *D* decreases and *R* increases, the target-rough surface interaction enhances, resulting in an increase of *Tr*. This phenomenon is consistent with our expectations because when the buried depth of the target increases, the signal propagation through the rough surface will be subject to greater attenuation and scattering. Therefore, a larger truncation order is required to accurately simulate this propagation process and achieve convergence accuracy.

In addition, we noticed that the minimum truncation order required to reach the convergence accuracy is different under different rough surface conditions. To further explore this phenomenon, we conducted experiments for different rough surface models and recorded the minimum truncation order required to reach convergence accuracy, as shown in Fig. 5. Among them, permittivity was taken as $2.0+0.01i$, $5.0+0.10i$, $10.0+1.00i$, and root mean square height was taken as 0.1λ, 0.3λ, 0.5λ. By comparing the experimental results, we found that changing the roughness of the rough surface did not change *Tr*; while increasing the permittivity, *Tr* gradually decreased. This is mainly because with the increase of permittivity, the reflection of the incident wave by the medium is enhanced, and the transmission is weakened, resulting in a decrease in the interaction between the rough ground and the target.

In summary, in this investigation, we found that the selection of *Tr* is closely related to the final accuracy, and the target radius, burial depth, and permittivity have

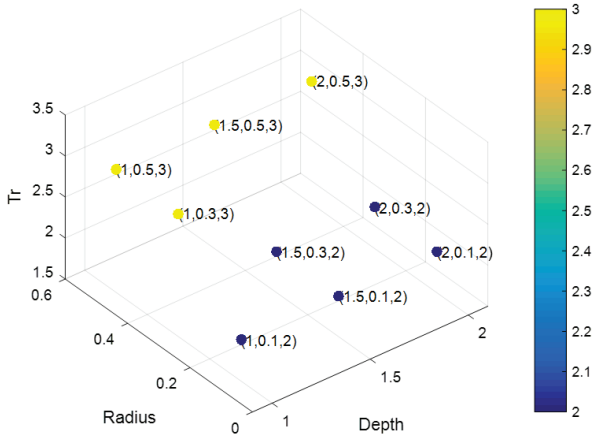

Fig. 4. The influence of target parameters on *Tr*.

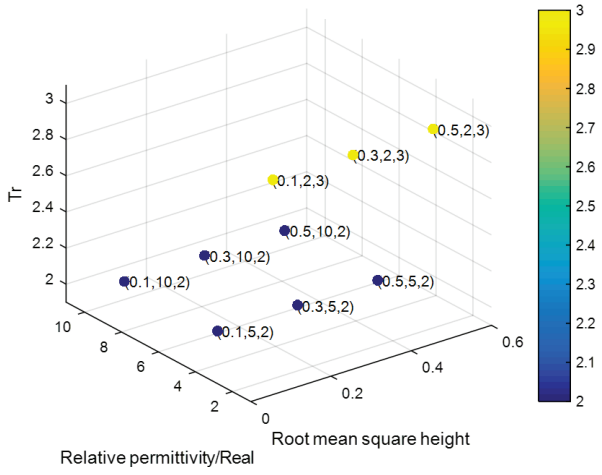

Fig. 5. The influence of rough surface parameters on *Tr*.

important effects on *Tr*. Therefore, in practical applications, it is necessary to choose an appropriate *Tr* based on target parameters and specific rough surface conditions to ensure that the convergence accuracy of the algorithm can meet the actual requirements. This finding has important significance for future research.

To further delve into the performance characteristics of the algorithm, a detailed study was conducted on memory and time consumption for calculating rough surfaces across different scales, with the relevant data summarized in Table 1. Upon thorough analysis, it was revealed that the algorithm exhibited outstanding computational performance, effectively demonstrating its efficiency and stability.

Table 1: Memory consumption and time of computations

	$L = 100\lambda$	$L = 160\lambda$	$L = 220\lambda$
Memory (MB)	206	309	432
Time (sec)	978	2226	2940

IV. NUMERICAL RESULTS AND ANALYSIS

Section IV reports the interaction between the target and the rough surface based on the G-PILE algorithm and analyzes the results, which are presented in Figs. 6 and 7.

According to Fig. 6, we can clearly see that the scattering coefficient of cylindrical targets exhibits a significant trend as the target radius changes. When the target radius increases, the scattering coefficient at all angles, except for the specular reflection direction, increases significantly. In the case of TE wave incidence, the scattering coefficient increases significantly in the range of -90° to 0°. This indicates that as the target radius increases, the interaction between rough ground and the target gradually increases, resulting in a significant increase in the scattering coefficient. Especially in the case of TM wave incidence, the scattering coefficient at all angles except for the region of 0° to 30° shows a significant increase. This further indicates that the interaction between rough ground and the target increases with the increase of target radius, and this change is more significant in the case of TM wave incidence.

In addition, Fig. 7 shows the trend of the scattering coefficient as a function of the target burial depth. When the target burial depth changes, the interaction between the target and the rough ground weakens, resulting in a decrease in the scattering coefficient. When TE waves are incident, the change in the scattering coefficient is relatively smooth. However, when TM waves are incident, the change in the scattering coefficient appears more significant. This indicates that the change in the target burial depth has a significant impact on the scattering coefficient, especially when TM waves are incident.

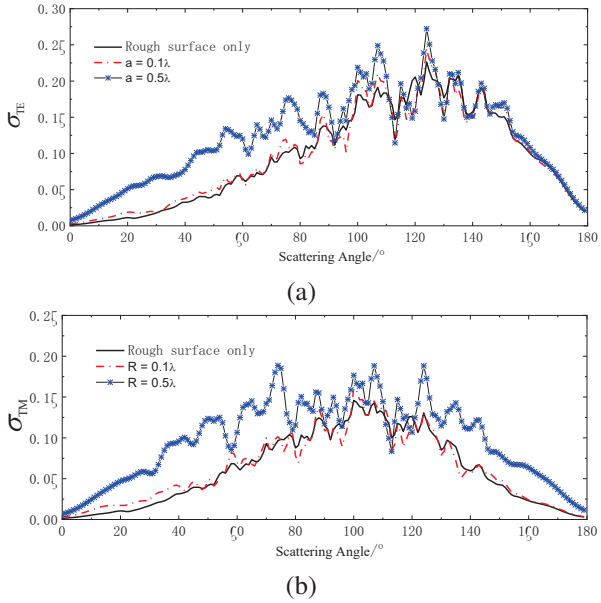

Fig. 6. The influence of radius on scattering coefficient. (a) TE incident wave and (b) TM incident wave. Black curve = Rough surface only; Red curve = R=0.1λ; Blue curve R=0.5λ.

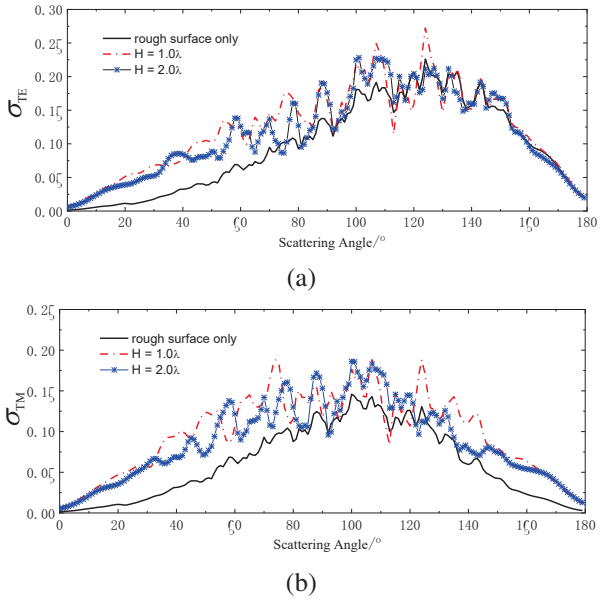

Fig. 7. Influence of target depth on scattering coefficient. (a) TE incident wave and (b) TM incident wave.

From a comprehensive observation of Figs. 6 and 7, it can be concluded that due to the interaction between the target and the ground, when there is a target buried under the ground, its scattering coefficient is higher than that without a target. As this interaction increases (e.g., the increase in target radius or the decrease in burial

depth), this difference becomes increasing more obvious, and vice versa. These observations indicate that the target radius and burial depth have a significant impact on the scattering coefficient. These results are of great significance for understanding and predicting the interaction between rough ground and targets, as well as the variation of scattering coefficients, and provide a reference for future research.

V. CONCLUSION

This article delves into an innovative algorithm called G-PILE, which is used to solve the complex electromagnetic scattering of large-scale dielectric rough surfaces and buried dielectric targets. Firstly, we establish the EFIE and comprehensively optimize and improve the traditional PILE algorithm. The improved algorithm not only overcomes the limitations of the traditional algorithm, which is only suitable for solving electromagnetic scattering problems of layered rough surfaces, but also extends its application range to studying the composite scattering characteristics of targets under rough surfaces.

In the iterative solution process, this study introduces the BMIA/CAG method, which greatly reduces the complexity of the algorithm and significantly improves the solution efficiency. At the same time, we also introduce a conical incident wave, which further reduces the error introduced by rough surface truncation.

To verify the accuracy and validity of the G-PILE algorithm, we calculate the scattering characteristics of an infinitely long dielectric cylinder buried under a dielectric rough surface and compare the results with existing algorithms in detail. The comparison results show that the G-PILE algorithm exhibits superior performance and reliability in key aspects such as the surface field of rough surfaces, the composite electromagnetic scattering coefficient of rough surfaces and targets, and truncation convergence characteristics.

Finally, we investigate the composite electromagnetic scattering under different target parameters. These results have important theoretical and practical values for deepening our understanding and accurately predicting the interaction between rough ground and targets, as well as the changes in scattering coefficients. In addition, these results also provide valuable references for future research in related fields. By studying the influence of different target parameters on composite electromagnetic scattering, we can better understand the interaction mechanism between targets and rough surfaces and provide strong theoretical support for electromagnetic scattering prediction and control in practical engineering applications.

REFERENCES

[1] Q. K. Wang, C. M. Tong, X. M. Li, Y. J. Wang, Z. L. Wang, and T. Wang, "Composite electromagnetic scattering and high-resolution SAR imaging of multiple targets above rough surface," *Remote Sensing,* vol. 14, no. 12, 2022.

[2] T. Liu, L. Zhang, Z. G. Zeng, and S. J. Wei, "Study on the composite electromagnetic scattering from 3D conductor multi-objects above the rough surface,"*Radioengineering,* vol. 30, no. 2, 2021.

[3] C. Y. Ma, Y. H. Wen, and J. B. Zhang, "A fast, hybrid, time-domain discontinuous Galerkin-physical optics method for composite electromagnetic scattering analysis," *Applied Sciences,* vol. 11, no. 6, 2021.

[4] G. X. Zou, C. M. Tong, J. Zhu, H. L. Sun, and P. Peng, "Study on composite electromagnetic scattering characteristics of low-altitude target above valley composite rough surface using hybrid SBR-EEC method," *IEEE Access,* vol. 8, 2020.

[5] H. L. Sun, C. M. Tong, and P. Peng, "Improved hybrid FEM/MOM combining MLFMA for composite electromagnetic scattering," *Electromagnetics,* vol. 37, no. 8, 2017.

[6] J. Li, L. X. Guo, and S. R. Chai, "Composite electromagnetic scattering from an object situated above rough surface," *Applied Optics,* vol. 53, no. 35, 2014.

[7] W. H. Ye, Z. S. Wu, H. Li, X. B. Wang, and J. J. Zhang, "A study of composite electromagnetic scattering from a simple target above an oceanic surface," in *ICMTCE 2011, Institute of Electrical and Electronics Engineers,* Beijing, China, pp. 485-488, 2011.

[8] B. Sami, B. Christophe, and K. Gildas, "3-D scattering from a PEC target buried beneath a dielectric rough surface: An efficient PILE-ACA algorithm for solving a hybrid KA-EFIE formulation," *IEEE Transactions on Antennas and Propagation,* vol. 63, no. 11, 2015.

[9] I. Mahariq, M. Kuzuoğlu, and I. H. Tarman, "On the attenuation of the perfectly matched layer in electromagnetic scattering problems with the spectral element method," *Applied Computational Electromagnetics Society (ACES) Journal*, vol. 29, no. 9, pp. 701-710, 2021.

[10] I. Mahariq, H. Kurt, and M. Kuzuoğlu, "Questioning degree of accuracy offered by the spectral element method in computational electromagnetics," *Applied Computational Electromagnetics Society (ACES) Journal,* vol. 30, no. 7, pp. 698-705, 2021.

[11] A. Kizilay and M. S. Yucedag, "Investigation of TMz scattering from conducting target buried in two-layered lossy medium with flat surfaces using a decomposition solution," *Journal of Electromagnetic Waves and Applications,* vol. 28, no. 5, 2014.

[12] S. Dey, W. G. Szymczak, A. Sarkissian, and J. A. Bucaro, "Scattering from targets in three-dimensional littoral and surf-zone environments with multi-layered elastic sediments based on an interior-transmission formulation," *Computer Methods in Applied Mechanics and Engineering,* vol. 260, 2013.

[13] Y. S. Choo, G. Y. Choi, K. H. Lee, S. H. Byun, and Y. M. Choo, "Ray-based analysis of subcritical scattering from buried target," *Journal of Marine Science and Engineering,* vol. 11, no. 2, 2023.

[14] X. K. Li, Y. S. Wu, G. Yu, and Y. F. Zou, "Acoustic scattering of buried stainless steel spheres: Theoretical analysis and experimental verification," *Applied Acoustics,* vol. 173, 2021.

[15] X. K. Li and Y. S. Wu, "Feature extraction for acoustic scattering from a buried target," *Journal of Marine Science and Application,* vol. 18, no. 3, 2019.

[16] V. M. Klibanov, E. A. Kolesov, and L. D. Nguyen, "Convexification method for an inverse scattering problem and its performance for experimental backscatter data for buried targets," *SIAM Journal on Imaging Sciences,* vol. 12, no. 1, 2019.

[17] G. S. Kargl, L. A. Espana, and L. K. Williams, "Scattering from a partially buried target: A modified acoustic ray model," *The Journal of the Acoustical Society of America,* vol. 138, no. 3, 2015.

[18] H. J. Simpson, Z. J. Waters, B. H. Houston, K. K. Jig, R. R. Volk, T. J. Yoder, and J. A. Bucaro, "Acoustic imaging and structural acoustic analysis of laboratory measurements of scattering from buried targets above critical grazing angles," *The Journal of the Acoustical Society of America,* vol. 130, no. 4, 2011.

[19] J. Z. Waters, "Acoustic imaging and structural acoustic analysis of scattering from buried targets at above-critical grazing angles," *The Journal of the Acoustical Society of America,* vol. 130, no. 4, 2011.

[20] A. Ishimaru, J. D. Rockway, and Y. Kuga, "Rough surface Green's function based on the first-order modified perturbation and smoothed diagram methods," *Waves Random Media,* vol. 10, no. 1, 2000.

[21] A. Iodice, G. Di Martino, A. D. Simone, D. Riccio, and G. Ruello, "Electromagnetic scattering from fractional Brownian motion surfaces via the small slope approximation," *Fractal and Fractional,* vol. 7, no. 5, 2023.

[22] X. H. Li, "Research on the electromagnetic scattering from foam sea based on small slope approximation," *The Journal of Engineering,* no. 4, 2021.

[23] I. Mahariq, "On the application of the spectral element method in electromagnetic problems involving domain decomposition," *Turkish Journal of Electrical Engineering and Computer Sciences,* vol. 25, no. 2, 2017.

[24] M. Sanamzadeh, L. Tsang, J. Johnson, R. Burkholder, and S. Tan, "Electromagnetic scattering from one dimensional random rough surfaces of dielectric layered media with waveguide modes using second order small perturbation method," *Progress in Electromagnetics Research B.,* vol. 80, 2018.

[25] T. Fang and Z. Cao, "Electromagnetic scattering modeling from Gaussian rough surface based on SPM," in *ICCT 2017, Institute of Electrical and Electronics Engineers,* Chengdu, China, pp. 1791-1795, 2017.

[26] J. S. Tian, J. Tong, J. Shi, and L. Q. Gui, "A new approximate fast method of computing the scattering from multilayer rough surfaces based on the Kirchhoff approximation," *Radio Science,* vol. 52, no. 2, 2017.

[27] M. Man, Z. Lei, Y. Xie, and X. Li, "Bistatic RCS prediction of composite scattering from electrically very large ship-sea geometry with a hybrid facet-based KA and shadow-corrected GRECO scheme," *Progress in Electromagnetics Research B,* vol. 60, no. 1, 2014.

[28] X. C. Ren, L. X. Guo, and D. Y. Ma, "Electromagnetic scattering from 2D band-limited Weierstrass fractal dielectric rough surface using Kirchhoff approximation," in *Chinese Institute of Electronics 2006, 7th International Symposium on Antennas, Propagation and EM Theory Proceedings Volume II of II. Institute of Electrical and Electronics Engineers,* pp. 274-277, 2006.

[29] X. Wang, C. F. Wang, and Y. B. Gan, "Electromagnetic scattering from a circular target above or below rough surface," *Progress In Electromagnetics Research,* vol. 40, 2003.

[30] L. Tsang, J. A. Kong, and K. H. Ding, *Scattering of Electromagnetic Wave: Numerical Simulation*. New York: John Wiley & Sons, 2001.

[31] A. Thorsos, "The validity of the Kirchhoff approximation for rough surface scattering using a Gaussian roughness spectrum," *Journal of the Acoustical Society of America,* vol. 83, no. 1, 1988.

Juan Zhao was born in Jiangxi, China. She received the bachelor's and master's degrees from Jiangxi Normal University, Jiangxi, China, in 2003 and 2009, respectively. Her research interests include computer applications and computer communication.

Design of Vortex Forward-Looking SAR Imaging using OAM Beam Modulation

Gaolong Cheng and Ping Li

College of Optoelectronic Information and Computer Engineering
University of Shanghai for Science and Technology, Shanghai 200093, China
chenggaolong3@gmail.com, liping@smic.edu.cn

Abstract **–** Forward-looking synthetic aperture radar (SAR) systems often suffer from low resolution and blurred imaging in the azimuthal direction due to the limited variation in Doppler frequency. To address this issue, this paper proposes a novel forward-looking SAR imaging technique leveraging vortex electromagnetic waves and orbital angular momentum (OAM) modulation. The core innovation lies in introducing a new azimuthal Doppler frequency component by establishing a linear relationship between the OAM mode number and slow-time, significantly enhancing azimuthal resolution.The method employs a transceiver system comprising a uniform circular array for transmission, with a single antenna at the center of the array for reception. Additionally, the traditional Range-Doppler (RD) algorithm is optimized to suppress motion-induced azimuthal Doppler interference and isolate mode-induced Doppler effects. Simulation results demonstrate that the proposed method effectively expands the azimuthal Doppler bandwidth, resolving left-right target ambiguity and substantially improving azimuthal imaging quality in forward-looking SAR systems.

Index Terms **–** Forward-looking SAR imaging, orbital angular momentum (OAM), two-dimensional imaging.

I. INTRODUCTION

Forward-looking imaging has recently attracted significant attention due to its potential applications in airborne reconnaissance, fire control, missile guidance, and aircraft landing under adverse meteorological conditions. However, forward-looking radar systems face inherent limitations compared to synthetic aperture radar (SAR), particularly in the ability to synthesize a larger virtual antenna. The forward-looking radar targets are located in a sector area in front of the carrier trajectory, where the radar-target angle is small. This results in a limited azimuthal Doppler bandwidth due to the small Doppler frequency variation caused by the radar motion. Consequently, the Doppler frequency of targets in the imaging area is highly correlated with both the target position and angle, leading to increased Doppler complexity and variability. This results in low resolution in the azimuthal direction, with left- and right-side targets producing similar Doppler frequencies, causing blurring in the imaging process [1]. As a result, achieving high azimuthal resolution in forward-looking radar imaging remains challenging.

As described in electrodynamics literature, the electromagnetic(EM) angular momentum can be decomposed into two independent parts, namely, spin angular momentum and OAM. The former is linked with polarization,whereas the latter leads to helical phase front. A beam carrying OAM usually has helical wavefront and a doughnut intensity shape , hence called vortex EM wave.Different OAM eigenmodes are topologically distinct, and they can span a Hilbert space of denumerably infinite dimension which has the prospect for improving the information transfer and acquisition abilities of the EM wave. Vortex EM wave imaging radar holds the potential to address the inherent limitations of forward-looking radar, particularly in enhancing azimuthal resolution. The wavefront phase of vortex EM waves is modulated by orbital angular momentum (OAM), enabling the generation of numerous orthogonal modes with unique phase distributions [2]. These characteristics make vortex EM waves advantageous for improving imaging resolution and efficiency.Previous studies have explored the application of vortex waves in radar imaging. For instance, Guo et al. [3] first applied vortex EM waves to radar imaging in 2013, laying the groundwork for EM vortex imaging. Subsequent research has investigated methods for enhancing azimuthal resolution [4] and applied vortex waves to side-looking SAR systems, demonstrating their superiority in improving azimuthal imaging performance [6–9]. However, there remains a significant gap in addressing the azimuthal resolution challenges specific to forward-looking SAR systems, where minimal Doppler frequency variation often results in low resolution and imaging ambiguity.

In terms of two-dimensional forward-looking imaging using vortex EM waves, [10] investigated the use

Submitted On: December 4, 2024
Accepted On: March 27, 2025

https://doi.org/10.13052/2025.ACES.J.400505

of vortex waves in forward-looking radar systems. The system employs phase characteristics of vortex waves to enable 2D imaging through FFT and sparse recovery methods. However, this approach assumes fixed time and considers only gaze-mode forward-looking imaging, which significantly limits its applicability in dynamic motion scenarios. Therefore, further research is needed to develop methods for vortex-based forward-looking imaging in moving scenarios.

This paper presents a novel method for forward-looking imaging using vortex EM waves, designed with OAM modes. Several techniques for generating vortex EM waves have been proposed, including helical phase plates [11], circular traveling-wave antennas based on ring resonant cavities [12], passive metasurface antennas [13], and uniform circular arrays (UCAs) with specific phase shifts [14]. Among these, the UCA-based approach utilizes a multi-channel phase control method to modulate various beam modes, providing a high degree of flexibility and variability. This approach can generate vortex beams in multiple modes, making it an ideal choice for EM vortex radar systems.

In this method, the forward-looking imaging system employs a uniform circular array for transmission and a single antenna for reception at the center of the array. First, we derive the EM vortex SAR echo model based on the OAM mode design, considering the established imaging scenario. Then, we design a variation function for the OAM mode number as a function of slow time to obtain an enhanced azimuthal term. This compensates for the small Doppler frequency shift typically observed in conventional forward-looking SAR systems. Finally, we address the range-Doppler frequency variation and achieve two-dimensional high-resolution imaging using the RD imaging algorithm.

As shown in Fig. 1, the UCA no longer transmits a single-mode vortex wave but instead uses OAM beams with a changing number of modes. The vortex radiation field generated by the UCA actually carries different orbital angular momenta.When appropriate parameters such as the number of elements,radius,and frequency are set,the generated OAM exhibits minimal field components in other modes,allowing for the production of nearly pure OAM,which will not affect the imagings quality [22]. A simulation of the proposed imaging method is carried out to demonstrate its effectiveness.

II. IMAGING MODELS

The scene geometry of the forward-looking imaging system is depicted in Fig. 2, where a UCA, located in the Cartesian coordinate system O-XYZ, moves along the X-axis with a constant velocity, transmitting vortex EM waves. In this coordinate system, the Z-axis points toward the center of the Earth, and the Y-axis is perpendicular to the X-axis, pointing to the right. The receiving antenna is positioned at the center of the UCA, which is also considered the radar's location. The initial position of the radar motion is treated as the origin of the 3D Cartesian coordinate system O-XYZ. The target's position is denoted as $P_0 = (x_0, y_0, z_o)$, while the radar's position is denoted as $P_R = (x, 0, 0)$, and the instantaneous distance between the target and the radar is represented as

$$R(\eta) = \sqrt{v^2(\eta_0 - \eta) + {y_0}^2 + z^2}. \tag{1}$$

Considering that the forward-looking motion trajectory is much smaller than the imaging distance of the target, the response of the Bessel magnitude term to changes in the target's elevation angle can be neglected. In other words, the instantaneous pitch angles between

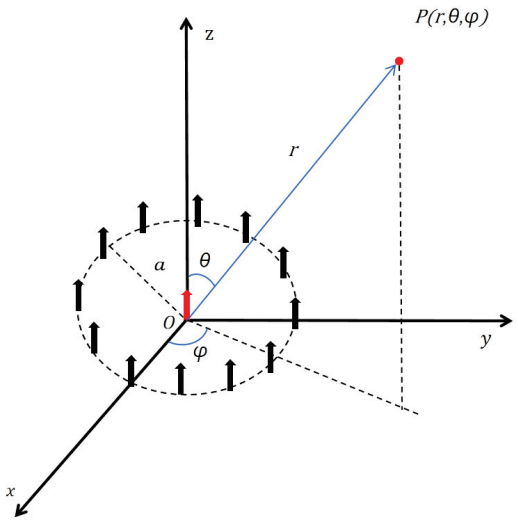

Fig. 1. Diagram of the UCA.

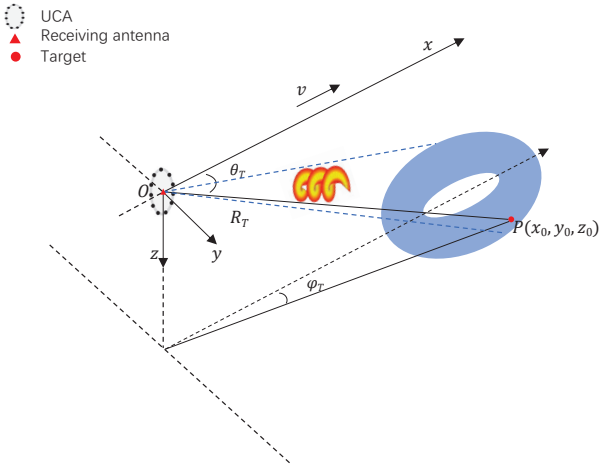

Fig. 2. Imaging geometry of an OAM-based radar imaging system.

the radar and the target are assumed to be equal, i.e., $\theta_i = \theta_T$. In this imaging system, the UCA no longer transmits a fixed-mode vortex EM wave. Instead, the OAM mode number varies linearly with time. The coefficient governing this linear variation is denoted as α. The UCA transmits linear frequency-modulated (LFM) signals to generate vortex beams, and the transmitted signal can be expressed as:

$$s(t, l_\eta) = rect\left[\frac{t}{T}\right]\exp(j\pi K_r t^2)\exp(j2\pi f_c t) \times \exp(jl_\eta \varphi(\eta)), \tag{2}$$

where T, K_r, and f_c represent the range time variable, pulse width, linear frequency modulation ratio, and center carrier frequency, respectively. Based on the above expression, the vortex SAR echo can be derived as follows:

$$\begin{aligned} s(t, \eta; l_\eta) = {} & \sigma J_{l_\eta}[ka\sin\theta]\exp[jl_\eta\varphi(\eta)] \\ & \times w_r\left[t - \frac{2R(\eta)}{c}\right] \\ & \times \exp\left[jK_r(t - \frac{2R(\eta)}{c})\right] \\ & \times w_a[\eta - \eta_0] \times \exp\left[-j\frac{4\pi R(\eta)}{\lambda}\right], \end{aligned} \tag{3}$$

where t, η and λ are denoted as fast time, slow time, and central wavelength, respectively. η_0 represents the slow time corresponding to the point where the carrier platform is closest to the target, and R_0 is the corresponding slant range. k is the wave number, and σ is the target scattering coefficient. J_{l_η} is the first type of Bessel function of order l_η, and a denotes the radius of the UCA. Additionally, $W_r[\cdot]$ and $W_a[\cdot]$ represent the distance and azimuthal envelopes, respectively, which are typically modeled using a rectangular window. $\varphi(\eta)$ is the instantaneous azimuthal angle of the target, which, according to the geometrical relationship, can be expressed as:

$$\varphi(\eta) = \arctan\left(\frac{y_0}{x_0 - v\eta}\right). \tag{4}$$

The Taylor expansion of the instantaneous azimuth expression, neglecting higher-order terms beyond the third order, is given by:

$$\varphi(\eta) \approx \frac{\pi}{2} - \frac{x_0}{y_0} + \frac{v}{y_0}\eta. \tag{5}$$

Due to the relationship between the OAM mode number and slow-time transformation, the new phase frequency modulation (FM) function can be obtained as follows:

$$l_\eta\varphi(\eta) = \left(\frac{\pi}{2} - \frac{x_0}{y_0}\right)\xi\eta + \frac{v}{y_0}\xi\eta^2. \tag{6}$$

Observing the above equation, we find that the azimuth factor term comprises two components. The first is a linear term, $(\frac{\pi}{2} - \frac{x_0}{y_0})\xi\eta$, representing a new single-frequency signal introduced in the azimuth direction, which can be compensated by designing an appropriate slow-time correction function. The second component is a quadratic term, $\frac{v}{y_0}\xi\eta^2$, related to slow time η, which manifests as a new quadratic curvature term in the traditional SAR azimuth echo.

In forward-looking SAR, azimuthal imaging faces challenges due to the minimal variation in Doppler frequency. Single-antenna SAR systems exhibit imaging blind spots, with left and right targets producing identical Doppler frequencies, leading to left-right blurring in the image. Compensation is therefore necessary to enhance azimuthal resolution in the imaging system.

The new azimuthal term derived through modal design addresses these limitations. It not only eliminates the issue of identical Doppler frequencies for left and right targets but also introduces a new linear frequency-modulated (FM) signal c with a tuning frequency of $\exp[j\pi\frac{-v\xi}{\pi y_0}\eta^2]$. This new term, characterized by a tuning frequency $K_l = \frac{-v\xi}{\pi y_0}$, contributes to improved azimuthal resolution and minimizes imaging ambiguities.

III. IMAGING ALGORITHMS

Based on the above analysis and compensations, an improved RD algorithm is proposed, with the processing flow illustrated in Fig. 3. Similar to the traditional RD algorithm, range compression is performed

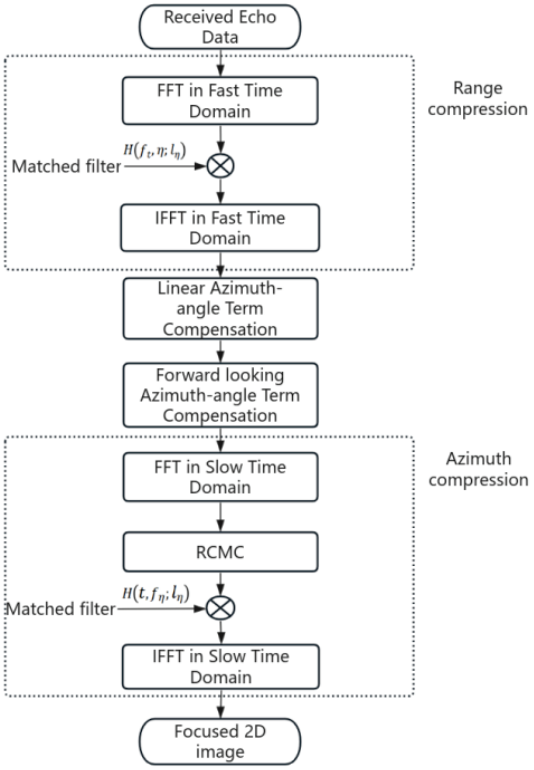

Fig. 3. The flowchart of the improved RD algorithm.

first. Applying the range FFT to the echo signal yields:

$$\begin{aligned} s(t,\eta;l_\eta) &= \sigma J_{l_\eta}[ka\sin\theta]\exp[jl_\eta\varphi(\eta)] \\ &\times w_r\left[\frac{f_t}{K_rT}\right]\exp[-j\pi\frac{f_t^2}{K_r}] \\ &\times\exp\left[-j4\pi f_t\frac{R(\eta)}{c}\right] \\ &\times w_a[\eta-\eta_0]\times\exp\left[-j\frac{4\pi R(\eta)}{\lambda}\right]. \end{aligned} \tag{7}$$

The corresponding matched filter $H(f_t,\eta;l_\eta)$ is designed as follows:

$$H(f_t,\eta;l_\eta) = w_r\left[\frac{f_t}{K_rT}\right]\cdot\exp\left(j\pi\frac{f_t^2}{K_r}\right). \tag{8}$$

Then, the range compression result is obtained as follows:

$$\begin{aligned} s_{rd}(t,\eta;l_\eta) &= IFFT\{s(t,\eta;l_\eta)H(f_t,\eta;l_\eta)\} \\ &= \sigma J_{l_\eta}[ka\sin\theta]\exp\left[j(\frac{\pi}{2}-\frac{x_0}{y_0})\xi\eta\right] \\ &\times\exp[j\frac{v}{y_0}\xi\eta^2]p_r\left(t-\frac{2R(\eta)}{c}\right) \\ &\times w_a[\eta-\eta_0]\exp\left[-j\frac{4\pi R(\eta)}{\lambda}\right], \end{aligned} \tag{9}$$

where the range envelope $P_r(t) = |K_r|T\sin c(|K_r|T\cdot t)$.Subsequently, the linear term affecting imaging quality, as well as the azimuthal FM term of conventional forward-looking SAR, are compensated by applying a conjugate phase factor.

$$\begin{aligned} s(t,\eta;l_\eta) &= s_{rd}(t,\eta;l_\eta)\cdot\exp\left[-j\left(\frac{\pi}{2}-\frac{x_0}{y_0}\right)\xi\eta\right] \\ &\times\exp\left[j\frac{4\pi R(\eta)}{\lambda}\right] \\ &= \sigma\cdot J_{l_\eta}[ka\sin\theta]w_a[\eta-\eta_0] \\ &\times\exp[-j\pi K_l\eta^2]p_r\left(t-\frac{2R(\eta)}{c}\right). \end{aligned} \tag{10}$$

Next, the range walk correction factor is constructed in the frequency domain as follows:

$$H = \exp\left(-j4\pi f_c\frac{v\cos\theta}{c}t\right). \tag{11}$$

By multiplying the range walk correction factor with the range-frequency and azimuth-time domain signal, the two-dimensional time-domain echo signal with corrected range walk is obtained:

$$\begin{aligned} s(t,\eta;l_\eta) &= \sigma J_{l_\eta}[ka\sin\theta]w_a[\eta-\eta_T] \\ &\times\exp[-j\pi K_l\eta^2]\cdot p_r\left(t-\frac{2R_T}{c}\right). \end{aligned} \tag{12}$$

Finally, the azimuth compression result is obtained through an azimuth matched filter, which is defined as follows:

$$H(t,f_\eta;l_\eta) = \exp\left(-j\pi\frac{f_\eta^2}{K_l}\right). \tag{13}$$

The final 2D compressed echo can be expressed as:

$$s_{2D}(t_t,\eta;l_\eta) = \sigma J_{l_\eta}[ka\sin\theta]\cdot p_r(t-\frac{2R_T}{c})\cdot p_r(\eta-\eta_0). \tag{14}$$

At this stage, the 2D focused image for the proposed vortex SAR is achieved, with the azimuth compression envelope expressed as follows:

$$\begin{aligned} p_r(\cdot) &= |K_r|T\sin c(|K_r|T\cdot t), \\ p_a(\cdot) &= |K_l|T\sin c(|K_l|T\cdot\eta). \end{aligned} \tag{15}$$

The range resolution is determined by the bandwidth $B_r = |K_r|T_S$ of the transmitted signal, which can be expressed as:

$$\rho_r = \frac{c}{2B_r}. \tag{16}$$

The azimuthal resolution of conventional forward-looking SAR imaging depends on the antenna aperture D. However, the small angle between the target area and the trajectory direction results in minimal variation in the azimuthal Doppler frequency, leading to poor imaging quality. By introducing an OAM mode that varies over time, the new azimuthal resolution can be derived as:

$$\rho_a = \frac{c}{2B_l}, \tag{17}$$

where the newly introduced Doppler bandwidth is $B_l = |K_l|T_S$. This bandwidth can be adjusted by designing a linear relationship ξ between the OAM mode number l and time, thereby achieving an azimuthal resolution that meets the desired requirements.

IV. SIMULATION AND DISCUSSION

The simulation results of the proposed 2D forward-looking EM vortex imaging method are presented and analyzed in detail in this section. These results demonstrate the significant impact of the method proposed in this paper on enhancing forward-looking SAR imaging performance.To achieve higher purity of OAM and improve imaging quality, the array radius is set to $a = 0.12m$ [23].The other key parameters used in the simulation experiments are listed in Table 1.

Table 1: Simulation parameters

Parameter	Value	Name
Flight height H	5000	m
Central Frequency f_c	35	GHZ
Bandwidth B	20	MHZ
UCA radius a	0.12	m
Radar flight speed v	150	m/s

Since the number of OAM modes generated is currently limited to integer values, $l_{\eta_i} = INT(|\xi|\cdot\eta_i)$ can be used to obtain the actual number of OAM modes transmitted from each slow-time sampling point $l_{\eta i}$, where $INT(\cdot)$ is an integer-valued function. Consequently, the number of transmitted OAM modes corresponding to the

entire slow-time sampling period can be expressed as $INT(l_\eta)$.

As shown in Fig. 4, the OAM mode curves of theoretical value and the designed value almost coincide with the slow time transition, and it can be found that the modes error is very small.This indicates the effectiveness of the OAM pattern design.

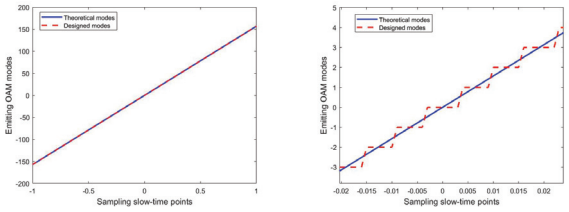

(a) (b)

Fig. 4. Comparison between the Rounded Mode Values and the Linear Mode Values.

To verify the effectiveness of the forward-looking imaging method proposed in this paper in enhancing azimuthal resolution, simulations were conducted comparing the new azimuthal Doppler frequency with that of conventional forward-looking SAR. Figure 5 shows the comparison between the azimuthal Doppler frequency with a linearity factor of 60π and the azimuthal Doppler frequency of conventional forward-looking SAR. A clear difference can be observed between the Doppler progression of conventional forward-looking SAR and that of the modal-based design. In the conventional method, azimuthal signals can be compressed in the RD domain using matched filtering, while in the modal-based design, the Doppler slope becomes smaller as the course direction approaches a point target within the same range cell during one synthetic aperture time.

Three targets with coordinates (1000, 200), (3000, 200), and (3000, 160) were placed in the imaging scene. The imaging results, obtained using the RD algorithm for conventional forward-looking SAR, are shown in Fig. 6. These results demonstrate a left-right blurring problem in forward-looking SAR imaging, attributed to the equal Doppler frequency values generated by left and right targets with equal azimuthal coordinate magnitudes. Additionally, as the azimuth angle between the target and radar decreases, the imaging resolution of the forward-looking SAR deteriorates, leading to an inability to distinguish between closely spaced target points.

Figure 7 presents a comparison of the azimuthal point spread function between the vortex forward-looking imaging and conventional forward-looking imaging. It is evident that the vortex forward-looking imaging demonstrates superior azimuthal resolving power at the same position, while the azimuthal resolution of conventional forward-looking imaging decreases as the distance value increases. Additionally, as shown in Fig. 8 (a) and Fig. 8 (b), the azimuthal imaging quality of conventional forward-looking SAR is significantly lower than that of the vortex forward-looking SAR. The vortex forward-looking imaging, based on modal design, achieves azimuthal resolution similar to that of forward-looking SAR.

Three ideal scattering points are placed in the imaging scene with coordinates $P1(3000, 200, 5000)$, $P2(3500, 200, 5000)$, and $P3(3500, 190, 5000)$ in the O-XYZ coordinate system. By designing a linear

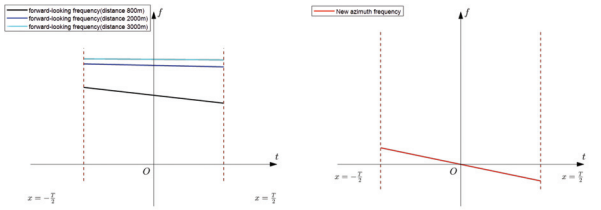

(a) (b)

Fig. 5. Azimuthal Doppler course for different distance values of forward looking SAR. (a) and new directions doppler history (b).

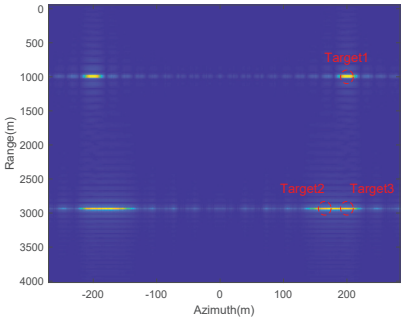

Fig. 6. Forward-looking SAR 2D point target imaging.

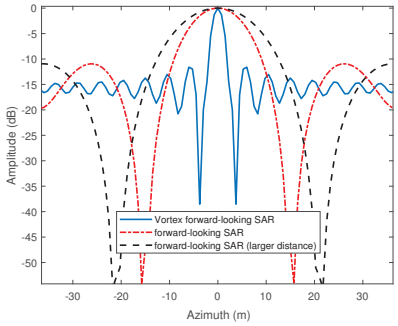

Fig. 7. The azimuthal profiles of conventional forward-looking and vortex forward-looking PSF.

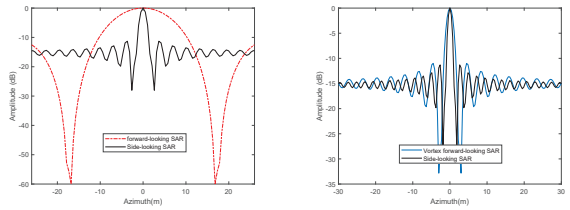

(a) (b)

Fig. 8. Imaging result after range compression. (a) Results after distance matched filtering. (b) Results after RCMC.

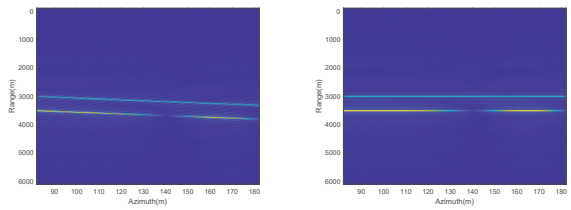

(a) (b)

Fig. 9. Imaging result after range compression. (a) Results after distance matched filtering. (b) Results after RCMC.

relationship ξ between the mode number l and time, different azimuthal Doppler frequencies can be obtained. These different linear relationships, along with the corresponding azimuthal resolutions and mode number ranges, are listed in Table 2. As shown in Table 2, each linear relationship ξ yields a distinct azimuthal resolution and associated performance index for imaging the target point P1. The radar's azimuthal resolution performance improves significantly as the number of OAM modes increases. When $\xi = 60\pi$, the simulated results after range compression, as shown in Fig. 9 (a), reveal two straight lines with identical tilt angles due to the forward-looking SAR trajectory. After applying the forward-looking SAR range migration correction method, the corrected results are displayed in Fig. 9 (b), where the range compression curves are no longer tilted, indicating that range migration has been effectively corrected.

Table 2: Simulation parameters

Linear Factor ξ	OAM Model Range	IRW (m)	ISLR (dB)	PSLR (dB)
0	––	––	––	––
30π	[-38,38]	7.14	-11.52	-12.98
40π	[-50,50]	5.56	-11.58	-13.00
50π	[-63,63]	4.46	-11.55	-13.07
60π	[-75,75]	3.74	-11.54	-13.27

Finally, the 2D imaging results are obtained using the designed azimuthal matched filter, as shown in Fig. 10. The figure clearly demonstrates that the imaging quality of the target points is excellent, with high differentiation between targets. This result illustrates the effectiveness of the proposed method in suppressing target blurring and enhancing resolution.

The conventional forward-looking SAR image of the targets 1 and 2 is shown in Fig. 6, wherein the two targets cannot be distinguished from the result view.As a comparison, the same targets are processed by the vortex forward-looking SAR, and two clearly focused target points are obtained in Fig. 10. Then the two targetsazimuth profiles of the conventional SAR and the vortex SAR are exhibited in Fig. 11 (a) and Fig. 11 (b), which illustrates the vortex SAR can achieve a higher azimuth resolution,and two peak positions can accurately correspond to the set targets.However,the conventional SAR can only obtain one peak and detailed position information cannot be obtained.

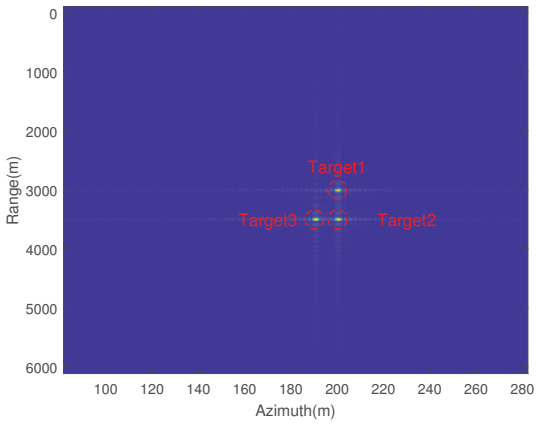

Fig. 10. 2D imaging simulation results.

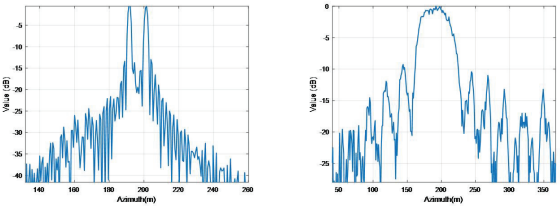

(a) (b)

Fig. 11. Comparison of imaging results. (a) Azimuthal profiles of conventional SAR. (b) Azimuthal profiles of the vortex SAR.

In addition, the factors influencing the azimuthal resolution of forward-looking SAR are analyzed. Based on the Doppler bandwidth expression for vortex forward-looking SAR, the azimuthal resolution can be expressed as:

$$\rho_a = \frac{v\pi y_0}{\xi L}, \tag{18}$$

It can be observed that, when the synthetic aperture length L is fixed, the azimuthal resolution of vortex forward-looking SAR imaging depends on the linear relationship ξ of the OAM mode number, the radar speed v, and the y-axis coordinate value y_0. The azimuthal resolution of vortex forward-looking SAR is influenced by radar speed. As shown in Fig. 12, for a given radar speed, the azimuthal resolution decreases as the target moves further from the beam axis, reflecting the temporal and spatial characteristics of azimuthal resolution. This compensates for the limitations of traditional forward-looking SAR in azimuthal resolution.

Additionally, for targets at a fixed distance, the azimuthal resolution can be significantly enhanced by increasing the linearity coefficient. However, the azimuthal resolution of the proposed vortex forward-looking SAR deteriorates as radar speed increases. In addition, the azimuthal resolution enhancement ratio between conventional forward-looking SAR and vortex forward-looking SAR can be derived from the azimuthal resolution expression in (12) as:

$$k_\rho = \frac{\rho_{con}}{\rho_r}, \tag{19}$$

where ρ_{con} represents the azimuthal resolution of conventional forward-looking SAR. As shown in Fig. 13, the influence curve approximates an extended straight line, indicating that the enhancement ratio increases linearly with the linearity coefficient, resulting in a significant improvement in azimuthal resolution. Additionally, the slopes of these lines vary with radar speed, confirming the effect of radar speed on the azimuthal resolution of vortex forward-looking SAR. However, due to the lower energy of higher-order OAM beams, increased mid-air

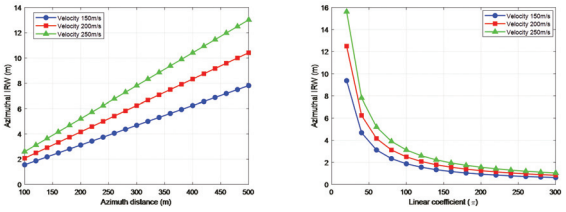

(a) (b)

Fig. 12. Analysis of factors affecting azimuthal resolution. (a) Resolution curves for different azimuthal axes for a certain radar speed. (b)Resolution curves for different linearity coefficients for a certain radar speed.

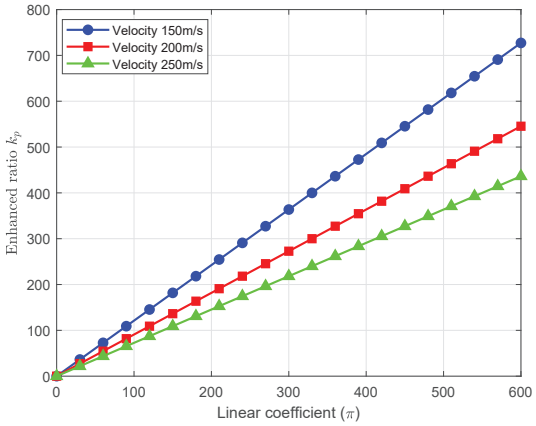

Fig. 13. Azimuthal resolution enhancement ratio.

divergence, and the complexity of antenna design, the proposed SAR imaging methods cannot achieve unlimited improvements in azimuthal resolution and enhancement ratio. The upper limit is currently constrained by the generation of the actual OAM pattern.

V. CONCLUSION

This paper proposes a forward-looking SAR imaging method based on orbital angular momentum (OAM) vortex EM waves to address the challenges of low azimuthal resolution and left-right target blurring in traditional forward-looking SAR imaging. First, an echo model was developed based on the characteristics of the designed OAM beam and the imaging scenario. Subsequently, a compensation method for the azimuthal term was introduced, and the RD algorithm was enhanced to achieve target range imaging through range compression and target-focused azimuth imaging through azimuth compression.

The designed OAM mode variations enable the forward-looking SAR system to achieve higher azimuthal resolution in 2D imaging and effectively distinguish between targets with identical left and right Doppler frequencies. Simulation results demonstrate that this method significantly improves the quality of forward-looking SAR azimuthal images, offering a promising solution to forward-looking imaging challenges.

While the proposed method focuses primarily on theoretical analysis and algorithm simulations, its implementation is feasible with current hardware designs. For instance, uniform circular arrays (UCA) can flexibly generate OAM beams through precise phase control. Adjusting the mode numbers requires controlling the phase shift between array elements, a capability well-supported by existing digital or analog phase control systems.

It is worth noting that generating higher-order OAM modes may introduce challenges such as increased hardware complexity and phase synchronization requirements. Nevertheless, for low- to moderate-order modes, these challenges remain manageable, enabling the proposed method to effectively enhance azimuth resolution without requiring significant hardware modifications. Future research will aim to address these challenges and further optimize the implementation process, ensuring the practicality and scalability of the approach in real-world applications.

REFERENCES

[1] M. E. Yanik, D. Wang, and M. Torlak, "Development and demonstration of MIMO-SAR mmWave imaging testbeds," *IEEE Access,* vol. 8, pp. 126019-126038, July 2020.

[2] J. D. Jackson, *Classical Electrodynamics,* 3rd ed. New York, NY:Wiley, Aug. 1998.

[3] G. GUO, W. HU, and X. DU, "Electromagnetic vortex based radar target imaging," *Journal of National University of Defense Technology*, vol. 35, no. 6, pp. 71-76, Dec. 2013.

[4] K. Liu, Y. Cheng, X. Li, and G. Yue, "Microwave-sensing technologyusing orbital angular momentum," *IEEE Veh. Technol. Mag.*, vol. 14, no. 2, pp. 112-118, Feb. 2019.

[5] K. Liu, Y. Cheng, and Z. Yang, "Orbital-angular-momentum-based electromagnetic vortex imaging," *IEEE AntennasWireless Propag. Lett.*, vol. 14, pp. 711-714, Dec. 2015.

[6] J. C. Curlander and R. N. McDonough, *Synthetic Aperture Radar Sys-tems and Signal Processing,* New York, NY: Wiley-Interscience, Nov. 1991.

[7] H. Bi, G. Bi, B. Zhang, and W. Hong, "Complex-image-based sparseSAR imaging and its equivalence," *IEEE Trans. Geosci. Remote Sens.*, vol. 56,no. 2, pp. 5006-5014, Sep. 2018.

[8] S. Li, O. Xu, W. Li, and Y. Wang, "Three dimensional SARimaging based on vortex electromagnetic waves," *Remote Sens. Lett.*, vol. 9, no. 4, pp. 343-352, Apr. 2018.

[9] X. Bu, Z. Zhang, and L. Chen, "Synthetic aperture radar interfer-ometry based invortex electromagnetic waves," *IEEE Access*, vol. 7, pp. 82693-82700, July 2019.

[10] T. Yang, W. Huang, and X. Lu, "Two dimensional forward-looking missile-borne radar imaging based on vortex electromagnetic waves," *IEEE Access*, vol. 8, pp. 221103-221110, Dec. 2020.

[11] G. A. Turnbull, D. A. Robertson, G. M. Smith, L. Allen, and M. J. Padgett, "The generation of free-space Laguerre-Gaussian modes at millimetre-wave frequencies by use of a spiral phase-plate," *Opt.Commun*, vol. 127, pp. 183-188, June 1996.

[12] S. Zheng, X. Hui, X. Jin, H. Chi, and X. Zhang, "Transmission characteristics of a twisted radio wave based on circular traveling-wave antenna," *IEEE Trans. Antennas Propag*, vol. 63, no. 4, pp. 1530-1536, Apr. 2015.

[13] M. Alibakhshi-Kenari, M. Naser-Moghadasi, R. A. Sadeghzadeh, B. S. Virdee, and E. Limiti, "A new planar broadband antenna based on meandered line loops for portable wireless communication devices," *Radio Sci*, vol. 51, no. 7, pp. 1109-11117, July 2016.

[14] S. M. Mohammadi, "Orbital angular momentum in radio A system study," *IEEE Trans. Antennas Propag*, vol. 58, no. 2, pp. 565-572, Feb. 2010.

[15] K. Liu, Y. Cheng, X. Li, Y. Qin, H. Wang, and Y. Jiang, "Generation of orbital angular momentum beams for electromagnetic vortex imaging," *IEEE Antennas Wireless Propag. Lett.*, vol. 15, pp. 1873-1876, 2016.

[16] J. Wang, K. Liu, Y. Cheng, and H. Wang, "Vortex SAR imaging method based on OAM beams design," *IEEE Sensors Journal*, vol. 19, no. 24, pp. 11873-11879, Dec. 2019.

[17] Q. Feng, Y. Lin, Y. Zheng, and L. Li, "Vortex beam optimization design of concentric uniform circular array antenna with improved array factor," *Applied Computational ElectromagneticsSociety (ACES) Journal*, vol. 36, no. 7, pp. 830-837, July 2021.

[18] P. Welch, "The use of fast Fourier transform for the estimation of power spectra: A method based on time averaging over short, modified periodograms," *IEEE Trans. Audio Electroacoustics*, vol. 15, no. 2, pp. 70-73, June 1967.

[19] R. Li, H. Hu, S. Lei, Z. Lin, and B. Chen, "TElevation imaging based on vortex electromagnetic wave," *in Proc. IEEE Int. Symp. Antennas Propag. USNC-URSI Radio Sci. Meeting*, pp. 827-828, July 2019.

[20] A. Tennant and B. Allen, "Generation of OAM radio waves using circular time-switched array antenna," *IEEE Trans. Audio Electroacoustics*, vol. 48, no. 21 pp. 1365-1366, Oct. 2012.

[21] Y. Luo, Q. Zhang, C. Qiu, S. Li, and T. Soon Yeo, "Micro-Doppler feature extraction for wideband imaging radar based on complex image orthogonal matching pursuit decomposition," *IETRadar, Sonar Navigat*, vol. 7, no. 8, pp. 914-924, Oct. 2013.

[22] K. Liu, H. Liu, and Y Qin, "Generation of OAM Beams Using Phased Array in the Microwave Band[J]," *IEEE Transactions on Antennas and*

Propagation,, vol. 64, no. 9, pp. 3580-3857, Oct. 2016.

[23] S. M. Mohammadietal, "Orbital angular momentum in radioa system study," *IEEE Trans. Antenn. Propag.*, vol. 58, no. 2, pp. 565-572, June 2010.

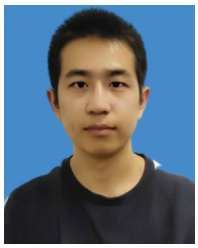

Gaolong Cheng received the BEng degree in electronic from Wenzheng College of Soochow University, Jiangsu, China, in 2022, and is now pursuing his MEng in electronic information at the University of Shanghai for Science and Technology, Shanghai, China. His research interests include synthetic aperture radar imaging as well as vortex radar imaging.

Ping Li received the master's degree in electromagnetic field and microwave technology and the Ph.D. degree in circuits and systems from Northwestern Polytechnical University, Xian, China, in 2006. She is currently a Researcher with the University of Shanghai for Science and Technology, Shanghai, China. Her research interests include millimeter-wave and terahertz technology, especially the terahertz imaging systems.

Antenna Array Pattern with Sidelobe Level Control using Deep Learning

Muhammad A. Abdullah[1], Alam Zaib[1], Shafqat U. Khan[2], Shoaib Azmat[1], Shahid Khattak[1], Benjamin D. Braaten[3], and Irfan Ullah[1]

[1]Department of Electrical and Computer Engineering
COMSATS University, Abbottabad, KPK 22060, Pakistan
ps23.asad@gmail.com, alamzaib@cuiatd.edu.pk, shoaibazmat@cuiatd.edu.pk, skhattak@cuiatd.edu.pk, eengr@cuiatd.edu.pk

[2]Department of Electronics
University of Buner, Buner, KPK 19290, Pakistan
shafqatphy@yahoo.com

[3]Department of Electrical and Computer Engineering
North Dakota State University, Fargo, ND 58102, USA
benjamin.braaten@ndsu.edu

***Abstract* –** Motivated by the demonstrated success of artificial intelligence (AI) in wireless communications systems, this paper proposes a deep learning-based approach for generating a desired radiation pattern with sidelobe level (SLL) control in active electronically scanned array (AESA) antennas. Recent works in this direction are mostly limited to generating radiation patterns with only beam scanning capability, inhibiting their wide-scale applicability. In this work, we propose a unified deep neural network (DNN) model that enable simultaneous control over both beam scanning angles and SLLs across a range of operating scenarios. To accomplish this task, the DNN model efficiently predicts the phase and amplitude of each array element. To learn the DNN model's parameters, we construct a training dataset comprising amplitude values and phases as labeled outputs and corresponding 181-point radiation patterns as input features. The training and validation process of the proposed DNN model reveals high accuracy in terms of R2 score and mean square error (MSE). For prediction, the desired radiation pattern consisting of 181 points is fed to the trained DNN model to yield optimized weights of antenna elements. The numerical results on a 1×8 linear phase antenna array, using an assortment of beam scanning angles and SLLs, demonstrate the effectiveness of the proposed model. The numerical results presented in MATLAB and CST simulators are validated by measurements on a 1×8 microstrip prototype array.

***Index Terms* –** AESA antennas, array pattern, deep learning, deep neural network, sidelobe level control.

I. INTRODUCTION

The overall radiation pattern of an antenna array is dictated by phases and amplitudes of individual array elements. The phases of the array elements are used for beam scanning, and sidelobe level (SLL) is controlled by amplitudes [1, 2]. Though traditional methods (such as numerical, windowing techniques and optimization) [3–6] of beam scanning and SLL control offer advantages such as simplicity and low complexity, but they are less adaptive in dynamic operating environments and under more sophisticated practical applications.

Recently, artificial intelligence (AI), machine learning (ML), and especially deep learning-based radiation pattern synthesis have emerged as strong alternatives that offer novel solutions [7–15]. Although various deep neural network (DNN) models have been proposed for beam scanning of linear antenna arrays, the problem of SLL reduction using deep learning has received limited focus in current research. This paper aims to fill this gap, where we introduce a novel unified approach using DNN for radiation pattern synthesis that simultaneously achieves beam scanning and SLL control. The proposed approach, therefore, generalizes the previously developed DNN-based techniques [14, 15], which are applicable for beam scanning only, enabling the antenna arrays to generate arbitrary radiation patterns with desired main lobe direction and SLLs.

In this work, we consider an eight-element linear antenna array to develop and train a DNN model to predict the phases and amplitudes of each array element for generating radiation patterns with desired scanning directions and SLL. The unified DNN model can

Submitted On: November 11, 2024
Accepted On: April 23, 2025

https://doi.org/10.13052/2025.ACES.J.400506

accurately predict the amplitudes and phases of all eight elements from a single input radiation pattern consisting of 181 points. The results are compared by plotting radiation patterns based on actual and learned antenna weights in MATLAB and CST simulators, which are also validated by actual measurements on a prototype array inside an in-house anechoic chamber. Our results show the efficacy of the proposed DNN approach for synthesizing an arbitrary array pattern.

The key advantages of the proposed unified DNN model are as follows.

(i) The proposed design offers simultaneous SLL control and beam scanning, thereby supporting a greater verity of applications.

(ii) Leveraging DNN's capabilities, the proposed design offers high accuracy and fast convergence. Also, it can learn complex radiation patterns and its performance improves with increasing data due to the scalability of DNN.

(iii) Once trained, the DNN model can instantly evaluate the complex weights (both amplitudes and phases) of the antenna elements for any input radiation pattern.

II. DNN ARCHITECTURE DESIGN

The architecture of our proposed unified DNN model is shown in Fig. 1. The radiation pattern of the linear antenna array, consisting of 181 points from 0 to 180 degrees, is fed as input features to the DNN model, resulting in 181 neurons in the input layer, each corresponding to one angular point in the radiation pattern. The model is designed by using five fully connected hidden layers, each with ascending neuron count: starting at 2048 in the first hidden layer, followed by 1536, 1024, and 800 nodes in the intermediate layers and culminating at 600 in the last layer. In order to reduce the size of the dataset, the amplitudes of the antenna elements are considered symmetrical, with the central element weights set to one. Therefore, it is only necessary to determine the amplitudes of the first three elements and the phases for the seven elements. Note that the phase of the first element is taken as a reference and set to zero. Consequently, the output layer of DNN consists of 10 neurons i.e., three for the amplitudes and seven for the phases. In non-symmetric scenarios with N antenna elements, the size of the output layer would be $2N-1$, comprising of N amplitudes and $N-1$ phases. An Adam optimizer is used to reduce the mean square error (MSE) between the actual and DNN estimated array weights.

III. DATASET GENERATION WITH REDUCED COMPUTATIONAL COMPLEXITY

For radiation pattern synthesis, our dataset contains equally spaced 181 points of the radiation patterns as features, which are used by the model to map their relationship with amplitudes and phases of each antenna element acting as output labels of the data. The amplitudes range from 0 to 1 and phases vary from 0° to 360° for each antenna element (0° for the first element).

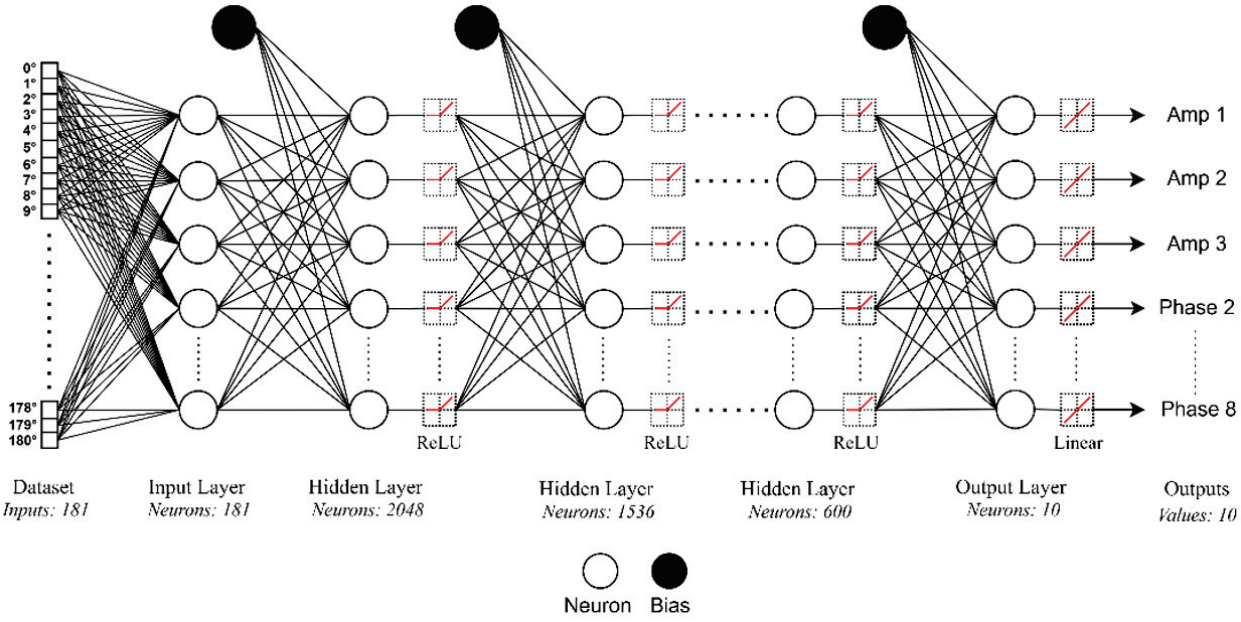

Fig. 1. Proposed DNN model architecture.

A. Amplitudes dataset

We use a structured approach that successively reduces the amplitudes dataset to a tractable size. This approach involves three steps.

1. Symmetry

To reduce the dataset size, we first exploit the symmetry of the radiation pattern about the main lobe which also implies symmetric amplitudes [16] across the array elements. It means if the model can predict the amplitudes of the first four elements in the eight-element array, the remaining four amplitudes can simply be mirrored. This significantly reduces the number of amplitude samples from 100 million to just 1000 (100,000-fold reduction) and with a reduced step size of 0.1 allowing us finer resolution in amplitude that improves model training accuracy.

2. Tapering

In this technique, the amplitudes of the array elements are generated by a suitable window function [3] to achieve the desired SLL. The effect of tapering on the radiation pattern would be that the main lobe remains high, the second sidelobes are smaller than the first, the third sidelobes are smaller than the second, and so on [17, 18]. The tapering step creates a highly relevant dataset and establishes a strong relationship between all the inputs and the desired radiation pattern.

3. Data cleaning

Tapering introduces redundancy in the dataset as it may result in many samples being repeated in the dataset. Thus, it is necessary to discard the recurring samples from the dataset by performing data cleaning. To efficiently generate the training dataset, tapering and data cleaning can be performed jointly in a single step. For the eight-element antenna array, again considering a step-size of 0.1, an additional up to 84% reduction in dataset size is possible by using both these steps.

The overall computational complexity for training the neural network can be expressed using big-O notation as $O(E \cdot D \cdot I \cdot H)$ as demonstrated in [19, 20], where E is the number of epochs, D is the size of training dataset, I is the size of the input layers and H is the number of hidden units. As the number of antenna elements N increases, a higher angular resolution is often required, leading to a proportional increase in the size of the input layer and hidden layers. For linear arrays, this results in a complexity that scales linearly with N. However, transitioning from a linear to a planar antenna array significantly increases the dimensionality of the radiation pattern, causing the complexity to scale quadratically with N [21].

B. Phases dataset

Since phases vary over a wide range 0° to 360°, the constant step size strategy is impractical here as it will generate a very large data set. To cope with this problem, we adopt a method proposed by the authors in [15] for reducing the dataset in array beamforming. The method in [15] uses uniformly spaced values of the phase difference (not the absolute phases) to generate the dataset This significantly reduces the dataset size without comprising phase diversity. The dataset is generated using MATLAB software and is publicly accessible for download as referenced in [22].

It should be noted that a dataset of reduced complexity can also be generated for planar arrays with the same number of antenna elements by under sampling their radiation patterns in two dimensions. The proposed DNN model predicts the antenna weights with high accuracy. However, these results have not been included due to space constraints.

IV. TRAINING AND VALIDATION

In our experiments, we considered 80% of the dataset for training, 10% for validation, and 10% for testing. Initially, the number of epochs is set to 250. Then, to speed up the training process, we incorporated early stopping, which halts the training if the validation loss does not improve or begin to increase. The patience for early stopping was set to 10, meaning that if the validation loss does not improve over 10 consecutive epochs, training will stop. The patience for reducing the learning rate, a technique to reduce the learning rate when the validation loss plateaued, was set to five epochs. This means that if the loss did not improve after reducing the learning rate and met the early stopping criteria, the training

Table 1: Hyperparameters of the proposed DNN model

Hyperparameters	Values
Total data	2,011,100
Training data	80%
Validation data	10%
Testing data	10%
Input layer neurons	181
Number of hidden layers	5
Hidden layer neurons (per layer)	2048, 1536, 1024, 800, 600
Activation function in hidden layer	*ReLu*
Output layer neurons	10
Activation function in output layer	Linear
Optimizer	Adam
Number of epochs	250
Learning rate	0.001

would stop. This approach ensures that the training process is efficient and helps the model converge towards a lower error or loss. Compared to other methods where training continues for the full number of epochs even if the loss increases or remains unchanged, this method optimizes training time and prediction performance. The hyperparameters of the proposed DNN model are given in Table 1.

V. NUMERICAL RESULTS

This section presents a detailed numerical analysis of the proposed DNN model, including training, validation, and prediction results for radiation pattern synthesis of an eight-element linear antenna array. In all these results, R2 score and MSE serve as performance metrics. The numerical results are generated using Python but plotted in MATLAB, which are also verified using CST software. These results are validated through actual measurements on the prototype antenna array in section VI.

A. Training and validation results

The training was performed on a system with an NVIDIA L4 GPU, CUDA 12.2, and 24 GB of GPU memory. Given the large dataset, we utilized Dask, a parallel computing library in Python, to efficiently handle and process large datasets. After the initial processing with Dask, we converted the data into a format compatible with TensorFlow for model training. Additionally, Joblib was employed to save the model weights and trained scaler to disk for later use. The training process was optimized by the ModelCheckpoint callback, which allowed us to save the best-performing model parameters, based on the lowest validation loss during training.

Figure 2 shows the results, in terms of MSE loss function for training and validation. Specifically, the MSE loss curve quickly converges to 0.000048391 indicating that the proposed method significantly reduces the model loss. Figure 2 also shows an average R2 score of nearly 1.0 across all epochs, indicating that our model faithfully captured the underlying patterns in the training data.

B. Prediction results

After completion of training and validation, the model's performance on entirely new data that is not part of the dataset needs to be evaluated. To this end, we generate optimal array patterns of the desired main

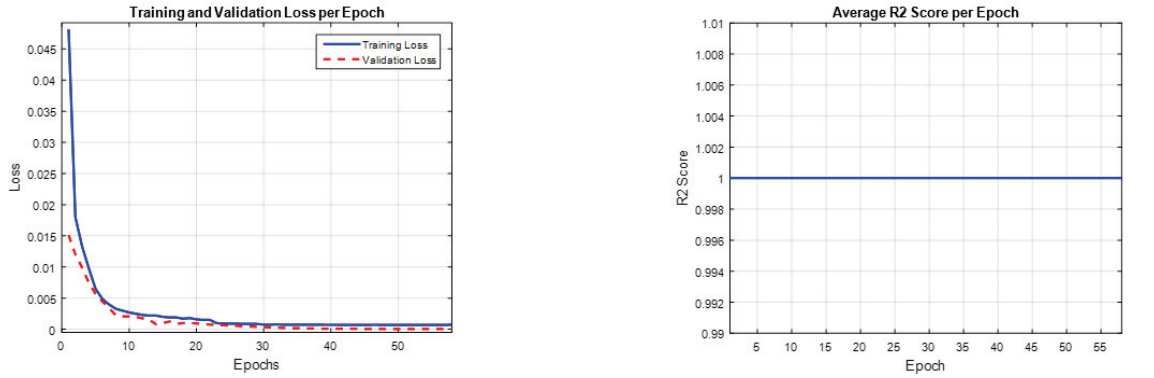

Fig. 2. Training and validation of the proposed DNN model: (a) loss curves and (b) R2 score.

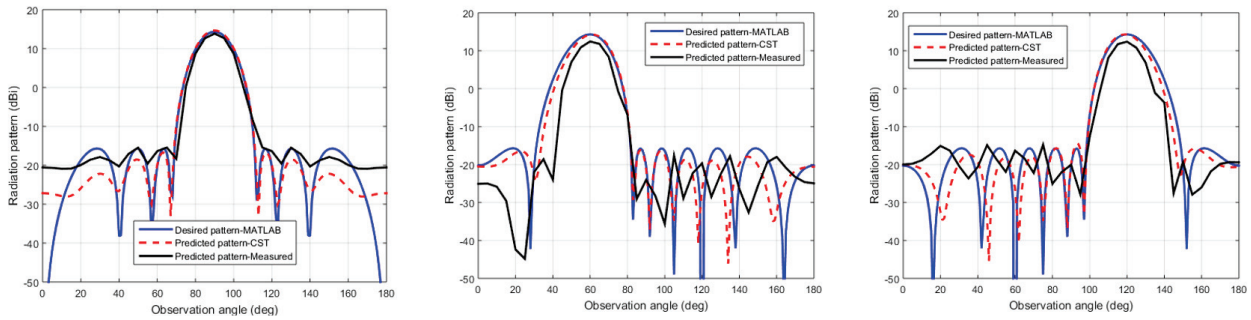

Fig. 3. Measured and predicted-simulated radiation pattern results of a 1×8 prototype array with SLL -30 dB and main beam at scan angles $\theta s = 90°$(left), $\theta s = 60°$(center), and $\theta s = 120°$(right).

beam direction and/or side lobe level (SLL), which are then fed to the DNN model to predict the amplitudes and phases of each array element. To test the robustness of the model, we perform a critical analysis by testing the predictions in the following scenarios: SLL of -30 dB. with main beam scanning at 60°, 90°, and 120° observation angles. These three scenarios are illustrated in Fig. 3, which compare the desired and predicted radiation patterns. The results in Fig. 3 show the desired and predicted radiation patterns generated in MATLAB (blue) and CST (red) by using the complex weights learned by the proposed DNN model. The complex weights computed with the proposed DNN model are given in Appendix A.

VI. MEASUREMENT VALIDATION

To validate the predicted amplitude-phase composite DNN model, a 1×8 linear patch antenna array operating at 2.45 GHz and with an inter-element spacing of $\lambda/2$ was manufactured and is shown in Fig. 4 in the in-house anechoic chamber. The individual patch elements are excited through commercially available phase shifters (part no. HMC928LP5E) and voltage variable attenuators (part no. ZX73-2500-S+) to set the complex weights (see Appendix A) on the individual antenna elements in the array. These measured results are also shown in Fig. 3 for comparison with simulated results. The differences in peak gain and SLLs between simulated and measured radiation patterns using the predicted array weights with the proposed DNN model are given in Table 2. The theoretical complex weights obtained with DNN model were quantized to the values achievable with available attenuators and phase shifters for the measurement validation. The quantized values obtained from measured datasheets of the attenuator and phase shifter reported in [23] are added in Appendix A. These quantized values were set through voltage-controlled attenuators and phase shifters and the resulting measured radiation patterns are shown in Fig. 3. As can be seen, there are differences in the measured and simulated radiation patterns due to quantized and theoretical weights feeding, however they are still within the acceptable range.

Based on the results in Fig. 3 and Table 2, several observations can be drawn: (a) the overall behavior of the predicted radiation patterns is similar to desired (ideal) patterns. This indicates the accuracy of the estimated composite amplitude-phase DNN model for phased array antennas; (b) there are acceptable small differences in phased array performance parameters of gain and SLLs, which shows that the proposed amplitude-phase DNN model can be used generically in SLL-controlled phased array applications, such as in massive MIMO and radar systems, to reject the interferes and clutters; and (c) the deviations in the measured and simulated patterns are mainly due to limitations of achieving the exact

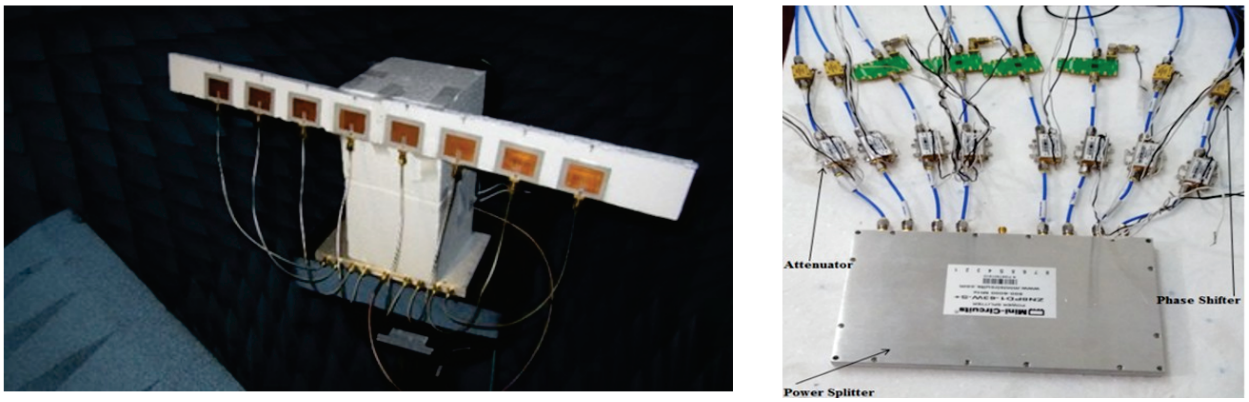

Fig. 4. A 1×8 prototype array (left) with integrated attenuators and phase shifters (right) in an in-house anechoic chamber measurements facility.

Table 2: Comparison between predicted, measured, and simulated results of a 1×8 prototype array with integrated attenuators and phase shifters

	Peak Gain (dB)			**Sidelobe Level (dB)**		
Scan Angle (θs)	**Simulated (MATLAB)**	**Simulated (CST)**	**Measured**	**Simulated (MATLAB)**	**Simulated (CST)**	**Measured**
90°	14.23	14.62	13.87	−29.78	−31.7	−29.32
60°	14.23	14.25	12.43	−29.83	−30.36	−31.03
120°	14.36	14.25	12.38	−30.06	−28.86	−27.18

amplitudes and phases with the microwave components (attenuators, phase shifters) and possibly imperfect measurement environment.

VII. CONCLUSION

In this paper, we proposed a DNN model that is capable of synthesizing the radiation pattern of an eight-element antenna array with precise control over SLL and main beam direction. We also proposed a structured way of generating the training data set that could speed up the learning of DNN model parameters. The model uses 181 points of the radiation pattern as input features set against the amplitudes and phases of array elements as labeled data. The prediction results carried out using MATLAB, CST, and measurements proved to be in close agreement with actual values showing the accuracy of the proposed DNN model with R2 scores approaching 1. In conclusion, deep learning models, especially DNNs, have proven their ability to learn and effectively be utilized in phased arrays. This work not only provides an innovative solution to current challenges in synthesizing radiation patterns but also paves the way for future developments. The success of DNN has opened the door to incorporating more advanced versions of deep learning, such as transformers and specialized transformers, to solve more complex real-world problems in phased array design and optimization.

ACKNOWLEDGMENT

This work is funded by the Higher Education Commission (HEC) Pakistan via Project No.20-17554/NRPU/R&D/HEC/2021.

REFERENCES

[1] R. L. Haupt, *Antenna Arrays: A Computational Approach*. Hoboken, NJ: John Wiley and Sons, 2010.

[2] R. C. Hansen, *Phased Array Antennas*. Hoboken, NJ: John Wiley and Sons, 2010.

[3] Md. R. Sarker, Md. M. Islam, Md. T. Alam, and M. H.-E. Haider, "Side lobe level reduction in antenna array using weighting function," in *International Conference on Electrical Engineering and Information & Communication Technology (ICEEICT)*, Dhaka, Bangladesh, pp. 1-5, Apr. 2014.

[4] S. Chatterjee, S. Chatterjee, and D. R. Poddar, "Side lobe level reduction of a linear array using Chebyshev polynomial and particle swarm optimization," in *International Conference on Communication, Circuits and Systems (IC3S-Number 1)*, June 2013.

[5] S. Liang, Z. Fang, G. Sun, Y. Liu, G. Qu, and Y. Zhang, "Sidelobe reductions of antenna arrays via an improved chicken swarm optimization approach," *IEEE Access*, vol. 8, pp. 37664-37683, 2020.

[6] K. Fu, X. Cai, B. Yuan, Y. Yang, and X. Yao, "An efficient surrogate assisted particle swarm optimization for antenna synthesis," *IEEE Trans. Antennas Propagat*., vol. 70, pp. 4977-4984, 2022.

[7] F. Andriulli, P.-Y. Chen, D. Erricolo, and J.-M. Jin, "Guest editorial: Machine learning in antenna design, modeling, and measurements," *IEEE Trans. Antennas Propagat*., vol. 70, pp. 4948-4952, 2022.

[8] W. T. Li, H. S. Tang, C. Cui, Y. Q. Hei, and X. W. Shi, "Efficient online data-driven enhanced-XGBoost method for antenna optimization," *IEEE Trans. Antennas Propagat*., vol. 70, pp. 4953-4964, 2022.

[9] R. Lovato and X. Gong, "Phased antenna array beamforming using convolutional neural networks," in *IEEE International Symposium on Antennas and Propagation and USNC-URSI Radio Science Meeting*, Atlanta, GA, USA, pp. 1247-1248, July 2019.

[10] T. Sallam and A. M. Attiya, "Convolutional neural network for 2D adaptive beamforming of phased array antennas with robustness to array imperfections," *International Journal of Microwave and Wireless Technologies*, vol. 13, pp. 1096-1102, 2021.

[11] H. Bilel, L. Selma, and A. Taoufik, "Artificial neural network (ANN) approach for synthesis and optimization of (3D) three-dimensional periodic phased array antenna," in *17th International Symposium on Antenna Technology and Applied Electromagnetics (ANTEM)*, Montreal, QC, Canada, pp. 1-6, Aug. 2016.

[12] Y.-S. Kim, D. Schvartzman, R. D. Palmer, and T.-Y. Yu, "Fast adaptive beamforming using deep learning for digital phased array radars," in *IEEE International Symposium on Phased Array Systems & Technology (PAST)*, Waltham, MA, USA, pp. 1-7, Oct. 2022.

[13] L. Merad, F. T. Bendimerad, S. M. Meriah, and S. A. Djennas, "Neural networks for synthesis and optimization of antenna arrays," *Radioengineering*, vol. 16, pp. 23-30, 2007.

[14] J. H. Kim and S. W. Choi, "A deep learning-based approach for radiation pattern synthesis of an array antenna," *IEEE Access*, vol. 8, pp. 226059-226063, 2020.

[15] A. Zaib, A. R. Masood, M. A. Abdullah, S. Khattak, A. B. Saleem, and I. Ullah, "AESA antennas using machine learning with reduced dataset," *Radioengineering*, vol. 33, pp. 397-405, 2024.

[16] I. Ullah, S. Khattak, and B. D. Braaten, "Improvement of the broadside radiation pattern of a

conformal antenna array using amplitude tapering," *Applied Computational Electromagnetics Society (ACES) Journal*, vol. 32, pp. 511-516, 2017.

[17] N. S. Khasim, Y. M. Krishna, J. Thati, and M. V. Subbarao, "Analysis of different tapering techniques for efficient radiation pattern," *e-Journal of Science & Technology (e-JST),* vol. 8, pp. 47-55, 2013.

[18] P. Delos, B. Broughton, and J. Craft, *Phased array antenna patterns—Part 3: Sidelobes and tapering*, ADI Inc, vol. 54, July 2020. [Online]. Available: https://www.analog.com/en/resources/analog-dialogue/articles/phased-array-antenna-patterns-part3.html

[19] I. Goodfellow, Y. Bengio, and A. Courville, *Deep Learning.* Cambridge, MA: MIT Press, 2016.

[20] J. Dean, G. Corrado, R. Monga, K. Chen, M. Devin, M. Mao, M. Ranzato, A. Senior, P. Tucker, K. Yang, Q. V. Le, and A. Y. Ng, "Large scale distributed deep networks," *Advances in Neural Information Processing Systems (NIPS)*, vol. 25, 2012.

[21] T. T. Nguyen and K.-K. Nguyen, "A deep learning framework for beam selection and power control in massive MIMO-millimeter-wave communications," *IEEE Transactions on Mobile Computing*, vol. 22, no. 8, pp. 4374-4387, 2022.

[22] M. A. Abdullah, *Dataset for antenna array pattern with sidelobe level control using deep learning* [Online]. Available: https://doi.org/10.5281/zenodo.14533762

[23] https://www.ndsu.edu/pubweb/~braaten/dissertation_Irfan.pdf

Appendix A: Desired vs predicted amplitudes and phases for 1×8 phased array antenna

	Desired Parameters	**Desired Weights (element 1 to element 8)**	**DNN Predicted Weights**
Amplitude-only scenario	SLL: –20 dB	0.5799∠0^o, 0.6603∠0^o, 0.8751∠0^o, 1∠0^o, 1∠0^o, 0.8751∠0^o, 0.6603∠0^o, 0.5799∠0^o	0.5964∠0.00^o, 0.6417∠0.00^o, 0.8822∠0.00^o, 1∠0.00^o, 1∠0.00^o, 0.8822∠0.00^o, 0.6417∠0.00^o, 0.5964∠0.00^o
	SLL: –30 dB	0.2622∠0^o, 0.5187∠0^o, 0.8119∠0^o, 1∠0^o, 1∠0^o, 0.8119∠0^o, 0.5187∠0^o, 0.2622∠0^o	0.2619∠0^o, 0.5146∠0^o, 0.815∠0^o, 1∠0^o, 1∠0^o, 0.8157∠0^o, 0.5187∠0^o, 0.2622∠0^o
	SLL: –40 dB	0.1460∠0^o, 0.4179∠0^o, 0.7594∠0^o, 1∠0^o, 1∠0^o, 0.7594∠0^o, 0.4179∠0^o, 0.1460∠0^o	0.1479∠0.00^o, 0.4167∠0.00^o, 0.7584∠0.00^o, 1∠0.00^o, 1∠0.00^o, 0.7584∠0.00^o, 0.4167∠0.00^o, 0.1479∠0.00^o
Phase-only scenario	$\theta_s = 60^\circ$	1∠0^o, 1∠90^o, 1∠180^o, 1∠270^o, 1∠360^o, 1∠450^o, 1∠540^o, 1∠630^o	0.9389∠0.00^o, 0.9853∠90.00^o, 0.9942∠179.99^o,1.00∠269.99^o, 1.00∠359.99^o, 0.9942∠449.99^o, 0.9853∠539.99^o, 0.9389∠629.98^o
	$\theta_s = 90^\circ$	1∠0^o, 1∠0^o, 1∠0^o, 1∠0^o, 1∠0^o, 1∠0^o, 1∠0^o, 1∠0^o	0.9581∠0.00^o, 0.9849∠0.00^o, 0.9849∠0.00^o, 1.00∠0.00^o, 1.00∠0.00^o, 0.9581∠0.00^o, 0.9849∠0.00^o, 0.9849∠0.00^o
	$\theta_s = 120^\circ$	1∠0^o, 1∠-90^o, 1∠-180^o, 1∠-270^o, 1∠-360^o, 1∠-450^o, 1∠-540^o, 1∠-630^o	0.9568∠0.00^o, 0.9809∠89.91^o, 0.9836∠179.89^o, 1.00∠269.89^o, 1.00∠359.87^o, 0.9836∠449.87^o, 0.9809∠539.86^o, 0.9568∠629.88^o
Amplitude-Phase scenario	SLL: –30 dB $\theta_s = 60^\circ$	0.2622∠0^o, 0.5187∠90^o, 0.8119∠180^o, 1∠270^o, 1∠360^o, 0.8119∠450^o, 0.5187∠540^o, 0.2622∠630^o	**Theoretical**: 0.2476∠0.00^o, 0.5201∠90.00^o, 0.8060∠179.99^o, 1.00∠269.99^o, 1.00∠359.99^o, 0.8060∠449.99^o, 0.5201∠539.99^o, 0.2476∠629.98^o **Quantized**: 0.25∠0^o, 0.5∠87^o, 0.65∠178^o, 0.65∠-92^o, 0.65∠0^o, 0.65∠87^o, 0.5∠178^o, 0.25∠-92^o
	SLL: –30 dB $\theta_s = 90^\circ$	0.2622∠0^o, 0.5187∠0^o, 0.8119∠0^o, 1∠0^o, 1∠0^o, 0.8119∠0^o, 0.5187∠0^o, 0.2622∠0^o	**Theoretical**: 0.2619∠0^o, 0.5146∠0^o, 0.815∠0^o, 1∠0^o, 1∠0^o, 0.8157∠0^o, 0.5187∠0^o, 0.2622∠0^o **Quantized**: 0.25∠0^o, 0.5∠0^o, 0.65∠0^o, 0.65∠0^o, 0.65∠0^o, 0.65∠0^o, 0.5∠0^o, 0.25∠0^o
	SLL: –30 dB $\theta_s = 120^\circ$	0.2622∠0°, 0.5187∠-0°, 0.8120∠-180°, 1∠-270^o, 1∠-360^o, 0.8120∠-450°, 0.5187∠-540°, 0.2622∠-630°	**Theoretical**: 0.2611∠0.00°, 0.5360∠-89.87°, 0.8144∠-179.77°, 1.00∠-269.69°, 1.00∠-359.57°, 0.8144∠-449.46°, 0.5360∠-539.36°, 0.2611∠-629.27° **Quantized**: 0.25∠0°, 0.5∠-86°, 0.65∠-178°, 0.65∠-90°, 0.65∠0°, 0.65∠-86°, 0.5∠-178°, 0.25∠87°

Note: Quantized values were obtained using the measured data sheets in [23]

Muhammad A. Abdullah holds a bachelor's degree in Computer Engineering from COMSATS University Islamabad, Pakistan. He is currently an AI Researcher and Engineer at ADK Technology Co., specializing in the development of machine learning (ML) and deep learning (DL) models for industrial applications, including neural architecture optimization and deployment of generative AI systems.

Alam Zaib received the Ph.D. degree in Electrical Engineering from KFUPM, Dhahran, Saudi Arabia, in 2016. He was an Erasmus Mundus scholar in MERIT master program from 2007 to 2009. Currently he is Associate Professor in the Department of Electrical Engineering at COMSATS University Islamabad, Abbottabad Campus. His research interests are in signal processing, wireless communications and applications of AI and machine learning in antenna arrays and wireless communication.

Shafqat U. Khan received M.S. and Ph.D. degrees in Electronic Engineering from International Islamic University Islamabad and ISRA University in 2008 and 2015, respectively. He was a Post Doc Fellow at the Faculty of Electrical Engineering, University Technology Malaysia, from 2016 to 2017. He is an Associate Professor at the University of Buner. His research interest includes the RF & microwave, antenna arrays and evolutionary algorithms.

Shoaib Azmat received his Ph.D. and M.S. degrees in Electrical and Computer Engineering from the Georgia Institute of Technology, Atlanta, GA, USA, in 2014 and 2011, respectively. Currently, he is an Associate Professor of Computer Engineering at COMSATS University, Abbottabad. His research interests include computer vision, machine learning, and digital image processing, with research publications in reputed international journals.

Shahid Khattak received Dr.-Ing degree from Technische Universität Dresden, Germany, in 2008. He is a distinguished academic and researcher specializing in electrical and computer engineering with a focus on advanced communication systems, signal processing, and applied electromagnetics. He has contributed extensively to both theoretical and applied research, with numerous publications in reputed international journals. Khattak is known for his dedication to academic excellence and mentoring, and he plays a pivotal role in advancing interdisciplinary research in engineering and technology.

Benjamin D. Braaten (Senior Member, IEEE) received the B.S. degree in electrical engineering, the M.S. degree in electrical engineering, and the Ph.D. degree in electrical and computer engineering from North Dakota State University, Fargo, ND, USA, in 2002, 2005, and 2009, respectively. During the 2009 Fall semester, he held a postdoctoral research position with the South Dakota School of Mines and Technology, Rapid City, SD, USA. His research interests include printed antennas, conformal self-adapting antennas, microwave devices, topics in EMC, topics in BIO EM, and methods in computational electromagnetics He is currently a Chairman of the ECE Department at NDSU, Fargo, ND, USA. He has authored or coauthored more than 100 reviewed journal and conference publications, several book chapters and holds one U.S. patent on wireless pacing of the human heart.

Irfan Ullah received a Ph.D. degree in Electrical and Computer Engineering from North Dakota State University, Fargo, ND, USA, in 2014. He is an Associate Professor in Electrical Engineering Department at COMSATS University Islamabad, Abbottabad Campus. His research interests include beamforming arrays, machine learning in antenna arrays, electromagnetic metamaterials, and topics in EMC.

Wideband Meta-dielectric Resonator Antenna

Wenke Jiang[1], Guanghui Xu[1,2,3], Yanbin Luo[2], Zhixiang Huang[1], Wei Wang[2], Mouping Jin[2], and Hong-Li Peng[3]

[1]Information Materials and Intelligent Sensing Laboratory of Anhui Province
Anhui University, Hefei 230039, China
1036697676@qq.com, ghxu86@ahu.edu.cn, zxhuang@ahu.edu.cn

[2]East China Research Institute of Electronic Engineering
Hefei 230088, China
luoyanb001@163.com, shu00ww@163.com, jinmoup_cn@sina.com

[3]Key Laboratory of Ministry of Education for Design and Electromagnetic Compatibility of High-Speed Electronics Systems
Shanghai Jiao Tong University, Shanghai 200240, China
hl.peng@sjtu.edu.cn

Abstract – A novel wideband meta-dielectric resonator antenna (MDRA) is presented in this paper. Metamaterial technology is introduced to broaden the impedance bandwidth of the DRA. The proposed MDRA comprises a 4×4 array of subwavelength meta-dielectric resonator cuboids ($0.096\lambda 0 \times 0.096\lambda 0 \times 0.116\lambda 0$, where $\lambda 0$ denotes the free space wavelength at the center frequency) fed by a microstrip-slot configuration. The proposed MDRA achieves a wideband -10 dB impedance bandwidth of 36% (1.88-2.71 GHz) with a stable radiation pattern. Due to its advantages of low profile, simple structure, wide bandwidth and stable radiation pattern, the MDRA may be applied to the wideband wireless communication systems.

Index Terms – Dielectric resonator antenna, metamaterial, stable radiation pattern, wideband.

I. INTRODUCTION

With the development of 5G and B5G wireless communications, data transmission capacity is in increasing demand [1]. Meanwhile, wideband antennas, as important transmitting and receiving devices, have attracted considerable attention for enhancing communication capacity. To date, many different types of antennas have been developed for broadband operation, such as L-probe fed antenna [2], E-shaped patch antenna [3], magneto-electric dipoles [4] and others [5]. In addition, dielectric resonator antennas (DRAs) are also adopted for wideband applications due to their light weight, cost efficiency, smaller size and high radiation efficiency.

To achieve wideband operation of DRAs, many techniques have been proposed and developed. One technique is to adopt special DRA structures to excite multiple modes for bandwidth enhancement, such as H- or T-shaped DRAs [6-9], but their radiation patterns do not exhibit stable broadside characteristics. For example, a diversity cylindrical DRA can achieve a wider impedance bandwidth of 30%, covering 3.08-4.16 GHz, but its broadside radiation pattern is degraded [9].

An alternative approach for bandwidth enhancement is to excite hybrid resonant modes in the DRA using a complex feeding network [10-12]; however, this method is limited by the intricate feed structure and increased antenna dimensions. In [10], a tri-mode stub-loaded resonator was employed as the feeding network to achieve an impedance bandwidth of 34%. In [11], a cup-like DRA with a coil feeding structure demonstrated a bandwidth of 29%. In [12], a 1-to-4 slot-coupled feeding mechanism was utilized to excite a cylindrical DRA, achieving an impedance bandwidth of 25.2% (without aperture mode) and 34% (with aperture mode). In addition, fractal geometries and multi-element configurations have been employed to significantly enhance the bandwidth of DRAs [13-17], but these designs typically exhibit asymmetric radiation patterns and high cross-polarization levels. In [18], a wideband DRA with a lattice structure was proposed, but it requires a high-permittivity (about 40) lattice body and an additional SIW cavity.

Recently, metamaterials have received a lot of attention due to their unique electromagnetic physics perspectives [19-21]. However, to date, few studies have focused on metamaterial-based DRAs. In [20], a DRA integrated with a top-loaded rotatable anisotropic metasurface was proposed, achieving an impedance bandwidth

Submitted On: December 12, 2024
Accepted On: April 29, 2025
https://doi.org/10.13052/2025.ACES.J.400507

of 0.65 GHz (6.52-7.17 GHz). In [21], by adding a 6×6 array of periodic metallic patch cells and shorting walls, the impedance bandwidth of the DRA is dramatically increased to about 17.2% (1.75-2.08 GHz), and it achieves a stable gain of 6.6 dBi and a lower cross-polarization level. However, its bandwidth is still narrow, and the rectangular structure of the DRA is not completely changed (extra metasurface patches are added).

In this work, metamaterial technology is adopted to enhance the impedance bandwidth of the DRA while maintaining good radiation patterns. A novel wideband meta-dielectric resonator antenna (MDRA) is proposed in this paper. The MDRA consists of a 4×4 meta-dielectric resonator cuboid array fed by a microstrip-slot configuration. Each cuboid element has a length of 12 mm, which is about 0.096λ0 (where λ0 denotes the free-space wavelength at the center frequency). Its 15 mm height corresponds to 0.116λ0. Therefore, the element size meets the subwavelength characteristic of metamaterials. Through the antenna fabrication and testing, the proposed MDRA achieves a 36% -10 dB impedance bandwidth (1.88-2.71 GHz) with a stable radiation pattern. Due to these advantages, including low profile, simple structure, wide bandwidth and stable radiation characteristics, the MDRA is highly suitable for modern wireless communication systems with stringent miniaturization requirements, such as 5G mobile terminals and IoT devices.

This paper is organized as follows. Section II presents the operation principle and design of the MDRA. Section III compares and discusses the simulated and measured results. Section IV draws the final conclusions.

II. THEORETICAL ANALYSIS OF THE MDRA

A. Configuration of the MDRA

Figure shows the top and side configurations of the MDRA on the grounded substrate with a thickness of t. The RT/duroid 5880 with a dielectric constant of 2.2 and loss tangent of 0.0009 is adopted as the substrate. The proposed MDRA consists of a 4×4 meta-dielectric resonator array composed of Al_2O_3 material cuboids with a length of d_l, width of d_w and height of h. Parameters s_1 and s_2 are the gaps between cuboid elements, as shown in Fig. 1 (a). The slot with a length of l_s and width of w_s provides electromagnetic coupling to the meta-dielectric resonator and a microstrip line is employed for the feeding.

B. Design of the proposed MDRA

Figure 2 shows the design flow of the proposed MDRA. Ant.I has one meta-dielectric element. The 2×2 meta-dielectric array is defined as Ant.II. Ant.III comprises the 3×3 meta-dielectric array. Finally, Ant.IV consists of the 4×4 meta-dielectric array. Their simulated |S11| is shown in Fig. 3. It is noted that the resonant frequency decreases from Ant.I to Ant.IV. This is because the dielectric structure size gradually increases.

According to Ant.IV, structural size optimization is performed. By fixing the gap width (s_1=s_2=1 mm), the side length d_w of the meta-dielectric cuboid is decreased from 14 to 10 mm, and the impedance bandwidths of the proposed MDRA change, as shown in Fig. 4 (a). When

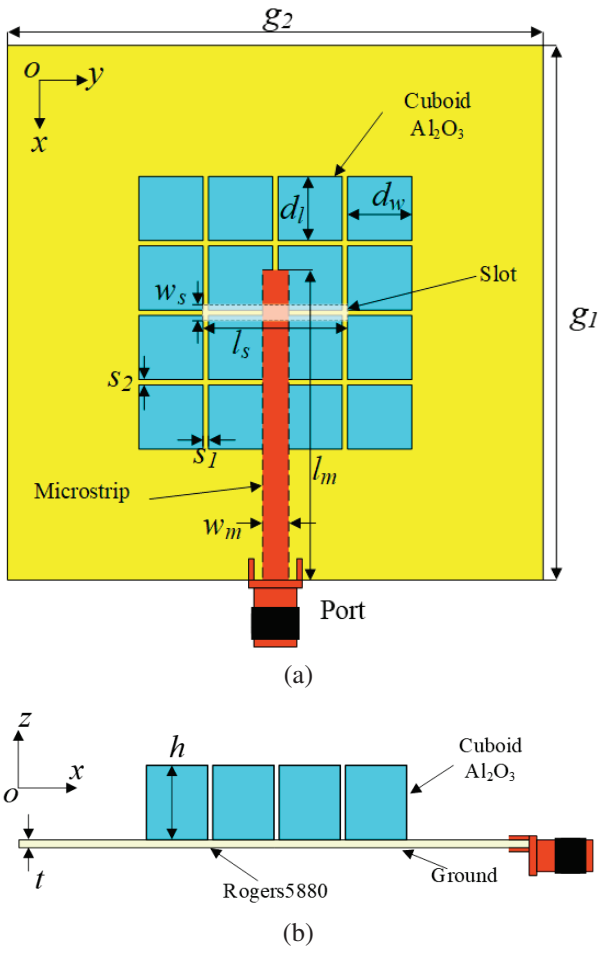

Fig. 1. Configuration of the wideband meta-dielectric resonator antenna: (a) top view and (b) side view.

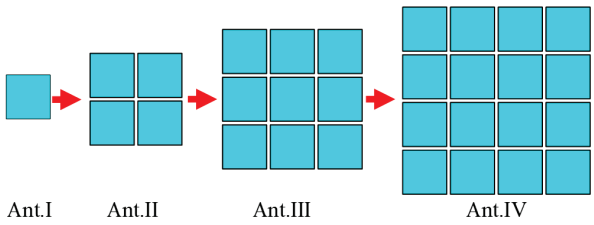

Fig. 2. Structural evolution of the wideband MDRA.

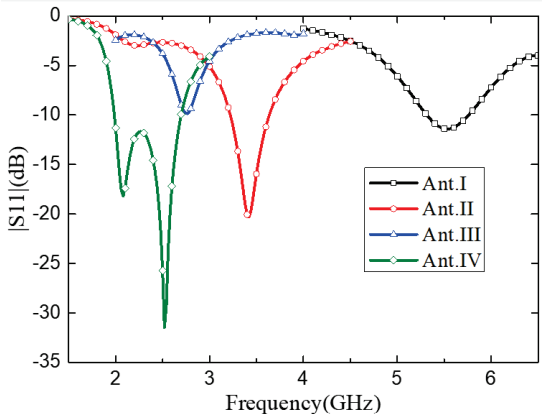

Fig. 3. Simulated |S11| of the four evolution antennas.

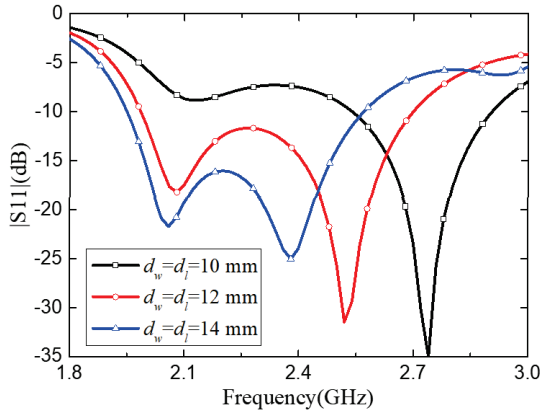

(a)

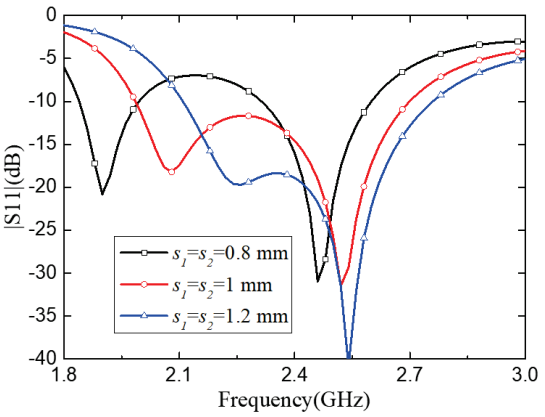

(b)

Fig. 4. Simulated |S11| of the proposed MDRA with sizes d_w, d_l, s_1 and s_2.

the gap width (s_1 and s_2) between the meta-dielectric cuboids changes, the simulated |S11| is displayed in Fig. 4 (b). When d_w=d_l=12 mm and s_1=s_2=1 mm, a wider impedance bandwidth is achieved and two resonant frequency points (2.08 and 2.54 GHz) are obtained for enhancing the impedance bandwidth. The final geometrical parameters of the proposed MDRA are summarized in Table 1.

Table 1: Key parameters of MDRA (Unit: mm)

g_1	g_2	d_l	d_w	l_s	w_s
10	10	12	12	27	2
s_1	s_2	l_m	w_m	h	t
1	1	58	4.85	15	1.57

C. Work principle of the proposed MDRA

To explore the working principle of MDRA, the electric field distributions at the two resonant frequency points are simulated and analyzed. First, the four side view planes (1#, 2#, 3# and 4#) of MDRA in the E-plane direction are selected to investigate the electric field, as shown in Fig. 5. In addition, the electric field of the MDRA from the top view is also a key observation surface and is provided for studying the radiation performances.

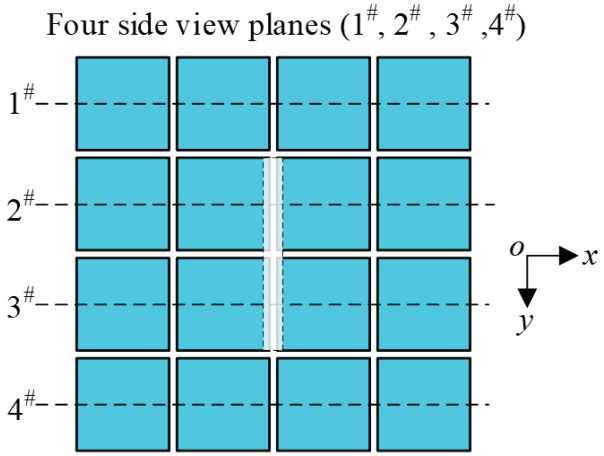

Fig. 5. Four side view planes (1#, 2#, 3# and 4#) of MDRA in the E-plane direction.

Figure 6 shows the simulated electric field distributions of MDRA at 2.08 GHz. The antenna operates in TE^{y}111 mode, with low-loss characteristics and uniform field distribution for efficient energy radiation. In the top view shown in Fig. 6 (a), the electric field in the middle part is stronger and those on both sides are weaker, but the electric field directions on the top surface of each meta-dielectric cuboid are almost the same. In the side view shown in Fig. 6 (b), the electric fields of each horizontal row cuboid have the same rotation direction. Therefore, the corresponding far-field radiation is good, as shown in Fig. 8.

Similarly, Figs. 7 (a) and (b) display MDRA's electric field distributions at 2.54 GHz in top and side views. The antenna's center operates in TE^{y}131 mode,

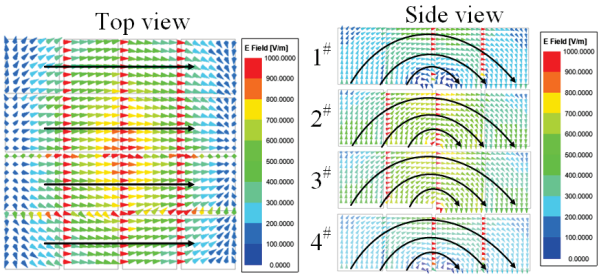

Fig. 6. Simulated electric field distributions of MDRA at resonant frequency of 2.08 GHz: (a) top view and (b) side view.

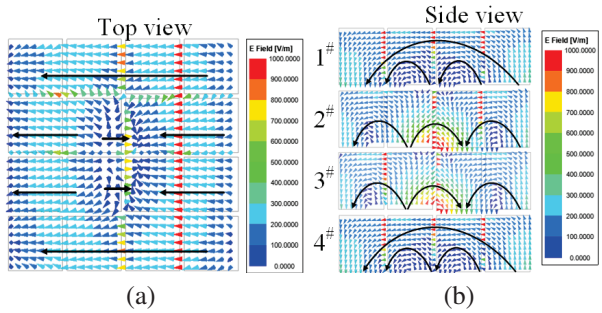

Fig. 7. Simulated electric field distributions of MDRA at resonant frequency of 2.54 GHz: (a) top view and (b) side view.

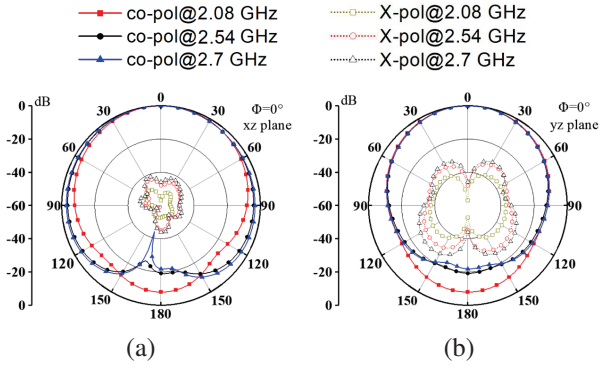

Fig. 8. Simulated normalized radiation patterns of proposed MDRA at frequencies of 2.08, 2.54 and 2.7 GHz: (a) in the E-plane and (b) in the H-plane.

where its multi-lobe field strengthens radiation coupling and boosts performance. Top view and side view show weaker electric fields in the middle and side regions but stronger fields at vertical gaps, while maintaining consistent field directions across all cuboids. The corresponding far-field radiation is good, as shown in Fig. 8. In addition, it is found that the main beams with different frequencies are similar and the antenna has a lower cross-polarization level in the E-plane (≤40 dB) and H-plane (≤30 dB).

III. EXPERIMENTAL RESULTS AND DISCUSSION

The results comparison between simulations and measurements of the proposed MDRA are performed in this section. Fabrication and measurement photos of the MDRA are given in Fig. 9. Simulated and measured |S11| and gains of the MDRA are compared in Fig. 10. Simulated and measured -10 dB impedance bandwidths of the proposed MDRA are about 30% (2-2.7 GHz) and 36% (1.88-2.71 GHz), respectively. Measured |S11| and gains have a frequency deviation with the simulated ones due to changes in dielectric constant and fabrication assembly errors. The simulated and measured radi-

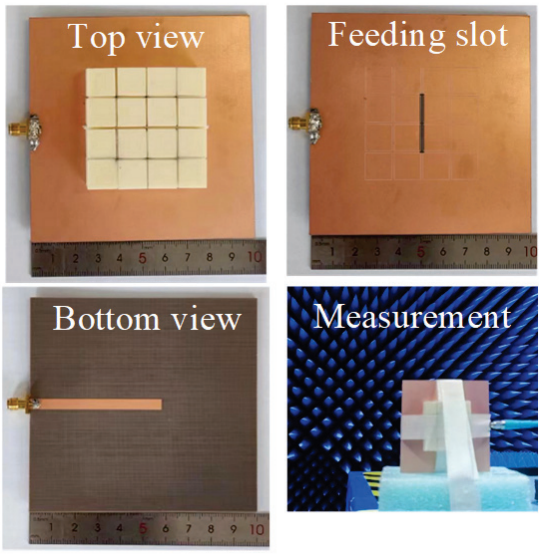

Fig. 9. Fabrication and measurement photos of MDRA.

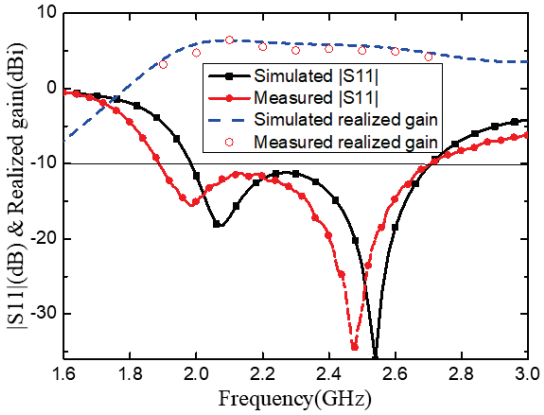

Fig. 10. Simulated and measured |S11| and gains of MDRA.

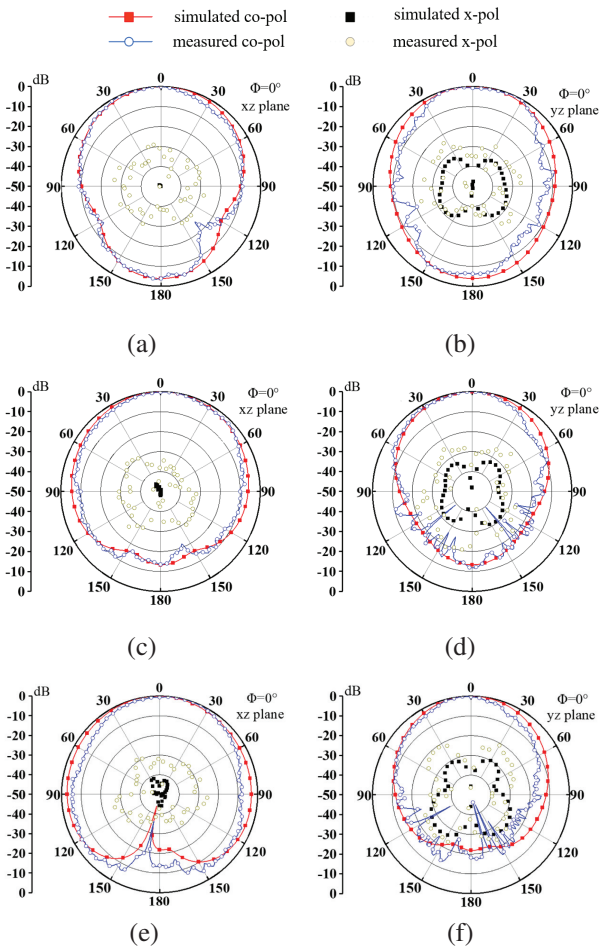

Fig. 11. Simulated and measured normalized radiation patterns of the antenna: (a) 1.9 GHz in the E-plane, (b) 1.9 GHz in the H-plane, (c) 2.3 GHz in the E-plane, (d) 2.3 GHz in the H-plane, (e) 2.7 GHz in the E-plane, and (f) 2.7 GHz in the H-plane.

ation patterns of MDRA at frequencies of 1.9, 2.3 and 2.7 GHz are compared in Fig. 11. Simulated and measured main lobes are similar and they have stable radiation pattern characteristics. Cross-polarization levels are less than −30 dB in the main lobe, but measured ones are less than −20 dB. The difference in cross-polarization level may be caused by errors in fabrication, assembly and radiation measurement. These differences indicate acceptable agreement.

Table 2 summarizes the comparison results of the proposed MDRA and other existing wideband DRAs. It is noted that the proposed MDRA features the advantages of low profile, simple structure, wide bandwidth and stable radiation pattern. Due to the symmetrical structure, the proposed MDRA has a lower cross-polarization level at the operating band. The design achieves broadband performance through coupling effects between subwavelength DRA arrays, offering a novel approach to address bandwidth limitations. Furthermore, while [20, 21] implemented metasurface properties by adding metal patches on the resonator surface, the proposed method directly realizes wideband functionality through the inherent material properties and periodic arrangement of dielectric resonators.

IV. CONCLUSION

In this paper, a novel wideband MDRA is presented based on metamaterial technology. By constructing a subwavelength resonant unit array, the bandwidth limitations of conventional DRAs have been successfully overcome. The MDRA employs a 4×4 periodically arranged dielectric resonator array, which is fed by a microstrip-slot configuration. Experimental verification demonstrates that the proposed MDRA achieves a wideband -10 dB impedance bandwidth of 36% (1.88-2.71 GHz) with a peak gain of 7.69 dBi and a stable radiation

Table 2: Comparison of proposed MDRA and previous wideband DRAs

Ref.	**Type of Structure**	**BW (%)**	**f_r (GHz)**	**ε_r**	**Size (λ0)**	**Peak Gain (dBi)**	**Complexity**	**Radiation Pattern**
[7]	Asymmetrical T-shaped with trapezoidal probe feeding	75.08	6.1	9.8	0.14×0.48×0.26	7.35	Medium	Unstable broadside
[8]	Triangular DRA	47.4	5.68	10	0.096×0.35×0.35	6.5	Simple	Unstable broadside
[10]	Rectangular DRA	34	2.6	10.2	2.27×2.27×1.45	9.1	Complex	Unstable broadside
[11]	Cup-shaped DRA	29	3.5	4.3	0.25×0.25×0.23		Medium	Stable
[16]	2×2 Cylindrical DRA array	13.7	8	12	1.89×1.89×0.24	17.8	Simple	Unstable broadside
[20]	DRA with a top-loaded rotatable anisotropic metasurface	9.5	6.8	20.5	0.88×0.63×0.072	5.57	Complex	Stable
[21]	DRA with metasurface patches and shorting walls	17.2	1.9	15	0.32×0.32×0.044	6.6	Complex	Stable
This Work	**4×4 meta-dielectric resonator**	**36**	**2.33**	**9.8**	**0.4×0.4×0.116**	**7.69**	**Simple**	**Stable**

λ0 denotes free space wavelength at center frequency

pattern. Compared with existing dielectric resonator antennas, the proposed MDRA utilizes a subwavelength resonator unit array, exhibiting advantages of low profile, simple structure, wide bandwidth and stable radiation performance. These characteristics make it particularly suitable for application scenarios with stringent requirements on antenna integration and radiation performance, including 5G mobile terminals and IoT devices.

REFERENCES

[1] W. Hong, Z. H. Jiang, C. Yu, P. Chen, Z. Yu, H. Zhang, B. Yang, X. Pang, M. Jiang, Y. Cheng, M. K. Taher Al-Nuaimi, Y. Zhang, J. Chen, and S. He, "Multibeam antenna technologies for 5G wireless communications," *IEEE Trans. Antennas Propag*, vol. 65, no. 12, pp. 6231-6249, Dec. 2017.

[2] L. Wang, Y.-X. Guo, and W.-X. Sheng, "Wideband high-gain 60-GHz LTCC L-probe patch antenna array with a soft surface," *IEEE Trans. Antennas Propag.*, vol. 61, no. 4, pp. 1802-1809, Apr. 2013.

[3] K. Fan, Z.-C. Hao, and Q. Yuan, "A low-profile wideband substrate integrated waveguide cavity-backed E-shaped patch antenna for the QLINKPAN applications," *IEEE Trans. Antennas Propag.*, vol. 65, no. 11, pp. 5667-5676, Nov. 2017.

[4] J. Sun, A. Li, and K.-M. Luk, "A high-gain millimeter-wave magneto-electric dipole array with packaged microstrip line feed network," *IEEE Antennas Wireless Propag. Lett.*, vol. 19, no. 10, pp. 1669-1673, Oct. 2020.

[5] J. Yin, Q. Wu, C. Yu, H. Wang, and W. Hong, "Broadband symmetrical E-shaped patch antenna with multimode resonance for 5G millimeter wave applications," *IEEE Trans. Antennas Propag.*, vol. 67, no. 7, pp. 4474-4483, July 2019.

[6] X. Liang and T. A. Denidni, "H-shaped dielectric resonator antenna for wideband applications," *IEEE Antennas Wireless Propag. Lett.*, vol. 7, pp. 163-166, 2008.

[7] Y. Gao, Z. Feng, and L. Zhang, "Compact asymmetrical T-shaped dielectric resonator antenna for broadband applications," *IEEE Trans. Antennas Propag.*, vol. 60, no. 3, pp. 1611-1615, Mar. 2012.

[8] S. Maity and B. Gupta, "Experimental investigations on wideband triangular dielectric resonator antenna," *IEEE Trans. Antennas Propag.*, vol. 64, no. 12, pp. 5483-5486, Dec. 2016.

[9] T. Yang, J. Ren, B. Zhang, Y.-T. Liu, T. Ma, and Y. Yin, "Wideband diversity cylindrical dielectric resonator antenna based on multimode resonance," *IEEE Antennas Wireless Propag. Lett.*, vol. 22, no. 9, pp. 2205-2209, Sep. 2023.

[10] H. Liu, H. Tian, L. Liu, and L. Feng, "Co-design of wideband filtering dielectric resonator antenna with high gain," *IEEE Trans. Circuits Syst. II Exp. Briefs*, vol. 69, no. 3, pp. 1064-1068, Mar. 2022.

[11] S. Zheng, Z.-Y. Zhang, X. Chen, and A. A. Kishk, "Wideband monopole-like cup dielectric resonator antenna with coil feeding structure," *IEEE Trans. Antennas Propag.*, vol. 70, no. 8, pp. 7118-7123, Aug. 2022.

[12] X. S. Fang, L. P. Weng, and Z. Fan, "Design of the wideband and low-height omnidirectional cylindrical dielectric resonator antenna using arced-apertures feeding," *IEEE Access*, vol. 11, pp. 20128-20135, 2023.

[13] A. Gaonkar, M. Ayyappan, and P. Patel, "A novel fractal RDRA for C-band applications," *IEEE Trans. Compon., Packag., Manuf. Technol*., vol. 13, no. 7, pp. 995-1002, July 2023.

[14] W. Luo, Y. Feng, Y. Ren, and B. Yin, "A novel wideband fractal rectangular dielectric resonator antenna with improved radiation performance," *AEU-Int. J. Electron. Commun.*, vol. 142, pp. 153-184, Dec. 2021.

[15] S. Dhar, R. Ghatak, B. Gupta, and D. R. Poddar, "A wideband Minkowski fractal dielectric resonator antenna," *IEEE Trans. Antennas Propag.*, vol. 61, no. 6, pp. 2895-2903, June 2013.

[16] Q. Wu, H. Li, S.-W. Wong, Z. Zhang, and Y. He, "A simple cylindrical dielectric resonator antenna based on high-order mode with stable high gain," *IEEE Antennas Wireless Propag. Lett.*, vol. 23, no. 11, pp. 3476-3480, Nov. 2024.

[17] M. K. Saleem, M. A. S. Alkanhal, and A. F. Sheta, "Two element dielectric resonator antenna with beam switching," *Applied Computational Electromagnetics Society (ACES) Journal*, vol. 30, no. 11, pp. 1209-1214, Aug. 2021.

[18] X.-Y. Dong, W.-W. Yang, H. Tang, and J.-X. Chen, "Wideband low profile dielectric resonator antenna with a lattice structure," *Electron. Lett.,* vol. 53, no. 19, pp. 1289-1290, Sep. 2017.

[19] M. Martinis, L. Bernard, K. Mahdjoubi, R. Sauleau, and S. Collardey, "Wideband antenna in cavity based on metasurfaces," *IEEE Antennas Wireless Propag. Lett.*, vol. 15, pp. 1053-1056, 2016.

[20] X. Shi, C.-W. Shen, Y.-H. Ke, and J.-X. Chen, "A frequency-tunable dielectric resonator antenna with rotatable anisotropic metasurface," *IEEE Antennas Wireless Propag. Lett.*, vol. 23, no. 1, pp. 429-433, Jan. 2024.

[21] S.-K. Zhao, N.-W. Liu, Q. Chen, G. Fu, and X.-P. Chen, "A low-profile dielectric resonator antenna with compact-size and wide bandwidth by using metasurface," *IEEE Access*, vol. 9, pp. 29819-29826, 2021.

Wenke Jiang was born in 1998. He received his B.S. degree from Henan Polytechnic University, Jiaozuo, China, in 2022. He is currently pursuing his M.S. degree at Anhui University. His current research interests include dielectric resonator antenna and millimeter-wave antenna.

Guanghui Xu was born in 1986. He received the B.E. degree from Anhui Jianzhu University, Hefei, China, in 2009, the M.E. degree from Shenzhen University, Shenzhen, China, in 2012, and the Ph.D. degree from the Department of Electronic Engineering, Shanghai Jiao Tong University, Shanghai, China, in 2019. His research interests include millimeter-wave (mm-wave) antenna and reconfigurable antennas.

Yanbin Luo received the B.S. degree from the China University of Mining and Technology, Xuzhou, China, in 2015. He is currently pursuing the Ph.D. degree with the Beijing University of Posts and Telecommunications, Beijing, China. His research interests include graphene/GaAs nanowire photodetectors, graphene reconfigurable antennas, wideband antennas and miniaturized antennas.

Zhixiang Huang was born in 1979. He received the B.S. and Ph.D. degrees from Anhui University, Hefei, China, in 2002 and 2007, respectively. His research interests include theoretical and computational research in electromagnetics and imaging, focusing on multiphysics and interdisciplinary research, and fundamental and applied aspects in metamaterials and active metamaterials.

Wei Wang received the Ph.D. degree in navigation, guidance, and control from Harbin Engineering University (HEU), Harbin, China, in 2005. He was a Post-Doctoral Research Associate at Harbin Institute of Technology, Harbin, from July 2006 to April 2009. His current research interests include location, mapping, and image processing.

Mouping Jin received the Ph.D. degree in electromagnetic field and microwave technology from Xidian University, Xi'an, China, in 2000. His current research interests include antenna systems and microwave passive devices.

Hong-Li Peng was born in Shangluo, China, in 1966. He received the B.S., M.S., and Ph.D. degrees from Xidian University, Xi'an, China, in 1988, 1991, and 2005, respectively. His current research interests mainly include tunable RF and microwave passive circuits research, reconfigurable compact antennas/array analysis and design, and spatial wireless channel modeling.

A Novel Matching Technique for Microstrip Feeds using Optimized Tapering

Nasim Zahra[1,2], Inam Elahi Rana[3], Farooq Mukhtar[1], and Mahrukh Khan[4]

[1]Department of Electrical Engineering
University of Engineering and Technology, Lahore, 54890, Pakistan
nasimzahra132@hotmail.com, mukhtar.farooq@uet.edu.pk

[2]Department of Electrical, Electronics and Computer Systems
University of Sargodha, 40162, Pakistan
nasim.zahra@uos.edu.pk

[3]Bismillah Electronics
Lahore, 54600, Pakistan
ierana@biselectronics.net

[4]Electrical and Computer Engineering Department, The College of New Jersey
Ewing, NJ 08628, USA
khanm@tcnj.edu

***Abstract* –** This paper presents an efficient impedance matching technique for microstrip feed structures, providing a practical solution for seamless connector integration in high-frequency systems. Unlike conventional approaches that assume predefined connector compatibility, this method allows adaptation to various connector constraints without requiring major structural modifications. A linearly tapered microstrip feed with tapered substrate is proposed to ensure stable impedance matching, reduce signal reflection, and enhance overall system performance. The technique is demonstrated on a fabricated substrate-integrated waveguide antenna, utilizing a Rogers RT/Duroid 5880 substrate configured for 50 Ω impedance and adapted for integration with a specific coaxial connector. Experimental validation confirms excellent agreement between simulated and measured results, verifying its effectiveness in achieving impedance matching, minimizing return loss, and ensuring seamless integration with the connector while preserving radiation characteristics. This work presents a versatile feed design approach that addresses a key challenge in RF and microwave engineering, paving the way for improved performance and broader applicability in advanced communication systems and integrated circuit applications.

***Index Terms* –** 5G antenna, impedance matching technique, microstrip feed, microstrip transition, substrate-integrated waveguide, tapered microstrip.

I. INTRODUCTION

The increasing demand for high-performance microwave and RF systems has driven extensive research into impedance-matching techniques for microstrip feed structures. Efficient impedance matching is critical for ensuring minimal signal reflection and optimal power transfer, particularly in high-frequency applications. A key challenge arises when microstrip feeds must interface with standard coaxial connectors, such as SMA connectors, whose dimensional constraints often lead to impedance mismatches with conventional microstrip feeds, thereby degrading overall system performance. At high frequencies, the coaxial connector pin becomes too thin for effective connection to the structure due to its small diameter, which prevents the wave from being launched efficiently.

Existing approaches to microstrip-to-coaxial transitions have primarily focused on either waveguide-based transformations or direct microstrip-to-coaxial transitions. Waveguide-based transitions [1–9] offer high performance but may require additional components, leading to increased bulk, sensitivity to manufacturing variations, precise alignment requirements, and added fabrication complexity. Since most electronic systems are equipped with coaxial ports, they are generally preferred over waveguide ports to simplify integration, making a direct microstrip-compatible transition more desirable. However, direct microstrip-to-coaxial transitions [10–11] typically assume predefined connector compatibility,

Submitted On: December 26, 2024
Accepted On: April 23, 2025

https://doi.org/10.13052/2025.ACES.J.400508

Table 1: Comparison of transition techniques

Parameter	Waveguide-Based [1–9]	Direct Coaxial [10–11]	Proposed Work
Bandwidth	Narrowband (cutoff-limited)	Wideband (connector-limited)	Wideband (connector-limited)
Adaptability	Fixed dimensions (e.g., WR-90)	Connector specific	Connector-adaptable
Extra components for Impedance Matching	Stepped ridges [9, 12] & impedance transformers [13]	Simple or Radial stubs [14]	None
Fabrication	Complex – requires precise alignment, mode converters, & adapters	Low to Moderate – might involve simple or radial stub etching	Simple
Scalability	Suited to standards (e.g., X-band)	challenges for miniaturization	scalable for next gen. systems
Sensitivity to manufacturing tolerances	High	Low	Low
Connector Compatibility	Low – Need for specialized interfaces	Good – integrates with predefined connectors	High – adaptive for integration with available connectors.

restricting their adaptability to varying design constraints. Moreover, techniques using stepped ridges [9, 12], impedance transformers [13], and radial stubs [14] improve impedance matching but do not specifically address the integration challenges imposed by connector dimensional limitations. Also, fixed connector-specific designs require structural redesign for evolving miniaturized standards (5G/6G), highlighting scalability challenges. This gap motivates the development of a compact, adaptable, and fabrication-friendly impedance-matching technique for microstrip feeds that ensures seamless microstrip-to-coaxial integration without requiring significant structural modifications.

In response, this work introduces a novel impedance-matching technique based on an optimized linearly tapered microstrip transition with tapered substrate. This approach minimizes signal reflection and preserves signal integrity while adapting the feed to the physical constraints imposed by available connectors. The method offers a direct and efficient solution, ensuring wideband performance without adding fabrication complexity. The primary contributions of this study include the development of the optimized tapered transition and the elimination of additional matching components. Experimental validation confirms strong agreement between simulated and measured results. Table 1 presents a comparative summary of different transition techniques.

The remainder of this paper is organized as follows. Section II presents the design methodology and theoretical formulation, detailing the development of the optimized transition. Section III discusses simulation and experimental results that confirm the efficacy of the proposed approach. Finally, section IV concludes the paper with a summary of key findings and future direction.

II. PROPOSED MICROSTRIP FEED DESIGN

In this work, a microstrip feed is designed for integration with a substrate-integrated waveguide (SIW) antenna fabricated on the same substrate. Among various SIW feed structures [15], the microstrip feed is selected for its extensive use in planar circuit designs and its ability to offer broad bandwidth coverage across the entire SIW spectrum. Design equations from [16] are employed to calculate the microstrip width (w) based on a given substrate height (h) and the targeted port impedance. The conventional microstrip feed, as described in [10], is carefully configured to match the port impedance with its characteristic impedance (Z_o), thereby ensuring optimal power transfer and minimal signal reflection, using the formulations presented in [11]. Specifically, equations from [16] indicate that the microstrip trace width at the port interface should be W_{t1} for a Rogers RT/Duroid 5880 substrate of height h_f and a target impedance of 50 Ω. Furthermore, the optimum taper length and corresponding terminal width for the transition to the SIW are computed to be L_{fs} and W_{t2}, respectively, using the formulas from [11]. Figure 1 illustrates the fabricated conventional microstrip feed design integrated with the SIW antenna.

However, the conventional microstrip feed dimensions, W_{t1} and h_f, are incompatible with the available 50 Ω SMA840A-0000 connector. To ensure connector compatibility while preserving a 50 Ω port impedance, the substrate thickness should be reduced to 20 mils (denoted as h_1), and the corresponding microstrip width is recalculated as W_1 using the formula in [16]. It is essential that the transition to W_1 instead of W_{t1} and from h_f to h_1 occurs gradually rather than abruptly. In pursuit of this, the subsequent formulas and procedures are applied to optimize the tapered length.

A. Secondary taper for microstrip feed

The objective is to design a secondary taper for an already fabricated microstrip feed, which originally tapers from W_{t1} to W_{t2} in width and with a constant substrate height of h_f. The goal is to achieve SMA connector compatibility by applying another taper to reduce the substrate height to h_1 and microstrip width to W_1

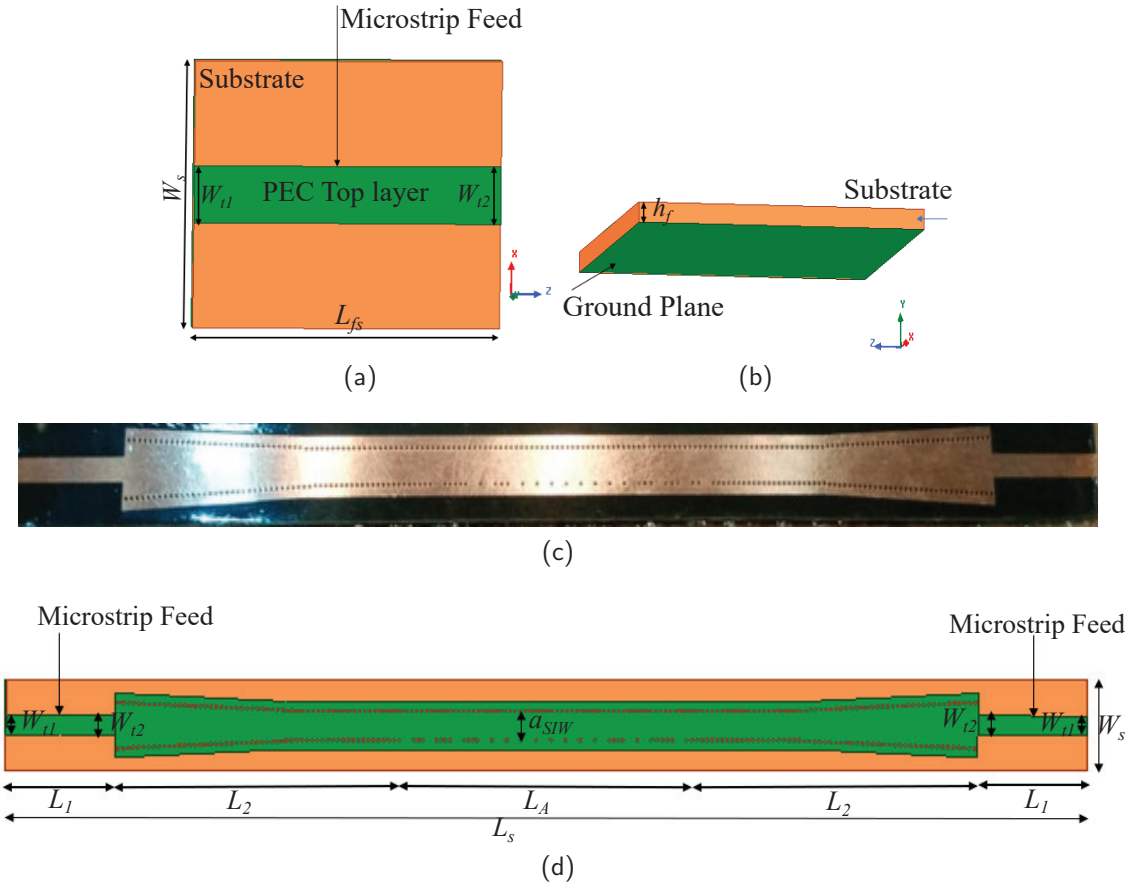

Fig. 1. Conventional simple tapered microstrip feed design to planar rectangular waveguide or SIW: (a) Top view, (b) Oblique View, (c) Fabricated feed integrated with SIW antenna [17], and (d) Feed part indicated by L_1 on both ends of the antenna [17].

gradually, ensuring that the impedance is matched and S_{11} is minimized below -10 dB.

1. Parameters and formulation

- Width at $z = 0$: $W_1 = 1.578\,\text{mm}$
- Substrate height at $z = 0$: $h_1 = 0.508\,\text{mm}$
- Width at $z = L$: $W_{t1} \leq w(L) \leq W_{t2}$
- Substrate height at $z = L$: $h_2 = 1.575\,\text{mm}$
- Length of taper L: Unknown but constrained by $0 < L \leq L_{fp}$
- Microstrip Impedance Formula: The characteristic impedance Z_o for a microstrip line, based on the variable width $w(z)$ and substrate height $h(z)$, is approximated from [16] as follows:

$$Z_o(z) = \begin{cases} \dfrac{60}{\sqrt{\varepsilon_e}} \ln\left(8\dfrac{h(z)}{w(z)} + 0.25\dfrac{w(z)}{h(z)}\right), & \text{for } \dfrac{w}{h} \leq 1 \\ \dfrac{120\pi}{\sqrt{\varepsilon_e}\left[\dfrac{w(z)}{h(z)} + 1.393 + 0.667\ln\left(\dfrac{w(z)}{h(z)} + 1.444\right)\right]}, & \text{for } \dfrac{w}{h} \geq 1 \end{cases} \quad (1)$$

where $w(z)$ is the microstrip width at position z, $h(z)$ is the substrate height at position z, and ε_e is the effective dielectric constant of the substrate.

- Linear Taper Functions: The microstrip width and substrate height taper linearly from $z = 0$ to $z = L$ as follows:

$$w(z) = W_1 + \left(\frac{w(L) - W_1}{L}\right) z, \quad (2)$$

where $W_{t1} \leq w(L) \leq W_{t2}$.

$$h(z) = h_1 + \left(\frac{h_2 - h_1}{L}\right) z. \quad (3)$$

- Reflection Coefficient $S_{11}(z)$: $S_{11}(z)$ is based on the mismatch between $Z_o(z)$ along the taper and the 50 Ω SMA connector:

$$S_{11}(z) = \frac{Z_o(z) - 50}{Z_o(z) + 50}. \quad (4)$$

B. Optimization problem

So the optimization problem can be expressed as:

$$\min_{L, w(L)} \int_0^L |S_{11}(z)|^2 \, dz \quad (5)$$

Table 2: Key design parameters and dimensions

Parameter	Symbol	Value (mm)	Parameter	Symbol	Value (mm)
Substrate Integrated Waveguide Antenna					
Microstrip to SIW transition	L_1	28.22	SIW to antenna section transition	L_2	74
Radiating Section (antenna length)	L_A	75	Substrate Thickness	h_s	1.575
Substrate Length	L_s	279.44	Substrate Width	W_s	23
Ground Plane Length	L_g	L_s	Ground Plane Width	W_g	W_s
SIW width in radiating section	a_{SIW}	8.32			
Simple Tapered Microstrip Feed					
Feed section Length	L_{fs}	L_1	Tapered Section Length	L_t	L_{fs}
Tapered Width (initial)	W_{t1}	4.9	Tapered Width (final)	W_{t2}	5
Tapered section substrate height	h_f	h_s			
Proposed Tapered Microstrip Feed					
Feed section Length	L_{fp}	L_1	Secondary Tapered Section Length	L	∼10.4 (optimal)
Secondary Tapered section Width (initial)	W_1	1.578	Secondary Tapered section Width (final)	$W_2 = w(L)$	∼4.932 (optimal)
Secondary Tapered section substrate height (initial)	h_1	0.508	Secondary Tapered section substrate height (final)	h_2	h_s

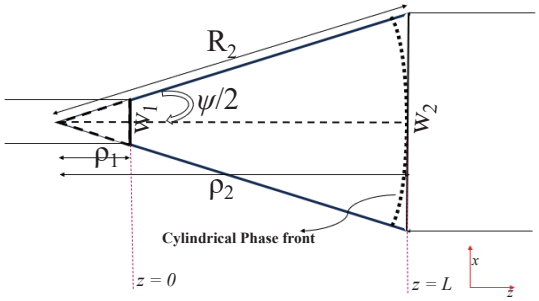

Fig. 2. Top view of E-plane horn-like configuration for proposed tapered microstrip feed.

Subject to:

$$W_{t1} \leq w(L) \leq W_{t2}\,, \tag{6}$$

$$0 < L \leq L_{fp}\,, \tag{7}$$

$$S_{11(dB)}(z) < -10\ \text{dB} \quad \forall z \in [0, L], \tag{8}$$

$$\psi \leq \psi_{\max} = 4\tan^{-1}\left(\frac{\pi}{2k_{\text{eff}} w(L)}\right). \tag{9}$$

where, $k_{\text{eff}} = k_o\sqrt{\varepsilon_r}$. k_o is free space wavelength and ε_r is the relative permittivity of dielectric.

Constraint (9) is derived to minimize the phase error associated with the cylindrical phase front of the wave launched into the waveguide as the proposed feed resembles an E-plane horn. Referring to Fig. 2, the derivation of (9) is provided in appendix A.

C. Optimization procedure

- Initial Guess: Start with an initial estimate for L and $w(L)$, ensuring $W_{t1} \leq w(L) \leq W_{t2}$.
- Iterative Optimization:
  1. Calculate $Z_o(z)$ along the taper.
  2. Compute $S_{11}(z)$ from impedance mismatch.
  3. Adjust L and $w(L)$ iteratively to minimize $S_{11}(z)$.
- Convergence Criteria: Stop when $S_{11}(z)$ stays below -10 dB across the taper, ensuring impedance matching.

This optimization problem can be solved using numerical methods or simulation tools to find the optimal

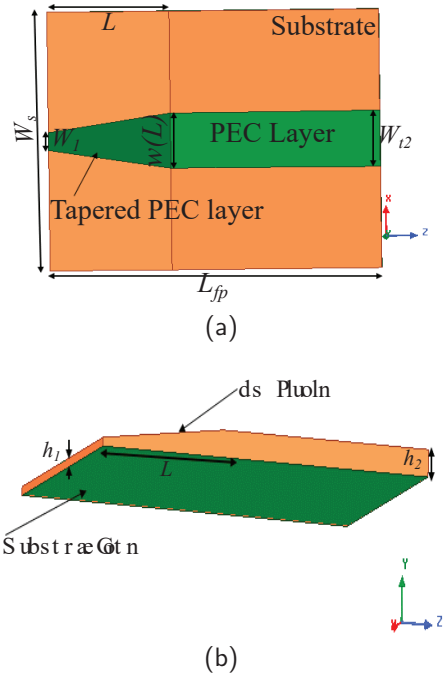

Fig. 3. Proposed tapered microstrip feed design for a planar rectangular waveguide or SIW: (a) Top view and (b) Oblique View.

taper length L that minimizes the impedance mismatch across the taper. The length for this gradual change is determined through optimization conducted in HFSS software, fine-tuning the design for its intended performance, and is found to be 10.4 mm. Figure 3 illustrates the proposed microstrip design along with all dimensions for the SIW antenna fabricated in [17]. Table 2 presents the key design parameters and dimensions across different structures.

III. IMPLEMENTATION AND RESULTS

The proposed microstrip feed is implemented using a cost-effective approach with minimal modifications. The process begins with the selective removal of the copper cladding on the top layer up to a length L. This is followed by carefully reducing the substrate height through mechanical polishing to create a tapered profile over the same length. To restore conductivity in the modified area and ensure continuous signal transmission, readily available materials such as copper strips, foils, or adhesive copper tape are applied. Figure 4 shows the proposed feed design integrated with the SIW antenna, demonstrating its successful implementation and connection to a standard SMA connector, specifically the SMA840A, which is well-suited for high-frequency applications up to 26.5 GHz. It should be noted that the signal pin of the connector is not in contact with the tapered section of the substrate at a single point; instead, it is properly soldered beneath the entire length of the pin.

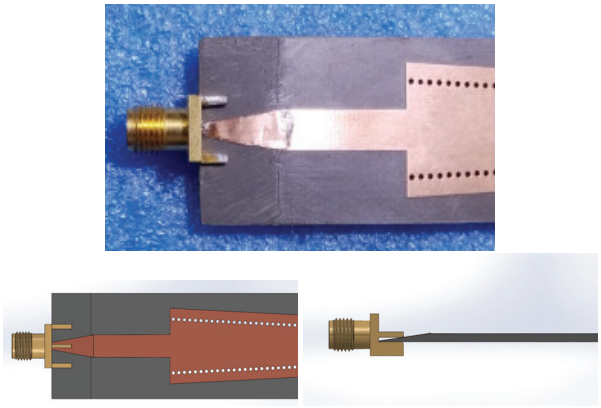

Fig. 4. Visualization of the proposed microstrip feed design for SIW leaky wave antenna fabricated in [17].

The two different feed structures shown in Figs. 1 and 3 are individually simulated using HFSS software, incorporating connector model of specific dimensions. However, when evaluating connector compatibility, it becomes evident that the proposed tapered feed aligns well with the SMA840A connector utilizing a substrate height of 20 mils (h_1) at the port end. In contrast, the simple tapered microstrip feed employs a substrate height of h_f. Figure 5 (a) illustrates that the simple tapered microstrip feed (SM) performs poorly when connected to the connector, whereas the proposed tapered microstrip feed (TM) excels in this context. The S_{11} parameter of the TM remains well below -10 dB across a wide bandwidth, indicating minimal reflection. In contrast, the SM exhibits S_{11} well above -10 dB, implying higher reflection. Additionally, the S_{21} parameter of the TM is close to 0 dB over the frequency range, signifying efficient power transfer. Conversely, the SM shows S_{21} below -10 dB, indicating minimal power transfer.

Simulated and measured S_{11} for the antenna integrated with the proposed feed and the connector are shown in Fig. 5 (b). It can be observed that S_{11} is below -10 dB for nearly the entire frequency range of beam steering of the antenna, indicating minimal reflection. Radiation characteristics of the antenna, as illustrated in Fig. 6, reveal good agreement between expected and measured normalized directivity (dB). Figure 7 (a) displays the simulated and measured gain of the antenna and demonstrates a consistent trend. Minor discrepancies

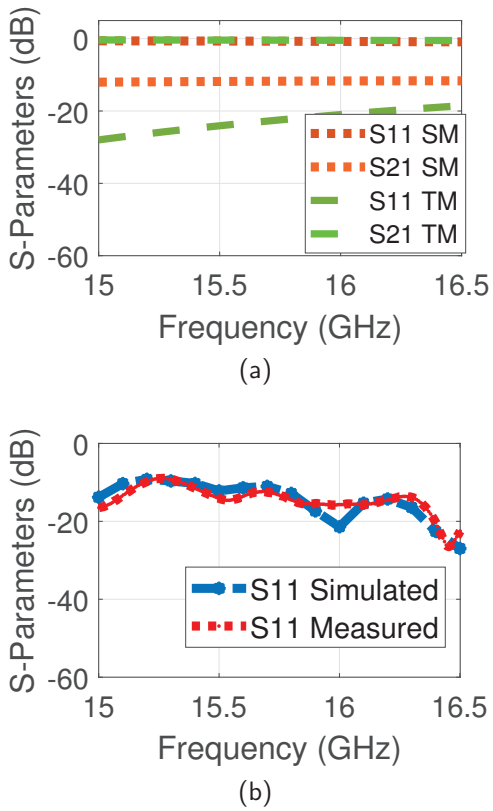

Fig. 5. S-parameters of: (a) simple and the proposed tapered microstrip feed designs (SM and TM) simulated as independent feed structures and (b) the SIW leaky-wave antenna integrated with the proposed feed design (TM).

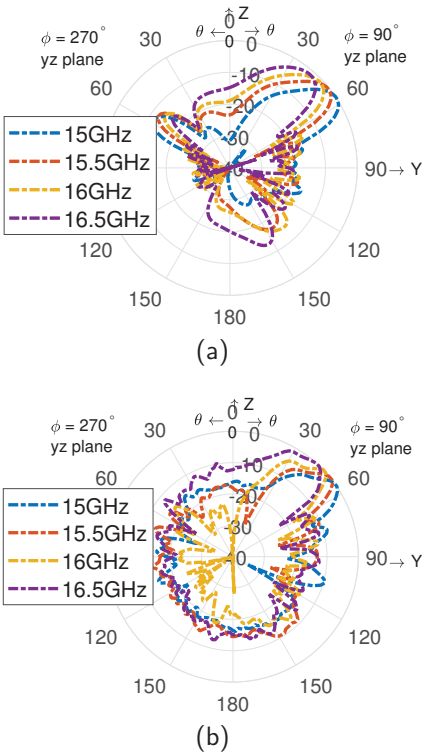

Fig. 6. Radiation patterns in the elevation plane for the SIW leaky-wave antenna demonstrating radiation perseverance: (a) Expected and (b) Measured.

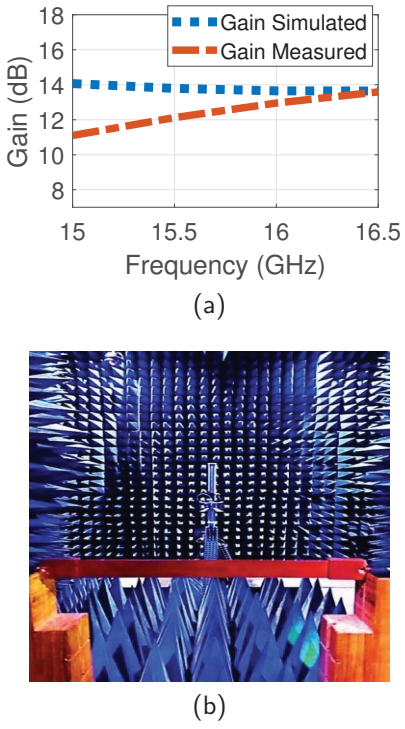

Fig. 7. (a) Simulated and measured gain results and (b) Measurement setup in anechoic chamber.

are due to fabrication tolerances and measurement uncertainties. Figure 7 (b) shows the anechoic chamber setup used for these measurements.

IV. CONCLUSION

This paper presents a microstrip feed design that overcomes connector compatibility challenges, ensuring seamless integration and optimal performance in high-frequency systems. By incorporating a linearly tapered microstrip transition with tapered substrate, the design achieves enhanced impedance matching and reduced signal reflection. Unlike conventional methods that assume predefined connector compatibility, this approach provides a practical and low-cost solution for adapting microstrip feeds to dimensional constraints of connectors without requiring major structural modifications. Demonstrated on a fabricated antenna intended for base station applications, the proposed feed design effectively resolves unforeseen mismatches while maintaining radiation characteristics. Though the study focuses on the SMA840A-0000 connector, the impedance matching approach applies to other connectors intended for specific frequency ranges with suitable parameter adjustments. This ensures broader applicability in RF and microwave systems, including 5G/6G antennas, integrated circuits, and signal interconnects, where precise impedance control and seamless connector integration are critical for reliable performance.

A potential future direction in microstrip design for connector compatibility is to reduce the substrate height by tapering it upward from the ground layer to the top, instead of tapering it downward.

ACKNOWLEDGMENT

The authors acknowledge Bismillah Electronics, Lahore, Pakistan, for their assistance in the manufacturing process. Appreciation is extended to Rogers Corporation, USA, for supplying the PCB sheets, and to NUST RIMMS, Pakistan, for providing the measurement facilities.

APPENDIX A

Phase Error Minimization

The constraint (9) arises from the cylindrical phase front of the wave launched into the waveguide. Because the feed resembles an E-plane horn, the wave launched into the waveguide will have a cylindrical phase front. Consequently, adhering to (9) is essential to preserve radiation performance. The radiation pattern resembles that of an aperture with a constant phase field, provided the phase error at the aperture edges does not exceed $\pm\frac{\pi}{4}$ [18].

Referring to Fig. 2, the relationship between the widths and radii of curvature at the taper is established,

leading to the following equations:

$$\rho_1 = \frac{w_1}{2\tan(\psi/2)}. \quad \text{(A1)}$$

$$\rho_2 = \frac{w_2}{2\tan(\psi/2)}. \quad \text{(A2)}$$

From these relationships, the width ratio of the microstrip taper is written:

$$\frac{w_2}{w_1} = \frac{\rho_2}{\rho_1}. \quad \text{(A3)}$$

Additionally, the following relationship describes the angle ψ in terms of the radius of curvature R_2:

$$\frac{w_2}{2R_2} = \sin\left(\frac{\psi}{2}\right). \quad \text{(A4)}$$

Substituting the values of R_2 and ρ_2 into inequality from [18]:

$$(R_2 - \rho_2)k_{\text{eff}} \leq \frac{\pi}{4}. \quad \text{(A5)}$$

The subsequent constraint for w_2 is as follows:

$$\left(\frac{w_2}{2\sin(\psi/2)} - \frac{w_2}{2\tan(\psi/2)}\right)k_{\text{eff}} \leq \frac{\pi}{4}.$$

$$\psi \leq \psi_{\max} = 4\tan^{-1}\left(\frac{\pi}{2w_2k_{\text{eff}}}\right). \quad \text{(A6)}$$

Furthermore, the length of the tapered line from this point can be expressed as:

$$\rho_2 - \rho_1 = \frac{w_2 - w_1}{2\tan(\psi/2)}. \quad \text{(A7)}$$

REFERENCES

[1] Y.-C. Leong and S. Weinreb, "Full band waveguide-to-microstrip probe transitions," in *IEEE MTT-S Int. Microw. Symp. Dig.*, Anaheim, CA, USA, vol. 4, pp. 1435-1438, 13–19 June 1999.

[2] E. S. Li, G.-X. Tong, and D. C. Niu, "Full W-band waveguide-to-microstrip transition with new E-plane probe," *IEEE Microw. Wireless Compon. Lett.*, vol. 23, pp. 4-6, 2013.

[3] A. U. Zaman, V. Vassilev, and P.-S. Kildal, "Millimeter wave E-plane transition from waveguide to microstrip line with large substrate size related to MMIC integration," *IEEE Microw. Wireless Compon. Lett.*, vol. 26, pp. 481-484, 2016.

[4] M. H. Yang, J. Xu, Q. Zhao, G. P. Li, and L. Peng, "Compact, broadband waveguide-to-microstrip transition using slotline antenna," in *Proc. 2010 Int. Conf. Microw. Millim. Wave Technol.*, Chengdu, China, pp. 744-747, 8–11 May 2010.

[5] Y. Zhang, J. A. Ruiz-Cruz, K. A. Zaki, and A. J. Piloto, "A waveguide to microstrip inline transition with very simple modular assembly," *IEEE Microw. Wireless Compon. Lett.*, vol. 20, pp. 480-482, 2010.

[6] J. Li, L. Li, Y. Qiao, J. Chen, J. Chen, and A. Zhang, "Full Ka band waveguide-to-microstrip inline transition design," *J. Infrared Millim. Terahertz Waves*, vol. 39, pp. 714-722, 2018.

[7] A. B. Granja, R. Jakoby, and A. Penirschke, "Outright W-band Chebyshev-based hollow waveguide to microstrip transition," in *Proc. 2017 42nd Int. Conf. Infrared Millim. Terahertz Waves (IRMMW-THz)*, Cancun, Mexico, 27 August-1 September 2017.

[8] A. U. Zaman, V. Vassilev, H. Zirath, and N. Rorsman, "Novel low-loss millimeter-wave transition from waveguide-to-microstrip line suitable for MMIC integration and packaging," *IEEE Microw. Wireless Compon. Lett.*, vol. 27, pp. 1098-1100, 2017.

[9] M. Simone, A. Fanti, G. Valente, G. Montisci, R. Ghiani, and G. Mazzarella, "A compact in-line waveguide-to-microstrip transition in the Q-band for radio astronomy applications," *Electronics*, vol. 7, p. 24, 2018.

[10] D. Deslandes and K. Wu, "Integrated microstrip and rectangular waveguide in planar form," *IEEE Microw. Wireless Compon. Lett.*, 11, pp. 68-70, 2001.

[11] D. Deslandes, "Design equations for tapered microstrip-to-substrate integrated waveguide transitions," in *IEEE MTT-S Int. Microwave Symp. Dig.*, pp. 704-707, 2010.

[12] W. Tang, J. Wang, X. Yan, J. Liu, X. Gao, L. Zhang, and T. J. Cui, "Broadband and high-efficiency excitation of spoof surface plasmon polaritons through rectangular waveguide," *Front. Phys.*, vol. 8, article 582692, 2020.

[13] J. M. Pérez-Escudero, A. E. Torres-García, R. Gonzalo, and I. Ederra,"A simplified design inline microstrip-to-waveguide transition," *Electronics*, vol. 7, 2018.

[14] S. Ladan, S. Hemour, and K. Wu, "A millimeter-wave wideband microstrip RF and DC grounding," in *Proc. 42nd Eur. Microw. Conf. (EuMC)*, Amsterdam, Netherlands, pp. 13-16, Oct. 2012.

[15] M. Bozzi, A. Georgiadis, and K. Wu, "Review of substrate-integrated waveguide circuits and antennas," *IET Microw. Antennas Propag.*, vol. 5, no. 8, pp. 909-920, 2011.

[16] D. M. Pozar, *Microwave Engineering*, 4th ed. Hoboken, NJ: John Wiley & Sons, pp. 147-149, 2012.

[17] N. Zahra, F. Mukhtar, I. E. Rana, and M. Khan, "Efficient numerical synthesis of radiation patterns using circuit model for substrate integrated waveguide leaky wave antennas," *IEEE Access*, pp. 54285-54298, 2024.

[18] Robert E. Collin, *Antennas and Radiowave Propagation*. New York, NY: McGraw-Hill, pp. 187-189, 1985.

Nasim Zahra received her B.Sc. degree in Electrical Engineering from the University of Engineering and Technology Lahore (U.E.T Lahore), Lahore, Pakistan, in 2007, and the M.Sc. degree in Electrical Engineering (Electronics and Telecommunication) from the University of Engineering and Technology Lahore (U.E.T Lahore), Lahore, Pakistan, in 2013. Currently pursuing a Ph.D. degree in Electrical Engineering from the University of Engineering and Technology Lahore (U.E.T Lahore), Lahore, Pakistan. Research interests include antenna theory and design, array signal processing, reconfigurable antennas, electromagnetics, and electromagnetic compatibility. She also serves as assistant professor at college of engineering and technology, AIC, University of Sargodha.

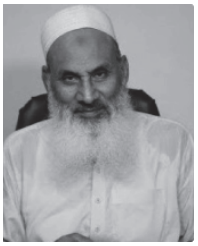

Inam Elahi Rana received his B.Sc. degree in Electrical Engineering from U.E.T, Lahore, in 1974 and joined Suparco. After receiving a scholarship from Suparco, he joined UCLA and earned M.S. and Ph.D. degrees in 1977 and 1979, respectively. Having had a mixed career in both industry and academia, he has been involved in the design and development of several projects for different organizations. He has taught various courses in electromagnetics, antennas, electromagnetic compatibility, and microwave engineering at different universities, both at undergraduate and graduate levels. Currently, he serves as the CEO of Bismillah Electronics Lahore.

Farooq Mukhtar received his B.Sc. degree in Electrical Engineering from the University of Engineering and Technology (U.E.T), Lahore, Pakistan, in 2007 and started his career as a tutor for high-frequency courses and as a Lab-Engineer for electromagnetic compatibility (EMC) testing at the same university. He then earned an M.Sc. in Microwave Engineering and a Dr.-Ing. degree under Prof. Peter Russer from the Technical University Munich, Germany, in 2009 and 2014. During that time, he worked as a part-time scientific co-worker at the Institute for Nanoelectronics on algorithms for Brune's synthesis of multiport circuits and conducted tutorials on the post-graduate course 'Quantum Nanoelectronics.' Currently, he is an assistant professor at U.E.T, Lahore, working on high-frequency topics: leaky wave and configurable antennas, filters, and metamaterials. He is also consulting Smart Wires, Inc. through Powersoft19 in the areas of electromagnetic simulations and compatibility.

Mahrukh Khan received her Bachelor of Science and Master of Science degrees in electrical engineering from the University of Engineering and Technology, Lahore, Pakistan, in 2007 and 2011, respectively. She earned her Ph.D. degree in electrical engineering from the University of Missouri-Kansas City (UMKC) in 2017. Before joining TCNJ, Dr. Khan served as an Assistant Research Professor at the Missouri Institute of Defense and Energy (MIDE) at UMKC. Prior to that, she was a Post-Doctoral Fellow in UMKC's Micro and Nano-Technology Lab from January 2018 to December 2019.

Dr. Khan is an assistant professor at The College of New Jersey (TCNJ) and co-director of the Microwave and Wireless Communication Lab (MWCL). She has published over 30 research articles and conference papers, receiving more than 250 citations. A 2022 IEEE APS Young Professional Ambassador, she has also earned recognition in the 2015 Altair FEKO student competition and the UMKC SGS fellowship. She serves as a reviewer for leading journals, including IEEE Antennas and Propagation Magazine and IET Microwaves, Antennas, and Propagation. Dr. Khan is a senior member of URSI and an active member of IEEE Young Professionals and IEEE Women in Engineering Societies.

A Miniaturized Wide-stopband Wide-passband Cavity Filter with Two Asymmetric Stepped Probes

Panfeng Bao[1,2], Yulun Wu[3], Yufeng Shen[1], Jinrong Liu[1], and Yaqi Li[3]

[1]Changsha Aeronautical Vocational and Technical College
Changsha 410000, China
223121110079@njust.edu.cn, 15116220284@163.com, longyong2025@163.com

[2]Nanjing University of Science and Technology
Nanjing 210000, China

[3]Northeastern University at Qinhuangdao
Qinhuangdao 066004, China
202112694@stu.neu.edu.cn, 202112708@stu.neu.edu.cn

***Abstract* –** In this paper, a miniaturized cavity filter with wide-stopband and wide-passband is proposed. Because of the bended stub-loaded resonator (BSLR), the proposed cavity filter successfully excites three TEM modes, namely TEM-I, TEM-II and TEM-III. The low-frequency transmission zero (LFTZ) is generated by the lateral probe, and the high-frequency transmission zero (HFTZ) is generated by the lateral stub. The lateral metal cylinder can concentrate the electric field of the stray mode, leading to a high suppression level. The asymmetric vertical arrangement of the probes can suppress the fundamental TE_{101} mode and several high-order modes. Therefore, a stopband with a bandwidth of 2.02 times the center frequency is formed. The proposed cavity filter has a bandwidth of 42% and an electrical size of $0.26\lambda_g \times 0.25\lambda_g \times 0.22\lambda_g$. It has several advantages applied to the 5G communication system.

***Index Terms* –** Cavity filter, miniaturization, wide-band, wide-stopband.

I. INTRODUCTION

With the development of modern communication technology, cavity filters have become an indispensable part of microwave systems. Cavity filters are gradually moving towards wide-stopband, high-power capacity and low insertion loss.

Nowadays, researchers and engineers are exploring ways to design multi-mode cavity filters. The first way is to cascade several single cavities whose resonant modes are generally TE or TM modes [1–3]. In [4], a rectangular cavity filter is proposed. This cavity filter uses two pairs of degenerate modes to excite a quadruple-mode passband response. The proposed cavity has a relative bandwidth of 1.35% and a high-quality factor of 14500. In [5], a cross-coupled cavity filter is proposed. A thin cavity is used to introduce a cross coupling between two main resonant cavities, the TE_{101} mode of this thin cavity has been set away from the center frequency. The proposed cavity filter realizes a bandwidth of 1.84% and a stopband with a bandwidth of 1.68 times the center frequency. It is worth noting that the first way can also be used to design the filtering antennas. In [6], several cavities with TE_{101} modes are cascaded as the horn of the proposed filtering antenna. The proposed filtering antenna has a bandwidth of 4% and a directional realized gain of 13.5 dBi.

The second way of designing cavity filters is to load multi-mode resonators into the resonant cavity [7–10]. In [11], several short-circuited metal cylinders are loaded inside the cavity to realize a triple-TEM-mode response. Although the performance of the cavity filter proposed in [11] is mediocre, it fully proves the feasibility of the second way. In [12] and [13], the method of cascading several resonators has been used to achieve multiple resonances. They all achieve high-selectivity and a high stopband suppression level. In [14], the ring-shaped microstrip lines are used to couple several coaxial resonators. The proposed cavity filter has 2% bandwidth and extremely low return loss. The dielectric coaxial resonators can also be used in cavity filters. In [15], a pair of dielectric coaxial resonators are used to make a wide-stopband and a high suppression level. The proposed cavity filter realizes a bandwidth of 9.6% and a stopband with a bandwidth of 4.5 times the center frequency. Like the first way, the second way can also be used to design filtering antennas. In [16], a coaxial filtering antenna is proposed with extreme high-selectivity of

Submitted On: March 13, 2025
Accepted On: May 16, 2025

https://doi.org/10.13052/2025.ACES.J.400509

2300 dB/GHz. The proposed filtering antenna uses dual-post coaxial resonators to transversely cascade. In [17], a filtering antenna is successfully designed by combining the first way and the second way. The proposed filtering antenna uses a main resonant cavity with a TE_{102} mode, a TE_{012} mode and a TEM mode.

For the cavity filters, the above works can hardly realize wide-passband and wide-stopband simultaneously. In this paper, a compact cavity filter with wide-passband and wide-stopband is proposed. The proposed filter uses three TEM modes to form a 42% passband. A special lateral metal cylinder and the asymmetric vertical arrangement of two probes are used to generate a stopband with a bandwidth of 2.02 times the center frequency. Due to the resonant frequencies of the TEM modes being lower than the resonant frequency of the fundamental TE_{101} mode, the proposed cavity filter can also achieve miniaturization. Moreover, the equivalent circuit is also proposed [18] for engineering applications.

II. DESIGN AND ANALYSIS

A. Physical structure of the proposed cavity filter

The structure of the proposed cavity filter is shown in Fig. 1. The proposed cavity filter is composed of a rectangular cavity, a bended stub-loaded resonator (BSLR), a perturbed metal cylinder and two stepped probes. The BSLR consists of a lateral stub and a longitudinal stub. Two mutually perpendicular probes are loaded inside the cavity to couple with the BSLR. The stepped metal cylinders are loaded onto the terminals of the probes. A lateral perturbed metal cylinder is loaded onto the sidewall of the cavity.

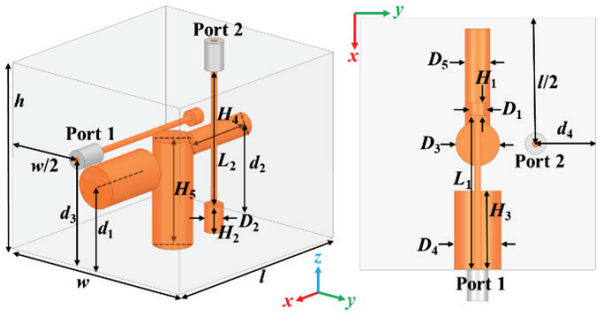

Fig. 1. Physical structure of the proposed cavity bandpass filter: (a) Three-dimensional view and (b) *xoy* plane (unit: *mm*): $h = 40$, $w = 45$, $l = 48$, $D_1 = 2.5$, $D_2 = 2$, $D_3 = 4.2$, $D_4 = 4.5$, $d_1 = 17$, $d_2 = 20.1$, $d_3 = 25.5$, $d_4 = 11.4$, $H_1 = 1.7$, $H_2 = 5.7$, $H_3 = 13.5$, $H_4 = 17.7$, $H_5 = 22.9$, $L_1 = 22.3$, $L_2 = 29.1$.

B. Evolution steps of the proposed cavity filter

In order to describe more clearly the design process of the proposed cavity filter, the evolution steps of the proposed cavity filter are displayed in Fig. 2. The reflection coefficients and the insertion losses are displayed in Figs. 3 (a) and (b), respectively.

The interior of the BPF.I is loaded with a longitudinal SLR and two mutually perpendicular probes. The BPF.I has two TEM modes and a low-frequency transmission zero (LFTZ) The stopband is narrow and the high-frequency selectivity is poor. Moreover, the impedance matching greatly needs to be improved. Figure 6 (c) shows the electric-field distribution of the LFTZ. At the LFTZ, the electric-field energy concentrates on the lateral probe, so the transmission is almost zero.

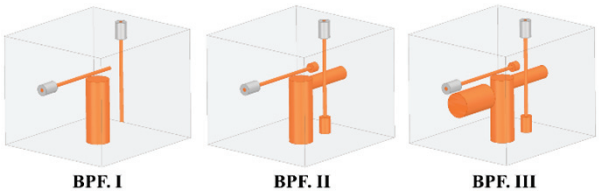

Fig. 2. Evolution steps of the proposed cavity filter.

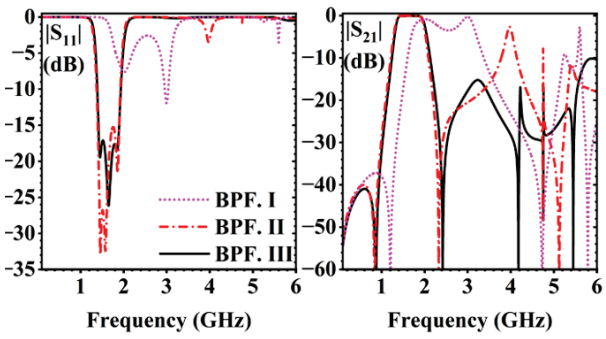

Fig. 3. S-parameters of the cavity filter mentioned in the evolution steps: (a) Reflection coefficients and (b) insertion losses.

After connecting a lateral stub to the longitudinal stub to form the BSLR, and loading stepped metal cylinders onto the terminals of two probes, the BPF.II is formed. Since the equivalent electrical length of the BSLR is smaller than the equivalent electrical length of the SLR in BPF.I, the center frequency of the passband moves towards low-frequency. The impedance matching has improved significantly because of the stepped impedance characteristics. Three TEM modes, namely TEM-I, TEM-II and TEM-III, are successfully generated at 1.46 GHz, 1.58 GHz and 1.87 GHz, respectively. Figure 4 shows the electric-field distribution of TEM-I, TEM-II and TEM-III in the *xoz* and *yoz* planes. Selectivity is improved significantly by introducing a new

high-frequency transmission zero (HFTZ) at 2.38 GHz. However, the stopband of BPF.II is still narrow because a stray mode, namely TEM-IV, is generated at 3.98 GHz. Figure 6 (d) shows the electric-field distribution of the HFTZ. At the HFTZ, the electric-field energy concentrates on the lateral metal cylinder, so the transmission is almost zero.

After loading a lateral perturbed metal cylinder onto the side wall of the cavity, the proposed cavity filter named BPF.III is formed. The TEM-IV is suppressed greatly by the perturbed metal cylinder. The origin and the suppressed TEM-IV are displayed in Figs. 6 (a) and (b), respectively. It can be seen that the perturbed metal cylinder can pull and focus most electric-field energy, so the electric-field energy cannot be coupled well from the lateral probe to the longitudinal probe. The stopband range increases to 3.4 GHz (2.2-5.6 GHz). The maximum return loss is lower than -18 dB. It is obvious that the proposed cavity filter has good impedance matching and wide-stopband.

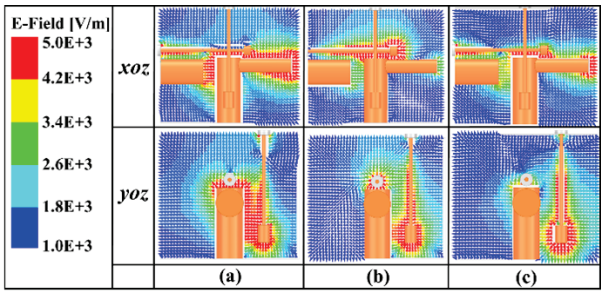

Fig. 4. Electric-field distributions of the proposed cavity filter: (a) TEM-I, (b) TEM-II, and (c) TEM-III.

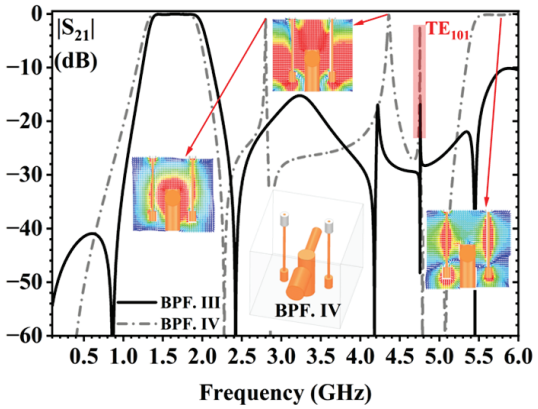

Fig. 5. Insertion losses, physical structure and electric-field distributions of the BPF.III and BPF.IV.

C. Illustration of the arrangement of the probes

In order to explain the reason for the arrangement of the mutually vertical probes in the proposed cavity filter, a comparison of the insertion loss of the proposed filter and BPF.IV are displayed in Fig. 5. It can be seen that several transmission modes with symmetric electric field are successfully excited due to the parallel stepped probes of BPF.IV. Intuitively, these transmission modes are destroyed by mutually perpendicular probes. In order to quantitatively explain why these transmission modes collapse in the proposed cavity filter, the coupling intensity K is introduced, as shown in (1). $\mathbf{E_p}$ represents the electrical field distribution introduced by the probes. $\mathbf{E_m}$ represents the electrical field distribution of a certain order mode in the cavity filter. V represents the volume of the metal cavity. Clearly, the K of the proposed cavity filter is significantly less than the K of BPF.IV.

$$K = \frac{\iiint \mathbf{E_p} \cdot \mathbf{E_m} dV}{\sqrt{\iiint |\mathbf{E_p}|^2 dV \cdot \iiint |\mathbf{E_m}|^2 dV}}. \tag{1}$$

To further prove the accuracy of the above principle, Figs. 6 (e) and (f) show the electric-field distribution of the TE_{101} mode in the proposed cavity filter and BPF.IV. In the proposed cavity filter, the direction of the electric field of the probe is perpendicular to the spatial distribution of the electric field of the TE_{101} mode, resulting in zero overlap integration of the two field distributions. This phenomenon leads to discontinuities in the TE_{101} mode, making it not well excited.

D. Parameters analysis of the proposed cavity filter

The S-parameters of the proposed cavity filter with different D_5, d_3 and H_4 are shown in Fig. 7. When the diameter of the lateral cylinder of BSLR D_5 increases from 3.8 mm to 5.8 mm, the center frequency of the passband moves to high-frequency. When the length of the lateral probe increases from 25 mm to 26 mm, the LFTZ moves to low-frequency. When the length of the lateral cylinder of BSLR H_4 increases, the HFTZ moves to high-frequency. The quality factor Q of TEM-I increases, the Q of TEM-II remains unchanged and the Q of TEM-III decreases. The Q of TEM-II remains stable due to the weak electric field around its lateral stub, where length variations minimally affect the characteristics of TEM-II.

E. Equivalent circuit of the proposed cavity filter

The equivalent circuit of the proposed cavity filter is also analyzed. The electrical impedance Z of a cylinder can be calculated by (2). The capacitor C can be calculated by (3). Parameter a denotes the axial length of the cylindrical cavity. Parameter r denotes the radius of the cylinder. The resonant frequency can be calculated by (4). The parameter p denotes the order of the proposed cavity filter. Parameters and denote the i-th inductor and j-th capacitor, while m and n represent the total number of inductors and capacitors, respectively.

Insertion loss and impedance matching of the proposed cavity filter were simulated using the Advanced

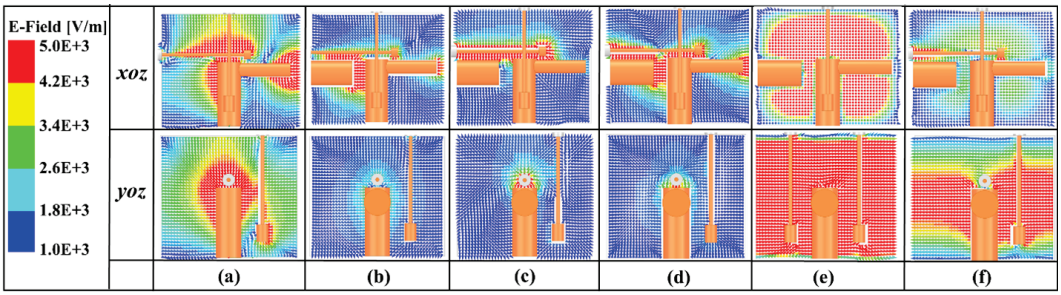

Fig. 6. Electric-field distributions of BPF.II, the proposed cavity filter and BPF.IV: (a) Electric field distribution of TEM-IV of BPF.II, (b) electric-field distribution of TEM-IV of the proposed cavity filter, (c) electric-field distribution at LFTZ, (d) electric-field distribution at HFTZ, (e) electric-field distribution of TE_{101} mode of BPF.IV, and (f) electric-field distribution of TE_{101} mode of the proposed cavity filter.

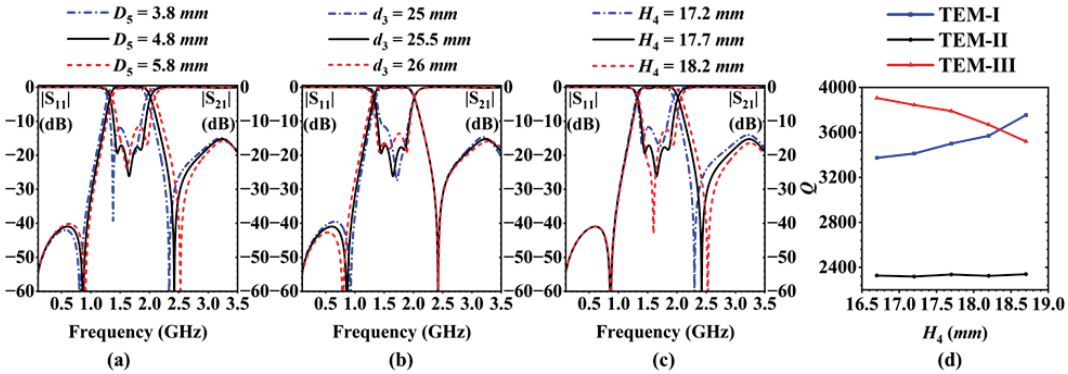

Fig. 7. Relative parameters of the proposed cavity filter: (a) S-parameters with different D_5, (b) S-parameters with different d_3, (c) S-parameters with different H_4, and (d) quality factor Q with different H_4.

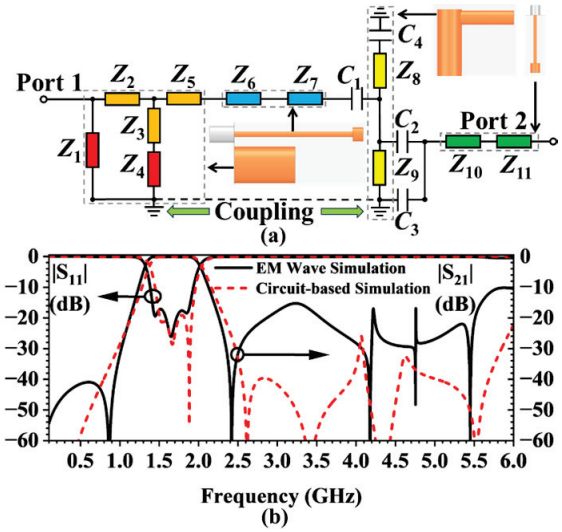

Fig. 8. Relative information about the equivalent circuit of the proposed cavity filter: (a) Equivalent circuit of the proposed cavity filter and (b) S-parameters of the EM wave simulation and circuit-based simulation.

Design System software based on the equivalent circuit, and the results are compared with those from electromagnetic (EM) wave simulation, as depicted in Fig. 8 (b). The center frequencies, the impedance matchings and the insertion losses in the passband of the two simulation methods are basically the same. Each part of the proposed cavity filter can be matched to the corresponding impedance value in the equivalent circuit. Therefore, the equivalent circuit has good consistency with the proposed EM model.

$$Z = 60 \ln\left(\frac{a}{r}\right), \tag{2}$$

$$C = \frac{\pi r}{30c}\left[\frac{\pi r}{4d} + \ln\left(\frac{a-r}{d}\right)\right], \tag{3}$$

$$f = \frac{p}{2\pi\sqrt{\sum_{i=1}^{m} L_i \sum_{j=1}^{n} C_j}}. \tag{4}$$

III. RESULTS AND DISCUSSION

To verify the rationality of the design, the proposed cavity filter is fabricated and then tested by the vector

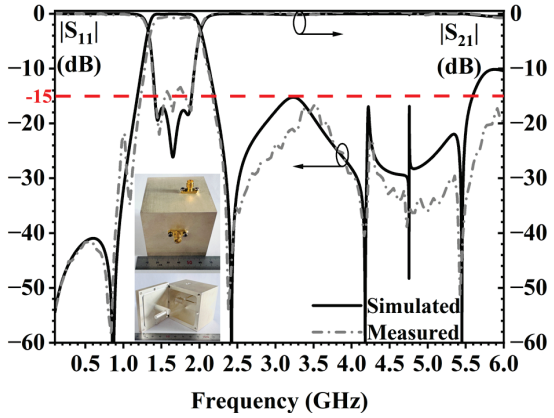

Fig. 9. Simulated and measured S-parameters (inset photograph of the fabrication).

Table 1: Comparison with previous works

Ref.	Electrical Size	BW	SR
[4]	$1.1\lambda_g \times 1.1\lambda_g \times 1.15\lambda_g$	1.35%	$0.08f_0$
[5]	$1.87\lambda_g \times 0.34\lambda_g \times 0.75\lambda_g$	1.84%	$1.68f_0$
[9]	$0.41\lambda_g \times 0.2\lambda_g \times 0.41\lambda_g$	58%	$0.63f_0$
[11]	$0.12\lambda_g \times 0.12\lambda_g \times 0.08\lambda_g$	4.64%	$0.25f_0$
[15]	$0.76\lambda_g \times 1.01\lambda_g \times 0.08\lambda_g$	9.6%	$4.5f_0$
Pro.	$0.26\lambda_g \times 0.25\lambda_g \times 0.22\lambda_g$	42%	$2.02f_0$

BW: relative bandwidth, SR: stopband range, f_0: center frequency.

network analyzer. Figure 9 shows the simulated and tested results, with a photograph of the fabricated cavity filter. The material of the fabrication is aluminum-plated silver. The proposed cavity filter achieves miniaturization with a compact size of $0.26\lambda_g \times 0.25\lambda_g \times 0.22\lambda_g$. It can be seen that the tested results are roughly consistent with the simulation ones. The measured impedance matching deviates slightly from the simulated results, which can be attributed to inaccuracies in the fabrication process and limitations of the testing equipment. The measured S-parameters show that the proposed cavity filter has three resonant frequencies (1.47 GHz, 1.65 GHz and 1.89 GHz). The operating bandwidth is 42% from 1.33 GHz to 2.03 GHz and the insertion loss of the passband is 0.6 dB. All stopband suppression levels are higher than 15 dB. For the fabrication, the bandwidth of the stopband is 3.8 GHz from 2.2 GHz to 6 GHz. Table 1 compares the proposed cavity filter and previous works. It can be seen that the proposed cavity filter has good performance in all aspects. Consequently, the proposed cavity filter achieves miniaturization, demonstrating superior filtering response and wide-stopband characteristics.

IV. CONCLUSION

A compact wide-passband wide-stopband cavity filter is proposed in this paper. The proposed cavity filter utilizing a BSLR stimulates three TEM modes, with the lateral probe creating LFTZ and the lateral stub generating HFTZ. Stray mode suppression is enhanced through electric-field concentration via lateral metal cylinders, while the asymmetric and vertical probes inhibit both fundamental TE_{101} and higher-order modes, forming a stopband with bandwidth of 2.02 times center frequencies. Featuring a wide-bandwidth of 42% and compact electrical dimensions, the design demonstrates engineering reliability through its proposed equivalent circuit. This solution offers significant advantages for 5G systems, including compact size, wide-stopband coverage and broad passband.

ACKNOWLEDGMENT

This research was funded by Hunan Provincial Department of Education Excellent Youth Project (Grant No. 23B1104). APC was funded by Hunan Provincial Department of Education.

REFERENCES

[1] Z.-C. Guo, L. Zhu, and S.-W. Wong, "Synthesis of transversal bandpass filters on stacked rectangular H-plane waveguide cavities," *IEEE Trans. Microwave Theory Tech.*, vol. 67, no. 9, pp. 3651-3660, Sep. 2019.

[2] S. Bastioli, R. Snyder, C. Tomassoni, and V. de la Rubia, "Direct-coupled TE-TM waveguide cavities," *IEEE Microwave Wireless Tech. Lett.*, vol. 33, no. 6, pp. 819-822, June 2023.

[3] E. López-Oliver and C. Tomassoni, "3-D-printed dual-mode filter using an ellipsoidal cavity with asymmetric responses," *IEEE Microwave Wireless Compon. Lett.*, vol. 31, no. 6, pp. 670-673, June 2021.

[4] G. Basavarajappa and R. R. Mansour, "A high-Q quadruple-mode rectangular waveguide resonator," *IEEE Microwave Wireless Compon. Lett.*, vol. 29, no. 5, pp. 324-326, May 2019.

[5] Z.-C. Guo, L.-Y. Li, A. Wang, X. Wang, and L. Zhu, "Cross-coupled waveguide bandpass filters with inline footprint and extremely flexible transmission zeros," *IEEE Microwave Wireless Tech. Lett.*, vol. 35, no. 5, pp. 525-528, May 2025.

[6] K. Mohan Patnaik, G. Basavarajappa, and H. Sigmarsson, "An innovative design methodology of a novel multifunctional all-pole filtering horn antenna," *IEEE Microwave Wireless Tech. Lett.*, vol. 35, no. 1, pp. 35-38, Jan. 2025.

[7] Z.-C. Zhang, X.-Z. Yu, S.-W. Wong, B.-X. Zhao, J.-Y. Lin, X. Zhang, and K.-W. Tam, "Miniaturization of triple-mode wideband bandpass filters," *IEEE Trans. Compon. Packag. Technol.*, vol. 12, no. 8, pp. 1368-1374, Aug. 2022.

[8] M. Y. Sandhu, S. Afridi, A. Lamecki, R. Gómez-García, and M. Mrozowski, "Miniaturized inline bandpass filters based on triple-mode integrated coaxial-waveguide resonators," *IEEE Access*, vol. 11, pp. 81196-81204, 2023.

[9] M. Hameed, G. Xiao, and L. Qiu, "Triple-mode wideband bandpass filter using simple perturbation in metallic-loaded rectangular waveguide cavity," *Electromagnetics*, vol. 38, no. 5, pp. 303-316, 2018.

[10] Z.-M. Li, Y.-Q. He, J.-Y. Lin, Z.-C. Zhang, X. Zhang, L. Zhu, and S.-W. Wong, "*X*-band air-filled coaxial bandpass filter with wideband input-reflectionless performance," *Microwave Opt. Technol. Lett.*, vol. 67, Jan. 2025.

[11] Y. Wu, L. Jin, and Z. Lu, "A triple-quasi-TEM-resonance dielectric cavity for bandpass filter design," *IEEE Microwave Wireless Compon. Lett.*, vol. 32, no. 8, pp. 950-952, Aug. 2022.

[12] M. Y. Sandhu, A. Lamecki, R. Gómez-García, and M. Mrozowski, "Compact quasi-elliptic-type inline waveguide bandpass filters with nonlinear frequency-variant couplings," *IEEE Trans. Microwave Theory Tech.*, vol. 71, no. 11, pp. 4933-4946, Nov. 2023.

[13] M. R. Salehi, B. Ghalamkari, and A. K. Nia, "Design and fabrication of a five-order narrowband coaxial filter based on cross coupling and non-cross-coupling methods," *IETE Journal of Research*, vol. 70, no. 11, pp. 8110-8117, 2024.

[14] M. Salek, Y. J. Wang, and M. Lancaster, "Two-GHz hybrid coaxial bandpass filter fabricated by stereolithography 3-D printing," *Int. J. RF Microw. Comput. Aided Eng.*, vol. 31, 2021.

[15] K. Zhao and D. Psychogiou, "Spurious suppression techniques for 3-D printed coaxial resonator bandpass filters," *IEEE Microwave Wireless Compon. Lett.*, vol. 32, no. 1, pp. 33-36, Jan. 2022.

[16] J. Ma, K.-R. Xiang, and F.-C. Chen, "A high-selectivity filtering antenna based on dual-post coaxial resonators," *IEEE Trans. Antennas Propag.*, vol. 72, no. 2, pp. 1899-1904, Feb. 2024.

[17] K.-R. Xiang, F.-C. Chen, Q.-X. Chu, and Q. Xue, "High selectivity waveguide filtering antennas using mixed-mode cavity resonator," *IEEE Trans. Microwave Theory Tech.*, vol. 70, no. 9, pp. 4297-4307, Sep. 2022.

[18] B. Dwivedy and S. K. Behera, "Modelling, analysis and testing of an active element based wideband frequency tunable compact rat-race hybrid," *AEU-Int. J. Electron. C.*, vol. 103, pp. 24-31, May 2019.

Panfeng Bao is currently pursuing the Ph.D. degree in Armament Science and Technology at the State Key Laboratory of Transient Physics, Nanjing University of Science and Technology, Nanjing, China. Since 2017, he has been with Changsha Aeronautical Vocational and Technical College, Changsha, China, where he is currently a lecturer with the School of Aeronautical Mechanical Manufacturing. His research interests focus on dynamic response analysis of weapon systems, mechanical fault diagnosis under extreme conditions, RF device design and RF communication in weapon systems.

Yulun Wu is currently pursuing the B.E. degree in Northeastern University at Qinhuangdao, Qinhuangdao, China. Since 2022, he has been working on RF devices and has published in several conferences and journals. His current interests include terahertz communication and microwave devices and systems.

Yufeng Shen is an Associate Professor at Changsha Aeronautical Vocational and Technical College, Changsha, China. His main research focus is aircraft digital manufacturing technology.

Jinrong Liu is an Experimental Engineer at Changsha Aeronautical Vocational and Technical College, Changsha, China. He is a recipient of the Hunan Province May 1st Labor Medal and National Technical Expert, with main research focus on mechatronics technology.

Yaqi Li is currently pursuing the B.E. degree at Northeastern University in Qinhuangdao, Qinhuangdao, China. Since 2022, she has conducted in-depth research on the design and application of microwave passive integrated devices such as coaxial cavity filters and power dividers.

Design and Analysis of High-thrust Magnetic Field Modulation Transverse Flux Motor for New Energy High-voltage Disconnector

Yi Su, Lei Gao, Wei Huang, Jian Qin, and Yufeng Lu

Guangxi Key Laboratory of Intelligent Control and Maintenance of Power Equipment
Electric Power Research Institute of Guangxi Power Grid Co. Ltd., Nanning 530023, China
935665054@qq.com, suyi935665054@126.com, huang_w.sy@gx.csg.cn, qin_jian@gx.csg.cn, lu_yf.sy@gx.csg.cn

***Abstract* –** In order to solve the problem of traditional high-voltage disconnector mechanism jamming and improve the thrust of the drive mechanism, a direct-drive magnetic field modulation transverse flux motor (MFM-TFM) is proposed in this paper. First, the three-dimensional structure of MFM-TFM is introduced. The expression of air gap flux density is derived according to the permeability method. The air gap flux density of the lower air gap dominated by the sixth harmonic is modulated into the air gap flux density of the upper air gap dominated by the fifth harmonic. The increase in the amplitude of low-order harmonics can increase the average thrust. Secondly, the upper and lower air gap widths, permanent magnets, iron cores, pole shoes and modulators are optimized. The optimized motor has good no-load back EMF and current waveform sinusoidality. Through core lamination, the loss of the transverse flux motor is effectively reduced. The rated average thrust of the motor reaches 612.54 N. Finally, the prototype was manufactured and the experimental test platform was built. The thrust and back EMF were measured and compared with the experimental values to verify the rationality of the proposed topology and the accuracy of the calculated results.

***Index Terms* –** High thrust, magnetic field modulation, new energy high-voltage disconnector, optimized design, transverse flux motor.

I. INTRODUCTION

Permanent magnet linear synchronous motor (PMLSM) is often used as the core drive mechanism in various circumstances such as aerospace, medical equipment and power systems [1]. PMLSM has the advantages of simple structure and strong reliability [2]. In addition, due to the simple mover structure, PMLSM has a short response time [3]. Compared with the traditional electric excitation motors, PMLSM has no excitation winding copper loss, which makes it more efficient [4].

As a type of permanent magnet motor, servo PMLSM can accurately control the motor speed and movement distance. Therefore, servo PMLSM has important potential in the intelligent development of power systems [5]. In the operation of large power grids, servo motors serve as the driving core of high-voltage disconnectors. The servo motor drives the contact to move through the transmission mechanism to complete the opening and closing actions [6–8]. Since the high-voltage switch operating mechanism is in an inactive state for a long time, the influence of the external environment will cause the components to age [9–11]. At the same time, during the opening and closing process, the contacts often melt due to high temperature [12–14]. When the contacts move again, melting may cause problems such as mechanism jamming [15], which will cause the switch to fail to work. When the instantaneous thrust or torque generated by the servo motor is too small to drive the mechanism to move, the motor cannot rotate. Stalling will cause the motor to heat up severely, which will affect the safe operation of the power grid [16–17]. In addition, due to the low speed of the opening and closing process, the motor has a large power or torque, which will make the motor have a large volume and low power density.

At present, in order to increase the torque or thrust of the motor, the common method is to connect the servo motor to the mechanical gear. Although the mechanical gear has the function of amplifying the torque of the motor, it has friction loss. The gear needs to be frequently repaired and lubricated. Mechanical gears often have problems such as jamming or even freezing, which leads to high maintenance costs [18–20]. In order to increase the thrust or torque of the motor, the direct-drive magnetic field modulation transverse flux motor (MFM-TFM) has attracted much attention. The direct-drive transverse flux motor can be directly connected to the contact without other transmission mechanisms. It has the characteristics of simple structure and high efficiency [21]. At the same time, based on the principle of magnetic field modulation, low-speed motion is

Submitted On: September 2, 2024
Accepted On: January 7, 2025
https://doi.org/10.13052/2025.ACES.J.400510

converted into high-speed motion of the magnetic field, which effectively improves the power density of the magnetic field modulation motor.

The magnetic flux direction of the transverse flux motor is perpendicular to the direction of motion. The stator part of the motor can be laminated with silicon steel to reduce losses, which can improve the efficiency of the motor. The transverse flux linear motor is combined with a magnetic gear to form an MFM-TFM. In low-speed direct drive applications, the MFM-TFM has the characteristics of high-thrust density or torque density. However, there is no literature published on high-thrust MFM-TFMs for high-voltage disconnectors.

An MFM-TFM is proposed in this paper. Firstly, the three-dimensional structure of the direct-drive MFM-TFM is introduced. According to the permeance method, the air gap magnetomotive force and air gap permeance are given. The expression of air gap flux density is derived. The relationship between the number of low-order working harmonic pole pairs and the low-order working harmonic speed is studied. Secondly, the MFM-TFM structural parameters are optimized and designed. The effects of upper and lower air gap widths, permanent magnets, cores, pole shoes and modulator sizes on back EMF, thrust and thrust fluctuation are studied. The hysteresis loss, eddy current loss and additional loss of laminated core and non-laminated core are calculated and compared. Finally, the prototype is manufactured and the experimental test platform is built. The motor thrust and back EMF are measured and compared with the experimental values, which verifies the rationality of the proposed topology and the accuracy of the calculation results.

II. MFM-TFM TOPOLOGY AND WORKING PRINCIPLE

A. MFM-TFM topology

The three-dimensional structure of the direct-drive field modulation transverse flux motor is given in Figs. 1 and 2. The two-dimensional structure of the MFM-TFM is given in Figs. 3–5. The MFM-TFM mainly includes stator I, stator II and linear mover. Stator I is a segmented structure. The armature windings of phase A, phase B and phase C are installed in the slots of stator I. Inclined magnetic conductive materials and inclined non-magnetic conductive materials are installed in the middle mover. The magnetic conductive material is made of laminated silicon steel to effectively reduce the core loss. The non-magnetic conductive material is made of stainless steel. Stator II mainly has segmented core, PM and excitation winding. The excitation winding can change the size of the excitation magnetic field by changing the excitation current. The permanent magnet and the excitation winding are arranged alternately. Based on the

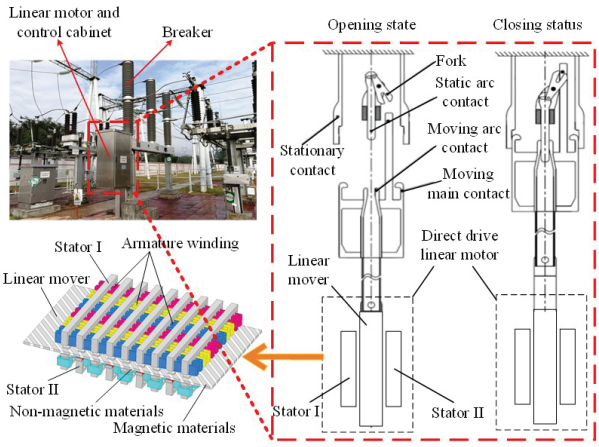

Fig. 1. MFM-TFM structure.

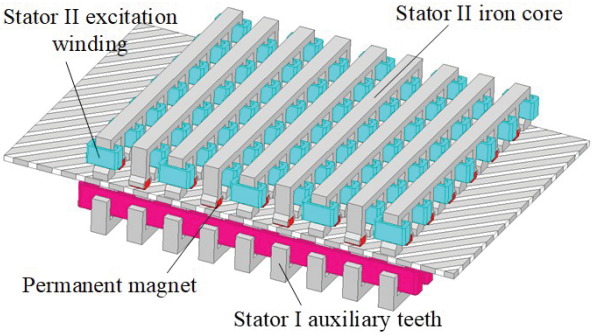

Fig. 2. Lower stator side of the 3D structure.

alternating arrangement, the leakage flux can be reduced. The air gap flux density is increased to make the motor power density higher. The detailed dimensional parameters of the MFM-TFM in the front view and oblique view are given in Figs. 6 and 7. The rated parameters and basic size parameters of MFM-TFM are shown in Table 1.

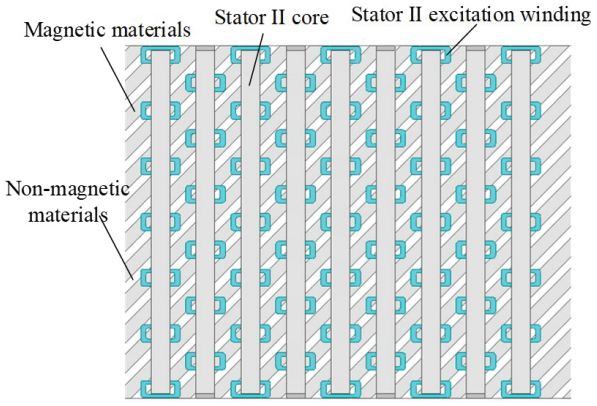

Fig. 3. 2D image of the lower stator side.

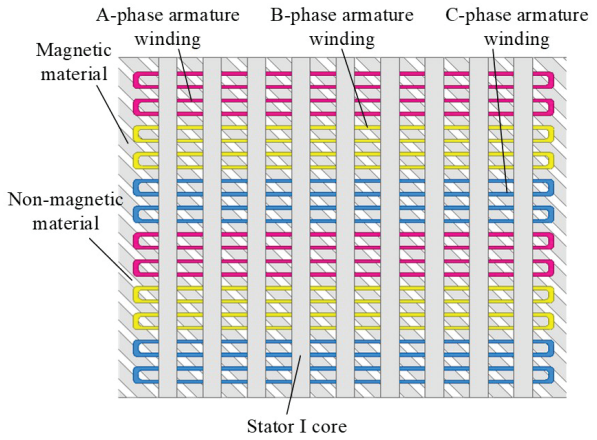

Fig. 4. 2D image of the upper stator side.

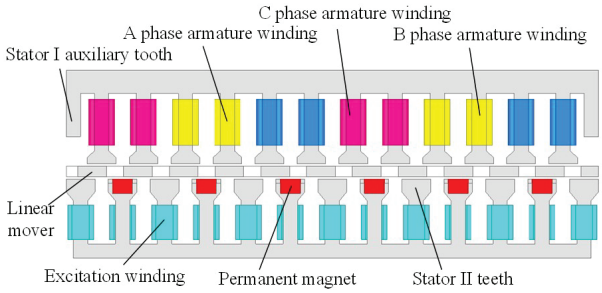

Fig. 5. Front view of MFM-TFM.

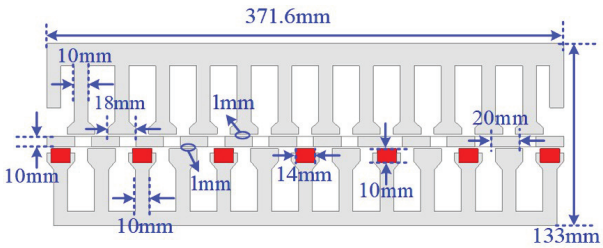

Fig. 6. Dimensions of front view.

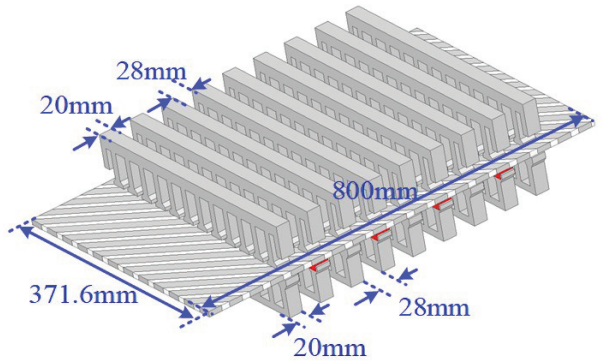

Fig. 7. Dimensions of oblique views.

Table 1: Rated parameters of the prototype

Parameter	Value	Parameter	Value
Rated thrust (N)	612.5	Rated current (A)	2
Linear speed (m/s)	1	Rated power (W)	612.5
Modulator pole number	11	Upper air gap width (mm)	1
Upper stator slot number	12	Lower air gap width (mm)	1
Upper stator poles	10	Lower stator pole number	12

Due to the inclined structure, when the stator moves linearly, the velocity component is generated in the direction of movement and the perpendicular direction of movement. When the mover moves, the changing magnetic flux is generated in the stator I core. The induced electromotive force is generated in the armature winding due to the changing magnetic flux, which is the working principle of MFM-TFM. Therefore, when the stator I armature winding is supplied with alternating three-phase voltage and current, a changing magnetic field is generated in the middle air gap. The mover generates thrust under the action of the magnetic field and moves linearly.

In the proposed MFM-TFM, the number of magnetic field pole pairs of the stator I armature winding is 5. The number of poles of the modulator is 11. The number of magnetic field pole pairs generated by PM and excitation winding is 6. The ratio of the number of modulator poles to the number of lower stator magnetic field pole pairs is 11:5. Therefore, the transmission ratio of MFM-TFM can be defined as 11:5. According to the magnetic field modulation principle, the speed of the mover is 5/11 of the speed of the stator I armature magnetic field. The thrust of the mover is 11/5 times that of the stator core I. Therefore, the thrust of the mover is effectively amplified. This is the fundamental reason why magnetic field modulation increases the thrust of the motor.

B. Calculation of air gap magnetic flux density based on permeability method

The total permeance per unit area of MFM-TFM can be expressed as:

$$\frac{1}{\Lambda(x,t)} = \frac{1}{\Lambda_{PM}} + \frac{1}{\Lambda_{ag}} + \frac{1}{\Lambda_{tr}(x,t)}, \tag{1}$$

where Λ_{PM} is the permeance per unit area of the permanent magnet, Λ_{ag} is the permeance per unit area of the air gap, $\Lambda_{tr}(x,t)$ is the permeance per unit area of the mover.

In the stator II of the MFM-TFM, the current of the DC excitation winding is adjusted to change the excitation magnetic field. The air gap flux density is adjusted to make the direction of the excitation magnetic field exactly opposite to the direction of the magnetic field

generated by the permanent magnet. The total permeance per unit area can be expressed by the Fourier series as equations (2), (3) and (4).

In equations (2), (3) and (4), Λ_0 is the DC part of the permeance per unit area,w_g is the width of MFM-TFM, v_t is the speed of the linear mover, x_0 is the initial position of the mover, N_m is the number of effective permeable materials of the modulator, Λ_m is the permeance of the modulator's tilted permeable material, Λ_n is the permeance of the modulator's tilted non-permeable material, w_m is the width of the modulator's tilted permeable material, w_n is the width of the modulator's tilted non-permeable material, l_t is the thickness of the modulator.

The magnetomotive force generated by stator II PM can also be expressed using Fourier series as equations (5) and (6).

In equations (5) and (6), B_r is the residual magnetism of PM, p_{PM} is the number of magnetic field pole pairs generated by PM.

Therefore, the air gap flux density can be expressed as equation (7):

$$\Lambda(x,t) = \Lambda_0 + \sum_{i=1}^{\infty} \Lambda_i \cos\left[iN_m \frac{2\pi}{w_g}(x - v_t t - x_0)\right]. \tag{2}$$

$$\Lambda_0 = \frac{N_m}{w_g}(\Lambda_m w_m + \Lambda_n w_n) = \frac{N_m \mu_0 w_m}{w_g\left(l_{gapu} + l_{gapl} + l_{PM}\right)} + \frac{N_m \mu_0 w_n}{w_g\left(l_{gapu} + l_{gapl} + l_{PM} + l_t\right)}. \tag{3}$$

$$\Lambda_i = \frac{2}{i\pi}(\Lambda_m - \Lambda_n)\sin\left(iN_m w_m \frac{\pi}{w_g}\right) = \frac{2}{i\pi}\left(\frac{\mu_0}{l_{gapu} + l_{gapl} + l_{PM}} - \frac{\mu_0}{l_{gapu} + l_{gapl} + l_{PM} + l_t}\right)\sin\left(iN_m w_m \frac{\pi}{w_g}\right). \tag{4}$$

$$F(x) = \sum_{j=1,3,5\cdots}^{\infty} \frac{4B_r l_{PM}}{j\mu_0 \pi}\cos\left(jp_{PM}\frac{2\pi x}{w_g}\right) = \sum_{j=1,3,5\cdots}^{\infty} \frac{2k}{j}\cos\left(jp_{PM}\frac{2\pi x}{w_g}\right). \tag{5}$$

$$k = \frac{2B_r l_{PM}}{\mu_0 \pi}. \tag{6}$$

$$\begin{aligned} B_\delta = F(x)\Lambda(x,t) = {} & 2k\Lambda_0 \cos\left(jp_{PM}\frac{2\pi x}{w_g}\right) + k\Lambda_1 \cos\left[\frac{2\pi(N_m + jp_{PM})}{w_g}\left(x - \frac{N_m v_t t + N_m x_0}{N_m + jp_{PM}}\right)\right] \\ & + k\Lambda_1 \cos\left[\frac{2\pi(N_m - jp_{PM})}{w_g}\left(x - \frac{N_m v_t t - N_m x_0}{N_m - jp_{PM}}\right)\right]. \end{aligned} \tag{7}$$

The main harmonic characteristics of the air gap flux density are shown in Table 2. Since the amplitude of low-order harmonics is much larger than that of high-order harmonics, the average thrust can be increased by increasing the amplitude of low-order harmonics. The relationship between the number of pole pairs of low-order harmonics and the speed is:

$$p_{PMeff} = |N_m - jp_{PM}|, \tag{8}$$

$$v_{PMeff} = \frac{N_m v_t}{N_m - jp_{PM}} = G_r v_t, \tag{9}$$

where p_{PMeff} is the pole pair number of the working harmonic, v_{PMeff} is the speed of the working harmonic, G_r is the transmission ratio.

Table 2: Harmonic distribution of main air gap magnetic flux density

Pole Pairs	Speed
jp_{PM}	0
$N_m + jp_{PM}$	$\frac{N_m v_t}{N_m + jp_{PM}}$
$\lvert N_m - jp_{PM}\rvert$	$\frac{N_m v_t}{N_m - jp_{PM}}$

The pole pitch of the working harmonic is:

$$\tau_{PMeff} = \frac{N_m w_n}{2(N_m - jp_{PM})} = \frac{1}{2}G_r w_n, \tag{10}$$

where τ_{PMeff} is the pole pitch of the working harmonic, w_n is the width of the modulator's tilted non-magnetic material.

The losses of the proposed MFM-TFM mainly include permanent magnet eddy current loss, core loss and copper loss. By increasing the armature current amplitude, the iron loss, copper loss, output power and efficiency of MFM-TFM are calculated. Iron loss mainly includes hysteresis loss, eddy current loss and additional loss, which can be expressed as:

$$p_{iron} = p_h + p_{ec} + p_e = k_h f B_m^{\alpha} + k_{ec} f^2 B_m^2 + k_e f^{1.5} B_m^{1.5}, \tag{11}$$

where k_h, k_{ec} and k_e are the hysteresis loss coefficient, eddy current loss coefficient and additional loss coefficient, $\alpha = 1.69$, $k_h = 32$, $k_{ec} = 0.13$, $k_e = 0.45$, B_m is the maximum magnetic density, f is the frequency.

Copper loss can be expressed as:

$$p_{cu} = MNI^2 R_{cu} = \frac{MNI^2 \rho_{cu} l_{cu}}{S_{cu}}, \tag{12}$$

where R_{cu} is the winding resistance, I is the current, ρ_{cu} is the copper resistivity, l_{cu} is the winding length, S_{cu} is the winding cross-sectional area, M is the number of slots, N is the number of winding turns.

III. MFM-TFM DESIGN AND OPTIMIZATION ANALYSIS

A. Calculation and analysis of air gap magnetic flux density based on finite element method

The air gap flux before and after modulation is calculated as shown in Figs. 8–11. The lower air gap flux and the upper air gap flux are shown in Figs. 8 and 10. The lower air gap flux in Fig. 8 is transformed by fast Fourier transform (FFT) to obtain the harmonic flux amplitude before modulation as shown in Fig. 9. The upper air gap flux in Fig. 10 is transformed by FFT to obtain the harmonic flux amplitude after modulation as shown in Fig. 11.

It can be seen in Fig. 9 that the 6th harmonic flux amplitude is the largest. This is mainly because the number of magnetic field pole pairs generated by the permanent magnet and the excitation winding of the lower stator is 6.

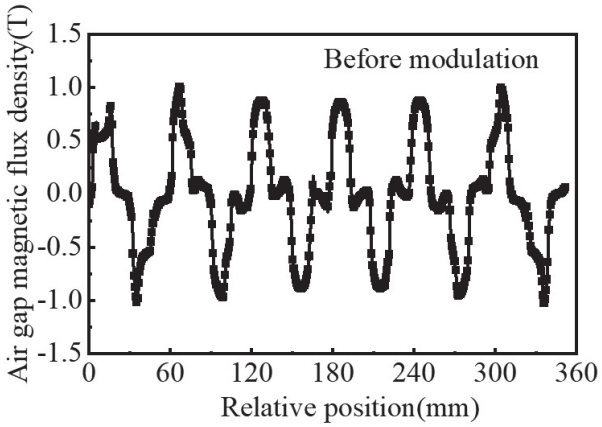

Fig. 8. Lower air gap magnetic flux before modulation.

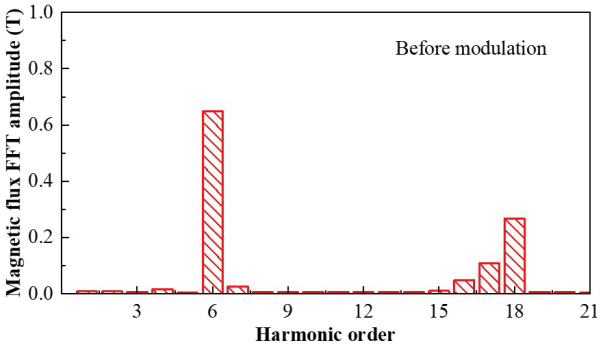

Fig. 9. Lower air gap magnetic flux harmonic.

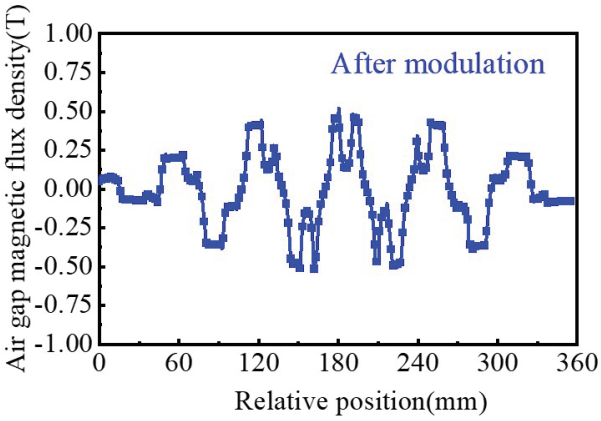

Fig. 10. Upper air gap magnetic flux after modulation.

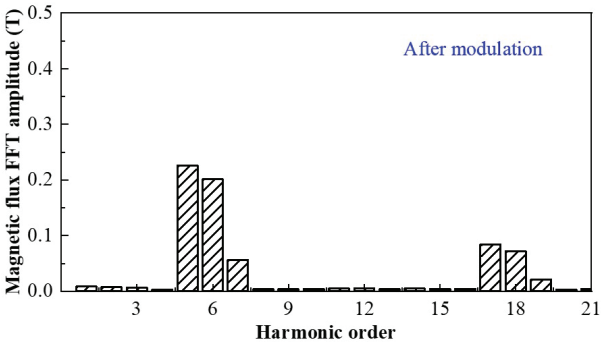

Fig. 11. Upper air gap magnetic flux harmonic.

Therefore, the flux in the lower air gap is mainly dominated by the 6th harmonic. That is, before the modulator is applied, the 6th harmonic flux amplitude in the lower air gap is the largest. The number of poles of the modulator is 11.

According to equation (8), in the upper air gap, the 5th harmonic flux amplitude is the largest. In Fig. 11, according to the finite element calculation, the 5th harmonic flux amplitude in the upper air gap is the largest, which is also consistent with the theoretical derivation. Therefore, when the 5th harmonic magnetic field is generated by the upper stator winding, stable energy transfer can be achieved, which is the basic working principle of the proposed MFM-TFM. Therefore, when the number of magnetic field pole pairs generated by the stator I winding is 5, stable power transmission can be achieved.

The distribution of magnetic field lines of the mover at different positions is shown in Fig. 12. At position A, the flux linkage of phase A is maximum. At position B, the flux linkage of phase A is short-circuited. The flux linkage of phase A is 0. At position C, the flux linkage of phase A is maximum in reverse direction.

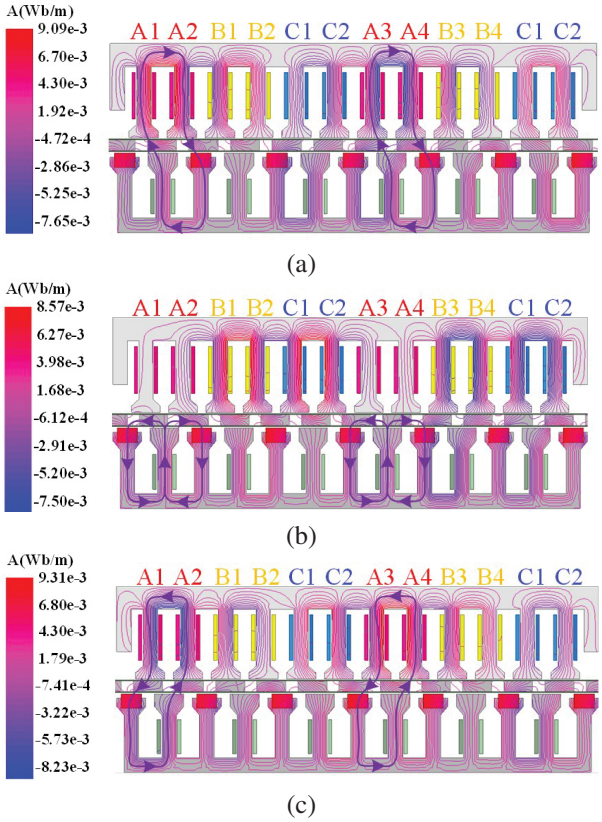

Fig. 12. Magnetic flux paths for different mover positions: (a) Position A, (b) Position B, and (c) Position C.

B. MFM-TFM optimization design and loss calculation

In this paper, a multi-objective optimization algorithm is used to optimize the main parameters of the MFM-TFM. The average thrust, output power and efficiency of the MFM-TFM are focused on. The influence of structural parameters on average thrust and thrust fluctuation needs to be considered comprehensively. The initial structural parameters and optimization design process of the MFM-TFM are shown in Table 3 and Fig. 13. First, the structural parameters of the MFM-TFM are analyzed by correlation to obtain the main structural parameters. According to the parameter variation range in Table 3, the electromagnetic performance of the MFM-TFM is parametrically calculated. The multi-objective optimization algorithm is used to find the optimal solution for the parameter optimization results. Compared with the width of the modulator, the electromagnetic performance of the MFM-TFM is more obviously affected by the modulator length. Although a larger modulator length can reduce thrust fluctuation and increase back EMF within a certain range, the reduction in average thrust is also very obvious. High average thrust and low thrust fluctuation are set as optimization targets. The number of winding turns and slot fill rate are comprehensively considered to obtain the optimized structural parameters as shown in Table 3.

In this paper, the second-generation non-dominated sorting genetic algorithm-II (NSGA-II) is adopted to optimize the proposed MFM-TFM structure. NSGA-II is an improved version of the non-dominated sorting genetic algorithm (NSGA), which improves the convergence of the algorithm by adopting a fast non-dominated sorting algorithm and a crowding algorithm.

Table 3: Optimization range of the main parameters

Optimization Parameters	Symbol	Range	Step Length	Final Value
PM width	w_{PM}	4-14	1	10 mm
Upper stator tooth boots length	$l_{u-stator}$	16-24	2	20 mm
Modulator length	l_m	14-28	1	20 mm
Lower stator tooth boots length	$l_{l-stator}$	16-24	2	20 mm
Modulator width	w_m	3-12.5	0.5	10 mm
PM length	l_{pm}	4-30	2	14 mm
Upper stator yoke width	$w_{u-stator}$	10-24	2	16 mm
Lower stator yoke width	$w_{l-stator}$	6-14	2	10 mm

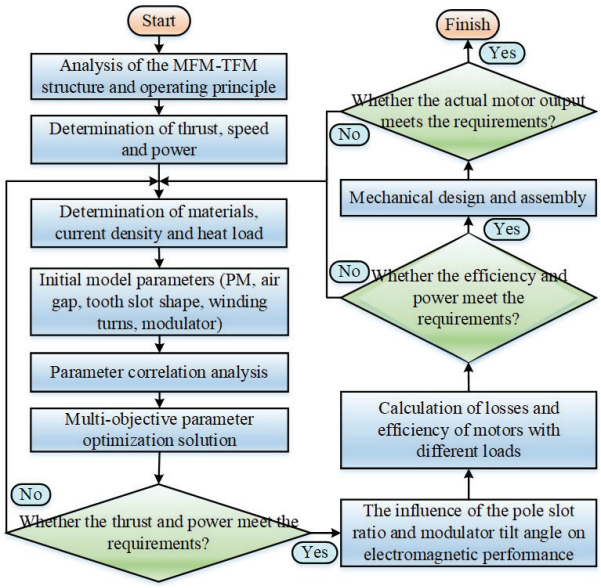

Fig. 13. Design and optimization process of the MFM-TFM.

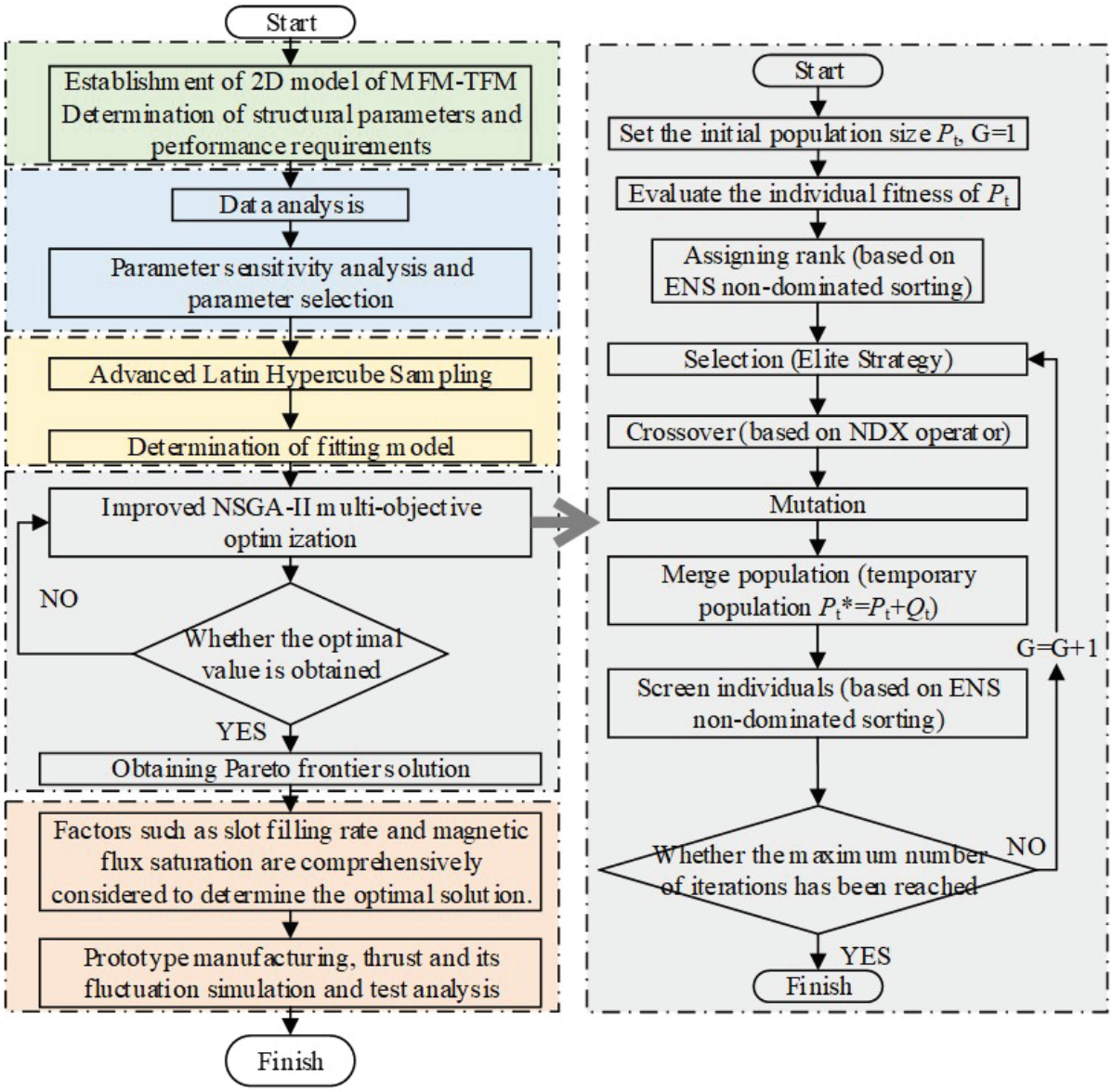

Fig. 14. Optimization process based on the improved NSGA-II algorithm.

In the design of MFM-TFM, the performance indicators of the MFM-TFM, such as load average thrust and thrust fluctuation, are used as objective functions. The optimization variables mainly include the structural parameters of MFM-TFM, such as permanent magnet shape, modulator shape and tooth slot shape as shown in Table 3. The optimization objectives are mainly the electromagnetic performance of the MFM-TFM, such as maximizing the average thrust and minimizing the thrust fluctuation.

The optimization process based on the multi-objective optimization algorithm is shown in Fig. 14. The specific steps are as follows:

① The optimization objectives and design variables are determined. The optimization objectives of the designed MFM-TFM are lower thrust fluctuation and higher average thrust.

② Based on ANASYS Maxwell software, the thrust fluctuation and average thrust data of MFM-TFM with different structural parameters are calculated. The sensitive parameter analysis method is used to calculate and analyze the sensitivity function of the design variables to the optimization objectives. Structural parameters with high sensitivity are selected to generate the required sample points. Based on the sample points, the response surface model is built.

③ The surrogate model is built. According to the sample points, the fitted model is obtained based on Advanced Latin Hypercube Sampling.

④ The improved NSGA-II algorithm is used to solve the model in step ③. In order to better solve the multi-objective optimization problem of MFM-TFM design, the normal distribution crossover (NDX) operator and the efficient non-dominated sorting (ENS) sorting were adopted. The joint model was built in Maxwell & Workbench & OptiSLang. According to the variable constraints and target requirements, the pareto front solution was generated.

⑤ The slot fill rate, magnetic flux saturation, slot width and assembly of MFM-TFM were comprehensively considered to determine the final parameters of the design variables. Based on the finite element method, the back EMF, average thrust and thrust fluctuation were calculated and experimentally verified.

The influence of different structural parameters on electromagnetic performance is studied. The motor thrust under different air gap widths is shown in Figs. 15 and 16. It can be seen that as the air gap width increases, the thrust of the modulator decreases. This is because when the air gap increases, the air gap magnetic resistance also increases, and the effective magnetic flux change decreases. So, the thrust also decreases. However, the air gap width needs to consider the performance and assembly difficulty comprehensively. The influence of PM and core width on thrust is given in Figs. 17 and 18. It can be seen that as the width of the permanent magnet increases, the thrust also gradually increases. However, the influence of the width of the permanent magnet on the thrust is not significant. The change of thrust under different width coefficients is given in Fig. 18. It can be seen that when the core width coefficient gradually decreases, the thrust of the mover gradually increases. But the thrust increase rate gradually decreases. When the width coefficient reaches 0.57, the thrust increase gradually reaches saturation.

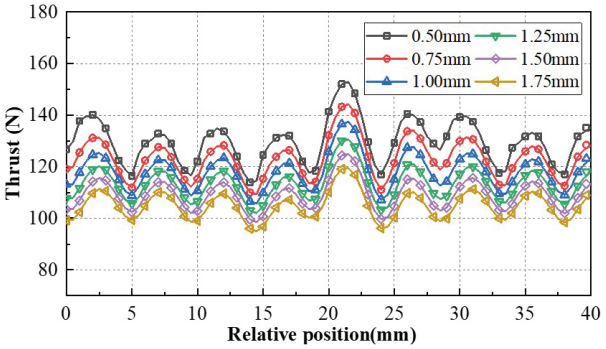

Fig. 15. Effect of upper air gap width on thrust of single stator.

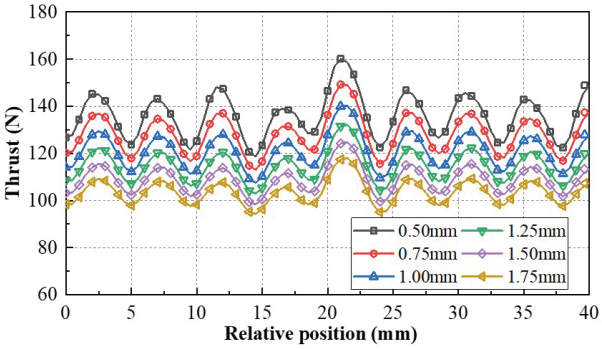

Fig. 16. Effect of lower air gap width on thrust of single stator.

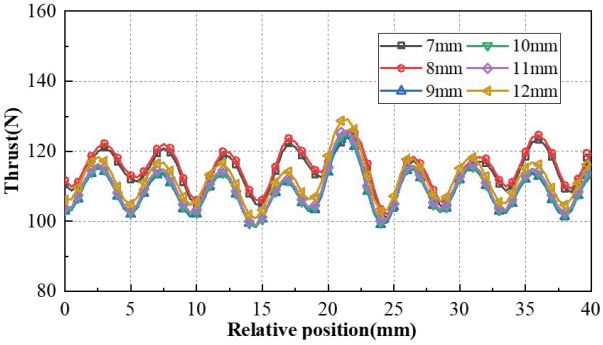

Fig. 17. Effect of PM lengths on thrust of single stator.

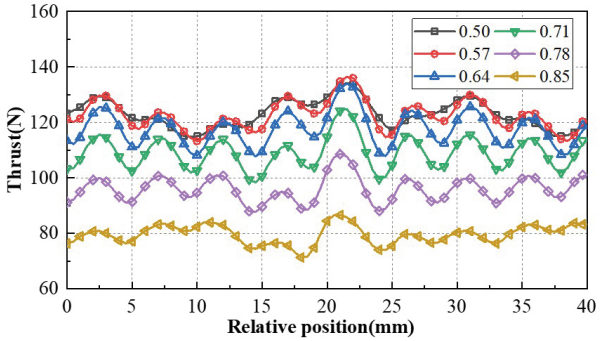

Fig. 18. Effect of core widths factor on thrust.

In order to study which variables have a greater impact on the performance of MFM-TFM, the sensitivity analysis is employed. The sensitivity index can be expressed as:

$$S_{ni} = \frac{\partial f}{\partial z_i}|_{NOP}\frac{z_i}{f} \approx \frac{\Delta f/f}{\Delta z_i/z_i}, \tag{13}$$

where f is the optimization target response, z_i is the design variable. The load average thrust and thrust fluctuation are the optimization target. Then, the weight coefficient is used to comprehensively evaluate each variable, and the comprehensive sensitivity index *G(ni)* is

introduced, which can be expressed as:

$$Gni = w_1 \left|SF_{\text{Average}}\right| + w_2 \left|SF_{\text{Fluctuation}}\right|, \quad (14)$$

where SF_{Average} and $SF_{\text{Fluctuation}}$ are the sensitivity indices of the load average thrust and thrust fluctuation, respectively, w_1 and w_2 are the weight coefficient of load average thrust and thrust fluctuation. The sum of w_1 and w_2 is 1.

The objective function is given in equation (15). The range of optimization variables and other constraints are given in Table 3 and equations (16), respectively:

$$\textit{The objective functions} \begin{cases} \max\{F_{\text{Average}} \\ \min\{F_{\text{Fluctuation}} \end{cases}. \quad (15)$$

$$\textit{Other restrictions} \begin{cases} 0.45 \leq \text{Slot fill rate} \leq 0.7 \\ 1.5 \leq \text{Magnetic density value} \leq 2.2 \end{cases}. \quad (16)$$

The voltage and current curves of MFM-TFM are given in Figs. 19 and 20. It can be seen that the waveform sinusoidality of the back EMF is relatively high. The waveform sinusoidality of the load current is also relatively high. This shows that the electromagnetic performance of the MFM-TFM proposed in this paper is relatively good. The influence of the modulator, permanent magnet and pole shoe on the electromagnetic performance of the motor is given in Figs. 21 and 22. It can be seen that when the modulator width is 10 mm and the length is 20 mm, the thrust of the mover is relatively high. For thrust fluctuation, it can be seen that the length of the stator I shoe has a greater influence on the thrust fluctuation.

When the length of the stator I shoe gradually increases, the thrust fluctuation also gradually increases. This is mainly caused by the interaction of the tooth slot force. The thrust fluctuation is relatively less affected by the width of the permanent magnet.

For the adopted NSGA-II, the genetic algorithm population size is 200. The crossover probability is 0.8. The mutation probability is 0.02. The number of iterations is 200 generations.

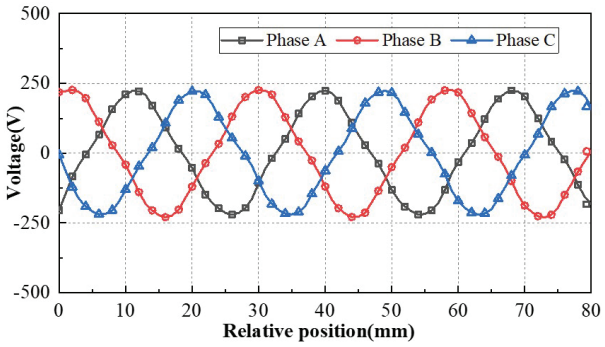

Fig. 19. Back EMF of MFM-TFM.

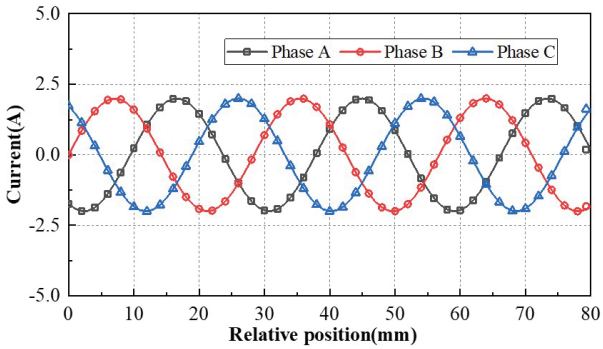

Fig. 20. Armature current of MFM-TFM.

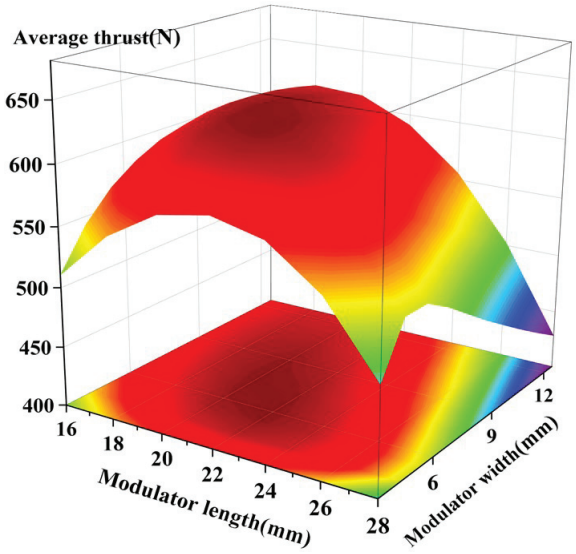

Fig. 21. Effect of modulator on average thrust.

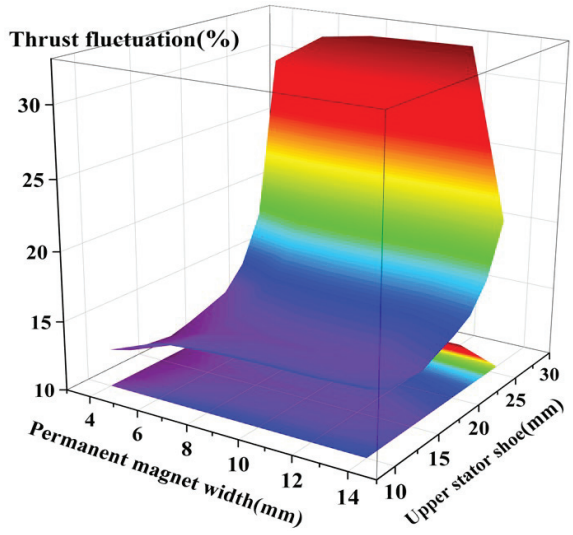

Fig. 22. Effect of permanent magnet and stator shoe on thrust fluctuation.

Scatter plots of average thrust and thrust fluctuation of MFM-TFM with different designs are given in Fig. 23. Sensitivity analysis of optimization parameters to average thrust and thrust fluctuation is given in Fig. 24. According to the variation range of MFM-TFM optimization parameters, the thrust fluctuation and average thrust are calculated and analyzed.

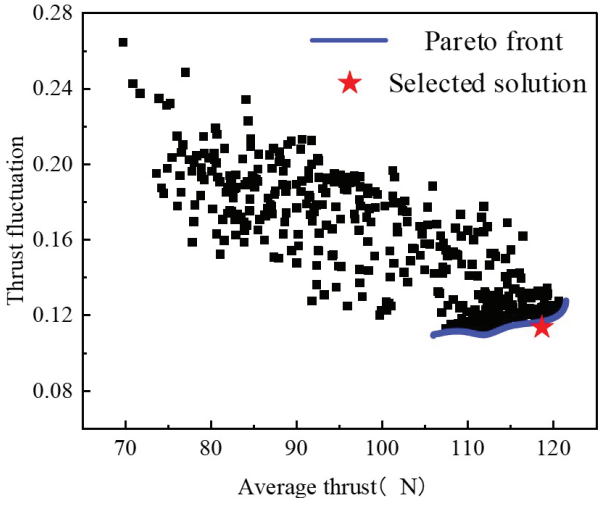

Fig. 23. Scatter plots of average thrust and thrust fluctuation of MFM-TFM with different designs.

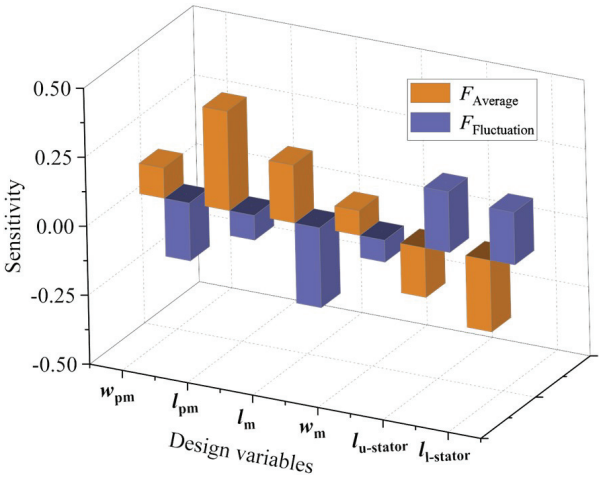

Fig. 24. Sensitivity analysis of optimization parameters to average thrust and thrust fluctuation.

In the calculation results, the pareto front solution is obtained. According to the comprehensive sensitivity index, slot filling rate and magnetic flux saturation constraints, the optimized design parameters are determined. For the selected design points, the sensitivity of different optimization parameters to the average thrust and thrust fluctuations are analyzed. In Fig. 24, the sensitivity of the permanent magnet length and the lower stator tooth boots length to the average thrust is relatively large. The sensitivity of the modulator length and the permanent magnet width to the thrust fluctuation is relatively large.

In order to further verify the stability and reliability of the designed structure, the magnetic flux distribution under no-load and rated-load conditions is shown in Figs. 25 and 26.

In Fig. 26, it can be seen that, except for the high magnetic flux saturation of the upper stator teeth, the saturation of most of the motor magnetic flux is low. Therefore, according to the magnetic flux calculation results, it can be seen that the electrical load selection of the MFM-TFM is reasonable.

In order to further study the loss and efficiency of the proposed MFM-TFM, the hysteresis loss, additional loss, eddy current loss and total loss are shown in Fig. 27. It can be seen that as the armature current gradually increases, the loss also gradually increases. Since the stator core is made of laminated silicon steel sheets, the hysteresis loss, additional loss, eddy current loss and total loss are much smaller than those of non-laminated sheets. At the rated current of 2 A, the average thrust of the motor reaches 612.54 N.

In order to reflect the advantages of the structure proposed in this paper, the electromagnetic performance comparison between MFM-TFM and different linear motors is shown in Table 4. When the armature current

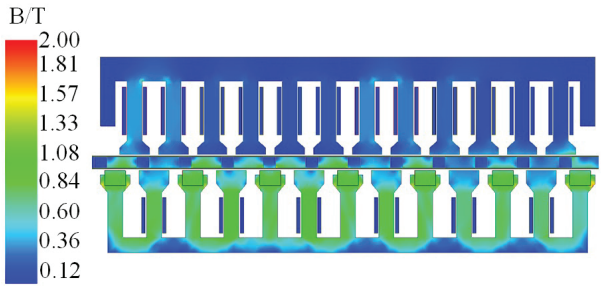

Fig. 25. No-load magnetic flux density distribution.

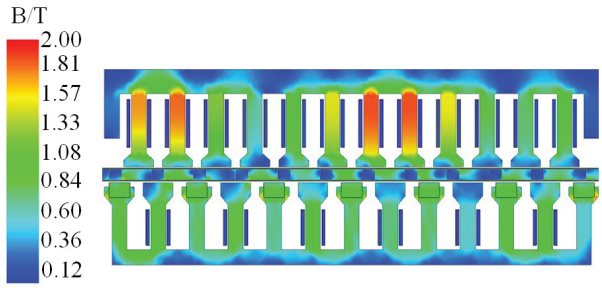

Fig. 26. Magnetic flux distribution at rated load.

Table 4: Comparison of machine performances

	Proposed MFM-TFM	TF-FRLM [22]	TF-PMLM [23]	EDT-PMLSM [24]	CT-PMLSM [25]
Rated thrust (N)	612.5	278.6	117.8	3335.7	2612.9
Rated power (W)	612.5	278.6	117.8	1214.9	951.1
Active volume (m^3)	6.2e – 3	1.8e – 3	1.3e-3	3.8e – 2	3.8e – 2
Thrust ripple (%)	17.4	34.4	2.6	5.0%	8.4%
Thrust per active volume (kN/m^3)	98.8	153.5	91.6	87.8	68.8
Power per active volume (kW/m^3)	98.8	153.5	91.6	35.2	27.1
Efficiency (%)	81.6	-	80.8	91.1	90.7

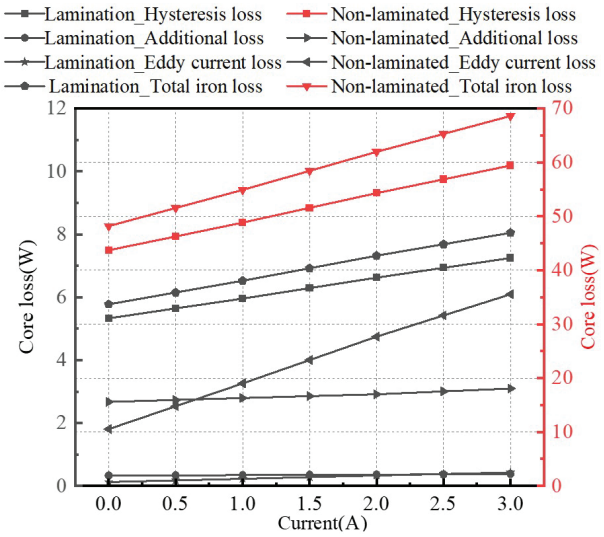

Fig. 27. Loss calculation and analysis of single stator.

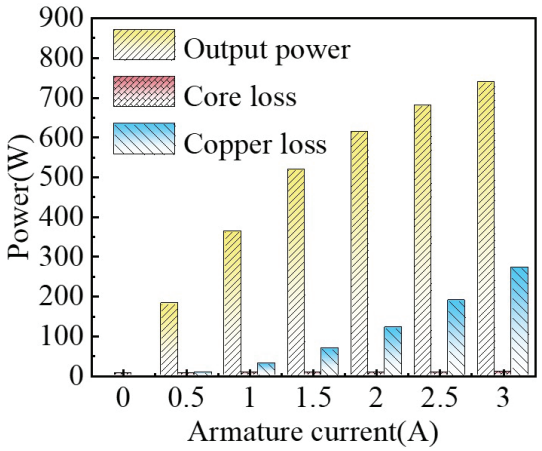

Fig. 28. Loss of MFM-TFM with the variation of armature current.

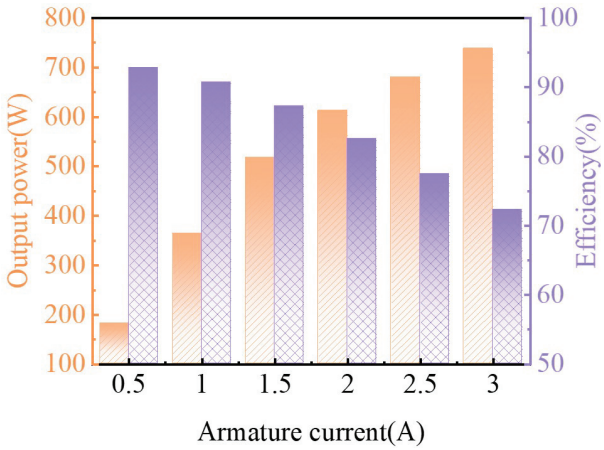

Fig. 29. Output power and efficiency of MFM-TFM with the variation of armature current.

is 2 A and the mover speed is 1 m/s, the calculated thrust of the mover is 612.5 N. It can be seen from Table 4 that the proposed MFM-TFM has a higher thrust density compared with the conventional PMLSM, which is mainly due to the magnetic field modulation effect of the mover. In addition, the thrust fluctuation of the proposed MFM-TFM is relatively small.

The proposed MFM-TFM has two very significant advantages. First, the mover of the ordinary PMSLM is covered with permanent magnets. Due to the high cost of permanent magnets, the manufacturing cost of the motor is very high when the mover is long. However, the mover of the proposed MFM-TFM is made of cheap ferromagnetic materials. The manufacturing cost of the MFM-TFM is lower. The MFM-TFM is very suitable for long stroke applications. Therefore, the MFM-TFM proposed in this article has huge application potential in new energy high-voltage disconnector. Second, based on the modulation effect of the magnetic field, the MFM-TFM has the advantages of high-power density and small thrust fluctuation in low-speed direct drive applications.

Loss of MFM-TFM with the variation of armature current is given in Fig. 28. Output power and efficiency of MFM-TFM with the variation of armature current are given in Fig. 29. As can be seen from Figs. 28 and 29, the

main loss of the motor is copper loss. As the armature current gradually increases, the loss and output power of the motor gradually increase. When the armature current exceeds 2 A, the increase in output power is no longer obvious. When the armature current is 2 A, the motor efficiency is 81.6%.

IV. PROTOTYPE AND EXPERIMENTAL TESTING

In order to verify the rationality of the MFM-TFM topology proposed in this paper and the accuracy of the calculation results, a prototype was designed and manufactured. An experimental platform was built to test the thrust and no-load back EMF of the motor at different armature currents.

Stator I punching, modulator and stator II punching are given in Fig. 30. The thrust curves at different positions of the mover are shown in Fig. 31. It can be seen from Fig. 31 that the calculated thrust value is larger than the measured value. On the one hand, this is mainly due to the fact that the mover will be affected by friction during the test.

On the other hand, there will be some errors during the motor assembly process. The calculated value of the average thrust and the measured value of the average thrust are compared and analyzed as shown in Table 5. It can be seen that the calculated value and the measured value are highly consistent. The error between the thrust test results and the calculation results is basically within 5%, which meets the engineering error requirements. The no-load back EMF calculation results and measurement results have good consistency as shown in Fig. 32. Therefore, the rationality of the MFM-TFM topology structure proposed in this paper and the accuracy of the calculation results are verified.

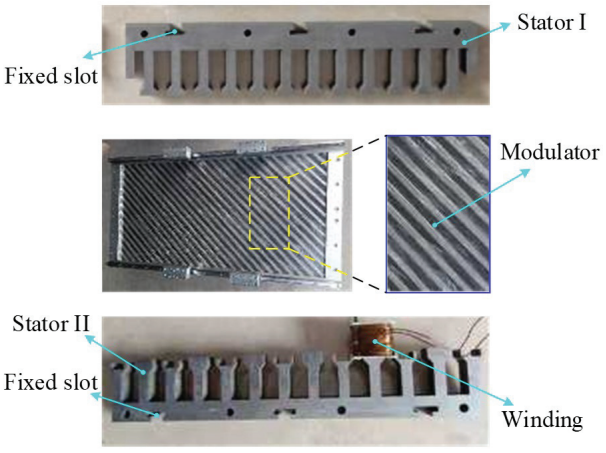

Fig. 30. Prototype.

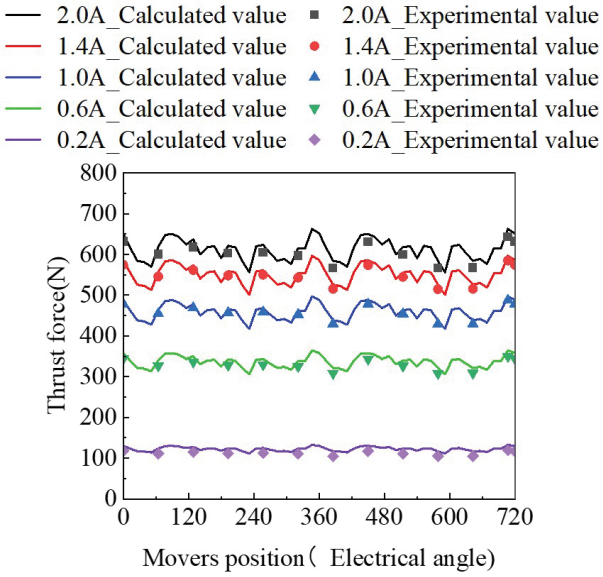

Fig. 31. Comparison of prototype test and calculation results.

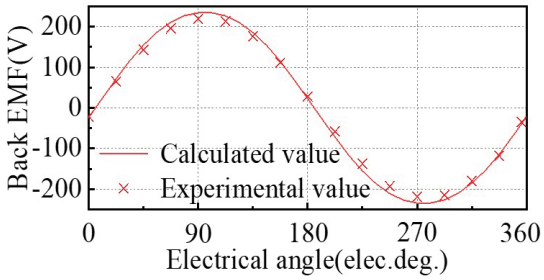

Fig. 32. No-load back EMF.

Table 5: Prototype thrust simulation and experimental measurement results

Current (A)	Calculated Thrust Average (N)	Measured Thrust Calculated Value (N)	Error (%)
0.2	71.97	68.1	-5.68
0.6	216.94	209.38	-3.61
1	363.21	356.18	-1.97
1.4	490.56	483.59	-1.44
2	612.54	605.52	-1.16

V. CONCLUSION

A direct-drive magnetic field modulation transverse flux motor is proposed in this paper. Based on the magnetic field modulation principle, high-speed magnetic field motion can be converted into low-speed high-thrust motion. Based on the transverse magnetic field, stator I and stator II are made of laminated silicon steel.

Hysteresis loss, eddy current loss and additional loss are effectively reduced. A prototype is manufactured. An experimental test platform is built. The thrust and back electromotive force are measured and compared with the experimental values. The rationality of the proposed topology and the accuracy of the calculation results are verified. The following conclusions are obtained:

(1) After the action of the tilt modulator, the air gap flux density dominated by the 6th harmonic in the lower air gap is modulated into the air gap flux density dominated by the 5th harmonic in the upper air gap. When the 5-pole magnetic field is generated by the stator I armature winding, the power can be stably transmitted from the stator I armature winding to the mover.
(2) In the modulated air gap flux density, the amplitude of the low-order harmonic is much larger than that of the high-order harmonic. Therefore, the average thrust can be improved by increasing the amplitude of low-order harmonics.
(3) After the air gap width, PM, core and modulator parameters are optimized, the no-load back EMF and current waveform sinusoidal properties are better. Through core lamination, the loss of the transverse flux motor is effectively reduced. The rated average thrust of the motor reaches 612.54 N.

REFERENCES

[1] X. Chai, J. Si, Y. Hu, Y. Li, and D. Wang, "Characteristics analysis of double-sided permanent magnet linear synchronous motor with three-phase toroidal windings," *Applied Computational Electromagnetics Society (ACES) Journal*, vol. 36, no. 08, pp. 1099-1107, Oct. 2021.

[2] I. I. Abdalla, T. B. Ibrahim, and N. M. Nor, "A study on different topologies of the tubular linear permanent magnet motor designed for linear reciprocating compressor applications," *Applied Computational Electromagnetics Society (ACES) Journal*, vol. 31, no. 01, pp. 85-91, Aug. 2021.

[3] N. Ullah, M. K. Khan, F. Khan, A. Basit, W. Ullah, T. Ahmad, and N. Ahmad, "Comparison of analytical methodologies for analysis of single sided linear permanent magnet flux switching machine: No-load operation," *Applied Computational Electromagnetics Society (ACES) Journal*, vol. 33, no. 08, pp. 923-930, July 2021.

[4] M. Jawad, Y. Haitao, Z. Ahmad, and Y. Liu, "Design and analysis of a novel linear oscillating actuator with dual stator rectangular geometry," *Applied Computational Electromagnetics Society (ACES) Journal*, vol. 36, no. 10, pp. 1384-1392, Oct. 2021.

[5] X. Deng, R. Li, L. Hao, A. Zhang, and J. Zhou, "Design and finite element analysis of a novel permanent magnet assisted reluctance synchronous motor," *Applied Computational Electromagnetics Society (ACES) Journal*, vol. 35, no. 9, pp. 1012-1021, Sep. 2020.

[6] R. Chen, C. He, S. Li, N. Li, L. Zhang, D. Liu, and X. Zhang, "Characterization of partial discharge of metal particles inside gas-insulated switchgear under excitation of disconnecting switch operating overvoltage," in *2024 7th International Conference on Energy, Electrical and Power Engineering (CEEPE)*, 2024.

[7] W. Liang and J. Lantao, "Research and development of intelligent control system for motor mechanism of high-voltage circuit breaker," *High Voltage Electrical Appliances,* vol. 54, pp. 59-69, Mar. 2018.

[8] C. Fuguo, H. Dawei, Z. Ruimin, and D. Guannan, "Intelligent control system for motor drive of 550 kV high-voltage disconnector," *Instrument Technology and Sensor,* pp. 78-82, 87, Apr. 2017.

[9] J. Lipeng, Z. Li, L. Hongliang, D. Chi, L. Kaibao, and J. Dongming, "Finite element numerical calculation of plum blossom contact of high-voltage switch cabinet based on magnetic field-temperature field coupling," *China Testing*, vol. 48, pp. 8-12, June 2022.

[10] L. Jianlin, Z. Hongwei, Z. Bin, X. Shaobin, H. Yuhua, L. Tao, and H. Bokai, "Transient temperature rise variation of low-voltage switchgear under short-circuit fault due to electromagnetic thermal coupling," *Journal of Xi'an University of Science and Technology*, vol. 41, pp. 1138-1147, June 2021.

[11] M. Xinyou, W. Lijun, W. Rui, and Z. Wenzhe, "Simulation study on temperature rise characteristics of medium voltage switchgear under fault conditions," *High Voltage Technology,* vol. 48 pp. 2276-2282, June 2022.

[12] P. Tao, T. Bingnan, Z. Lihua, H. Zhipeng, L. Mingxian, and G. Xiaoxue, "Study on temperature rise characteristics of medium voltage switchgear under typical contact fault," *High Voltage Technology,* vol. 47, pp. 4331-4345, Dec. 2021.

[13] L. Jiangtao, S. Yi, and L. Qingyu. "Research on thermal defect assessment algorithm for high current switch cabinet plum blossom contact," *High Voltage Electrical Appliances*, vol. 56, pp. 124-129, 138, Nov. 2020.

[14] H. Xinbo, X. Zhipeng, T. Yi, J. Botao, and C. Li, "Thermal fault warning strategy and its application for high voltage switch cabinet," *Electric Power Automation Equipment,* vol. 39, pp. 181-187, July 2019.

[15] Z. Wentao, Z. Yiming, W. Zichi, L. Shaohua, and L. Dexiang, "Research on fault diagnosis and analysis method of electromagnet of spring operating mechanism," *High Voltage Electrical Appliances,* vol. 56, pp. 209-214, Apr. 2020.

[16] H. Xinbo, W. Haidong, H. Haiyan, Z. Yongcan, Z. Hao, and X. Zhipeng, "Anti-blocking technology and application of electric chassis vehicle for high-voltage switch cabinet," *High Voltage Electrical Appliances,* vol. 54, pp. 205-211, 218, Mar. 2018.

[17] L. Jing, M. Jiajian, Z. Dianbo, W. Jing, and C. Kenan, "Simulation analysis and experimental study of temperature field of metal-enclosed high-voltage switchgear trolley contact," *High Voltage Electrical Appliances,* vol. 51, pp. 74-79, Aug. 2015.

[18] F. Jiawei, G. Yu, Y. Xingchao, Z. Xiang, and W. Hongwei, "Gear local fault detection using servo motor built-in encoder," *Journal of Vibration Engineering*, pp.1-8, June 2024.

[19] C. Ruihong and T. Zhaozhan, "Design of loading and unloading manipulator for gearbox gear meshing test machine," *Machine Tool and Hydraulics,* vol. 48, pp. 41-46, Mar. 2020.

[20] S. Rui, L. Pingping, L. Huazhi, H. Yangsen, and W. Jun, "Experimental study on transmission principle of new wind turbine generator set," *Renewable Energy,* vol. 36, pp. 1086-1091, July 2018.

[21] L. Jun, K. Baoquan, and Y. Xiaobao, "Optimization and design of double alternating pole transverse flux linear motor," *Transactions of China Electrotechnical Society*, vol. 35, pp. 991-1000, May 2020.

[22] B. Q. Kou, J. Luo, X. Yang, and L. Zhang, "Modeling and analysis of a novel transverse-flux flux-reversal linear motor for long-stroke application," *IEEE Trans. Ind. Electron*, vol. 63, no. 10, pp. 6238-6248, Oct. 2016.

[23] X. Zhao and S. Niu, "Development of a novel transverse flux tubular linear machine with parallel and complementary PM magnetic circuit for precision industrial processing," *IEEE Trans. Ind. Electron*, vol. 66, no. 6, pp. 4945-4955, June 2019.

[24] Z. Yan, J. Si, R. Nie, Z. Cheng, L. Dong, and Z. Li, "Performances analysis of a tubular permanent magnet linear generator with 120° phase belt toroidal windings," in *Proc. 13th Int. Symp. Linear Drives Ind. Appl.*, 2021.

[25] Z. Yan, J. Si, R. Nie, Z. Cheng, L. Dong, and Z. Li, "Comparative analysis of tubular permanent magnet linear generator with equidirectional toroidal windings and conventional toroidal windings," *IEEE Trans. Ind. Appl.,* vol. 58, no. 4, pp. 4614-4624, July-Aug. 2022.

Yi Su received the master's degree from Guangxi University, Nanning, China, in 2015. He is currently a senior engineer and researcher. His research interests are motor design, power switchgear design and operation and maintenance technology.

Lei Gao received the B.S. degree from Harbin Institute of Technology, Harbin, China, in 2007. He is currently a senior engineer. His research interests are motor design, power switchgear design and operation and maintenance technology.

Wei Huang received the master's degree from Guangxi University, Nanning, China, in 2021. He is currently an engineer. His research interests are power switchgear design and operation and maintenance technology.

Jian Qin received the B.S. degree from North China Electric Power University, Beijing, China, in 2000. He is currently a senior engineer. His research interests are power switchgear design and operation and maintenance technology.

Yufeng Lu received the Ph.D. degree from Harbin University of Science and Technology, Harbin, China, in 2013. He is currently a senior engineer and senior researcher. His research interests are power switchgear design and operation and maintenance technology.